Dissertation zur Erlangung des Doktorgrades
der Fakultät für Chemie und Pharmazie
der Ludwig-Maximilians-Universität München

Structural and functional characterization of MRN & ATM in DNA double strand break repair

von

Kristina Stakyte

aus

Panevėžys, Litauen

2022

Erklärung

Diese Dissertation wurde im Sinne von § 7 der Promotionsordung vom 28. November 2011 von Herrn Prof. Dr. Karl-Peter Hopfner betreut.

Eidesstattliche Versicherung

Diese Dissertation wurde eigenständig und ohne unerlaubte Hilfe erarbeitet.

München, den 24.06.2022

.....

Kristina Stakyte

Dissertation eingereicht am	28.06.2022
1. Gutachter	Prof. Dr. Karl-Peter Hopfner
2. Gutachter	Prof. Dr. Roland Beckmann
Mündliche Prüfung am	10.08.2022

"Two roads diverged in a wood, and I –

I took the one less traveled by,

And that made all the difference."

Robert Frost

This thesis has been prepared from July 2017 to June 2022 in the laboratory of Professor Dr. Karl-Peter Hopfner at the Gene Center of the Ludwig-Maximilians-University Munich.

This is a cumulative thesis based on following publications:

Jansma M., Linke-Winnebeck C., Eustermann S., Lammens K., Kostrewa D., Stakyte K., Litz C., Kessler B., Hopfner K.P. 2020. Near-Complete structure and model of Tel1ATM from *Chaetomium thermophilum* reveals a robust autoinhibited ATP state. **Structure** 28:83–95.

Stakyte K.*, Rotheneder M.*, Lammens K.*, Bartho J.D*, Grädler U., Fuchß T., Pehl U., Alt A., van de Logt E. and Hopfner K.P. 2021. Molecular basis of human ATM kinase inhibition. **Nature Structure & Molecular Biology**. 2021 Oct;28(10):789-798.

* These authors contributed equally.

Rotheneder M.*, Stakyte K.*, Lammens K., Bartho J.D, van de Logt E., Alt A., Kessler B., Jung Ch., Roos W., Steigenberger B. and Hopfner K.P. 2022. Cryo-EM structure of the Mre11-Rad50-Nbs1 complex reveals the molecular mechanism of scaffolding functions. **Manuscript in revision.**

* These authors contributed equally.

Table of Contents

Summary *1*

1. Introduction *3*

1.1 DNA damage **3**

1.1.1 Sources of DNA damage 5

1.1.2 DNA double strand breaks 6

1.1.3 Programmed DNA double strand breaks 7

1.2 DNA double strand break repair **8**

1.2.1 Non-homologous end joining 8

1.2.2 Homologous recombination 11

1.2.3 Repair pathway choice 13

1.3 The MRN complex **14**

1.3.1 Mre11 15

1.3.2 Rad50 19

1.3.3 Nbs1 22

1.3.4 Cellular functions of the MRN complex 24

1.3.5 MRN associated human diseases 28

1.4 The ATM kinase **29**

1.4.1 The PIKK family of protein kinases 30

1.4.2 Cellular functions of ATM 32

1.4.3 ATM kinase in cancer 36

1.4.4 ATM inhibition as cancer treatment 36

1.5 Objectives **39**

2. Publications *41*

2.1 Near-Complete structure and model of Tel1ATM from *Chaetomium thermophilum* reveals a robust autoinhibited ATP state **41**

2.2 Molecular basis of human ATM kinase inhibition **61**

2.3 Cryo-EM structure of the Mre11-Rad50-Nbs1 complex reveals the molecular mechanism of scaffolding functions **87**

3. Discussion *145*

3.1 The auto-inhibited conformation of *ct*MRN **145**

3.2 DNA binding modes of eukaryotic MRN complex **147**

3.3 The structural and functional roles of Nbs1 in the MRN complex **149**

3.4 Rad50 zinc-hook mediated MRN dimerization **152**

3.5 Functional clustering of MRN complexes **155**

3.6 DNA binding activity of ATM/Tel1 kinase **156**

3.7 Auto-inhibited state of ATM/Tel1 kinase and potential activation mechanisms **158**

3.8 Inhibitors of ATM in cancer treatment **161**

4. References *164*

Acknowledgements *181*

Summary

Our DNA is constantly subjected to various types of endogenous and exogenous agents and cellular processes that cause different sorts of DNA damages. DNA double strand breaks (DSBs) are one of the most dangerous kinds of DNA damage as they can result in chromosomal rearrangements and cell death. To avert the consequences of persistent DNA DSBs, cells have developed two basic repair mechanisms: non-homologous end joining (NHEJ) and homologous recombination (HR). NHEJ involves direct ligation of two broken DNA ends. This pathway is active throughout the cell cycle and is the predominant way to eliminate DSBs in mammalian cells, however, it can occasionally lead to loss of genetic information. HR is a more complex and highly accurate process. It is limited to S/G2 phases of the cell cycle as it requires a homologous DNA sequence to act as a template for synthesis-dependent repair.

The evolutionarily conserved Mre11-Rad50-Nbs1 (MRN) complex plays a key role in the initial recognition, processing and signaling of DNA DSBs. It also functions in DNA tethering and telomere maintenance. The MRN complex is composed of two meiotic recombination 11 (Mre11), two SMC-like ATPase (Rad50) and one Nijmegen breakage syndrome protein (Nbs1) subunits. Mre11 is a manganese dependent endonuclease and 3'-5' exonuclease. Rad50 consists of a bipartite nucleotide binding domain (NBD) and up to 50 nm long coiled-coils that terminate with a zinc-hook. Eukaryote specific Nbs1 acts as a regulator and protein recruitment module of the MR complex. Ataxia telangiectasia mutated (ATM) kinase is one of the proteins recruited by Nbs1 and is responsible for initiation of the DSB signaling cascade.

ATM is a member of the phosphoinositide 3-kinase related kinases (PIKK) family. Most PIKKs are involved in cellular responses to various stresses. ATM, like all members of the PIKK family, has a C-terminal kinase domain, which shares significant homology with the catalytic domain of PI3-lipid kinases. The catalytic domain of ATM is surrounded by regulatory domains that link kinase to a large N-terminal HEAT-repeat domain. The latter acts as a scaffolding platform for interacting proteins. ATM resides in the nucleus as an autoinhibited dimer, but gets rapidly activated by the MRN complex following detection of DNA DSB. Activation of ATM is postulated to involve an autophosphorylation-induced change in conformation, or monomerization. Due to the key role that ATM plays in responding to DNA DSBs, this kinase has become a target for anticancer drug development.

A few decades of research on MRN complex and ATM kinase have led to a better understanding of structural features and functions of these proteins. However, some important questions remain to be answered. Regarding MRN, the structure of the full-length eukaryotic complex is still missing; especially the function of Rad50 coiled-coils and Nbs1 remains poorly characterized. A high-resolution structure of human ATM, which could aid structure-based drug design, remains to be solved. Due to the shape and size of MRN and ATM, structural studies of full-length proteins by X-ray crystallography were not successful.

The first part of this thesis focuses on structural studies of Tel1, a fungal ATM ortholog from *Chaetomium thermophilum (ct)*, and human ATM. The first near-complete high-resolution structure of Tel1 was determined using cryo-electron microscopy (cryo-EM), with the kinase domain at 2.8 Å and overall structure including N-terminal HEAT repeat domains at 3.7 Å. The well-resolved ATPγS-bound active sites revealed that catalytic residues are in the active conformation, but the kinase stays in the autoinhibited state. The PIKK regulatory domain acts as a pseudo-substrate and blocks a direct access to the active site. Using cryo-EM, structures of human ATM with ATPγS and chemically diverse ATM inhibitors KU-55933 and M4076 were solved to below 3Å resolution. These structures revealed the inhibited conformation of ATM active site and explained inhibition and selectivity profiles of kinase inhibitors based on their binding modes. The N-terminal HEAT repeat domains of human ATM were built at high resolution for the first time exposing two zinc-binding motifs.

In the second part of this thesis the structural and biochemical data of *ct*MRN is presented. The combination of cryo-EM, X-ray crystallography and AlphaFold2 led to a near complete structure of full-length *ct*MRN, which was validated by crosslinking mass spectrometry. This structure clarified the overall architecture of eukaryotic MRN, expanded the knowledge on the structure of Nbs1 and revealed the conformation of Rad50 coiled-coils in the “resting” state. In agreement with cryo-EM density, the crystal structure of the tetrameric Rad50 zinc-hook revealed a molecular basis for the DNA tethering by MRN. In addition, structure-based mutations of hsRad50 zinc-hook indicated a requirement for zinc-hook tetramerization to perform efficient DNA repair in human cells. The results of DNA binding assays allowed us to conclude that *ct*MRN possesses two DNA binding sites, which show different ATP dependency and DNA topology preference.

Taken together, the work described in this thesis provides new insights into the molecular architecture and regulation of the ATM kinase and the MRN complex.

1. Introduction

1.1 DNA damage

Deoxyribonucleic acid (DNA) is a hereditary molecule that stores genetic information in all known organisms and many viruses. DNA is susceptible to chemical modifications by various sources of DNA damaging agents (see section 1.1.1 for sources of DNA damage). Additionally, regular cellular processes, such as replication, can alter the genetic code[1]. On one hand, mutagenesis plays a crucial role in the generation of diversity needed for evolution. On the other hand, changes in DNA can lead to disadvantageous mutations resulting in cell death or disease development. Therefore, DNA damage repair (DDR) mechanisms have evolved to protect the integrity of the genome[2].

As sources of exogenous and endogenous DNA damage are very diverse (section 1.1.1), they lead to a variety of DNA aberrations ranging from simple base modifications to DNA double-strand breaks (DSBs)[1]. Hence, different types of DDR mechanisms are needed to eliminate the individual damage (Figure 1). Base excision repair (BER) functions in removal of endogenous DNA damage, such as deamination, alkylation, oxidation, depurination and single-strand breaks (SSBs)[3]. Nucleotide excision repair (NER) is responsible for eliminating helix-distorting DNA lesions that are mainly caused by exogenous mutagens. For instance, UV radiation induced pyrimidine dimers and bulky DNA adducts formed by mutagenic chemicals[4]. Mismatch repair (MMR) removes errors from newly synthesized DNA leading to increased fidelity of DNA replication[5]. The repair of DNA strand breaks is mediated by SSB repair or DSB repair pathways depending on the extent of the damage. There are two main pathways for DSB repair: non-homologous end joining (NHEJ) and homologous recombination (HR) (see sections 1.2.1 and 1.2.2)[6,7]. In addition, a few specific DNA lesions can be eliminated by direct reversal, like photolyase-mediated reversal of UV-induced cyclobutane pyrimidine dimers[8].

Unrepaired DNA damage can cause stalled replications forks, which can be overcome by translesion synthesis (TLS). This process uses specific TLS polymerases that are less strict in their base-pairing requirements and, therefore, can replicate damaged DNA. In this case the avoidance of deleterious consequences of stalled replication forks is associated with an increased risk of mutagenesis because TLS polymerases are error prone[9].

DNA damage accumulates over time and many DNA lesions are tolerated by the cell. Nevertheless, there is an alternative cellular strategy for coping with DNA lesions, that cannot be repaired and are too severe to be tolerated, known as DNA damage-induced cell death. This acts as a protective mechanism against genomic instability that could lead to cancer development[10].

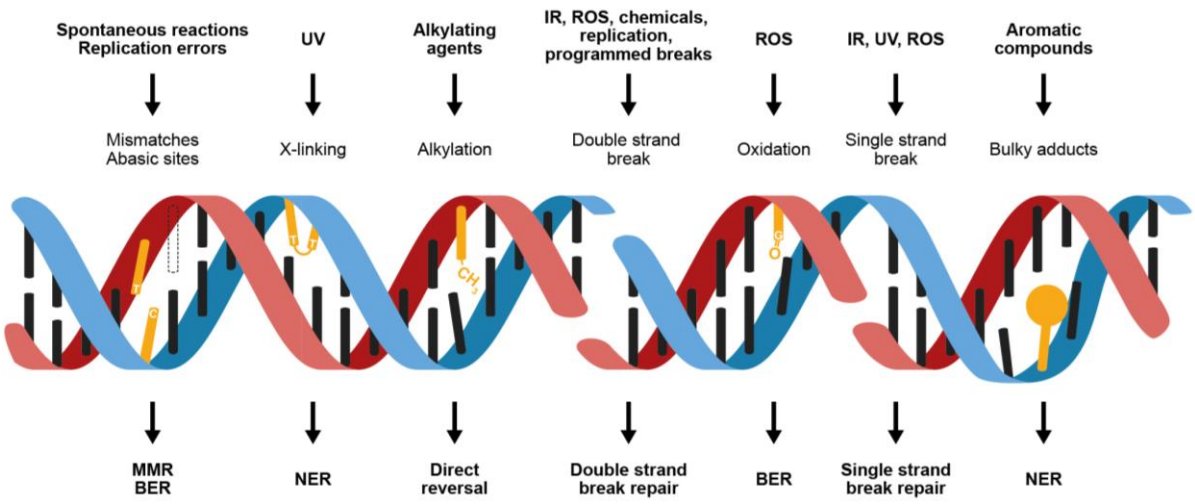

Figure 1. Overview of different types of DNA damage and repair pathways used for damage elimination. Top labels indicate endogenous and exogenous sources of DNA damage with types of DNA damage that can be generated. Latter are also illustrated in a schematic DNA structure. Bottom labels name the pathways of DNA damage repair that are used to eliminate respective types of DNA damage.

Cancer and various other diseases are linked to dysfunctional DNA repair machinery. Fast accumulation of unrepaired DNA damage and failure for all damaged cells to undergo programmed cell death cause genomic instability and cancer. This was first observed in skin cancer cases, in xeroderma pigmentosa patients that have a dysfunctional NER pathway[11]. Excessive DNA damage is also associated with neurodegenerative disorders like Alzheimer's and Parkinson's as well as ageing[12].

Dysfunctional DDR in cancer cells can render them hypersensitive to genotoxic agents as accumulating damage can eventually trigger cell death. Hence, ionizing radiation (IR) and chemotherapeutic agents are used as primary anti-cancer therapies[13]. The efficiency of these therapies is increased by combining them with inhibitors of DDR, based on the concept of synthetic lethality, where simultaneous targeting of two genes in the same pathway is lethal[14].

Studies of the DDR machinery are crucial for understanding mechanisms of DNA repair and causes of various human diseases allowing development of more effective treatments.

1.1.1 Sources of DNA damage

Sources of DNA damage can be divided into two main classes: endogenous and exogenous. The latter includes environmental, physical and chemical agents that can affect DNA integrity. For instance, UV and IR, alkylating and crosslinking agents. On the other hand, the main endogenous sources are water and reactive oxygen species (ROS) that can lead to hydrolytic and oxidative DNA damage, respectively[1].

IR is a term that encompasses multiple different types of high-energy radiation including alpha-, beta- and gamma-radiation, and X-rays. IR can damage the DNA directly or indirectly by radiolysis of water and generation of highly reactive hydroxyl radicals[15]. Roughly 65% of radiation-induced DNA damage comes from hydroxyl radicals and results in a variety of base lesions[16]. In addition, IR can cause SSBs with unique 3'-phosphate or 3'-phosphoglycolate DNA ends and DSBs resulting from closely positioned multiple damage sites on both DNA strands[16,17]. UV radiation is another exogenous source of DNA damage and is a leading cause of skin cancer in humans. UV damages DNA by inducing formation of covalent linkages between two adjacent pyrimidines that can cause distortion of the DNA helix[1].

Alkylating agents are exogenous chemicals that can modify DNA with alkyl groups having mutagenic and carcinogenic effects. These chemicals are highly abundant in our environment; can be found in food and tobacco smoke[1]. They are also used as chemotherapeutic agents, for instance, cyclophosphamide is used to treat lymphoma, leukemia and solid tumors[18]. Crosslinking agents, like psoralen, can cause damage by intercalating into DNA and forming inter-strand crosslinks upon photoactivation[1]. Another type of DNA-damaging environmental chemicals are polycyclic aromatic hydrocarbons (PAHs) that are commonly found in charred foods, tobacco smoke and car exhaust[19]. The DNA-reactive intermediates of PAHs are generated in the liver by the P-450 system. These intermediates can intercalate into DNA and form carcinogenic DNA adducts[1].

Some toxins produced by microorganisms and fungi as a defense mechanism have DNA-damaging modes of action. For instance, aflatoxin B1 is a very strong liver carcinogen. This toxin gets metabolized in the liver leading to the formation of its active form, which causes depurination by weakening the glycosidic bond[20].

One of the main endogenous sources of DNA damage is replication. Each time cell divides it has to make a copy of its whole genome and errors can occur resulting in DNA damage. The high-fidelity replicative polymerases (δ and ε) have 3'-5' exonuclease (proofreading) activity and a low error rate. However, there are more polymerases that synthesize DNA during replication and repair without proofreading, like Polα and Polβ[21]. Resulting errors can be single base substitutions, deletions and insertions. In addition, strand slippage at repetitive sequences can lead to more extensive insertions and deletions resulting in alterations of the reading

frame[1]. All these errors, if they remain unrepaired, can give rise to mutations in the next round of replication. Another endogenous source of DNA damage linked to protein activity is topoisomerases (TOPs), which function to remove helical DNA tension during replication and transcription[22]. TOP activity involves formation of a DNA nick and TOP-DNA intermediates. In some cases (e.g., in the presence of nicks, mismatches) the intermediate gets trapped resulting in DNA damage known as suicidal complex[1].

In human cells, one of the major causes of spontaneous mutagenesis is base deamination. This process results in DNA bases cytosine, adenine, guanine and 5-methyl cytosine becoming uracil, hypoxanthine, xanthine and thymine, respectively. Hence, in the first round of replication following base deamination a wrong base pairing occurs resulting in point mutations[1]. Base deamination occurs more frequently when DNA is single-stranded and, therefore, is linked to replication, transcription and recombination, that involve single-stranded DNA steps[23]. DNA bases can also be damaged by their cleavage from the sugar-phosphate backbone creating an abasic site. This can be caused by spontaneous hydrolysis or as an intermediate of the (base excision repair) BER pathway[24].

ROS are the byproducts of cellular respiration in mitochondria and peroxisomal metabolism[25]. Excessive intracellular amounts of ROS can cause different sorts of oxidative base lesions and 2-deoxyribose modifications[26]. The most reactive type of ROS is the hydroxyl radical, that is able to damage not only DNA, but also proteins and lipids. Regarding DNA damage, hydroxyl radicals can react with DNA bases by abstracting hydrogens from their methyl groups, attacking nearby sugar residues and adding to their double bonds[1]. In addition, oxidation of lipids by hydroxyl radicals can form aldehydes that react with adenine, guanine and cytosine forming mutagenic adducts[27]. ROS can also damage the DNA backbone by introducing SSBs[28]. There is a link between high intracellular levels of ROS, and therefore excessive amounts of DNA damage, and human diseases, like Alzheimer's, Parkinson's and cancer[29].

Abnormal DNA methylation can also be damaging by introducing point mutations. For instance, O^6-methylguanine (O6MeG) leads to transition from G:C to A:T as there are equal chances that DNA polymerase inserts cytosine and thymine opposite the O6MeG[30]. Endogenous sources of DNA methylation include betaine, choline and S-adenosylmethionine. The latter is used as a methyl donor during normal methylation reactions, but it can spontaneously methylate adenine and guanine[1].

1.1.2 DNA double strand breaks

DNA DSBs are considered to be the most genotoxic type of DNA lesions. If misrepaired, DSBs may lead to chromosomal translocations that can cause fusion of genes or altered gene expression in some cases resulting in cancer. If unrepaired, DSBs can result in cell death[31].

The most prominent external source of DSBs is IR, which can induce closely positioned SSBs on both DNA strands. DSBs can also be caused by DNA exposure to chemotherapeutic agents[32]. For instance, TOPII inhibitor etoposide traps covalently linked DNA-TOPII intermediate after TOPII induced DSB[33].

A large number of DSBs are linked to DNA replication, where such breaks can arise by processing of stalled replication forks[32]. These can form when replication machinery encounters unusual DNA and chromatin structures or collides with DNA-binding proteins or transcription process. There are a few explanations for replication associated DSBs. Cells aim to eliminate stalled replication forks by using pathways that involve endonucleolytic cleavage and fragile DNA structures. In addition, stalled replication forks form persistent single-stranded DNA, which is exposed to endonucleases and prone to spontaneous breakage upon prolonged stalling resulting in DSBs[34].

Interestingly, not all DNA DSBs are unwanted consequences of DNA damaging agents or dysfunctional cellular processes. Programmed site-specific DSBs are required by several cellular processes.

1.1.3 Programmed DNA double strand breaks

Even though DNA DSBs are one of the most genotoxic types of DNA lesions, they are used by several physiologically and developmentally important processes and subsequently repaired[32].

In mammals, DSBs are used to initiate V(D)J recombination. B and T lymphocytes use B-cell and T-cell receptors, respectively, to recognize foreign pathogens. In order to recognize a large number of pathogens, a diversity of these receptors is required and is achieved by the V(D)J recombination. This process assembles previously scattered Variable, Diversity and Joining gene segments using a specialized somatic DNA rearrangement, which is initiated by the RAG protein complex induced DNA DSBs[35]. The resulting damage is often repaired by a regular DSB repair pathway of NHEJ (see section 1.2.1)[36].

DSBs are also important intermediates during the class switch recombination (CSR). There are five different classes of antibodies (IgM, IgD, IgG, IgA and IgE) that are identified by the different heavy-chain constant regions, which have different effectiveness against different pathogens[37]. Naïve B-cells express IgM and IgD antibodies, but depending on the encountered pathogen a specific type of antibody could be more effective. CSR exchanges the constant region of an antibody without altering the antigenic specificity. CSR involves deamination of cytosines in two switch regions upstream of the constant regions, generating uracil, which are recognized by the MMR and BER repair pathways and converted to DSBs[37,38]. DSBs are

repaired by classical or alternative NHEJ pathways omitting DNA between the switch regions (see section 1.2.1)[37].

Meiotic recombination is another cellular process that involves formation and repair of DNA DSBs. Meiosis is a special type of cell division that involves two rounds of chromosome segregation and generates haploid cells from diploid progenitors. The first round of meiosis is responsible for segregation of homologous chromosomes[39]. Meiotic recombination is used to connect maternal and paternal chromosomes to one another during prophase I and assure accurate chromosome segregation[40]. This recombination is initiated by topoisomerase-related Spo11, which catalyzes the creation of DSBs via formation of a covalently linked Spo11-DNA intermediate[41]. This structure gets recognized and repaired by HR factors (see section 1.2.2). Contrary to a regular HR pathway where sister chromatids are used as templates for repair, in this case recombination often occurs between homologs. Thus, meiotic recombination can lead to exchange of genetic information between maternal and paternal chromosomes[40].

1.2 DNA double strand break repair

In order to circumvent deleterious consequences of persistent DNA DSBs, cells have evolved intricate DNA repair mechanisms. These are conserved from bacteria to eukaryotes and share key events: sensing of the DSB, signaling of the damage to the cell and repair of the lesion. The two main pathways are template independent and mutagenic classical NHEJ (c-NHEJ), and template dependent and non-mutagenic HR[7,42]. A third pathway is an alternative-NHEJ (alt-NHEJ), which is even more error prone than c-NHEJ, but needed in cases when other pathways fail[42].

The importance of DNA DSB repair pathways is highlighted by the fact that defects in these pathways lead to severe outcomes ranging from embryonic lethality to disorders with pleiotropic features[43].

1.2.1 Non-homologous end joining

In mammals, NHEJ is the predominant pathway for the DNA double strand break repair. It involves recognition of broken ends, DNA end resection to generate microhomology or remove chemical modifications, and direct ligation[6]. Due to loss of genetic information during the process and lack of a template, NHEJ is a mutagenic pathway[44]. NHEJ can be divided into two sub-pathways; c-NHEJ and alt-NHEJ, as well as microhomology mediated end-joining (MMEJ)) (Figure 2). The composition of the DNA ends determines which of the NHEJ sub-

pathways is able to join the broken ends. C-NHEJ does not depend on microhomology, while alt-NHEJ requires 2-20 nucleotides microhomology and therefore a more extensive processing of the DNA ends[6].

The initial step in c-NHEJ is the recognition of the DSB by Ku70/80 heterodimer and recruitment of DNA-dependent protein kinase catalytic subunit (DNA-PKcs) to form a DNA-PK complex (Figure 2)[45–47]. This complex acts as a binding platform for other proteins involved in joining of DNA ends. Depending on the nature of the DNA ends, they are made suitable for ligation by minimal end resection or gap filling[48]. Artemis is a NHEJ specific nuclease, which can remove overhangs and hairpins that cannot be used for direct ligation[49]. Polymerases λ and μ (members of the Polymerase X family) can fill-in nucleotides at overhangs and extend DNA ends generating microhomology, respectively, making ends compatible for ligation[50,51]. Once processing of DNA ends is finished, they are ligated by DNA ligase IV in complex with X-ray repair cross-complementing protein 4 (XRCC4)[52]. The ligase activity is aided by XRCC4-like factor (XLF) [53]. In cases when no DNA end processing is required, DNA ligase IV and XRCC4 recruited by DNA-PK complex are sufficient to repair DSBs[48].

The alt-NHEJ is more error prone than c-NHEJ pathway of DNA DSB repair and is considered to be a major source of genomic instability and acts as a backup[42]. The alt-NHEJ requires 2-20 nucleotides microhomology and 3’ overhangs[6]. Proteins involved in initial stages of alt-NHEJ are poly ADP-ribose polymerase 1 (PARP1), MRN and CtBP-interacting protein (CtIP) (Figure 2)[54–56]. After DNA end processing, which could also be a part of failed HR or c-NHEJ, the 5’ strand is further resected by ERCC1/XPF[57]. Subsequently, polymerase θ extends DNA from the site where two 3’ overhangs are held together by microhomology using the other strand as a template[58]. Eventually, the resulting nicks are re-ligated by DNA ligase I or ligase III/XRCC1[59].

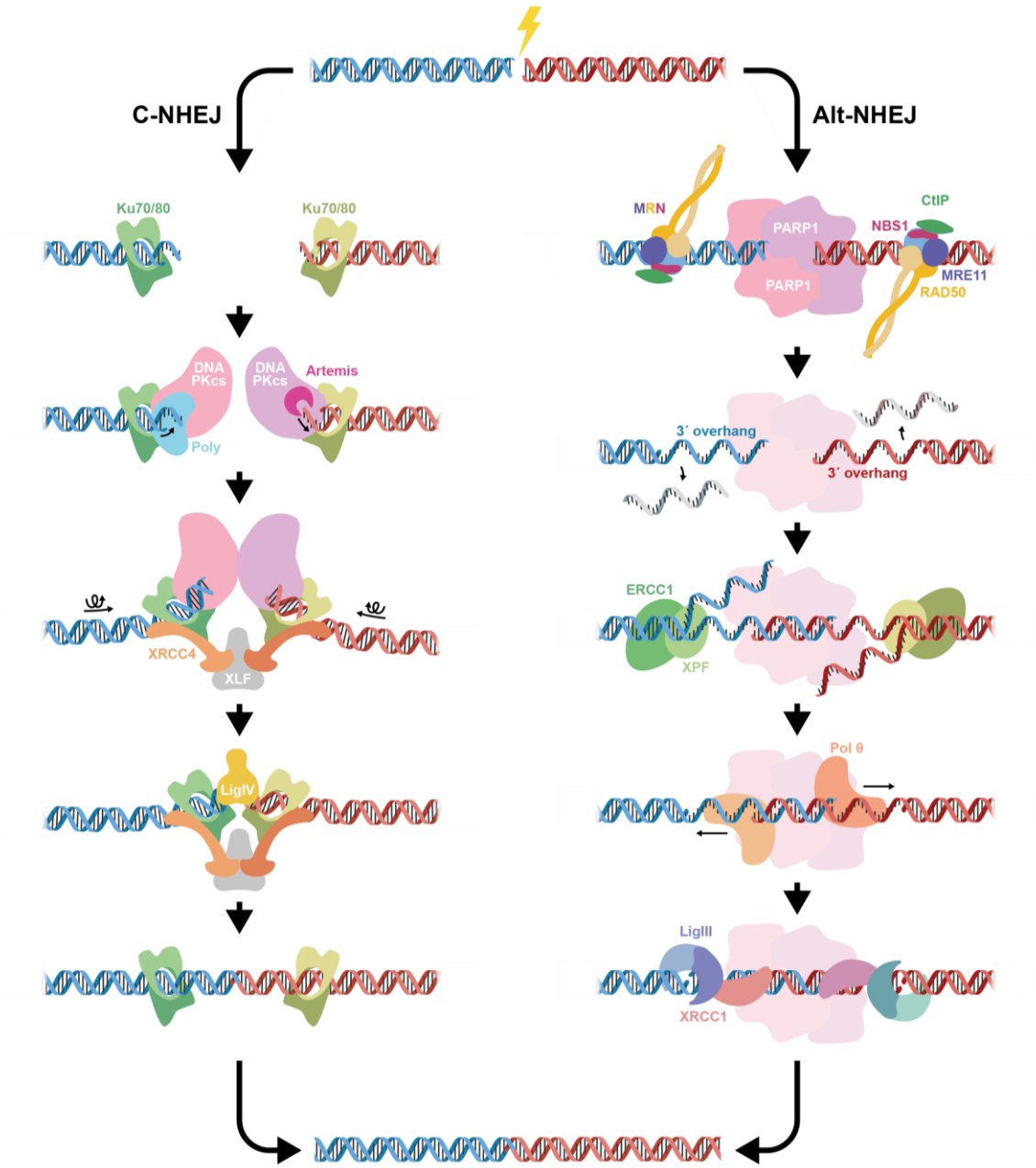

Figure 2. Overview of c-NHEJ and alt-NHEJ pathways of DSB repair. On the left, in c-NHEJ DNA ends are detected by Ku70/80 heterodimer leading to recruitment of DNA-PKcs and other factors involved in end processing and ligation. End processing involves addition and/or removal of nucleotides resulting in diverse DNA sequences at the repair site. On the right, in alt-NHEJ DNA ends are recognized and processed by PARP1 and MRN-CtIP complex generating 3' overhangs. Further processing can reveal microhomology, which keeps the strands together allowing gap filling and ligation.

1.2.2 Homologous recombination

HR is an evolutionarily conserved pathway that catalysis the exchange of genetic information between DNA molecules and is known to function in meiosis, horizontal gene transfer, rescue of collapsed or stalled replication forks and DNA DSB repair[60]. Hence, HR contributes to maintenance of genome integrity and enhancement of genetic diversity. In DSB repair, HR provides an error-free repair pathway as it proceeds after DNA is replicated and an intact copy can be used as a template. The canonical HR involves: detection of the DSB, initial short-range processing of broken ends, long-range processing and resection to generate a 3' strand overhang, strand invasion, ssDNA pairing with the homologous donor DNA, formation of synaptic complex, DNA synthesis, migration of displacement loop and holiday junction (HJ), resolution of HJ and nick ligation (Figure 3)[7].

In eukaryotes, DSBs are sensed by the MRN (Mre11-Rad50-Xrs2 (MRX) in *Saccharomyces cerevisiae*)[61]. MRN subsequently recruits ATM kinase, which gets activated at the site of the damage and phosphorylates a large number of substrates promoting efficient DNA repair and coordinating DNA repair with other DNA metabolic processes, e.g., replication and mitosis[62]. Together with CtIP (Ctp1 in *S.pombe*, Sae2 in *S. cerevisiae*), MRN is responsible for the initial 5' strand resection at the broken ends[63]. At first, it was not clear how the MRN complex with 3'-5' exonuclease activity could generate 3' overhangs[64]. It is now understood that MRN-CtIP performs an endonuclease cut of the 5'strand in the proximity of DNA ends and resects towards the DSB[65–67]. In addition, CtIP functions in the recruitment of breast cancer 1 (BRCA1) factor, which functions in further HR stimulation[68].

The initial short-range processing is followed by extensive 5' strand resection. This process is carried out by the helicase Bloom syndrome protein (BLM) in complex with either exonuclease 1 (Exo1) or DNA2 nuclease[69]. The resulting long ssDNA fragment is immediately coated by replication protein A (RPA), which is later replaced by Rad51 forming a recombinogenic filament[70]. The RPA to Rad51 exchange is mediated by multiple proteins with a crucial role played by BRCA2, which displaces RPA and recruits Rad51[71]. BRCA2 also functions in blocking Rad51 ATP hydrolysis and maintaining the active ATP-bound Rad51-ssDNA nucleofilament[71].

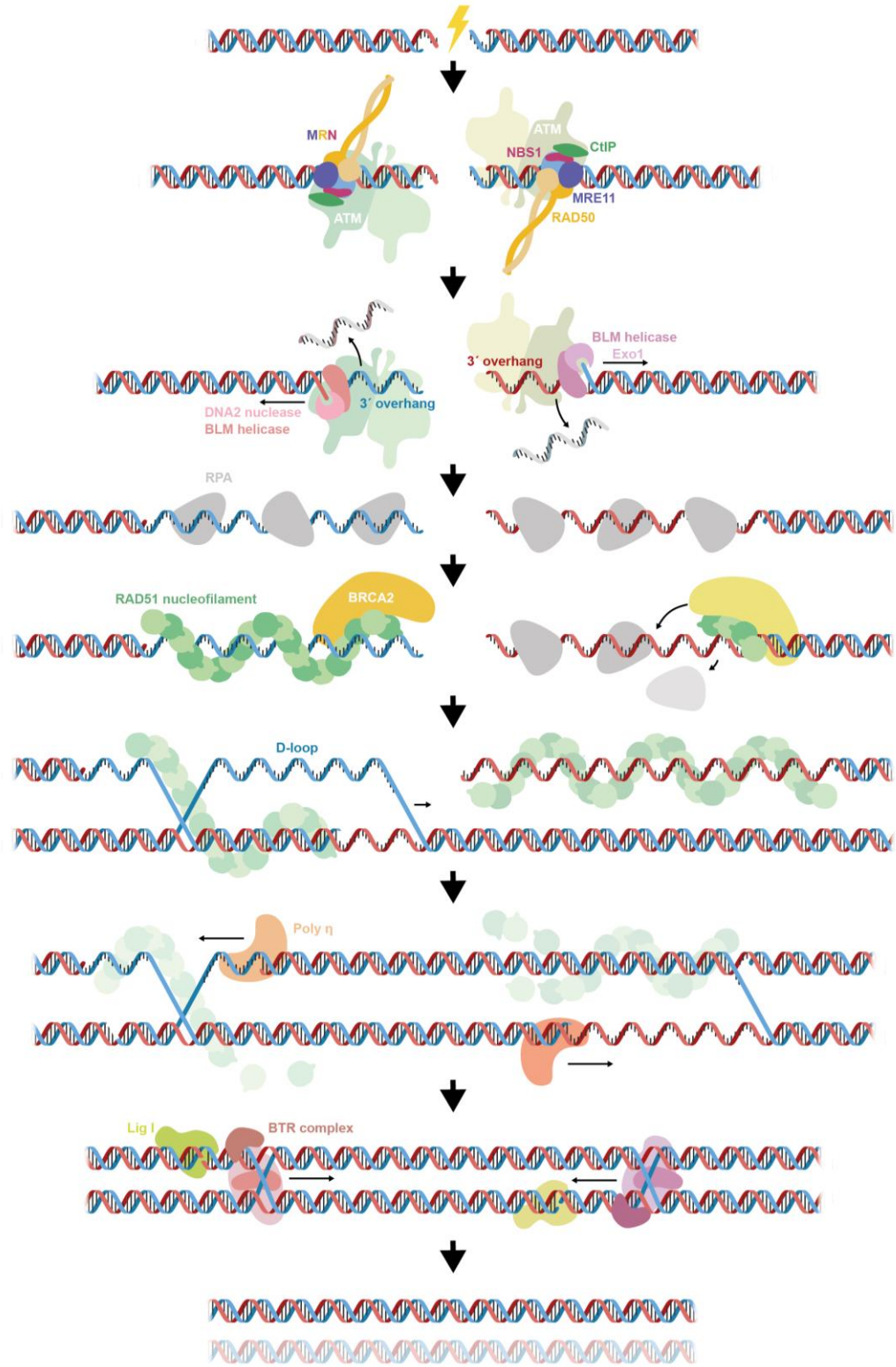

Figure 3. Overview of the canonical HR pathway of DSB repair. DSB formation is followed by DNA end recognition and processing resecting 5' strand. Generated 3' overhangs are coated by RPA and then Rad51 forming a recombinogenic filament that can search for homology and invade a homologous donor. The 3' end of the invading strand within the D-loop can serve as a primer for DNA polymerase, which copies information from the donor strand. Subsequent

ligation may lead to formation of double HJs, which are commonly resolved by the BTR complex. In other cases, nuclease and ligase activity is needed.

The Rad51 nucleofilament scans for a homologous DNA sequence. Once the target sequence is located, Rad51 mediates DNA strand invasion; complementary DNA strand gets displaced forming a displacement loop (D-loop) structure[72]. Rad51 dissociates from the invading DNA strand exposing a 3' DNA end, which can prime DNA synthesis mediated by polymerase η[73]. This process is followed by ligase I mediated DNA ligation and generation of a four-way branched DNA structure known as a Holliday junction (HJ)[74]. Depending on the type of recombination that occurs, single or double HJ intermediates can be formed and it is crucial to resolve them to achieve a proper chromosome segregation. Double HJs are primarily resolved by the BLM helicase-TopoisomeraseIIIα-RMI1-RMI2 (BTR) complex and result in non-crossover products. Single HJs are predominantly resolved by structure-selective endonucleases called HJ resolvases leading to either crossover or non-crossover products[75].

1.2.3 Repair pathway choice

The choice of DSB repair pathways is highly regulated by the cell cycle. The occurrence of HR is restricted to late S and G2 phases, when a template strand is available[76]. On the other hand, NHEJ can proceed throughout the most of the cell cycle. Classical HR and NHEJ pathways are both limited during mitosis, when a less understood mechanism of DSB elimination involving factors from both repair pathways is thought to take place[77]. The master regulators of DNA repair pathways are cyclin-dependent kinases (CDKs), activity of which rises progressively from entry into S phase until mitotic entry [76]. The main process that commits DSB repair to the HR pathway is the long-range resection of 5' strands[78]. Hence, rising levels of CDK activity in S phase result in phosphorylation and activation of enzymes promoting resection and HR, e.g. BRCA1, Nbs1, CtIP and Exo1 (Figure 4)[79–81]. While BRCA1 works to promote HR, 53BP1 functions to recruit factors involved in blocking DNA end resection (PTIP and RIF1) and moves repair pathway towards NHEJ [76,82]. Hence, for HR to be activated in S/G2 phases, the end protection activity of 53BP1 has to be weakened by processes involving BRCA1.

As a result of the cell cycle dependent regulation of DSB repair, NHEJ is a predominant pathway throughout the cell cycle with HR occurrences rising in the presence of a DNA template[76].

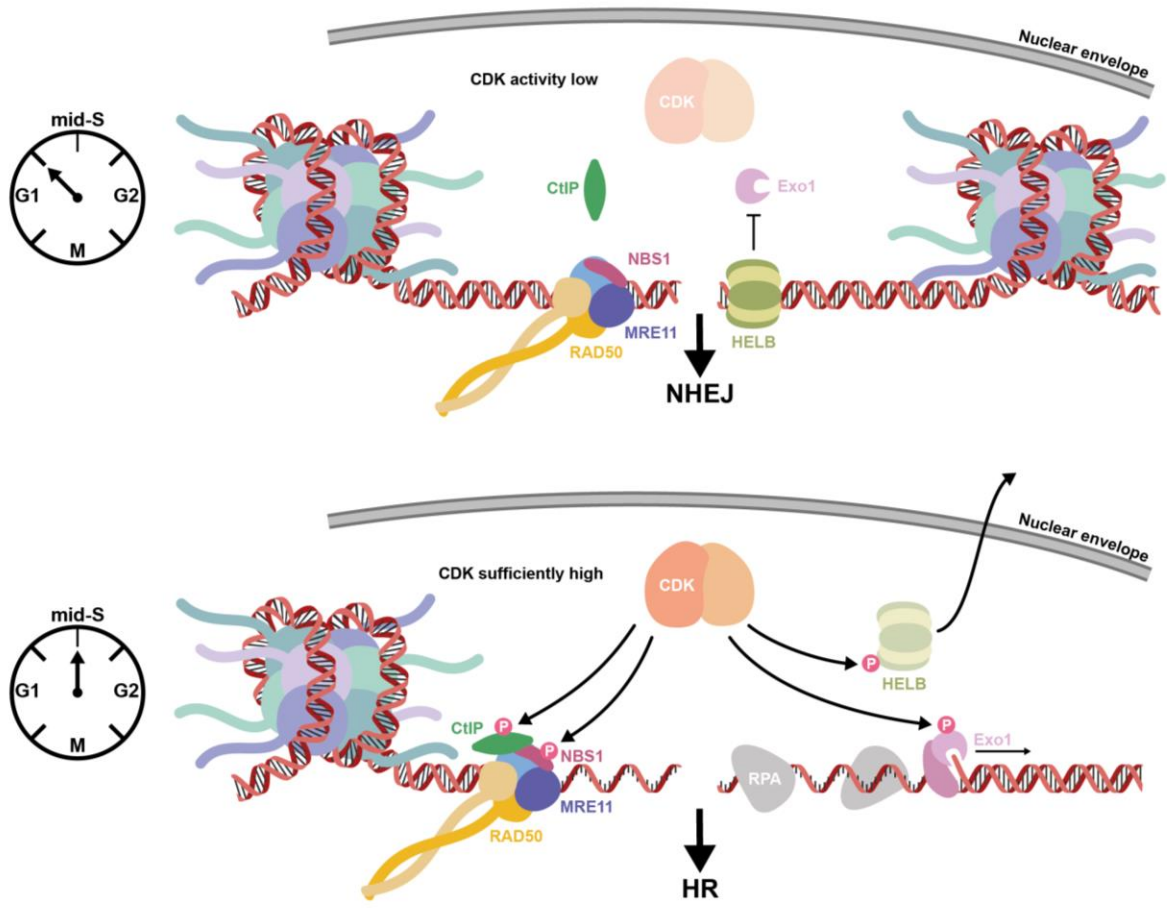

Figure 4. The timer model of cell cycle dependent activation of DSB repair by HR. The activity of CDKs progressively rise during the S phase, leading to phosphorylation and activation of factors, like Nbs1, CtIP and Exo1, stimulating resection and HR progression.

1.3 The MRN complex

The eukaryotic MRN complex is composed of three components: meiotic recombination 11 (Mre11), radiation sensitivity 50 (Rad50) and Nijmegen breakage syndrome 1 (Nbs1, also known as NBN or nibrin, X-ray sensitive 2 (Xrs2) in yeast). Both Mre11 and Rad50 are evolutionarily conserved and can be found in organisms ranging from bacteria to humans, and even viruses[83,84]. On the other hand, Nbs1 is only found in eukaryotes[85]. The stoichiometry of the complex is also conserved; dimeric Mre11 interacts with dimeric Rad50 and, in eukaryotes, a single Nbs1 binds to the core hetero-tetramer[63,86].

The MRN complex functions in different cellular processes, one of them being DNA DSB repair. The MRN is involved in detection of DNA damage as well as initial processing of broken DNA ends, making them reparable by HR or alt-NHEJ pathways[63]. In addition, MRN

mediates signaling of DNA damage to the cell via the ATM kinase, which then orchestrates the cellular response to the DNA damage, including cell cycle arrest [87].

This section will describe structures and functions of individual MRN components and cellular functions of the MRN complex.

1.3.1 Mre11

Mre11 is a highly conserved nuclease component of MRN complex. It consists of N-terminal nuclease domain followed by the capping domain, a flexible linker and a helix-loop-helix (HLH) motif, that binds to the coiled-coils of Rad50[88]. The HLH is followed by the C-terminal extension in eukaryotes. This extension shows DNA binding activity and contains a glycine-arginine-rich (GAR) motif (Figure 5A). The GAR motif has been shown to affect nuclease activity and recruitment of Mre11 to DNA damage foci[89].

Structural studies of Mre11 from different organisms show consistent architecture of its catalytic core with extra loop insertions in eukaryotes (Figure 5 B, C)[86,88,90]. Mre11 dimerizes via its phosphodiesterase domains and together with capping domains forms a U-shaped structure with a large cleft where Rad50 nucleotide binding domain (NBD) dimer or DNA bind (Figure 5 B-D)[86,88]. Each Mre11 molecule has a nuclease site composed of five conserved phosphodiesterase motifs with two coordinated Mn^{2+} ions (Figure 5 B)[88]. The capping domain, which partially shields the nuclease active site and was proposed to have a role in DNA substrate specificity, is separated from the nuclease domain by a short loop allowing flexibility (Figure 5 B)[88]. The Rad50 coiled-coil binding HLH domain is separated from the nuclease module by a long, flexible linker, which wraps around NBD of Rad50 and allows for large conformational changes[91,92]. The eukaryote specific C-terminus of Mre11 is predicted to be unstructured.

In the context of eukaryotic MR or MRN complex, Mre11 has 3’ to 5’ exonuclease activity on double-stranded DNA (dsDNA) and endonuclease activity on single-stranded DNA (ssDNA) as well as ability to open hairpins in the presence of ATP[64,85,93,94]. Endonuclease activity of the complex requires ATP hydrolysis by Rad50[95]. In addition, eukaryotic Mre11 shows 3’ to 5’ exonuclease activity in the absence of Rad50 indicating that Mre11 could have Rad50 independent functions[64,94]. For many years it was not understood how a complex with 3’ to 5’ exonuclease produces 3’ overhangs during DSB repair. Research in *S. cerevisiae* on processing of Spo11 induced breaks revealed that 5’ strand endonuclease activity is followed by limited 3’ to 5’ resection towards the DNA end resulting in 5’ resection[66].

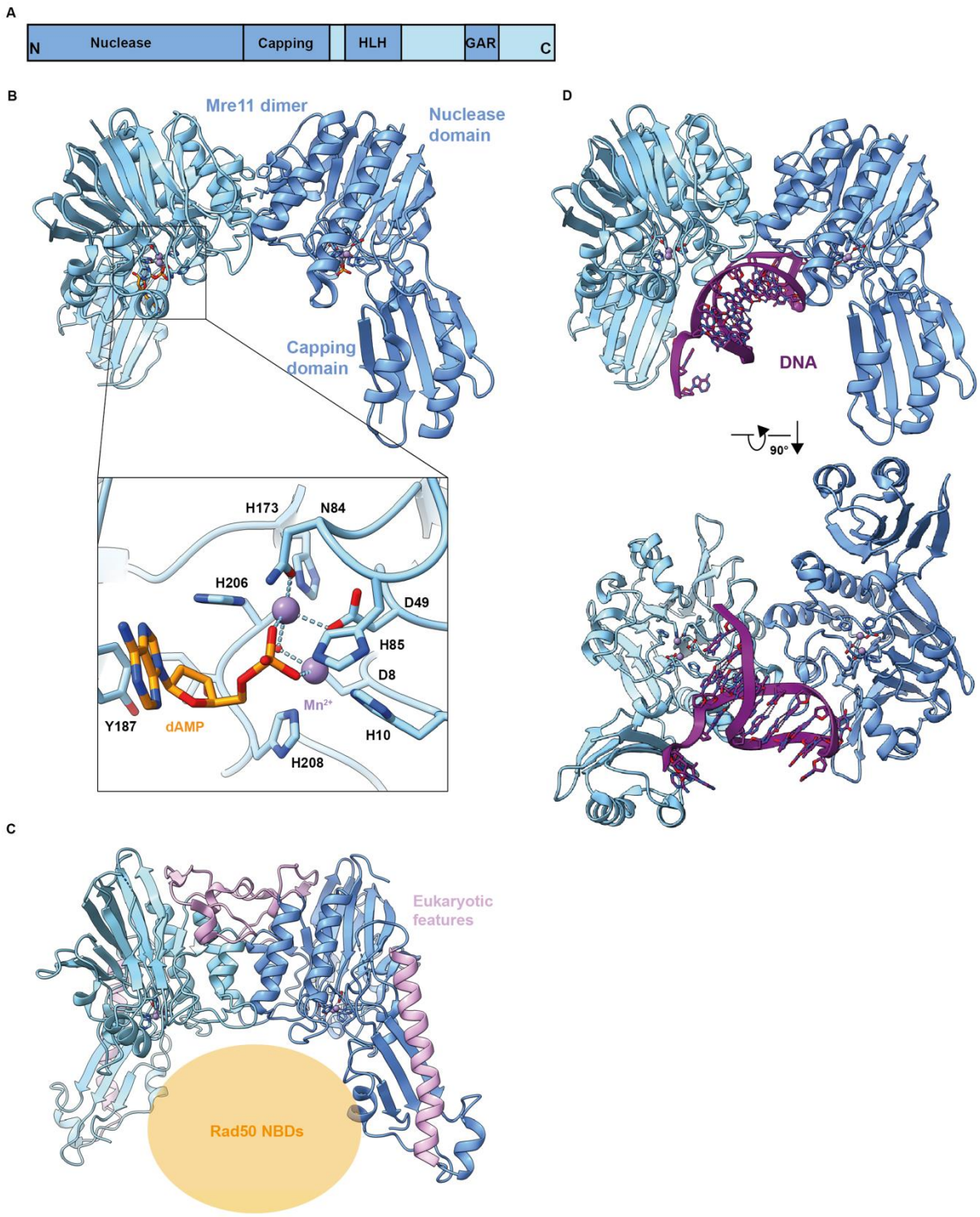

Figure 5. Crystal structures of eukaryotic and prokaryotic Mre11 dimers. A, domain map of eukaryotic Mre11. **B,** structure of *P. furiosus* Mre11 dimer with dAMP and Mn^{2+} ions in the active site (inset) (PDB: 1II7). **C,** structure of *C. thermophilum* Mre11 dimer with eukaryotic specific features highlighted and Rad50 binding site indicated (PDB: 4YKE). **D,** side and bottom views of *P. furiosus* Mre11 dimer bound to DNA (PDB: 3DSD).

The Nbs1 component (described in section 1.3.3) of the MRN complex regulates catalytic activities of Mre11 and Rad50. In humans, Nbs1 promotes Mre11 endonuclease activity on blocked DNA ends and hairpin structures[85,96]. Nbs1 also increases the positive effect of DNA ends on the rate of ATP hydrolysis by Rad50[95]. Interestingly, Nbs1 hinders MR 3' to 5' exonuclease activity on the free DNA ends and promotes the same activity on the protein blocked DNA ends[96]. In addition, Nbs1 mediates MRN interaction with CtIP, which stimulates endonuclease activity of MRN[67].

The ability of MRN complex to perform endonucleolytic incisions is essential for clearing protein blocked DNA ends and this plays important roles in multiple cellular processes. Initiation of meiotic recombination (section 1.1.3) involves a Spo11-bound DNA end, which gets eliminated by MRN mediated endonucleolytic cleavage and subsequent 3' to 5' degradation towards the block[66]. Mre11 deletion mutants in yeast are defective in meiotic recombination and formation of viable spores[97]. In cycling cells, abortive TOPs lead to formation of covalent TOP-DNA crosslinks (section 1.1.1) that accumulate in the absence of Mre11 nuclease activity[98]. Following DNA DSB formation, it gets quickly recognized by highly abundant Ku70/80 heterodimer. In order for HR (section 1.2.2) to take place, DNA ends have to be cleared of Ku70/80 and this also requires endonucleolytic incision performed by the MRN-CtIP complex[99].

Only recently the mechanism of DNA end processing by the prokaryotic MR complex was revealed[100]. Numerous crystallographic studies using truncated Mre11 and Rad50 proteins led to structures of individual proteins as well as the general architecture of the globular catalytic head of MR complex[86,88,90–92]. The latter is composed of U-shaped Mre11 dimer and two Rad50 NBDs, which dimerize and form a DNA-binding cleft upon ATP binding[92]. These findings led to a conundrum: ATP is needed for Mre11 nuclease activity, but in the ATP-bound state Rad50 blocks Mre11's nuclease active sites. Recent structures of full-length prokaryotic MR in "resting" and "cutting" states revealed that two major conformational changes occur upon ATP hydrolysis cycle (Figure 6). First, coiled-coils of Rad50 come together and clamp around the dsDNA. Second, Mre11 dimer relocates to the side of the Rad50 dimer, where it can access the Rad50-clamped DNA end[100].

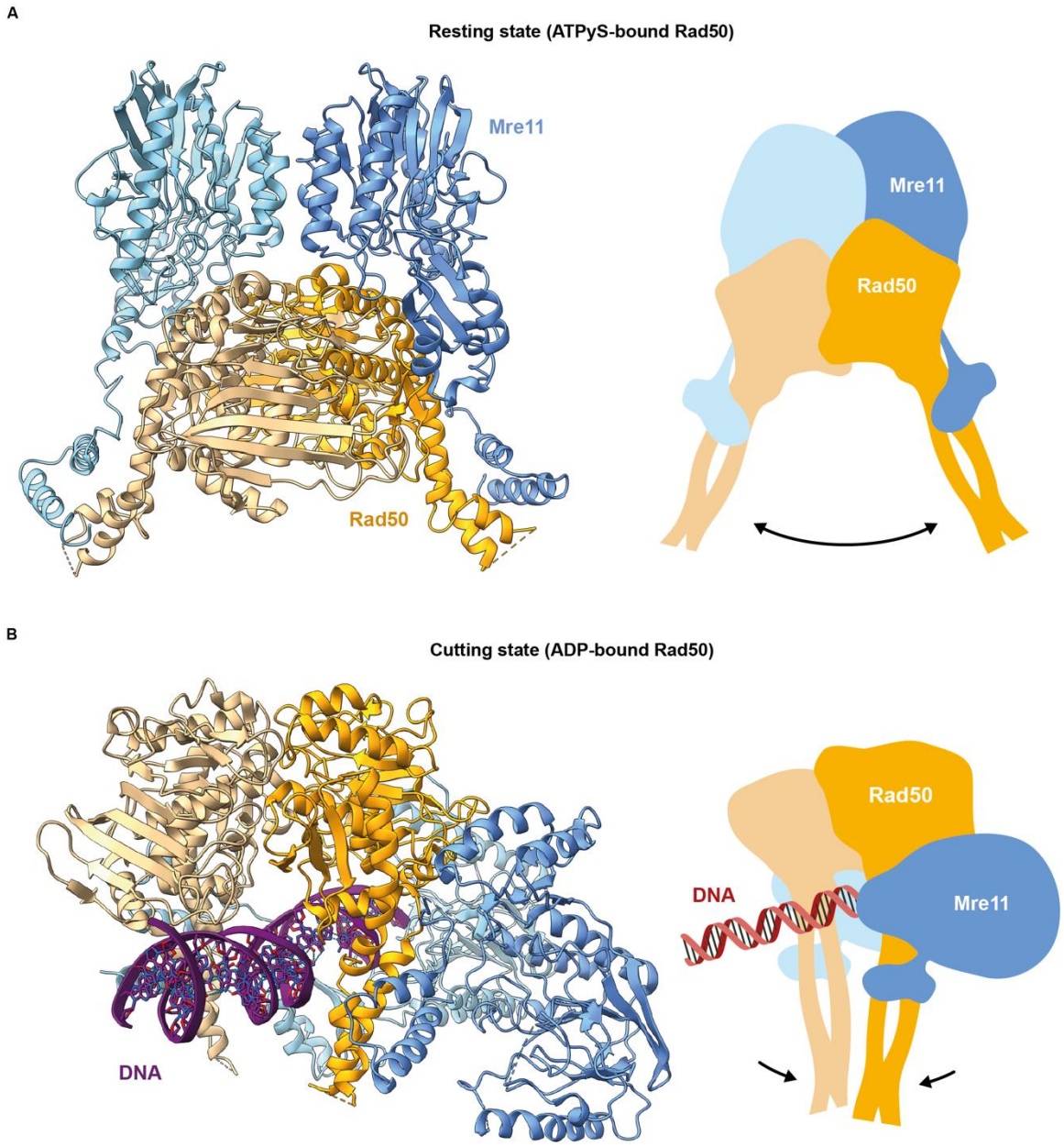

Figure 6. Cryo-EM structures of *E.coli* Mre11-Rad50 complex in resting and cutting states. A, atomic model of Mre11-Rad50 complex catalytic head in "resting" state (PDB: 6S6V) (left) and schematic representation of catalytic head in "resting" state using the same color code (right). **B,** atomic model of Mre11-Rad50 complex catalytic head in "cutting" state (PDB: 6S85) (left) and schematic representation of catalytic head in "cutting" state using the same color code (right).

1.3.2 Rad50

Rad50, an ATPase of the MRN complex, belongs to the structural maintenance of chromosomes (SMC) family of proteins together with cohesin and condensin[101]. All SMC proteins share the same general composition with globular NBDs at N- and C-termini separated by a long extended coiled-coil structure (Figure 7 A). In Rad50, the coiled-coils fold back on themselves in an antiparallel manner bringing the N and C-terminal parts of the ATPase domains together and forming a distal zinc-hook domain with an invariant CXXC motif (Figure 7 B)[101].

The NBDs place Rad50 in a conserved family of ATP-binding cassette (ABC) ATPases, members of which share structural and mechanistic features of their ATPases[102,103]. The N-terminal part of the NBD of Rad50 contains the Q-loop and Walker A motif, while the C-terminus harbors the D-loop, signature and Walker B motifs (Figure 7 C)[88]. Upon ATP binding Walker A and B NBDs of one Rad50 molecule dimerize with Walker B and A NBDs, respectively, of another Rad50 sandwiching two ATP molecules in between (Figure 7 D)[102,104]. Dimerization of Rad50 leads to formation of the DNA binding grove between the extending coiled-coils, explaining ATP-dependent Rad50 DNA binding activity[102,104]. This is confirmed by multiple crystal structures of dsDNA-bound Rad50 NBDs, where DNA binds across the NBDs in *Methanococcus jannaschii* and *Chaetomium thermophilum* and between the coiled-coil and NBD in *Thermotoga maritima* (Figure 7 E-G)[104–106]. In prokaryotes, subsequent ATP hydrolysis leads to previously described (section 1.3.1) conformational changes that expose bound DNA to the Mre11 nuclease active site (Figure 6)[100].

Eukaryotic Rad50 shows especially slow ATP hydrolysis rates with 0.1 ATP per molecule per minute by yeast MR and 0.026 ATP per molecule per minute by human MR[107,108]. Addition of dsDNA increases ATP hydrolysis by 10 and 20-fold in yeast and human MR, respectively, *in vitro*[95]. Nbs1 can further increase ATP hydrolysis by the human complex, while addition of Xrs2 shows no further stimulatory effect in the yeast system[95]. The slow rate of ATP hydrolysis by MR can be explained by its function to switch between the “resting”/scanning and “cutting” state of the complex[100]. The ATPase activity is critical for Rad50 function as mutations of residues involved in ATP binding and hydrolysis lead to a phenotype equivalent to Rad50 deletion *in vivo*[109–111]. The NBDs of Rad50 are known to have a few separation-of-function mutations, known as Rad50S, located on the β-sheets. The Rad50S mutants exhibit much stronger defects in meiotic recombination than in DNA repair[109].

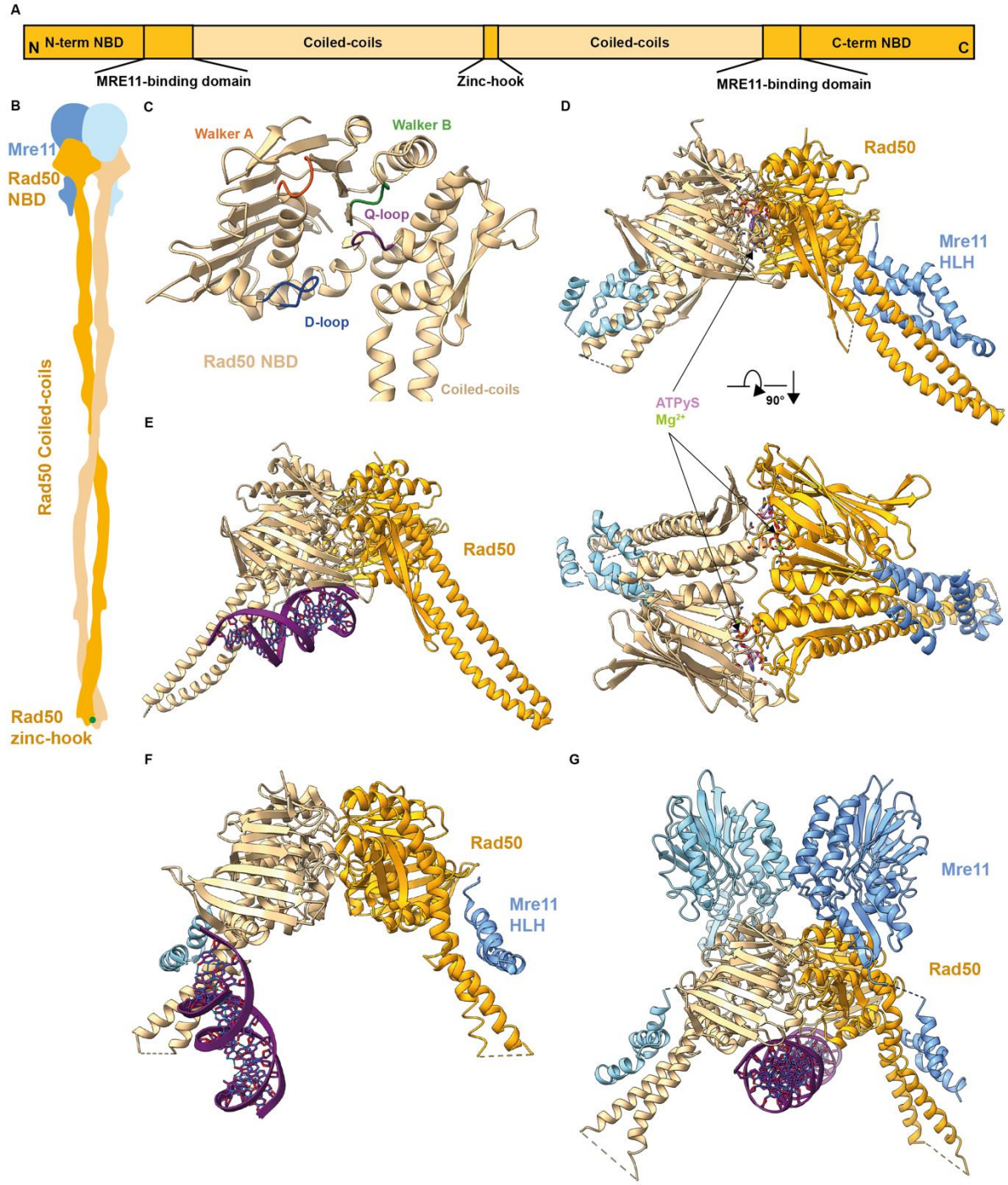

Figure 7. Crystal structures of prokaryotic and eukaryotic Rad50 NBDs. A, domain map of eukaryotic Rad50. **B,** schematic model of Mre11-Rad50 complex with structural features of Rad50 indicated. **C,** *P. furiosus* Rad50 ATPase domain with functional loops and motifs labelled (PDB: 1II8). **D,** *C. thermophilum* Rad50 dimer sandwiching ATPγS and Mg^{2+} ions and Rad50-binding helix-loop-helix motifs of Mre11 (side and top views) (PDB: 5DA9). **E,** *C. thermophilum* Rad50 NBD dimer bound to ATPγS in complex with dsDNA (PDB: 5DAC). **F,** AMPPNP-bound *T. maritima* Rad50 NBD dimer in complex with dsDNA and helix-loop-helix motifs of Mre11 (PDB: 4W9M). **G,** ATPγS-bound *M. jannaschii* Mre11-Rad50 catalytic head in complex with dsDNA (PDB: 5F3W).

The characteristic structural feature of Rad50 is the long coiled-coil region, which extend outwards from NBDs and range in length from 15 nm in T4 bacteriophage to up to 50 nm in eukaryotes[63]. The coiled-coil structures remain quite mysterious: the exact function and reason for a particular length in different organisms are not clear. The internal truncations of coiled-coils in yeast reveals that length of coiled-coils is not necessary for the MRN complex formation, but long range action of MRN is required for its function in HR, meiotic recombination and telomere maintenance[112]. Structural studies of bacterial MR show "resting" and "cutting" states of the complex where Rad50 coiled-coils adopt open and DNA-clamping rod conformations, respectively[100]. Hence, conformations of elongated Rad50 coiled-coils are coupled to the state of compact NBDs.

Another dimerization motif of Rad50 is the zinc-hook, located at the opposite end of coiled-coils from the globular NBDs and consisting of CXXC motif. Zinc induces formation of a zinc-hook dimer, where a single zinc ion is tetrahedrally coordinated by four cysteines (two from each Rad50 molecule) (Figure 8 A)[113]. Structural studies revealed two different conformations of zinc-hook dimer. *Pyrococcus furiosus (Pf)* zinc-hook dimer shows an interaction of two oppositely protruding coiled-coil domains of Rad50 (Figure 8 A)[113]. In the case of inter-complex dimerization, MRN catalytic head domains linked by this mode of zinc-hook interaction could be up to 1,200 Å apart and bridge two DNA ends following DSB or two sister chromatids (Figure 8 B). In the case of intra-complex dimerization, Rad50 coiled-coils would adopt an open structure (Figure 8 B). On the other hand, human and *Pf* zinc-hook dimers can adopt a rod-shaped intra-complex conformation (Figure 8 C-E)[114,115]. Taken together, zinc-hook structures imply a striking structural transition, which would fit to open and closed conformational states of coiled-coils observed in "resting" and "cutting" states of bacterial MR, respectively (Figure 6)[100].

The functional importance of the zinc-hook is highlighted by mutational studies[113,114,116]. In yeast assays, removal of the zinc-hook or mutations of the invariant cysteines resulted in phenotypes similar to Rad50 deletion with increased sensitivity to DNA damaging agents and telomere shortening[116]. Rad50 zinc-hook, as well as NBDs, have separation of function mutations that affect the zinc-hook proximal dimerization interface and conserved residues between the invariant cysteines. These mutants show intact DNA repair, but defected DNA-damage signaling indicated by decreased Rad53 phosphorylation levels[114].

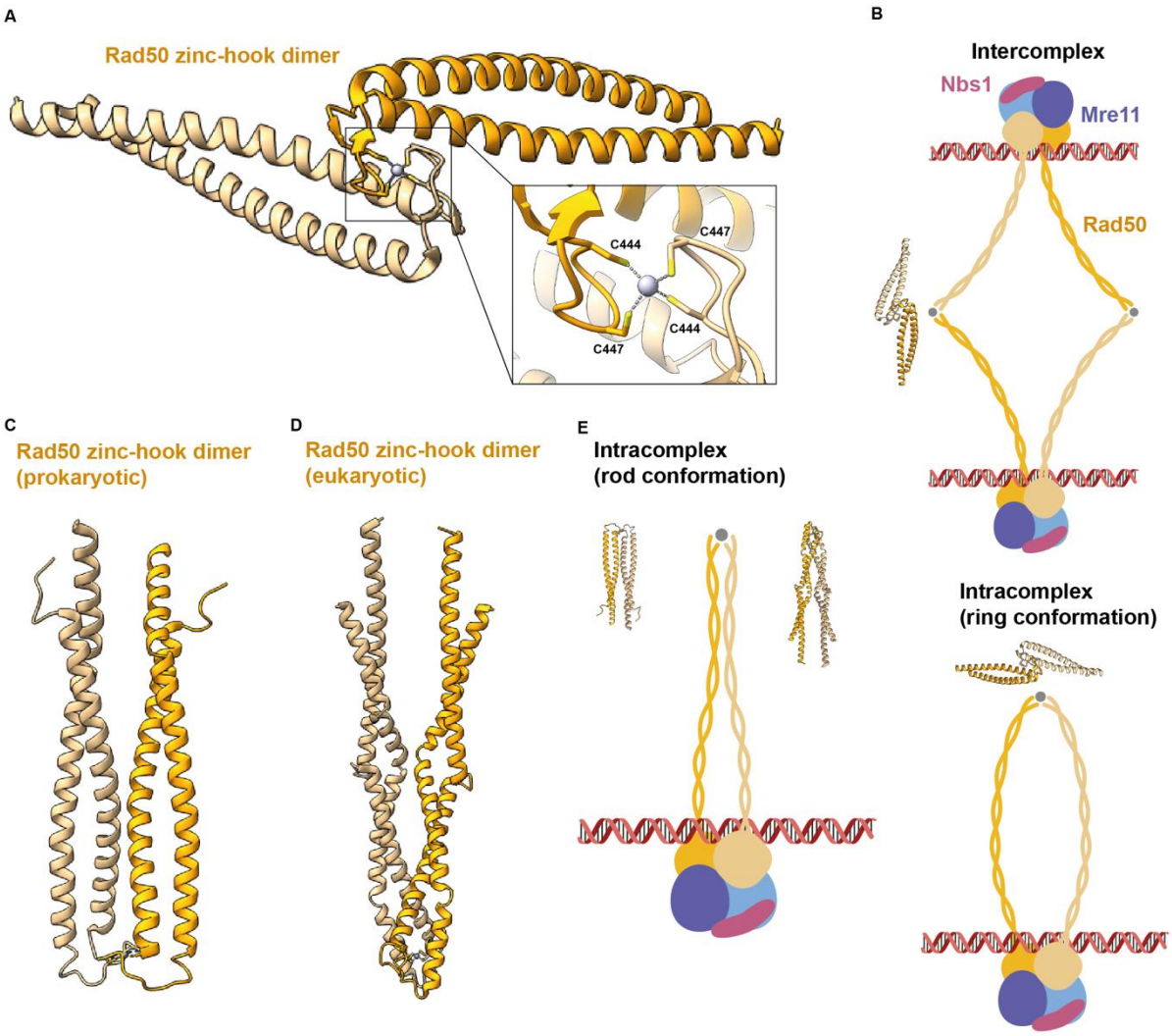

Figure 8. Crystal structures of prokaryotic and eukaryotic Rad50 zinc-hooks. A, *P. furiosus* Rad50 zinc-hook dimer in open conformation with close-up on cysteine-coordinated zinc ion (PDB: 1L8D). **B,** interpretation of open conformation *P. furiosus* Rad50 zinc-hook dimer in the context of MRN complex. **C,** *P. furiosus* Rad50 zinc-hook dimer in closed conformation (PDB: 6ZFF). **D,** *H.sapiens* Rad50 zinc-hook dimer in closed conformation (PDB: 5GOX). **E,** interpretation of closed conformation *P. furiosus* and *H. sapiens* Rad50 zinc-hook dimer in the context of MRN complex.

1.3.3 Nbs1

Nbs1 (Xrs2 in yeast) is the only eukaryote specific component of the MRN complex and shows less sequence conservation than Mre11 and Rad50. Nbs1 is composed of three functional regions. The structured N-terminal region contains a fork head-associated (FHA) domain followed by two breast cancer-associated 1 C terminus (BRCT) domains (Figure 9 A)[117,118]. FHA domains recognize phosphothreonine epitopes on proteins while BRCT domains are

known to bind DNA, poly ADP-ribose and proteins, in both a phosphorylation dependent and independent manner[119,120]. Hence, the N-terminal region functions as a phosphoprotein sensor and interaction platform for MRN-binding proteins. One of those is CtIP, which is required for MRN endonuclease activity and removal of blocks at the DNA end. Nbs1 FHA domain binds CtIP in its phosphorylated form and recruits CtIP to DSBs (Figure 9 B)[121]. The N-terminal region of Nbs1 also binds to phosphorylated H2AX, which marks DNA damage sites, leading to recruitment of Nbs1 and the whole MRN complex to the DSBs[122].

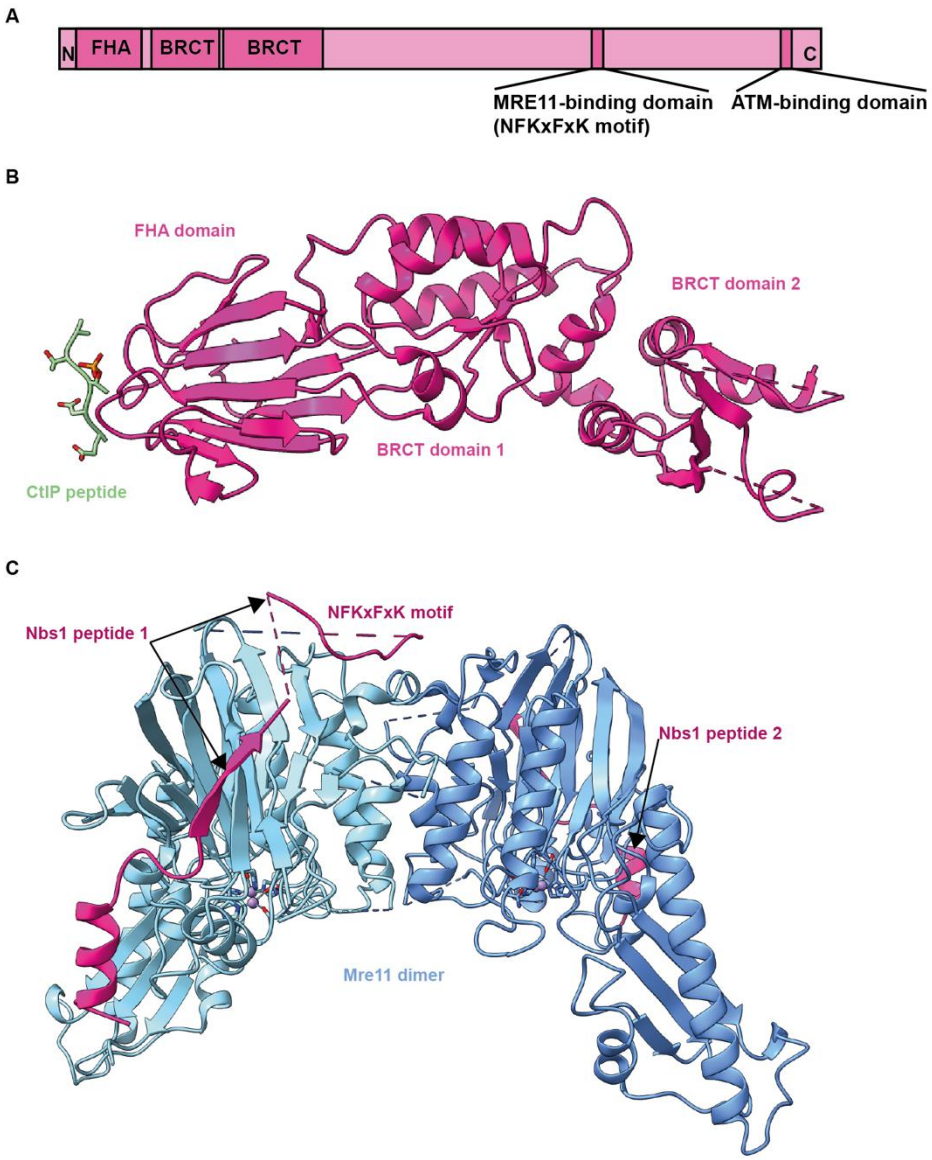

Figure 9. Structural characterization of Nbs1 fragments. A, domain map of Nbs1 protein. **B,** crystal structure of *S.pombe* Nbs1 N-terminal FHA and BRCT domains in complex with CtIP peptide (PDB: 3HUF). **C,** crystal structure of *S.pombe* Mre11 dimer with Nbs1 peptides wrapped around it (PDB: 4FBQ).

The central region of Nbs1 is highly unstructured and does not have many well-characterized functions (Figure 9 A). However, this region is known to contain a nuclear localization signal (NLS) in humans. As Nbs1 is the only component of the MRN complex that has a NLS, this feature is crucial for the nuclear localization of the whole complex[123].

The C-terminal region is predicted to have an extended structure without any distinct structural motifs. However, this region has areas of high sequence conservation and functional significance, like Mre11 and ATM binding sites (Figure 9 A)[124,125]. A crystal structure of the *S. pombe* catalytic domain of Mre11 and Mre11-binding portion of Nbs1 revealed that Nbs1 wraps as an extended chain around the Mre11 phosphodiesterase domain with two Nbs1 molecules contacting the sides of dimeric Mre11, but only one Nbs1 binds across the eukaryote specific latching loops of Mre11 via the highly conserved NFKxFxK motif (Figure 9 C)[86]. The importance of these interactions is highlighted by several ataxia-telangiectasia-like disease (ATLD) and Nijmegen breakage syndrome-like disorder (NBSLD) mutations located there[86]. In addition, mouse studies have shown that a 108 amino acid Nbs1 fragment comprising the Mre11 binding site is sufficient for its essential roles[126]. The very C-terminus of Nbs1 has a conserved FXF/Y motif which interacts with HEAT repeats of ATM kinase. In *Xenopus* egg extracts, it has been shown that this Nbs1-ATM interaction is important for recruitment and activation of ATM kinase and, therefore, signaling of DNA damage[125].

1.3.4 Cellular functions of the MRN complex

MRN is an essential complex in mammals indicating its central roles in vital cellular processes. In addition to MRN functions in DNA damage repair (section 1.3.4.1) and telomere maintenance (section 1.3.4.2), there is evidence showing that MRN is essential for resolving replication intermediates that are not necessarily replication induced DSBs[127]. MRN also functions in meiotic recombination (section 1.1.3) by removing Spo11-blocked DNA ends and initiating recombination[128]. V(D)J recombination (section 1.1.3) is another programmed DSBs involving process where MRN plays a role as its deficiency leads to accumulation of unrepaired coding ends[129].

1.3.4.1 DNA damage repair

In addition to the enzymatic activities of MRN at DNA ends upon DSBs, it functions in sensing and signaling of DNA damage via ATM and ATR kinases[130]. Levels of MRN remain constant through the cell cycle and the complex distributes uniformly throughout the nucleus with some of it sequestered in sub-nuclear compartments called promyelocytic leukemia (PML)

bodies[131,132]. Immunofluorescence studies show that upon the formation of DSBs, the MRN complex from the nuclear pool and PML bodies rapidly relocates to the sites of damage[132,133]. This fast action of the sensor is important in order to reduce time for non-specific degradation and further separation of broken ends to take place.

ATM, ATR and DNA-PKcs belong to the phosphatidylinositol 3-kinases (PI3K)-like protein kinase (PIKK) family and function in DNA damage repair (section 1.4.1)[130]. Each kinase is activated in response to a different type of damage-associated DNA-protein structure. DNA-PKcs is recruited to and activated by Ku70/80-bound DNA ends, while ATR interacts with ssDNA coated by RPA, which occurs during HR pathway of DSB repair (section 1.2.2)[134,135]. The ATM kinase is recruited to DSBs via interaction with the C-terminus of Nbs1 component of the MRN complex, where it gets activated[136]. It has been shown, using yeast proteins, that both DNA and MRX complexes lead to synergistic 20- to 30-fold increases in ATM activity, indicated by phosphorylation of the ATM substrate Rad53[137]. In addition, MRN mediated ATM activation requires ATP binding to Rad50, but not ATP hydrolysis, and Mre11 nuclease activity is not essential[138]. Following ATM activation, it phosphorylates hundreds of target proteins resulting in a broad-spectrum DNA-damage signaling cascade and changes in various cellular processes like cell cycle progression (section 1.4.2)[139].

The MRN complex can also be directly involved in activation of ATR kinase, as shown in *Xenopus* egg extracts. MRN associates with ATR-activating DNA structures composed of circular ssDNA and junctions of ssDNA and dsDNA, and recruits ATR as well as ATR activator DNA Topoisomerase II binding protein 1 (TOPBP1)[140]. Activated ATR phosphorylates numerous targets that include Chk1 and Chk2 leading to activation of p53 and can induce a G2/M checkpoint[141,142].

Even though the MRN complex is one of the factors directing the DSB repair pathway towards HR (section 1.2.3), it also functions in both c-NHEJ and alt-NHEJ (section 1.2.1)[54,78]. In mammalian cells, the knockdown of Mre11 leads to decreased efficiency of end-joining by both NHEJ pathways[143]. In alt-NHEJ, Mre11 nuclease might be needed for the initial short-range end resection[144]. The MRN complex could also influence early processes that are common for both NHEJ pathways. In addition, *S. cerevisiae* cells with defective c-NHEJ, due to Mre11 deletion, are partially rescued by nuclease-dead Mre11 indicating a structural rather than catalytic function of MRN[145].

1.3.4.2 Telomere maintenance

The evolutionary transition from circular to linear genomes resulted in two new challenges to the genome integrity in eukaryotes. The first challenge is known as the end replication problem, where every round of replication results in loss of nucleotides from the 5’ terminus of the

lagging strand. The second challenge arises from the structure of linear chromosome termini, which resembles broken DNA ends. Hence, chromosome termini have to be protected from being recognized and processed as DSBs. Telomeres are present at the ends of linear chromosomes to prevent loss of genetic information and protect ends from being processed by DSB repair pathways[146].

Telomeres consist of DNA sequence repeats that are bound by telomere-binding proteins. In mammals, telomeric DNA consists of double stranded repeats (TTAGGG in humans) followed by a G-rich 3' strand overhang. A T-loop structure is formed when a single-stranded DNA overhang invades the DNA duplex and base pairs with the complementary strand (Figure 10)[144]. Due to a high G content, the single-stranded telomere overhang can form G-quadruplexes, which are associated with telomere protection and suppression of recombination[147]. The formation and stability of the telomeric DNA structure is facilitated by six proteins forming the shelterin complex (Figure 10)[148]. Loss of the shelterin complex components can lead to unprotected chromosome ends. These can be recognized by DNA damage sensors and initiate NHEJ or HR pathway of DNA repair potentially causing chromosomal aberrations[149].

As telomeres get shorter with each division of differentiated somatic cells they impose a limit on cell replication (Hayflick limit) and eventually lead to a permanent cell cycle arrest (cellular senescence)[150]. The way to escape cellular senescence involves telomerase enzyme, which can elongate telomeres by addition of G-rich repetitive sequences. Telomerase activity is seen in gametes and stem cells; it is also used by tumor cells to keep dividing[151].

The involvement of MRN in the telomere maintenance was noticed in *S. cerevisiae*, when deletion or disruption of individual MRX (yeast MRN) components led to shortened telomeres and cell senescence [152–154]. Further research suggested that MRX facilitates the recruitment of telomere replication proteins to telomeres in the S-phase[155]. In higher eukaryotes MRN also contributes to the maintenance of telomeres. The first indication of this function was the observation that Nbs1 and Mre11 sequester at telomeres in meiotic human fibroblasts[156]. In addition, it was observed that all three components of the MRN complex interact with the telomeric repeat-binding factor 2 (TRF2) protein of shelterin complex in cell cycle dependent manner[157]. One of the known MRN-TRF2 interactions is mediated via Nbs1 and requires phosphorylation by CDK2, which couples this interaction to the cell cycle[158]. Analogous to findings in yeast, lack of Mre11 or Nbs1 in human fibroblasts led to telomere shortening indicating the role of MRN in the facilitation of telomerase activity[159].

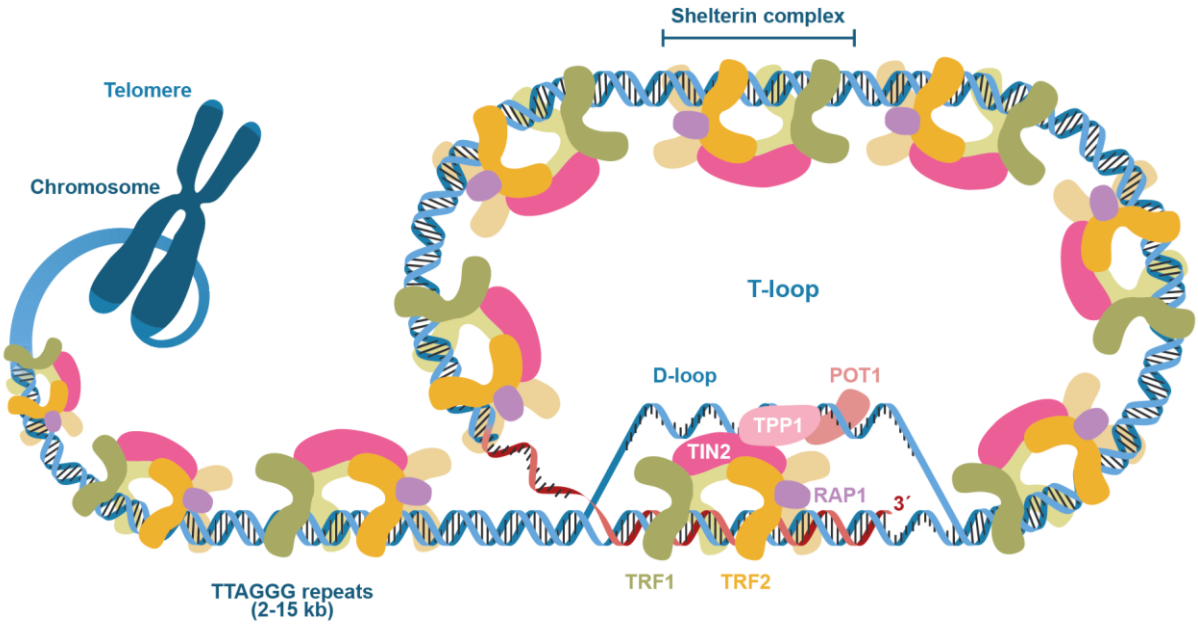

Figure 10. Schematic representation of telomere structures at chromosome ends. Telomeres are DNA-protein structures at the ends of linear chromosomes. The telomeric DNA consists of repeats (TTAGGG in vertebrates) that form double stranded DNA structure (in blue) with 3' overhang (depicted in red). Single-stranded DNA invades double-stranded DNA region forming a displacement loop (D-loop) and a telomere loop (T-loop). Telomere DNA structure is coated by shelterin protein complex, which has protective and regulatory functions. Shelterin complex is composed of POT1 (Protection of Telomere 1), TRF1 and TRF2 (Telomeric Repeat binding Factors 1 and 2), TIN2 (TRF1-and TRF2-Intercating Nuclear Protein 2), RAP1 (Repressor/Activator protein 1) and TPP1.

The removal of the shelterin complex protein TRF2 can leave telomeres dysfunctional. The MRN complex functions to detect and signal the presence of exposed telomere ends via the ATM signaling pathway. In the absence of TRF2, MRN can remove 3' telomeric overhang promoting NHEJ mediated chromosome fusion[160]. On the other hand, MRN can protect newly replicated telomere ends from NHEJ by generating 3' telomeric overhang[161].

One of the hallmarks of cancer is an unlimited proliferation, which is not the case in normal somatic cells due to the telomere imposed Hayflick limit[151]. Usually, cancer cells overcome this limit by upregulating telomerase activity, but in some cases a different mechanism known as the alternative lengthening of telomeres (ALT) is used. ALT requires the MRN complex, which recruits ATM to telomeres initiating recombination process, generates telomeric 3' overhang that can invade adjacent telomeric DNA and use it as a template for extension of the telomere[162].

1.3.5 MRN associated human diseases

The MRN complex plays critical roles in the maintenance of genome stability via its functions in DNA DSB repair and telomere maintenance. There are no human diseases associated with a complete loss of any of the individual MRN genes, possibly due to incompatible with life phenotypes, as reported in mouse studies. Even so, hypomorphic germline mutations and alterations in protein levels of MRN components have been associated with a number of human disorders[163].

Mutations in Mre11 can lead to ataxia-telangiectasia-like disease (ATLD), which is similar to ATM dysfunction associated ataxia-telangiectasia (A-T). ATLD is an autosomal recessive disorder caused by decreased levels of Mre11 or loss of the Mre11-Nbs1 interaction. Clinical features of ATLD involve cerebellar ataxia (like in A-T), immunodeficiency and developmental disorders[164]. In addition, sporadic Mre11 mutations have been detected in different types of cancers, like breast, lung and ovarian[163].

Alterations of Rad50, including point mutations and deletions, can cause abnormal protein expression levels and result in a disorder known as Nijmegen breakage syndrome-like disorder (NBSLD). Cells from the NBSLD patient were characterized by chromosomal instability, failure to form DNA damage-induced MRN foci and inability to activate the ATM signaling cascade[165]. Mutations in Rad50, frequently located in its NBDs, have also been associated with a predisposition to certain types of cancer, for instance, Burkitt Lymphoma, endometrial carcinoma and lung cancer[163].

Deletions, mutations or abnormal expression levels of Nbs1 can lead to Nijmegen breakage syndrome (NBS). This is a rare autosomal recessive disorder characterized by sensitivity to IR, microcephaly, mental and growth retardation and immunodeficiency. On the cellular level, NBS patients show chromosomal instability, abnormal cell cycle checkpoint activation and increased shortening of telomeres[166]. Germline mutations of Nbs1 increase risks of leukemia, melanoma, breast, prostate and ovarian cancer[163].

The MRN complex is not only linked to increased risks of cancer when mutated, but also thought of as a target for cancer therapy. Due to an increased genomic instability, cancer cells are more sensitive to DNA damaging agents, that are used in radio/chemotherapy. In tumor cells, altered MRN expression levels have been shown to be associated with resistance towards radio/chemotherapy. For instance, overexpression of Mre11 can lead to chemoresistance by removing covalent adducts from DNA ends[167]. Targeting of Rad50 and inhibiting Mre11 have shown some promise in in tumor sensitization[167,168].

1.4 The ATM kinase

The ATM kinase was identified as a gene mutated in the autosomal recessive disorder ataxia-telangiectasia (A-T). Hence, the name ataxia-telangiectasia mutated (ATM) was selected. Classic A-T is characterized by progressive cerebellar ataxia, immunodeficiency, frequent infections and an increased risk of cancer, especially leukemia and lymphoma[169]. In yeast, ATM was identified as a protein involved in the telomere maintenance and named Telomere length regulation protein 1 (Tel1)[170].

ATM is a relatively large protein; dimeric ATM forms a 700 kDa butterfly-shaped structure. The N-terminal half of the protein consists of HEAT (huntingtin, elongation factor 3, protein phosphatase 2A, and TOR1) repeat spiral and pincer domains and acts as protein/DNA binding platform (Figure 11)[125,171]. The following FAT (FRAP, ATM, and TRRAP) domain wraps around the kinase and contributes the main dimerization interface. The C-terminal kinase domain of ATM is related to phosphoinositide 3 lipid kinases placing ATM into phosphatidylinositol 3-kinases (PI3K)-like protein kinase (PIKK) family of kinases[139].

ATM functions in the orchestration of cellular response to certain stress factors, like DNA damage and reactive oxygen species (ROS)[172]. ATM gets recruited to DNA DSBs and activated by the MRN complex leading to phosphorylation of hundreds of ATM substrates[139,173]. This results in recruitment and activation of proteins involved in the repair process, chromatin remodeling, cell cycle arrest and other cellular processes. In addition, ATM functions in other types of DNA repair, like base excision repair, removal of topoisomerase cleavage complex and repair of transcription associated lesions[174–176]. ATM also gets activated by oxidative stress through the formation of intermolecular disulfide bonds. Under these conditions, ATM phosphorylates a different set of target proteins than during the DNA damage response. ATM functions to alter metabolic pathways to produce antioxidants, induce mitophagy and enhance pexophagy to maintain cell homeostasis[177].

Alterations in the ATM kinase affecting its structure and/or function are frequently associated with cancer development. This makes ATM an attractive target for cancer therapies. It has been shown that ATM inhibitors can increase radiosensitivity of cancer cells and show promising results when used in combination with other DNA damage repair inhibitors[178].

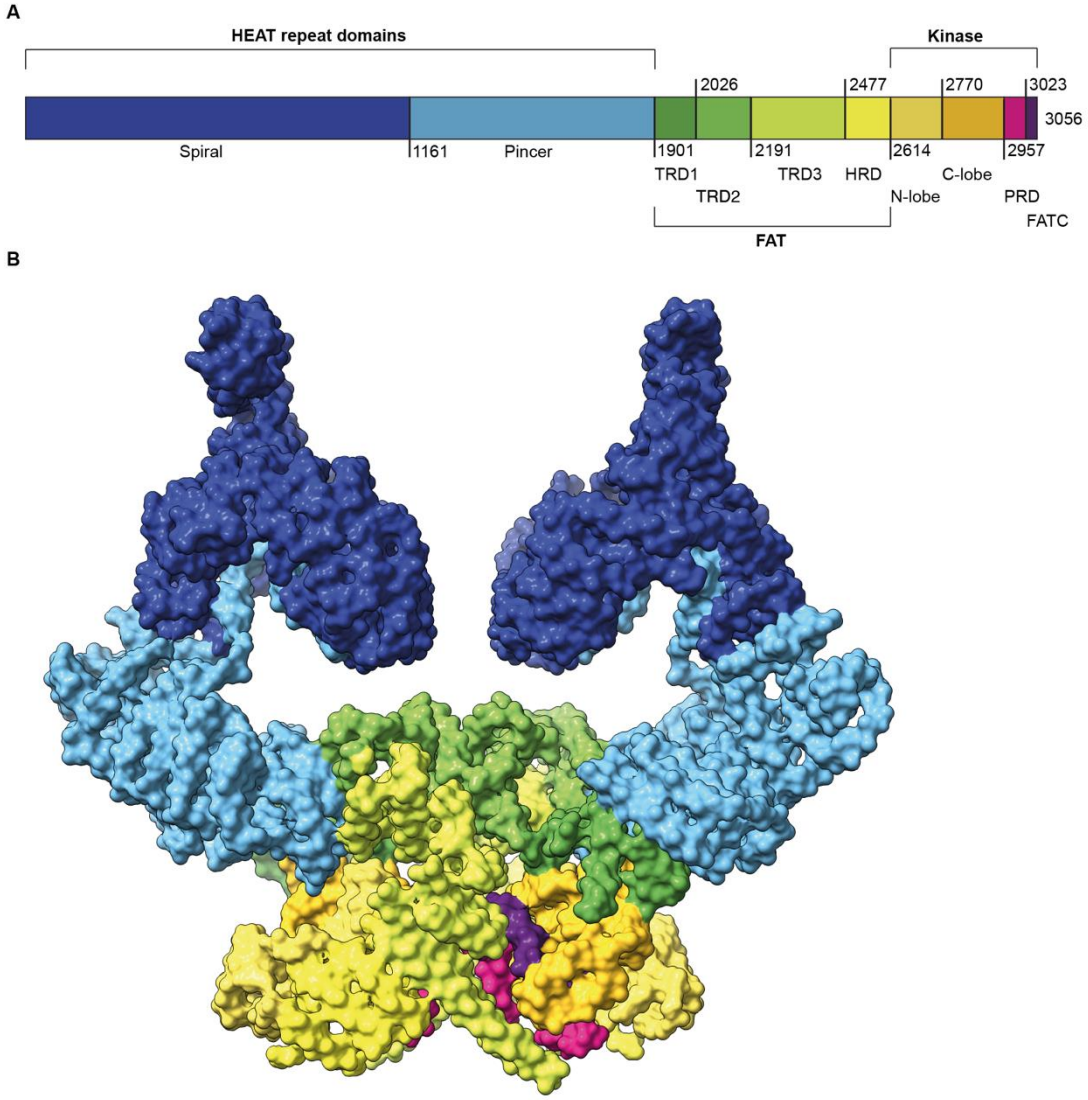

Figure 11. Architecture of human ATM kinase. A, domain map of ATM kinase. **B,** structure of dimeric human ATM with domains colored based on the color code in **A** (PDB: 5NP0).

1.4.1 The PIKK family of protein kinases

The PIKK family of protein kinases was defined in the mid-1990s following a discovery of a set of related serine/threonine kinases with shared features[179,180]. They all are large proteins with molecular weights ranging from 280 to 470 kDa. All members of the family share a similar architecture consisting of an extensive N-terminal HEAT repeat domain(s), followed by a kinase-surrounding regulatory FAT domain and a highly conserved C-terminal kinase domain (Figure 12). The sequence of kinase domains of PIKK family members differ from other known serine/threonine or tyrosine protein kinases. Instead, they show a higher sequence identity to

the kinase domain of the PI3K phospholipid kinases without having specificity towards lipid targets[181]. Members of the PIKK family function in a diverse set of cellular processes.

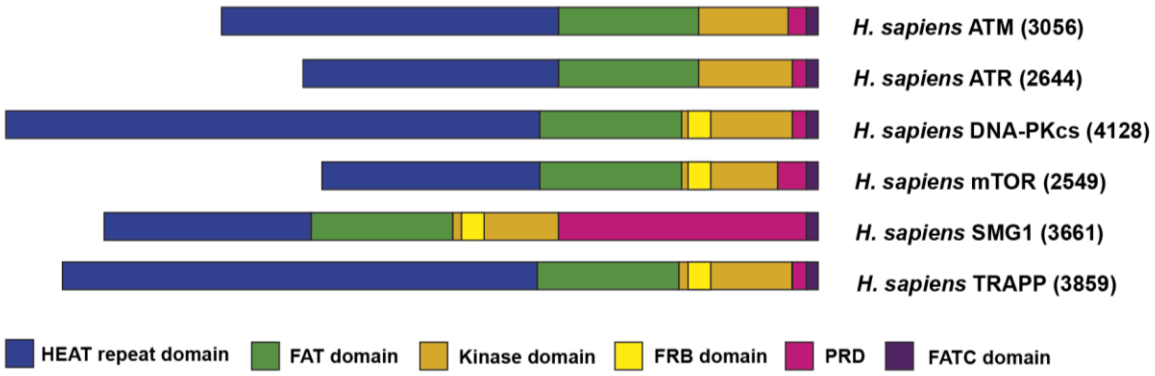

Figure 12. The domain maps of human PIKKs. The names of the kinases are indicated on the right with their sizes in amino acids in the brackets. At the bottom, color code for domains is explained. All PIKKs have extensive N-terminal HEAT repeat domains followed by regulatory FAT and catalytic kinase domains. In some cases, kinase domain includes regulatory FRB domain composed of a four-helix bundle. C-terminal PRD and FATC domains, present in all PIKKs, also play regulatory roles.

DNA-PKcs is the largest of the PIKKs and functions in the maintenance of genome integrity. It is crucial for the NHEJ pathway (see Section 1.2.1) of DNA DSB repair, where it forms a DNA-PK complex together with Ku70/80 and functions in bridging of broken DNA ends, recruitment of repair factors and stimulation of NHEJ nuclease Artemis[182,183]. Via the role of DNA-PKcs in NHEJ, it also functions in V(D)J recombination during the immune system development[184]. In addition, DNA-PKcs plays a role in the DNA replication stress response pathway by activating the replication stress checkpoint, regulating replication fork restart and mitotic catastrophe[185]. In telomere maintenance, DNA-PK facilitates telomere capping and is involved in regulation of telomere length[186]. DNA-PKcs is also known to be involved in the regulation of DNA damage-induced autophagy and foreign DNA-activated innate immune response[187,188].

The ATM Rad3-related (ATR) kinase is an essential protein working to maintain genome integrity. ATR functions in DNA damage repair and is activated in response to a persistent ssDNA[189]. ATR signaling suppresses progression of the cell cycle and origin firing after DNA damage to suppress replication catastrophe[190]. ATR functions in prevention and restart of collapsed replication forks[191]. In addition, ATR is important for a correct timing of the mitotic entry as loss of ATR leads to a premature mitotic entry with increased DNA damage and before completion of DNA replication[189,192].

The ATM kinase is well-known as a master regulator of DNA DSB signaling and is involved in the response to other types of DNA damage, for instance, single-strand breaks and transcription-associated lesions. This kinase also functions in DNA damage unrelated processes, like, regulation of RNA metabolism and levels of reactive oxygen species[172]. Cellular functions of ATM will be described in a greater detail in the section 1.4.2.

Another member of the PIKK family is a suppressor of morphogen gradient 1 (SMG1) protein. It functions in the nonsense-mediated mRNA decay (NMD), which is a conserved surveillance mechanism that eliminates faulty mRNAs and prevents accumulation of truncated proteins[193]. SMG1 forms a complex with SMG8 and SMG9 and specifically phosphorylates RNA helicase UPF1. This phosphorylation recruits other NMD factors resulting in the cleavage of RNA[194].

The mechanistic target of rapamycin (mTOR) kinase is the catalytic subunit of two distinct complexes known as mTOR complex 1 (mTORC1) and 2 (mTORC2). mTORC1 plays a crucial role in regulating cellular processes that are required for cell growth, like synthesis of proteins, lipids and nucleotides, and autophagy. The activity of mTORC1 is influenced by environmental factors (e.g., growth factors, amino acids, oxygen and stress), this way coupling cell growth to a favorable environment[195]. On the other hand, mTORC2 controls cell proliferation and survival. One of the most important targets of mTORC2 is Akt, a key effector of insulin signaling[195,196]. As mTOR is a core regulator of cell growth and metabolism, mutations affecting its functions are linked to many diseases, including cancer, neurological diseases, inflammation and metabolic disorders[197].

The transformation/ transcription associated protein (TRRAP) functions as a transcriptional cofactor by recruiting histone acetyltransferase (HAT) complexes to sequence-specific transcriptional activators[198]. TRRAP is known to be involved in a number of cellular processes, for instance, B-cell development and regulation of mitotic checkpoint [199,200].TRRAP is the only member of the PIKK family that does not possess a kinase activity. Nonetheless, the kinase domain of TRRAP plays a crucial structural role for the formation of the functional HAT complex[201].

1.4.2 Cellular functions of ATM

The ATM kinase is a central factor in recognition and signaling of DNA DSBs. During the HR pathway of DSB repair (see section 1.2.2 for more details), DNA ends are recognized by the MRN complex leading to recruitment and activation of the ATM kinase[62]. The number of ATM-dependent phosphorylation events that follow ATM activation in response to DSB is very large. Therefore, only a few key events will be mentioned here (Figure 13). One of them being a phosphorylation of C-terminal tail of histone H2AX leading to recruitment and accumulation of DNA repair factors[202]. ATM phosphorylates CtIP on Thr859 aiding the

resection of 5' strand by the MRN-CtIP complex[203]. Subsequent long-range resection of 5' strand is mediated by nucleases Exo1 or DNA2-BLM complex leading to RPA coating of the 3' overhang and BRCA2-mediated formation of the recombinogenic Rad51 filament[69,70]. ATM activity plays an important role in this process as ATM is known to phosphorylate Exo1, BLM and BRCA2[204–206]. Apart from promoting the DNA repair, ATM also activates the cell cycle checkpoint to prevent transition from G2 to M in the presence of DNA damage. Central to this activation by ATM is phosphorylation of checkpoint kinase 2 (CHK2) leading to phosphorylation of p53, a tumor suppressor blocking cell cycle progression[207,208].

ATM functions also extend to NHEJ (described in section 1.2.1) (Figure 13). ATM is known to promote NHEJ by phosphorylating some of the proteins involved, including DNA-PKcs, Artemis, XRCC4 and XLF[209–212]. Interestingly, DNA-PKcs phosphorylation by ATM has an activating function, while ATM phosphorylation by DNA-PKcs decreases ATM binding to MRN complex[209,213]. Hence, these two related kinases directly regulate one another.

In addition, ATM can be activated by blocked DNA ends. This frequently arises from a covalent linkage between topoisomerases and the DNA phosphate backbone (Figure 13). Topoisomerases are enzymes that participate in the overwinding or underwinding of DNA in replication, transcription, chromosome segregation and recombination[214]. At transcription sites, ATM is activated by the DNA damage arising from topoisomerase 1 3' covalent conjugates (TOP1cc) and functions in TOP1cc removal[176]. ATM phosphorylates and activates tyrosyl-DNA phosphodiesterase 1 (TDP1), an enzyme that hydrolyses the phosphodiester bond between TOP1 and DNA[215]. ATM also functions in signaling and removal of TOP2cc, which results from 5' linkage of TOP2 with both strand of the DNA[216]. The accumulation of SSBs can also activate ATM, where it phosphorylates CHK2 leading to activation of the SSB repair factor XRCC1 (Figure 13)[217,218]. XRCC1 regulates the recognition of DNA damage and excision steps of the base excision repair pathway[218].

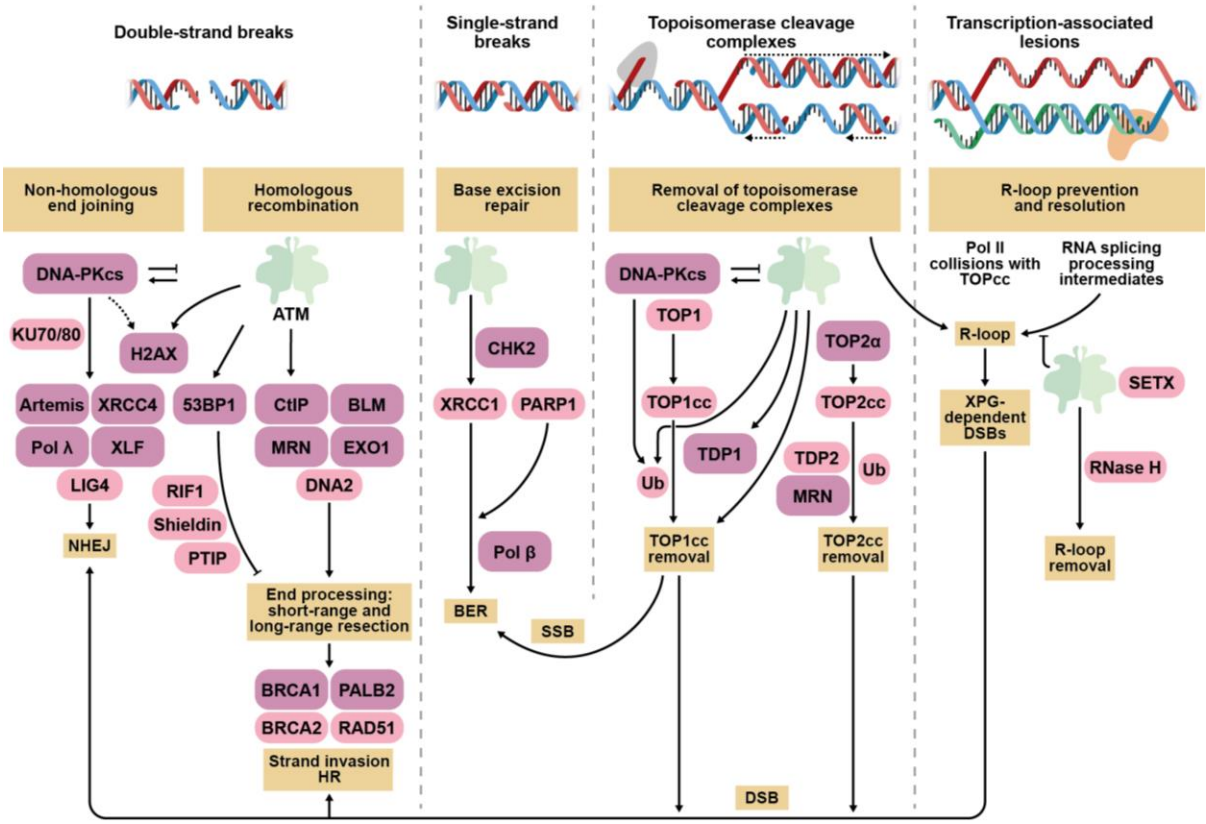

Figure 13. Examples of ATM roles in different DNA damage repair pathways. In DNA double-strand break repair, ATM phosphorylates factors like CtIP and MRN leading to short-range end resection and initiation of HR pathway of repair as well as proteins involved in long-range end resection (BLM and EXO1), which facilitate strand invasion by RAD51. In NHEJ, ATM has a positive effect on this repair pathway by phosphorylating DNA-PKcs, Artemis and other involved proteins. In addition, ATM modifies 53BP1 leading to recruitment of factors involved in the restriction of end resection. In DNA single-strand break repair, ATM functions in BER by regulation of XRCC1 through phosphorylation of CHK2. In topoisomerase cleavage complexes (cc), ATM regulates TOP1cc removal by phosphorylation of TDP1 and DNA-PKcs, activity of which causes ubiquitination and subsequent degradation of TOP1cc. TOP2α and MRN are substrates of ATM that are involved in TOP2cc removal. In transcription-associated lesions, ATM functions in both prevention and removal of R-loops via activity of helicases, like senataxin (SETX), and RNase H enzymes. Proteins in purple are direct targets of ATM, while the ones in pink are affected by ATM activity indirectly[172].

The ATM kinase plays important roles in the maintenance of the redox homeostasis. As observed in A-T patients and ATM-null mouse models, lack of ATM leads to higher levels of ROS, abnormal levels of redox-reactive thiols and hypersensitivity to oxidative stress[172]. An important intra-cellular source of ROS is the peroxisome, which produces ROS during the fatty acid metabolism. In response to increase in ROS, ATM signaling leads to inhibition of mTORC1, which functions in the inhibition of autophagy, to induce autophagy[219]. In order to specifically induce pexophagy (autophagy of peroxisomes), ATM phosphorylates the peroxisome import receptor PEX5 resulting in PEX5 recognition by autophagy adaptor protein

p62 (Figure 14)[220]. Another major intra-cellular source of ROS is mitochondrial oxidative metabolism. It is known that ATM keeps mitochondrial ROS production in check and can initiate mitophagy (autophagy of mitochondria) in response to damaged mitochondria-associated increase in ROS levels. However, the mechanism of ATM induced mitophagy is not fully understood[221]. In addition to mitophagy, ROS induced activation of ATM can lead to increase in production of antioxidants in mitochondria by promoting activity of glucose 6-phosphate dehydrogenase (G6PD). This increases antioxidant levels by producing NADPH, which functions in reduction of oxidized glutathione and thioredoxins[222].

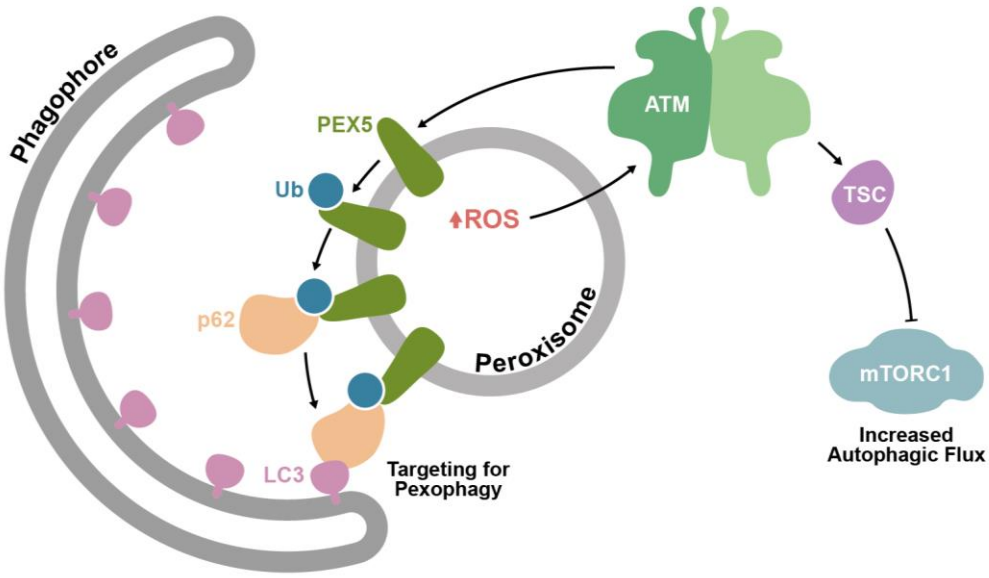

Figure 14. Peroxisomal ROS related ATM activities. ATM gets activated following an increase in ROS levels in the peroxisome. ATM signals via TSC to suppress mTORC1 activity resulting in an increase of autophagic flux. In addition, ATM phosphorylates PEX5, protein present on peroxisomes, causing its ubiquitination and subsequent recognition by p62. This adaptor protein tethers peroxisome to phagophore via LC3 binding resulting in formation of the nascent autophagosome.

More recently, a role of ATM in the maintenance of protein homeostasis has been revealed. In the absence of ATM function, intrinsically disordered protein aggregates form at the sites of SSBs that are dependent on transcription and more abundant in the presence of elevated ROS levels. In this case, the formation of protein aggregates is caused by PARP mediated hyper-PARylation. Normally phosphorylation by ATM can prevent the formation of insoluble protein domains[223].

1.4.3 ATM kinase in cancer

The ATM kinase has been linked to cancer since its discovery, as A-T patients show increased risks of cancer development, including a 20-30% lifetime risk of lymphoid, gastric, breast, skin and other cancers. ATM has been shown to be among the most commonly mutated genes in sporadic cancers[224]. The COSMIC database contains hundreds of somatic ATM mutations that have been observed in different types of tumors. These ATM mutations are distributed throughout the entire length of the protein and occur in each functional domain[225]. ATM plays key roles in the maintenance of genome integrity (described in section 1.4.2). Hence, it is not surprising that mutations in ATM are linked to cancer as alterations of its structure and function can lead to increased genetic instability, which is a hallmark of cancer.

A fully-functional ATM acts as a tumor suppressor, mainly due to its roles in the induction of cell cycle arrest in response to DNA damage or other types of cellular stress (described in section 1.4.2). In order to escape the effects of ATM activation, cancer cells use multiple ways to decrease ATM levels. For instance, in breast cancer microRNA miR-18, which downregulates ATM expression, is upregulated[226]. ATM activity can be reduced by increasing activity of WIP1 phosphatase, which dephosphorylates ATM and some of its substrates that function in ATM-mediated cell cycle arrest[227]. In other cancers, hypermethylation of the ATM promoter region is frequently used to decrease ATM levels[228]. Interestingly, ATM signaling is upregulated in some cancers. This can be achieved by different mechanisms. For instance, pancreatic cancer cells can overexpress the transcription factor CUX1, the activity of which leads to increased ATM levels[229,230]. Most likely these cancer cells that upregulate ATM already found a way to bypass cell cycle arrest without involving ATM or managed to uncouple ATM signaling from the cell cycle arrest. Cancer cells benefit from ATM signaling as it can promote radio/chemoresistance, metastasis and cell survival[231]. The increased capacity to fix DSBs upon upregulated ATM signaling can be sufficient to provide cancer cells with radio/chemoresistance. Metastasis can be promoted by ATM through NF-κB-mediated secretion of pro-tumorigenic cytokines[232]. Taken together, ATM activity can facilitate tumorigenesis and protect cancer from radio/chemotherapy in certain cancers. Hence, in these cases it is important to inhibit ATM as part of anti-cancer therapy.

1.4.4 ATM inhibition as cancer treatment

The ATM kinase protects cells against DNA DSBs. Therefore, inhibition of ATM should sensitize cells to radio/chemotherapy. As cancer cells are proliferating much faster and accumulate DSB quicker, they should be affected by ATM inhibition more than healthy cells. In addition, some cancers upregulate ATM levels to benefit from protective functions of this

kinase (see section 1.4.3 for more details)[231]. Hence, ATM is an attractive target for anti-cancer therapy. Inhibition of ATM requires development of highly specific small molecule inhibitors to prevent off-target effects by simultaneous inhibition of related PIKKs and PI3Ks. Currently, clinical development of ATM inhibitors is at an early stage with a few inhibitors in preclinical studies and early-stage clinical trials (Figure 15)[233].

The first selective ATP-competitive ATM inhibitor is KU-55933, which has been shown to significantly block HR repair in human melanoma[234,235]. However, the use of KU-55933 *in vivo* is limited due to high lipophilicity[236]. An analogue of KU-55933, KU-60019 has improved pharmacokinetics and bio-availability. KU-60019 was shown to induce synthetic lethality in PTEN-deficient breast cancer cells when combined with cisplatin (chemotherapy medication)[237]. P53 is a tumor suppressor protein that functions in cell cycle arrest upon DNA damage and is frequently mutated in cancers. Another ATM inhibitor KU-59403 has no anti-tumor effect on its own, but when combined with radio/chemotherapy can cause death of cancer cells independent of the p53 status[238].

CP-466722 is a reversable ATM inhibitor that has no effect on other members of PIKK family. Usage of CP-466722 in colony-forming assay has shown that even transient inhibition of ATM leads to cell sensitization to IR[239]. Short-term inhibition of ATM is also used to evaluate ATM functions under different conditions. For instance, CP-466722 treatment of non-small cell lung cancer cells shows reduction in cisplatin-resistance induced epithelial-mesenchymal transition, which is a characteristic of metastatic cells. These results were confirmed by knocking-down ATM[240].

AZD0156 and AZD1390 are very potent, selective and orally available inhibitors that entered clinical trial (results not available)[241,242]. AZD0156 can prolong life of acute myeloid leukemia xenografted mouse models[243]. AZD1390 shows a better blood-brain barrier permeability than AZD0156. AZD1390 combination with IR leads to a striking G2 cell cycle arrest in p53 mutant cells and suppresses tumor growth in *in vivo* models[242].

ATM inhibition as a monotherapy might not be effective enough for cancer treatment. However, ATM inhibition in combination with other DNA damage repair inhibitors and/or chemotherapeutic agents, which induce DNA damage, shows promising results in the preclinical research and can result in a viable cancer therapy approach.

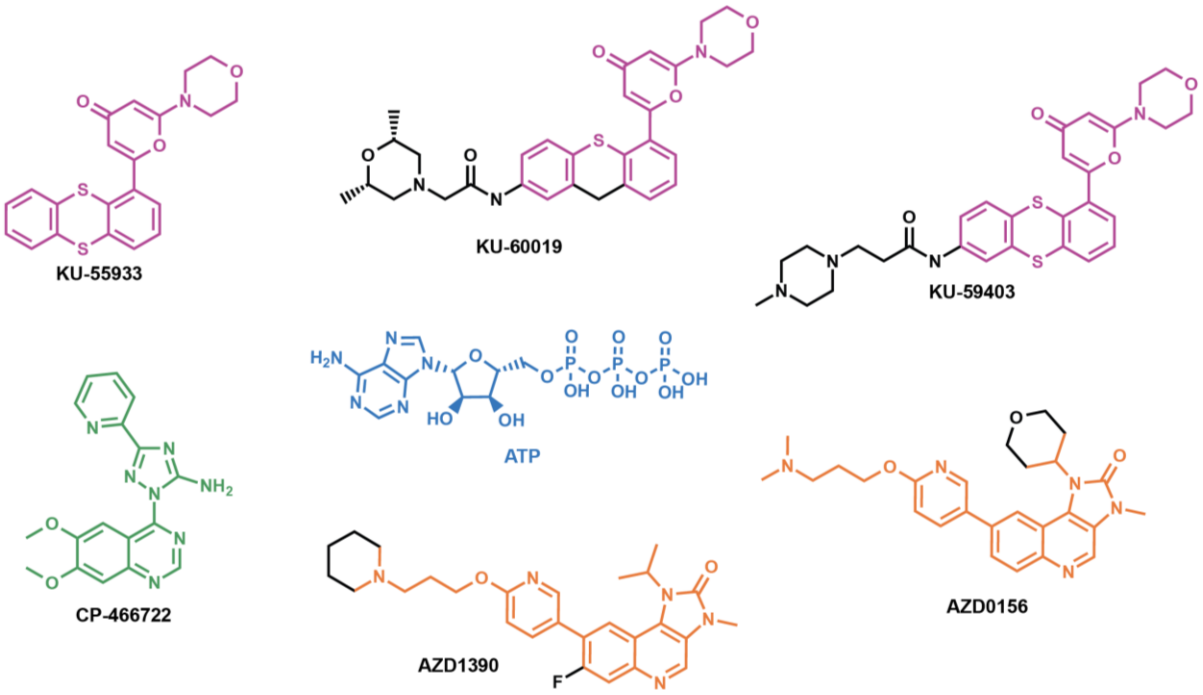

Figure 15. An overview of ATM inhibitors. ATP (in the middle, blue) is a molecule that naturally binds to the active site of ATM and is used as a source of phosphate moiety for substrate phosphorylation. Various ATP competitive molecules are designed to act as kinase inhibitors. Colored inhibitor areas indicate chemical structures in common.

1.5 Objectives

The MRN complex and ATM kinase play crucial roles in the maintenance of genome integrity as well as numerous other cellular processes. Both of these factors have been extensively studied revealing important structural and functional aspects. However, many questions regarding the ATM activation and inhibition mechanisms as well as MRN regulation and DNA tethering functions remain unanswered.

The architecture of eukaryotic MRN complex includes elongated and flexible features, for instance, Mre11 C-terminus, Rad50 coiled-coils and almost the entire Nbs1 protein. For decades the main method used for structural studies of the MRN has been X-ray crystallography. Hence, structural characterization of the MRN complex was limited to rigid portions of the complex and always involved severe truncations of the functionally important coiled-coils of Rad50 and other flexible features. On the other hand, recombinant production of ATM kinase has been challenging, due to the large size of dimeric ATM kinase. Hence, structural and biochemical characterization of the kinase has been limited. Lack of a high-resolution structure of human ATM restricted development of structure-based inhibitors.

The primary aim of the MRN project was to obtain a structure of an intact full-length eukaryotic MRN complex using cryo-EM, which allows usage of samples with flexible motifs. This led to a near-complete model of *Chaetomium thermophilum* MR in complex with ATPγS and a structure of the Nbs1 peptide wrapping around the Mre11 dimer. The Rad50 coiled-coils are in a closed rod conformation and a tetrameric Rad50 zinc-hook indicates MRN dimerization. Based on the new structural insights, the further work included analysis of the MRN DNA-binding and ATPase activity, as well as crystallization of Rad50 zinc-hook tetramer and investigation of its importance for DNA damage repair *in cellulo*.

The first part of the ATM project focused on *ct*Tel1, an ortholog of ATM from the thermophilic fungus *Chaetomium thermophilum*. The aim was to determine a structure of full-length ctTel1 using cryo-EM and analyze its DNA binding properties. The second part of this project focused on human ATM with the main aim being a set of high-resolution structures of this kinase in complex with ATPγS and ATM inhibitors KU-55933 and M4076. These structures led to an atomic model of full-length human ATM, with only a few flexible loops missing, and understanding of ATM inhibitor specificity allowing for an improved structure-based drug design in the future.

2. Publications

2.1 Near-Complete structure and model of Tel1ATM from *Chaetomium thermophilum* reveals a robust autoinhibited ATP state

Jansma M., Linke-Winnebeck C., Eustermann S., Lammens K., Kostrewa D., Stakyte K., Litz C., Kessler B., Hopfner K.P. 2020. Near-Complete structure and model of Tel1ATM from *Chaetomium thermophilum* reveals a robust autoinhibited ATP state. **Structure** 28:83–95.

Summary

In this publication we report the high-resolution structure of fungal ATM kinase (Tel1), with the kinase domain at 2.8 Å resolution and overall structure with the more flexible HEAT repeat domains at 3.7 Å. This quality of data allowed building of a near-complete atomic model of Tel1; with only a few flexible loops missing. Our structure of dimeric Tel1 reveals a hydrophobic dimer interface, challenging the idea of monomerization being a part of the ATM activation mechanism. In the kinase active site catalytic loops are in the catalysis proficient state, coordinating a Mg^{2+} ion and ATPγS. However, access to the active site is physically blocked by the PIKK regulatory domain (PRD) that acts as a pseudo-substrate. This finding suggests that the mechanism of Tel1 activation requires conformational change induced removal of the PRD allowing substrate access to the active site. We showed that the N-terminal domains have DNA binding activity, but changes in their conformation showed no structural effect on the kinase domains. Cancer and ataxia-telangiectasia mutations were mapped onto the structure highlighting functionally important elements.

Author contribution

I purified Tel1 and prepared grids for cryo-EM together with Marijke Jansma. I processed cryo-EM data with help of Marijke Jansma and was involved in structure building.

Article

Structure

Near-Complete Structure and Model of Tel1ATM from *Chaetomium thermophilum* Reveals a Robust Autoinhibited ATP State

Graphical Abstract

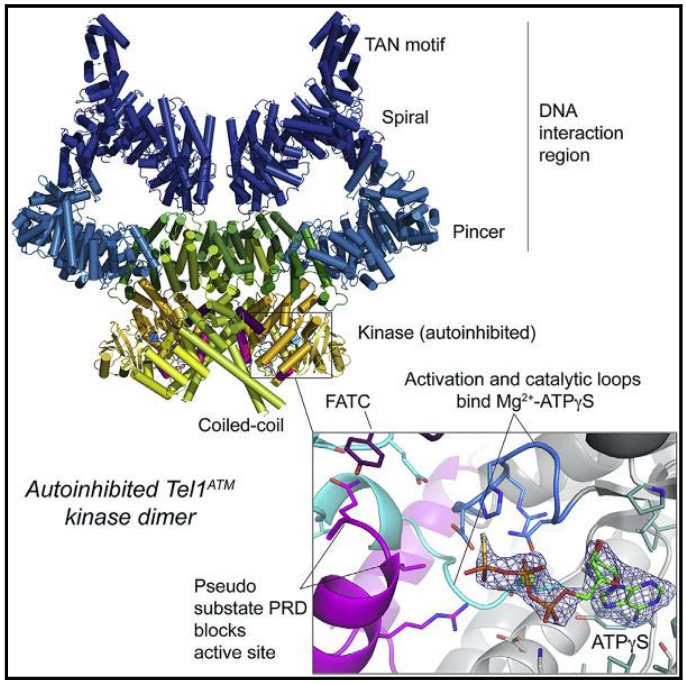

Authors

Marijke Jansma, Christian Linke-Winnebeck, Sebastian Eustermann, ..., Claudia Litz, Brigitte Kessler, Karl-Peter Hopfner

Correspondence

hopfner@genzentrum.lmu.de

In Brief

Jansma et al. use cryoelectron microscopy to determine the structure and provide a near-complete atomic model of the Tel1^{ATM} kinase dimer, showing how this DNA-damage response sentinel is kept in an ATP-bound but autoinhibited state prior to proper activation by DNA breaks.

Highlights

- 3.7-Å structure and near-complete atomic model of autoinhibited Tel1^{ATM}
- 2.8-Å active site with Mg^{2+}-ATPγS reveals elements of catalysis and autoinhibition
- PRD is locked by FATC and blocks active-site access as pseudo-substrate
- The N-terminal solenoid has DNA binding activity

Jansma et al., 2020, Structure *28*, 83–95
January 7, 2020 © 2019 Elsevier Ltd.
https://doi.org/10.1016/j.str.2019.10.013

CellPress

Structure
Article

Near-Complete Structure and Model of Tel1ATM from *Chaetomium thermophilum* Reveals a Robust Autoinhibited ATP State

Marijke Jansma,[1,2] Christian Linke-Winnebeck,[1,2,3,6] Sebastian Eustermann,[1,2,4,6] Katja Lammens,[1,2,6] Dirk Kostrewa,[1,2] Kristina Stakyte,[1,2] Claudia Litz,[1,2,5] Brigitte Kessler,[1,2] and Karl-Peter Hopfner[1,2,7,*]
[1]Department of Biochemistry, Ludwig-Maximilians-Universität, Feodor-Lynen-Strasse 25, 81377 Munich, Germany
[2]Gene Center, Ludwig-Maximilians-Universität, Feodor-Lynen-Strasse 25, 81377 Munich, Germany
[3]Present address: ChromoTek GmbH, Am Klopferspitz 19, 82152 Planegg-Martinsried, Germany
[4]Present address: Structural and Computational Biology, European Molecular Biology Laboratory (EMBL), Meyerhofstrasse 1, 69117 Heidelberg, Germany
[5]Present address: Max Planck Institute for Biochemistry, Am Klopferspitz 18, 82152 Planegg-Martinsried, Germany
[6]These authors contributed equally
[7]Lead Contact
*Correspondence: hopfner@genzentrum.lmu.de
https://doi.org/10.1016/j.str.2019.10.013

SUMMARY

Tel1 (ATM in humans) is a large kinase that resides in the cell in an autoinhibited dimeric state and upon activation orchestrates the cellular response to DNA damage. We report the structure of an endogenous Tel1 dimer from *Chaetomium thermophilum*. Major parts are at 2.8 Å resolution, including the kinase active site with ATPγS bound, and two different N-terminal solenoid conformations are at 3.4 Å and 3.6 Å, providing a side-chain model for 90% of the Tel1 polypeptide. We show that the N-terminal solenoid has DNA binding activity, but that its movements are not coupled to kinase activation. Although ATPγS and catalytic residues are poised for catalysis, the kinase resides in an autoinhibited state. The PIKK regulatory domain acts as a pseudo-substrate, blocking direct access to the site of catalysis. The structure allows mapping of human cancer mutations and defines mechanisms of autoinhibition at near-atomic resolution.

INTRODUCTION

DNA double-strand breaks (DSBs) are among the most dangerous form of DNA damage and can lead to gross chromosomal rearrangements, aneuploidy, and cell death. In humans, genome instability following insufficient repair of DSBs is one of the hallmarks of cancer (Hanahan and Weinberg, 2011). To maintain genome integrity, cells have evolved sensitive mechanisms to detect and repair DSBs in all phylogenetic kingdoms (Hoeijmakers, 2009).

In eukaryotes, DSBs evoke a robust DNA-damage response (DDR). DSBs are sensed by the MRN (Mre11-Rad50-Nbs1, MRX in *Saccharomyces cerevisiae*) complex, which recruits and activates the kinase Ataxia-Telangiectasia Mutated (ATM) at the site of the lesion (Bakkenist and Kastan, 2003; Shiloh and Ziv, 2013). Activated ATM phosphorylates hundreds of target proteins with an SQ or TQ motif (Kim et al., 1999; Matsuoka et al., 2007; O'Neill et al., 2000), including H2A.X, MRN itself, the checkpoint kinases CHK1 and CHK2, and many other proteins that associate with the lesion or function in the DDR. In this way ATM orchestrates the DDR, leading to cell-cycle arrest and/or cell death, regulates gene expression and protein degradation, and modulates the chromatin structure adjacent to DSBs to regulate and enable subsequent DNA repair processes.

ATM (denoted Tel1 in *S. cerevisiae*) was originally identified on the base of genetic mutations in the rare autosomal recessive disorder ataxia-telangiectasia (A-T), which is characterized by neurodegeneration and genomic instability (Savitsky et al., 1995). Mutations in ATM have also been identified in several forms of cancer, reflecting its central role in genome maintenance (Choi et al., 2016). ATM together with ATR (denoted Mec1 in *S. cerevisiae*), mTOR, DNA-PK, TRRAP, and SMG1 constitute a family of very large kinases, the phosphatidylinositol 3-kinase-like kinases (PIKKs) (Keith and Schreiber, 1995). PIKKs form a homeostasis surveillance system by monitoring genome integrity (ATM, ATR, DNA-PK), oxidative stress (ATM), mRNAs (SMG1), and nutrient states (mTOR).

With the exception of TRRAP, which has lost its enzymatic activity, each PIKK targets a broad set of proteins, thereby orchestrating its characteristic cellular stress response such as cell-cycle control, chromatin alterations, regulation of transcription and translation, protein degradation, and autophagy. PIKKs are very large proteins (300–500 kDa for monomers) and share a similar domain organization. All PIKKs possess an α-solenoid N-terminal domain, which is mainly composed of HEAT repeats and spans 1,000–3,000 residues (Baretic and Williams, 2014). The kinase domain, surrounded by a conserved α-helical FAT (FRAP, ATM, and TRAPP) domain, is at the C terminus, together with the PIKK regulatory domain (PRD) and the FATC domain. Together these domains form an integral FATKIN unit (Baretic

and Williams, 2014; Imseng et al., 2018; Yang et al., 2013). The HEAT repeats play a role in the interaction with other proteins and regulate the activation of the kinase domain.

In the last years several ATM structures have been reported, which revealed the overall architecture and enabled assignment of secondary structure, but only allowed building of side-chain models for parts of the protein (Baretic et al., 2017; Lau et al., 2016; Llorca et al., 2003; Sawicka et al., 2016; Wang et al., 2016; Xiao et al., 2019; Xin et al., 2019). ATM is a butterfly-shaped dimer, where both protomers interact via the FATKIN domain. Conformational mobility in the N-terminal parts of the protein have prevented the determination of high-resolution structures to date, and suggested a dynamic equilibrium between open and closed conformations (Baretic et al., 2017; Xin et al., 2019). It was suggested that these conformations are coupled to the activity of the kinase, and are stabilized by different regulators.

Despite the recent progress, the regulatory mechanisms underlying the pivotal role of ATM during DDR orchestration and cell-fate determination remain elusive. Initial models suggested that ATM resides as inactive, autoinhibited dimer in the absence of DNA damage, and that autophosphorylation on Ser1981 is critical for monomerization and activation of *Homo sapiens* (hs)ATM (Bakkenist and Kastan, 2003). Subsequent work suggested that factors other than autophosphorylation play more important roles (Daniel et al., 2008; Pellegrini et al., 2006; You et al., 2005). The ATM dimer interface is hydrophobic, favoring a model of a constitutive dimer and indicating that conformational changes within the dimer are a possible mechanism of activation. However, a recent study provided an initial structure of monomeric hsATM at 7.8 Å resolution and showed that the monomer is more active than the dimer. In any case, interactions with DNA, or a complex of DNA and MRX, triggers activation of ATM/Tel1 (Hailemariam et al., 2019). Human ATM is also activated by oxidative stress-mediated formation of a disulfide bond (Guo et al., 2010). However, at a detailed molecular level, key questions remain: how is the inactive state of ATM maintained despite its apparent inherent dynamics and which are the conformational changes required to explain the modes of ATM activation and the impact of disease associated mutations?

To improve our understanding of the (auto)regulatory circuitry of ATM, we used cryoelectron microscopy (cryo-EM) and nanobodies to determine the structure of endogenous, dimeric ctTel1, a 650-kDa homolog of ATM from the thermophilic fungus *Chaetomium thermophilum*, to an overall resolution of 3.7 Å, with major parts including the kinase domain at 2.8 Å. This resolution allowed us to build the first atomic model of a Tel1/ATM homolog to date. The unusual structure of the N-terminal HEAT repeat domain reveals a flexibly connected platform with tentacle-like insertion loops, serving as a hub for its numerous interaction partners, including DNA for which we demonstrate binding activity. A detailed picture of the kinase active site, including the bound Mg^{2+}-ATPγS, suggest that ATP binding and activation of the kinase are distinct events and identifies a putative SQ/TQ specificity site. An extensive network of intra- and intermolecular domain contacts, conserved across species, visualizes how ATM remains in a tightly controlled, autoinhibited state, providing a structural framework for future studies of ATM activation by larger effector complexes and aiding the design of inhibitors for cancer therapy.

RESULTS AND DISCUSSION

Structure Determination

We provide a near complete atomic model of the fungal ATM ortholog ctTel1 from *C. thermophilum* (Figure 1 and Video S1). *C. thermophilum* has gained popularity in recent years as the increased thermostability of its proteins is beneficial for structural studies (Amlacher et al., 2011; Bock et al., 2014; Kellner et al., 2016). We identified ctTel1 by sequence homology; a multiple sequence alignment shows a degree of sequence conservation between ctTel1 and human ATM and between ctTel1 and yeast Tel1 of around 18% sequence identity and 34% sequence similarity (Data S1). Endogenous ctTel1 was purified from *C. thermophilum* using an immunoaffinity pull-down with a recombinant nanobody (Figures S1A and S1B). To raise nanobodies, we made use of a finding that the N-terminal domain of ctTel1 (residues 1–1,864) can be produced in *Escherichia coli* in a soluble form in high amounts (Figures S2A and S2B). CtTel1(1–1,864) was then used to immunize alpacas. We obtained nine nanobodies that were characterized further (Figure S1). With two of them (nanobodies D4 and F7), we purified endogenous ctTel1 and determined corresponding structures by cryo-EM. First reconstructions around 7 to 8 Å resolution revealed very similar overall dimeric structures of these nanobody-Tel1 complexes (Figure S3A). As the nanobodies bind to different parts of the protein, they evidently do not affect the overall structures of the Tel1 dimer. We therefore focused on one of those complexes and used nanobody F7 to obtain the final high-resolution structure, as this nanobody appeared to stabilize the very N-terminus.

Using 863,937 particles and classification and masked refinement procedures, we reconstructed the three-dimensional (3D) structure of the ctTel1 dimer in different conformations (Figures S3–S5). For the FATKIN domain dimer, we obtained an overall resolution of 2.8 Å (Figures S3B and S3C). Using masked 3D classification and refinements for one protomer, we obtained reconstructions for the N-terminal α-solenoid domain in a closed conformation at 3.4 Å resolution, and in an open conformation at 3.6 Å resolution. Since the closed conformation was determined to higher resolutions, the particle subset yielding the closed conformation was sorted further in another round of masked 3D classification with a mask for the α-solenoid domain for the other protomer. This yielded a class in which both N-terminal domains were in a closed conformation. Refinement of these particles resulted in maps of the entire particle with resolutions up to 4.0 Å (no symmetry imposed) and 3.7 Å (C2 symmetry imposed). Since the obtained densities indicated still multiple conformations of the N-terminal domains of both protomers, a final round of masked 3D classification was performed with a mask for both N-terminal domains. Refining the subset of particles with both protomers in a closed conformation with C2 symmetry yielded an overall map with a resolution to 3.7 Å in which all parts are similarly well resolved (Figures S3 and S5).

The different reconstructions allowed us to build a side-chain model for 90% of the polypeptide, except for some disordered loop regions and the very N terminus (Figures 1, S3, and S6).

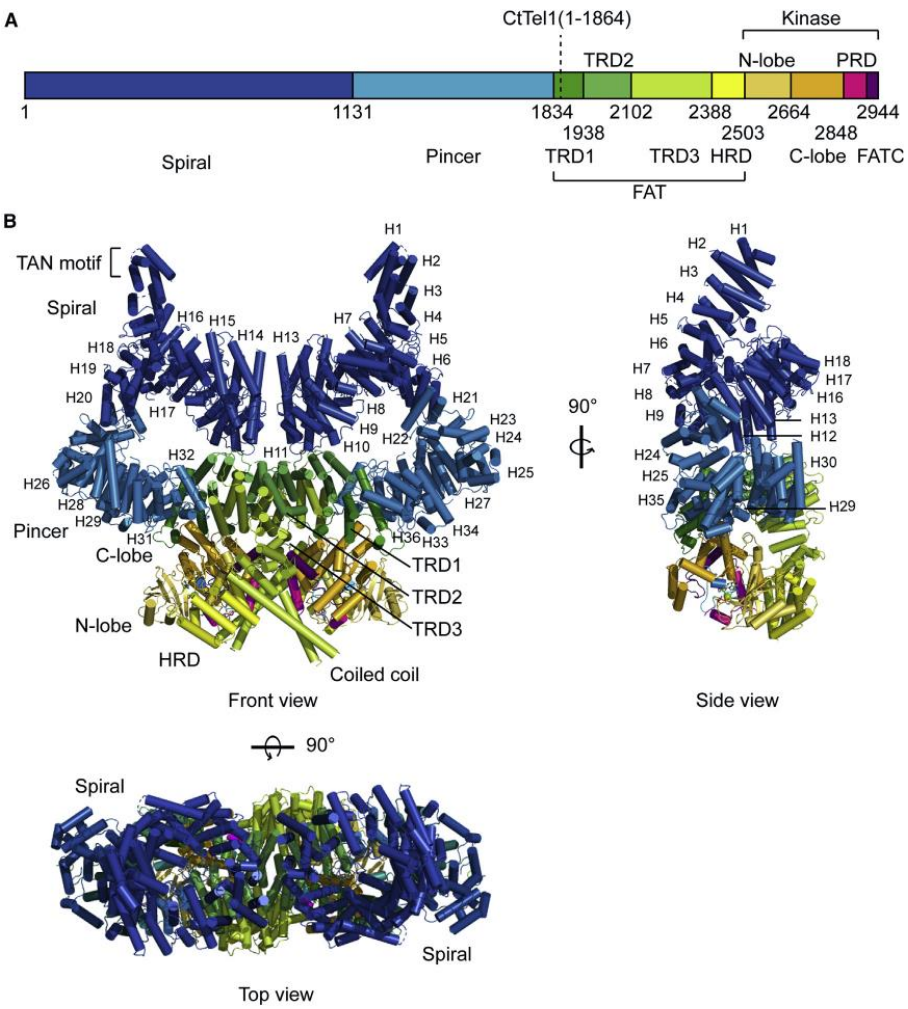

Figure 1. The Cryo-EM Structure of ctTel1 in a Closed Conformation

(A) Domain organization of ctTel1 indicated in different colors. The same color scheme is used throughout this paper. Truncated ctTel1(1–1,864) is indicated by a dashed line.

(B) Front and top views of dimeric ctTel1 with highlighted secondary structure, and side view of one protomer. The 36 HEAT repeats are labeled sequentially from N terminus to C terminus.

See also Data S1; Figures S1–S3 and S5; Video S1.

In total, the model comprises 2,652 out of 2,944 residues and shows good stereochemistry (Figure S6 and Table S1). Our structure particularly helps clarifying parts that could not be interpreted in studies of *S. cerevisiae* Tel1 (Yates et al., 2019 [~45% complete] and Xin et al., 2019 [~60% complete]).

Overall Architecture

Like other ATMs, ctTel1 forms a dimer with a butterfly shape (Baretic et al., 2017; Lau et al., 2016; Sawicka et al., 2016; Wang et al., 2016; Xiao et al., 2019; Xin et al., 2019). The fold comprises the Spiral domain at the N terminus, followed by Pincer, which together form the α-solenoid, FAT, and kinase domains at the C terminus. It has the same overall arrangement of domains and repeat elements as the yeast and human orthologs, showing the exceptional conservation throughout evolution. This applies as well for the HEAT repeats in the α-solenoid part, where the sequence similarity is much lower than in the FATKIN domain (Figure 1 and Data S1).

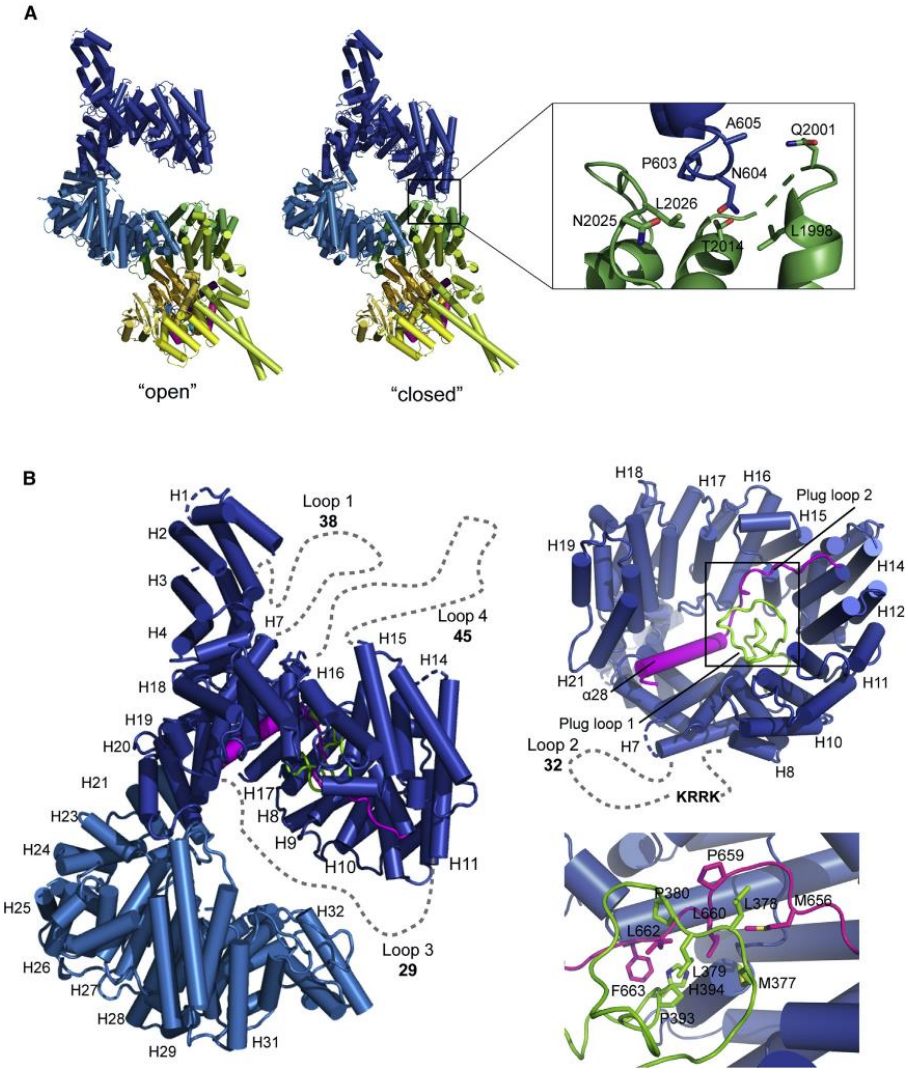

Figure 2. Structure of N-terminal α-Solenoid

(A) (Left) The Spiral domain of ctTel1 can move between an open and closed conformation on a hinge in the Pincer. (Right) In the closed conformation, Spiral and the FATKIN domain have a small interface.

(B) Details of the intricate fold of the Spiral and Pincer, viewed from the front, and of the Spiral, viewed from the bottom. HEAT repeats are labeled as in Figure 1. Locations of unstructured loops are indicated by a dotted line and length by numbers. The α-solenoid is stabilized by two central Plug loops and a helix in the Spiral domain, with Plug loop 1 indicated in green and Plug loop 2 indicated in magenta. The Plug loops interact mainly via hydrophobic interactions.

See also Data S1; Figures S3 and S5; Video S2.

CtTel1 forms a dimer with a total of around 3,500 Å^2 buried surface area, as calculated by using PISA (Krissinel and Henrick, 2007). Most of the dimer interface is formed by the FATKIN domain, as observed for other species. We observe motions of the Spiral domain in relation to the FATKIN domain, which have also been reported for other species (Baretic et al., 2017; Xin et al., 2019). We denote two orientations of the Spiral relative to the FATKIN as an "open" conformation and a "closed" conformation (Figures 2, S3C, and S3D). While in the open ctTel1 conformation the FATKIN dimer interface is the sole interaction

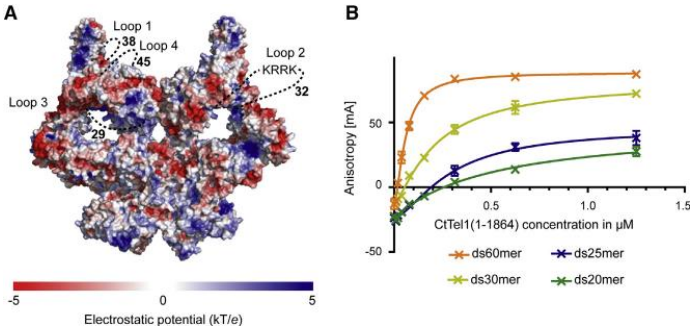

Figure 3. The α-Solenoid Domain of ctTel1 Has DNA Binding Properties

(A) Calculated electrostatic potential at the solvent-accessible surface of ctTel1 shows positively charged patches as potential DNA binding sites. Locations of the unstructured loops that are not part of the surface are indicated, with their length in numbers.

(B) Fluorescence polarization anisotropy titrations with various lengths of fluorescently labeled double-stranded DNA and increasing amounts of ctTel1(1–1,864) as indicated show length-dependent DNA binding activity of the Spiral-Pincer region of Tel1 (n = 3 technical repeats). Error bars indicate the standard deviation.

See also Data S1; Figures S1 and S2.

site between the two protomers, in the closed conformation there is an additional, transient interaction between the Spiral domains of each protomer. The Spirals of the protomers move independently of each other, leading to either symmetric open or closed conformations, or to asymmetric configurations where one protomer is in an open state and the other is in the closed state.

In contrast to other studies, our data do not provide evidence for conformational coupling of the open or closed configurations with the dimeric structure of the FATKIN module, as there are no significant rearrangements in the FATKIN domain when comparing the different conformational states (Video S2). Thus, ctTel1 appears to be in a structurally robust, dimeric autoinhibited state (see below), and mere pivot movements of the Spiral are not sufficient to alter the structure of the kinase module. Supporting a stable dimer configuration, we did not observe monomers on the EM micrographs. Endogenous ctTel1 appears to be in a robust dimeric conformation, and the N-terminal Spiral can move independently without inducing structural changes in the autoinhibited kinase. It is likely that more robust conformational transitions are required to alter the FATKIN region, most likely structural changes induced by interactions with MRN and DNA.

Structure of the N-Terminal Spiral Domain

HEAT repeats often mediate protein-protein interactions, and therefore the Spiral is also believed to be a hub for interactions. Growing genetic and biochemical evidence suggests that the N-terminal Spiral domain is indeed a hub for components of larger effector complexes of the DNA-damage repair machinery, such as Nbs1 (Falck et al., 2005; You et al., 2005), and key DDR signaling substrates such as p53 (Fernandes et al., 2005). To provide detailed structural insight into the N-terminal regions of ctTel1 implicated in these interactions, we determined cryo-EM densities by 3D classification and focused refinement methods, which allowed for building a side-chain model of nearly the entire N-terminal Spiral domain in an open and a closed conformation. The obtained structure, sequence registry, and connectivity may enable interpretation of lower-resolution maps from other species (Figures S3C, S6, and 2A).

The ctTel1 Spiral domain (HEAT repeats H1–H22) consists mainly of α-helical HEAT repeats and a number of helical and loop insertions of various lengths. We designated all α-helical repeats as HEAT repeats (Figures 1 and 2), although we are aware that some are interspersed with longer loops than is typical and may therefore not represent canonical HEAT repeats.

The N terminus, H1–H3, forms a species-conserved protrusion. H1–H2 are flexible in our map, which limits the resolution in this area, but clear density for the α helices along with secondary structure predictions allowed us to trace this part. The first two helices and their connecting loop contain the Tel1/ATM N-terminal (TAN) motif (Figure 1), which is highly conserved from yeast to humans and is essential for telomere maintenance and the DDR (Seidel et al., 2008). It is therefore plausible that this remote tip of the protein serves as important macromolecular interaction site.

H3 and H4 at the bottom of the protrusion interact with H17 and H18, mainly via hydrophilic interactions, and through this interaction stabilize the highly bent conformation of the α-solenoid. The α-solenoid is bent sharply at H11–H13, which is also the site where the closed conformation the Spiral domains from the two protomers interact with each other and with the TRD2 of the FAT domain (Figures 2A and 5).

Interestingly, in ctTel1, the entire Spiral except for the more flexible H1–H3 protrusion appears to be in a rigid conformation and moves as a rigid body from open to closed conformations (Video S2). The folded conformation of the Spiral is reinforced through two "Plug" loops that originate from the sides and fill the cavity between the two solenoid arms. The two Plug loops are non-helical insertions and form a structured core in the Spiral (Figure 2B). The first Plug loop is a 40-residue insertion between helices α16 and α17 that forms a HEAT-like bundle. This insertion is in ctTel1 longer than in ATMs from higher eukaryotes, but two patches (367–374 and 389–400) are conserved. Plug loop 2 (650–715) is a very long insertion into HEAT elements H12 and H13. Its first hydrophobic part forms with Plug loop 1 the core of the Spiral. Thereafter it reaches across the Spiral and forms a helix (α28) that packs along the interface between the N-terminal (H4) and C-terminal (H20–H22) elements of the Spiral. The third part of Plug loop 2 is a long hydrophilic insert that spans 60 Å on the inside of the gap to reach back to H13 and is disordered in our structures.

Apart from the Plug loops, the Spiral contains several tentacle-like loop insertions (Figures 2B and 3A), for which missing density suggests a highly dynamic nature. A 32-residue loop (residues 417–447), located on the outside of the Spiral,

connects helix 17 with H8. This loop is noteworthy because it contains a highly conserved positively charged patch (KRRK in *Chaetomium*, KRKK in humans). This loop might, for instance, play a role in the interaction with DNA, since we find that the α-solenoid has DNA binding properties (see below).

The Spiral domain is connected to the FATKIN via the Pincer, which also consists of HEAT repeats. The N-terminal part of the Pincer is less resolved in our structure, reflecting its high flexibility. In fact the region functions as a hinge, allowing the entire Spiral to move as a rigid body between an open and a closed conformation (Video S2). Interestingly, in yeast two-hybrid studies of fission yeast Tel1 and Nbs1, two closely adjacent patches that map to the region around the hinge were observed to form interaction sites (You et al., 2005). Thus, it is possible that interactions between ATM and MRN could modulate the conformations around this hinge region.

The ctTel1 α-Solenoid Domain Binds DNA

Several studies have described that ATM has DNA binding properties, and that its kinase activity can be stimulated by DNA. We made use of the N-terminal fragment ctTel1(1–1,864), consisting of both the Spiral and the Pincer, to test DNA binding. We performed fluorescence anisotropy with fluorescein-labeled, blunt-ended, double-stranded DNA of varying lengths (20-, 25-, 30-, and 60mers) (Figure 3B) showing that ctTel1(1–1,864) indeed binds DNA, with a progressively higher affinity for longer DNA oligomers. While a double-stranded 60mer is bound with a K_D = 58 ± 4 nM, the affinity to 30-, 25-, and 20mers is K_D = 220 ± 27 nM, K_D = 300 ± 49 nM, and K_D = 500 ± 230 nM, respectively. These data are in accordance with previous published work in which ATM was described to bind more strongly to longer DNA or to be more stimulated by longer DNA (Dupre et al., 2006; Hailemariam et al., 2019; Lee and Paull, 2005; Xiao et al., 2019).

The strongly enhanced DNA binding of a 60mer compared with a 30mer suggests that DNA binding by ATM/Tel1 is not primarily driven by local recognition of a DNA end, but requires interactions with a longer region on the DNA. Consistently, for *S. cerevisiae* Tel1, a length between 60- and 80-bp double-stranded DNA was necessary to activate the protein, with even longer DNA activating scTel1 more strongly. Since the longest dimensions of the ctTel1 dimer are in a range of 200 Å, which corresponds to around 60 bp of linear B-DNA, it is likely that high-affinity DNA binding and activation of ATM occurs within an ATM dimer or multimer. Such a multimer could be based on the dimer architecture following an activating conformational change, but we do not want to rule out alternative modes of multimerization. Right-angle light scattering indicated that ctTel1(1–1,864) indeed forms a dimer, consistent with a similar length dependence of binding to DNA as ScTel1. However, we cannot rule out that its dimerization is somewhat artificial, since the construct lacks the main Tel1 dimer interface and is perhaps mediated by exposed hydrophobic regions at the truncated C terminus.

The electrostatic potential at the solvent-accessible surface displays a number of positively charged regions that may contribute to DNA binding (Figure 3A). The Spiral has several positively charged patches, including one in the N terminus close the TAN motif. Although this patch appears to be partially concealed by the nanobody, it does not compete with DNA binding (Figure S1C). Thus, it is less likely that this region is the main DNA binding site. Another noteworthy patch is at the apical bend of the Spiral, a groove formed by Spiral, Pincer, and FAT domains. A third region with a potential role in DNA binding is the conserved RKKK motif in the loop insertion between H7 and H8, which is located on the other side of the groove but is disordered in our structures.

Taken together, our data show that α-solenoid of ctTel1 has intrinsic DNA binding properties. The DNA binding studies favor a model in which recognition of a DNA end is not the primary driving force at this region, although high-affinity DNA binding requires contacts with the N-terminal domain of ctTel1 over some length of DNA. Length considerations argue that high-affinity binding of DNA occurs in Tel1 dimers or multimers, but details need to be addressed in future studies.

The ctTel1 FATKIN Domain

All PIKKs have a conserved FAT domain, which wraps around the kinase domain and likely plays a key regulatory role. The ATM/Tel1 FATKIN is extremely conserved in terms of sequence and architecture. As in other ATM structures, the ctTel1 FAT domain is entirely α−helical and consists of three tetratricopeptide domains (TRD1, residues 1,834–1,937; TRD2, residues 1,938–2,101; and TRD3, residues 2,102–2,387) and one HEAT repeat domain (HRD, residues 2,388–2,502). TRD3 has a coiled-coil-like extension (residues 2,285–2,387), which is believed to directly regulate the kinase activity (Figures 1 and 4).

The kinase domain has the canonical bilobal kinase architecture consisting of a C-terminal lobe and an N-terminal lobe, with the active site in a cleft between the lobes. The C lobe interacts directly via residues 2,681–2,715 with the coiled-coil extension of TRD3. Additionally, the C lobe contains a PRD (residues 2,848–2,910) and FATC domain (residues 2,911–2,944), which are common for all PIKKs.

The FAT domain wraps around the kinase, but only interacts at a number of distinct locations mainly via hydrogen bonds and salt bridges (Figure 4). The nature of these interactions is remarkably conserved throughout evolution, and several salt bridges are the same from yeast to human (Baretic et al., 2017; Xin et al., 2019).

TRD1 and the Pincer interact directly with the C lobe via Lys1885 (TRD1)-Glu1654 (Pincer)-Asp2733 (C lobe). Further interactions between TRD1 and the kinase domain are the highly conserved salt bridge Glu1892–Arg2739, which has also been described for hsATM and scTel1, and Arg2642-Asp1928-Arg2819. The presence of this salt bridge shows that this interaction is a highly conserved functional interaction in ATM/Tel1 orthologs.

The coiled-coil insertion of TRD3 and the HRD also interacts directly with the kinase domain. Glu2638 to Arg2176 form a salt bridge between the kinase domain and TRD3 while Ser2121 potentially forms a hydrogen bond with Arg2640. A more extensive surface exists between the HRD and the kinase, with highly conserved salt bridges/interactions formed by Arg2397–Asp2840, Asn2393–Glu2631, and Gln2433–Gln2624.

These interactions are highly conserved and have been reported to be mutated in hsATM in some forms of cancer (Sandoval et al., 1999; Stoppa-Lyonnet et al., 1998), reflecting their importance in maintaining the structural integrity of the protein.

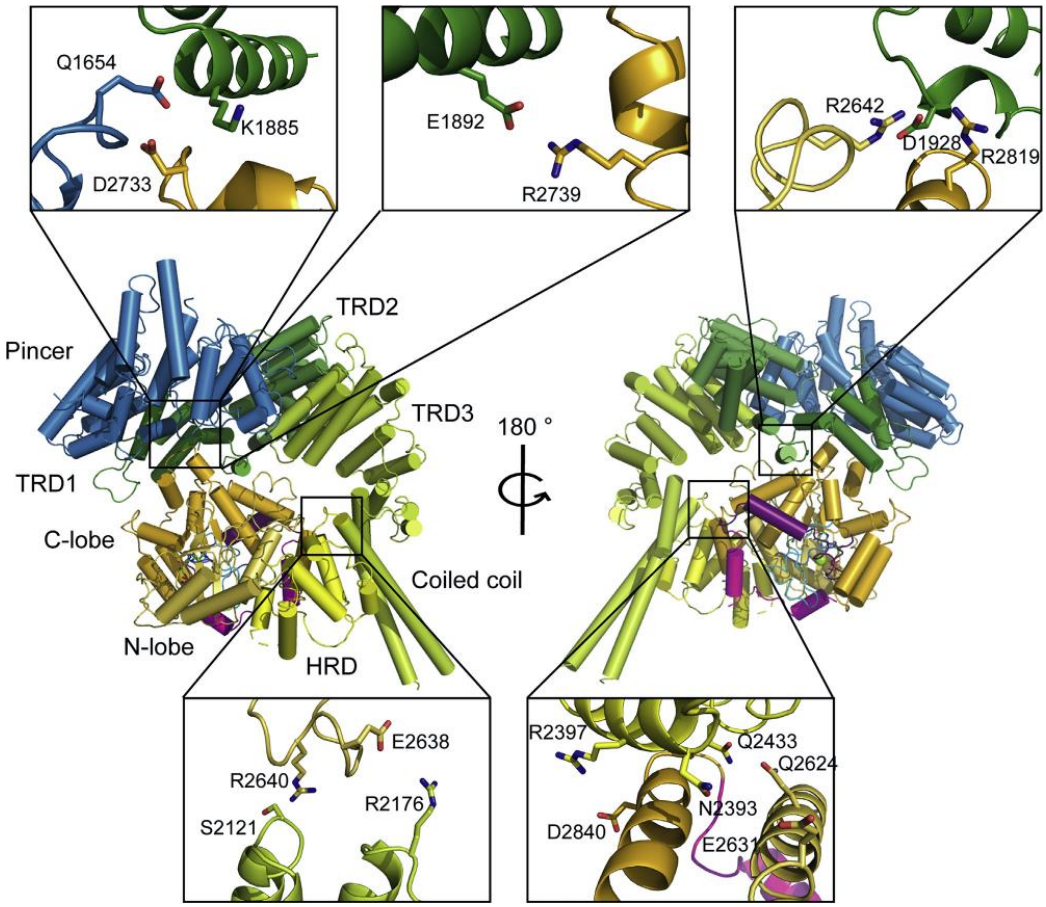

Figure 4. Overview of the Interactions between FAT/Pincer and Kinase Domain
Two 180° rotated views of the Pincer and FATKIN domain of one ctTel1 protomer, with the interacting residues displayed in boxes.

Intermolecular Interactions Dimer Interface

Current structural studies, including ours, consistently point toward a model in which ATM/Tel1 is a dimeric protein in the autoinhibited state. However, the mode of activation is controversial, and proposed mechanisms range from a conformationally altered dimer to a dimer-to-monomer transition. Therefore, we investigated the nature of the ctTel1 dimer interfaces. We see a stable, hydrophobic dimer interface in the FATKIN module that is preserved between open and closed conformations, and a second, transient interface at the Spiral module (Figure 5).

The major dimer contacts in the FATKIN dimerization site are formed by TRD2-TRD2 interactions. Other contacts are contributed by TRD2-TRD3 and by interactions between TRD3 and the kinase domain. Previous work showed that charged and polar residues mediate the interactions between TRD2 and TRD3 and TRD3 and the kinase domain. These interactions are also present in ctTel1 and will not be discussed here.

The residues of the TRD2-TRD2 interface were not described extensively in previous work, but our higher-resolution structures allow us to resolve this part in greater detail (Figure 5). We observe that the TRD2-TRD2 interface consists predominantly of leucines that form, together with Tyr1963, a hydrophobic interface. Additionally, a hydrogen bond may be formed between Ser1996 of both protomers. In addition to the FATKIN dimerization interaction, we observe that in the closed conformation, the two Spiral domains also form a protein-protein interface. This interface is hydrophilic and driven by ion pairs. For instance, Asp576 and Arg615 from opposing Spirals are at a suitable distance to stabilize this transient interaction. Whether this interface is a particular feature of ctTel1 or also exists in other orthologs needs to be clarified in future studies.

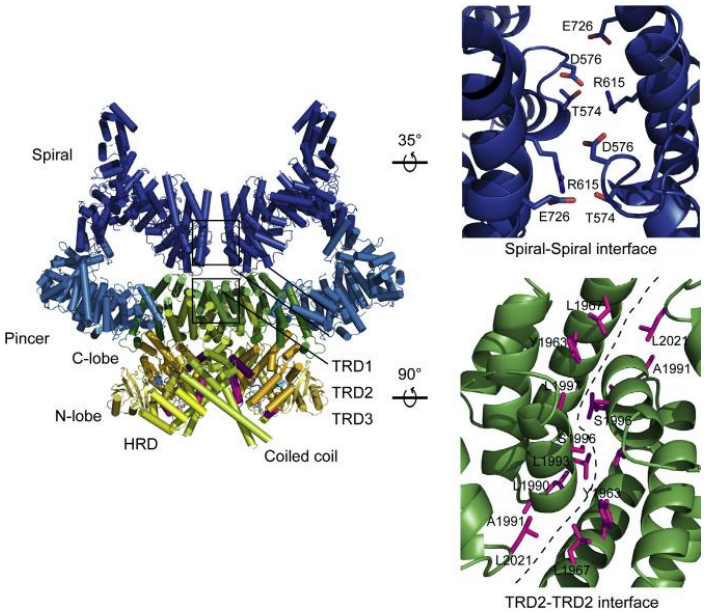

Figure 5. Details of Selected Dimerization Interfaces of ctTel1

The Spiral domains interact via polar interactions and potential salt bridges. The TRD2-TRD2 interface has an extensive, predominantly hydrophobic interface.

In summary, ctTel1 has both a transient and a stable dimer interface. The FATKIN interface has an extensive hydrophobic core and a buried surface area of ~870 Å^2, as calculated with PISA (Krissinel and Henrick, 2007), so a dimer-to-monomer transition will require a substantial compensational free energy contribution. Considering the types of interfaces, we argue that the transient interface might be broken, for example, by binding of activating macromolecules, while the hydrophobic core at TRD2 remains intact during activating conformational changes. However, recent work (Xiao et al., 2019) showed that human ATM can form a monomer that can be separated from the dimer and shows higher kinase activity than the dimer. The ATM monomer has a fold similar to that of dimeric ATM, but since the resolution of the monomer is limited to 7.8 Å, it remains difficult to identify the conformational changes that might rationalize the exposed hydrophobic patch. Eventually, structures of ATM bound to MRN and/or DNA are required to provide further insights into the mechanism and mode of activation.

Structure of the Kinase Domain and Active Site

We determined the structures of ctTel1 in complex with ATPγS to discern how a nucleoside triphosphate is positioned in the active site, and whether ATP binding leads to a more active conformation. The 2.8 Å resolution we obtained for ctTel1 allowed us to delineate the ATPγS moiety and active-site features in near-atomic detail (Figure 6).

The structure of the kinase domain of ctTel1 is very similar to that of the other PIKK structures reported previously. Elements required for catalysis, namely the activation loop and the catalytic loop, are well structured through hydrophobic interactions with the FATC domain, indicative of an active kinase. However, access to the active site is limited by the PRD, which consists of two helices that are connected by a long polar/charged and partially unstructured insertion (in ctTel1 amino acids 2,863–2,896) (Figure 6). The sequence of the loop insertion is not highly conserved (Data S1). In apo-ATM structures, the PRD was shown to block the substrate binding cleft by comparison with CDK2 bound to peptide substrate (PDB: 3QWH) (Baretic et al., 2017; Xin et al., 2019).

ATPγS and one Mg^{2+} are bound in the cleft between two kinase lobes (Figure 6A). The adenine moiety is coordinated by hydrogen bonds of the NH2 and N6 to the backbone carbonyl of Glu2662 and backbone nitrogen of Val2664 (Figure 6B). It also stacks against Phe2663's side chain on one side of the purine ring system and binds to a hydrophobic patch formed by the side chains of Val2664, Ile2778, and Leu2767 on the other side. The sugar 2′ hydroxyl group is coordinated by the backbone carbonyl of His2764. The triphosphate moiety is bound by the Mg^{2+} ion, which is coordinated either directly or via a water molecule by the side chains of Asn2765 and Asp2779 in the activation loop. An additional contact to the α-phosphate can be formed by Lys2610 in the C lobe, which plays a role in binding ATP and catalysis. Finally, Asp2760 in the catalytic loop is well positioned as the key residue for orienting the substrate for nucleophilic attack (Yang et al., 2013), while His2762 interacts with the hydroxyl group of the substrate and is believed to stabilize the transition state. Evidently, ctTel1 in the autoinhibited conformation can properly bind the substrate nucleoside triphosphate, and—as has been described for mTOR—the ctTel1 active site appears to be in an intrinsically active conformation.

Comparison with structures of yeast Tel1 in the apo state and of human mTOR in the ATPγS-bound state reveals only minor structural alterations in the active site in response to ATPγS binding (Figure 6C), in particular in the side-chain orientations of the catalytic and Mg^{2+}-coordinating residues. In both ATPγS-mTOR and ATPγS-ctTel1, these residues adopt a highly similar configuration, which is different in apo scTel1. In fact, the structure shows a remarkable conservation of catalytic and activation loop geometries of ATPγS-mTOR and ATPγS-ctTel1 and highlights the structural conservation among the family. Interestingly, in the active site of mTOR a second Mg^{2+} is observed, whereas we only see density for one Mg^{2+} ion. It is possible that a proper activated state with a substrate protein present is necessary to also promote binding of a second metal ion to ATM. The divergent number of metals in the otherwise

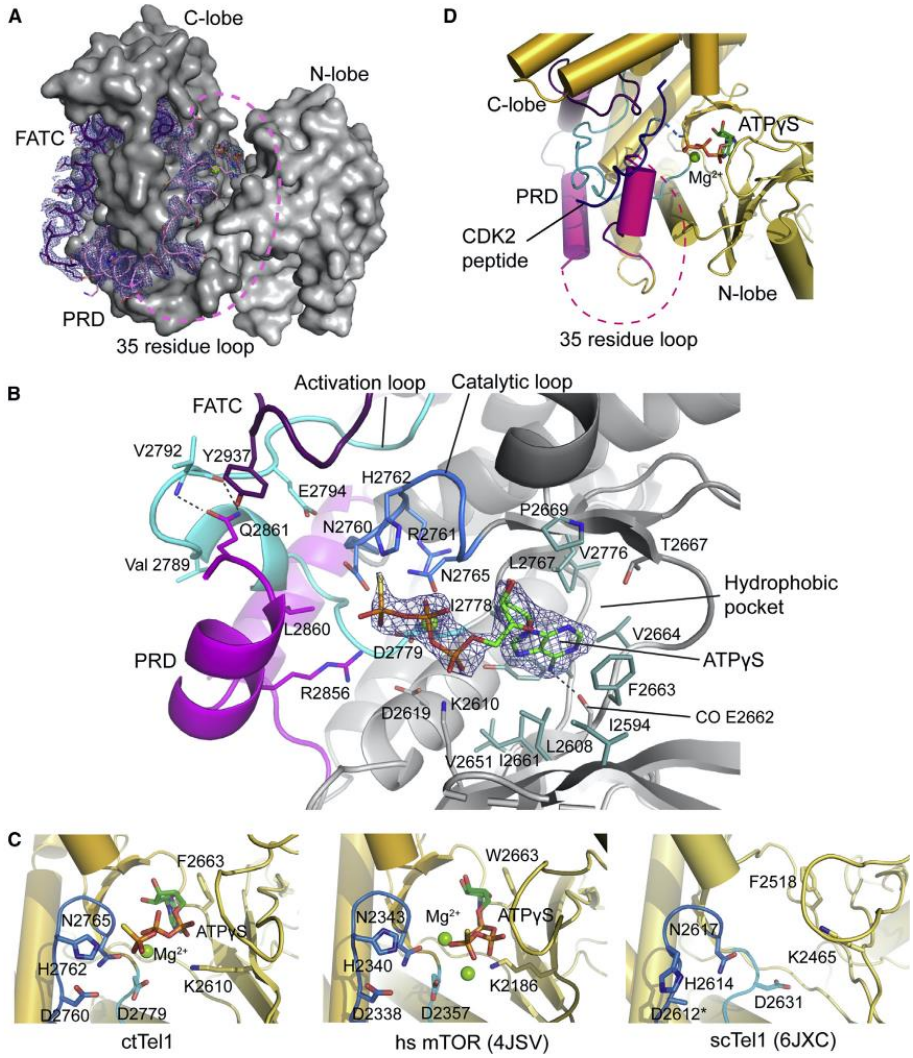

Figure 6. Overview of Kinase Domain and Active Site

(A) Overview of the kinase domain with the N lobe in light gray and C lobe in dark gray, the PRD in magenta, and the FATC domain in purple, with deep-blue density displayed for the PRD and the FATC. The N-terminal PRD helix blocks the active-site cleft formed by the two lobes.

(B) Detailed view of the active site with the coordinated ATPγS and Mg^{2+}, with the density for ATPγS and Mg^{2+}. The catalytic loop is depicted in blue and the activation loop in cyan. Other elements are colored as in (A). The residues forming the hydrophobic pocket are shown in light teal.

(C) Comparison of the active sites of ctTel1 to hsmTOR and scTel1 shows that the architecture of the active site is highly conserved among ATMs and PIKKs.

(D) CtTel1 with a peptide substrate of CDK2 modeled (PDB: 3QWH, in navy blue). The active sites with ATP(γS) were superimposed, showing that in ctTel1, the peptide substrate would clash with the PRD, suggesting that the PRD renders ctTel1 inactive by blocking substrate access.

See also Data S1.

conserved active centers of mTOR and ATM needs to be addressed in future studies.

Importantly, however, upon ATPγS binding, the PRD undergoes a conformational change so that the tip of the helix interacts directly with the activation and catalytic loops adjacent to the γ-phosphothioate of ATPγS. Consequently, binding of ATPγS is not sufficient to lift active-site access, but it rearranges the PRD instead as a pseudo-substrate

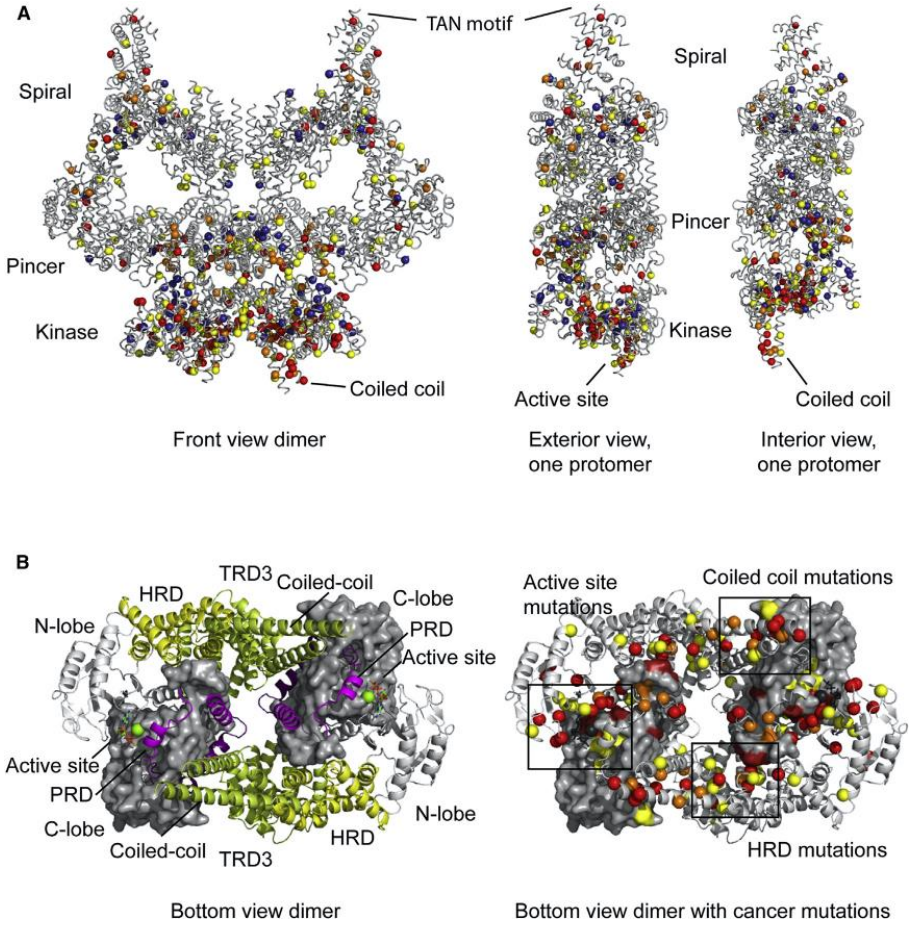

Figure 7. Mapping of Cancer Mutations Reported in the COSMIC Database

(A) Overview of the positions of commonly reported cancer mutations. CtTel1 is depicted in gray and shown from the front as a dimer, and from the side as one protomer. The positions of the cancer mutations are shown as spheres. Yellow indicates that a mutation has been reported three times, orange four times, and red five times or more. The A-T mutations, as listed by UniProt, are shown in blue.

(B) Two bottom views of the ctTel1 dimer, with and without the cancer mutations from the COSMIC database mapped. The C lobe is shown as surface and the other domains of the protein as cartoons. In the left panel, the same coloring scheme as previously is used; in the right panel, the same coloring as in (A) is used. See also Data S1.

that directly blocks access to the heart of the active site (Figure 6).

To find out whether in our ctTel1 structure the PRD blocks a putative substrate peptide binding site, we aligned the crystal structure of CDK2 bound to peptide substrate (PDB: 3QWH) with ctTel1 by overlaying the ATPs in the active sites, as was done previously for human ATM (Baretic et al., 2017). In our structure the peptide substrate also clashes with the PRD, indicating that the PRD indeed regulates the activity by blocking the active site (Figure 6D).

Several residues of the interaction of PRD with the kinase and FATC are noteworthy. A central stabilizing interaction appears to be the insertion of PRD Arg2856 into a negatively charged pocket formed by Asp2619, Asp2760, and Asp2779. In other orthologs, this arginine is either conserved or a lysine residue, showing the conservation of the charge-mediated interaction (Figure 6B and Data S1). Another noteworthy interaction is formed by Leu2860–Gln2861. Both residues are highly conserved in other orthologs, except *S. cerevisiae* Tel1. Leu2860 binds to a hydrophobic patch at the bottom of the active site while Gln2861 stacks with Tyr2937 and forms hydrogen bonds to the backbone of Val2792. Tyr2937 is a Phe in other orthologs, so stacking and hydrogen bonding are likely preserved interactions. The intriguing aspect of this interaction is that the invariant Gln2861's Cα is only

~10 Å away from the Pγ of the ATPγS, with the preceding leucine even closer. Since ATMs predominantly phosphorylate targets with an SQ or a TQ motif, it is possible that the glutamine side chain of PRD binds and blocks the substrate specificity pocket.

Taken together, ctTel1 appears to be in an inactive conformation, not because the catalytic residues are misaligned but because the PRD blocks directly the active site that is otherwise in a catalytically proficient state. Interactions with FATC and PRD ensure that the catalytic elements are structured, which has been observed to contribute to the intrinsic basal activity of scTel1 (Hailemariam et al., 2019) and other PIKKs (Yang et al., 2013). Recent work showed more open and closed conformations of Tel1 in the absence of ATP and proposed that these changes in the conformation of the N terminus are directly coupled to changes in the active site and transition in the PRD from ordered to disordered (Xin et al., 2019). Even though we also see large conformation changes in the N-terminal domain of ctTel1, we do not see any significant changes in the active site, implying that this opening and closing are not enough for activation of ctTel1. It appears that large-scale conformational changes, different from the observed pivot mobility of the Spiral module, are required to liberate the active-site block by PRD.

Mapping of Disease Mutations

Using our full model and the high similarity between ATM/Tel1 orthologs, we mapped somatic cancer mutations as reported in the COSMIC database (Tate et al., 2019) and germline A-T mutations, as listed in UniProt (The UniProt Consortium, 2019). We only included cancer mutation sites that occur three times or more (Figure 7A and Data S1). Mutations occur throughout the entire protein but are more clustered and frequent in the kinase domain and its surrounding regions. Many mutations are found in the active site, where they likely have a detrimental effect on catalysis. The catalytic residues are indeed often mutated. In the PRD several mutations have been reported, with mutations in Arg3008 in hsATM (Arg2901 in ctTel1) being reported 53 times, reflecting the importance of the PRD for the regulation of ATM activity. Curiously, however, the side chain of Arg2901 has no apparent protein contacts, making it unlikely that this particular mutation perturbs the protein folds or autoinhibited state. Possibly, $Arg2901^{Ct}/Arg2008^{Hs}$ adopts a functional role in the active conformation or binds substrate proteins.

Interestingly, the interface between HRD and the kinase domain is also frequently mutated. This may reflect that this interface is important for the regulation of the kinase. This interface is directly connected to the coiled coils of TRD3, which also contain two clusters of cancer mutations (Figure 7B). This coiled coil has been described to be important for the transition from an inactive state to an active state (Baretic et al., 2017). These clusters of mutations suggest that ATM activation may be due to a mechanism whereby changes in the coiled coil are mediated through the HRD to the active site.

In the Spiral, mutations occur less frequently than in the FATKIN domain. Some frequent mutations, however, are found in some of the loops described above. Arg337 in hsATM, corresponding to Gln400 in ctTel1, is mutated 77 times and is located at the joint between the Plug loop 1 and H7. Gln400 stabilizes the packing of H6 and H7, and a mutation at this position might destabilize the Spiral. Interestingly, the 45-residue insert connecting HEAT repeats H15 and H16 (residues 856–899) also contains multiple frequent cancer mutation sites, with the most common mutation Phe858 being reported 19 times. As this loop appears to be in close proximity to the N terminus, it is possible that these mutations perturb interactions with regulators. In the very N-terminal region, Arg23 in the TAN motif (Arg29 in ctTel1) is also reported to be mutated, reflecting the importance of this highly conserved residue.

Conclusions

We provide here, with a 3.7 Å resolution structure of the dimeric resting state of *C. thermophilum* ctTel1, the first near-complete atomic model of an ATM kinase, with major parts resolved to 2.8 Å. The structure shows details of the binding of Mg^{2+}-ATPγS and mechanisms of autoinhibition.

Although the catalytic residues are properly positioned for catalysis, the active site is rendered inactive by the PRD, which functions as a pseudo-substrate. A recent study on ScTel1 comes to a similar conclusion (Yates et al., 2019). Of particular note is a conserved glutamine in the PRD located near the ATP γ-phosphate, which may be analogous to the glutamine in the SQ/TQ motif of ATM substrates.

The Spiral can move from an open to a closed conformation around a hinge within the Pincer, without having major impacts on the kinase even in the ATPγS-bound state. While earlier studies suggested that these movements are coupled to changes in the kinase module and activate the protein (Baretic et al., 2017; Xin et al., 2019), our structure supports a model whereby binding of activators, such as MRN or DNA, to the N-terminal region induces more profound conformational changes that activate the kinase.

To summarize, the structure identifies multiple features of preventing premature activation of Tel1 in a cell, allows mapping and structural interpretation of disease mutations, and, due to its near-atomic resolution in the active site, can support the development of ATM-specific kinase inhibitors.

STAR★METHODS

Detailed methods are provided in the online version of this paper and include the following:

- KEY RESOURCES TABLE
- LEAD CONTACT AND MATERIALS AVAILABILITY
- EXPERIMENTAL MODEL AND SUBJECT DETAILS
- METHOD DETAILS
  - Cloning of ctTel1
  - Purification of ctTel1(1-1864)
  - Right Angle Light Scattering
  - Generation of Nanobodies
  - Purification and Analysis of Nanobodies
  - Fluorescence Polarisation Anisotropy
  - Nanobody-Based Purification of ctTel1
  - Grid Preparation
  - EM Data Acquisition
  - Image Processing
  - Model Building
  - Model Interpretation and Analysis

- QUANTIFICATION AND STATISTICAL ANALYSIS
- DATA AND CODE AVAILABILITY

SUPPLEMENTAL INFORMATION

Supplemental Information can be found online at https://doi.org/10.1016/j.str.2019.10.013.

ACKNOWLEDGMENTS

We thank Aaron Alt for technical advice and discussions, and Joseph Bartho for help with cryo-EM data collection and comments on the manuscript. We thank also members of the Gene Center and MPI of Biochemistry cryo-EM facilities, in particular Otto Berninghausen and Mike Strauss, for technical help. We furthermore thank Lloyd Ruddock (University of Oulu) for the pMJS187 vector for the expression of nanobodies and Ed Hurt (University of Heidelberg) for providing *Chaetomium thermophilum* gDNA, cDNA, and spores, and for valuable advice on culturing this organism. M.J. acknowledges support by a Boehringer Ingelheim Fonds PhD Fellowship. S.E. acknowledges support by an EMBO long-term fellowship. K.-P.H., M.J., and K.S. are supported by GRK1721. K.-P.H. acknowledges support by the European Research Council (Advanced Grant ATMMACHINE), by the Deutsche Forschungsgemeinschaft (CRC 1361, GRK1721), and by the Center for Integrated Protein Science (CIPSM). K.L. is supported by CRC 1054 of the Deutsche Forschungsgemeinschaft.

AUTHOR CONTRIBUTIONS

M.J. and C.L.-W. established purification of full-length endogenous ctTel1. M.J., C.L.-W., and C.L. purified proteins, performed biochemical assays, and characterized the nanobodies. B.K. helped with culturing *C. thermophilum*. M.J., with the assistance of K.S., prepared the sample for cryo-EM. M.J., with the guidance of K.L. and S.E., optimized grid preparation and collected cryo-EM data. S.E. designed the data-processing strategy. M.J. processed cryo-EM data with the guidance of S.E. and with the assistance of K.S., M.J., D.K., K.L., and K.-P.H. performed model building. M.J., C.L.-W., S.E., and K.-P.H, wrote the paper with input from the other authors. K.-P.H., K.L., and S.E. supervised various aspects of the work.

DECLARATION OF INTERESTS

C.L.-W. is currently an employee of ChromoTek, a company that develops and markets nanobody-based products. The other authors declare no competing interests.

Received: August 13, 2019
Revised: October 2, 2019
Accepted: October 21, 2019
Published: November 15, 2019

REFERENCES

Adams, P.D., Afonine, P.V., Bunkoczi, G., Chen, V.B., Davis, I.W., Echols, N., Headd, J.J., Hung, L.W., Kapral, G.J., Grosse-Kunstleve, R.W., et al. (2010). PHENIX: a comprehensive Python-based system for macromolecular structure solution. Acta Crystallogr. D Biol. Crystallogr. *66*, 213–221.

Altschul, S.F., Gish, W., Miller, W., Myers, E.W., and Lipman, D.J. (1990). Basic local alignment search tool. J. Mol. Biol. *215*, 403–410.

Amlacher, S., Sarges, P., Flemming, D., van Noort, V., Kunze, R., Devos, D.P., Arumugam, M., Bork, P., and Hurt, E. (2011). Insight into structure and assembly of the nuclear pore complex by utilizing the genome of a eukaryotic thermophile. Cell *146*, 277–289.

Bakkenist, C.J., and Kastan, M.B. (2003). DNA damage activates ATM through intermolecular autophosphorylation and dimer dissociation. Nature *421*, 499–506.

Baretic, D., Pollard, H.K., Fisher, D.I., Johnson, C.M., Santhanam, B., Truman, C.M., Kouba, T., Fersht, A.R., Phillips, C., and Williams, R.L. (2017). Structures of closed and open conformations of dimeric human ATM. Sci. Adv. *3*, 1–10.

Baretic, D., and Williams, R.L. (2014). PIKKs—the solenoid nest where partners and kinases meet. Curr. Opin. Struct. Biol. *29*, 134–142.

Bienert, S., Waterhouse, A., De Beer, T.A.P., Tauriello, G., Studer, G., Bordoli, L., and Schwede, T. (2017). The SWISS-MODEL Repository—new features and functionality. Nucleic Acids Res. *45*, 313–319.

Bock, T., Chen, W.-H., Ori, A., Malik, N., Silva-Martin, N., Huerta-Cepas, J., Powell, S.T., Kastritis, P.L., Smyshlyaev, G., Vonkova, I., et al. (2014). An integrated approach for genome annotation of the eukaryotic thermophile *Chaetomium thermophilum*. Nucleic Acids Res. *42*, 13525–13533.

Buchan, D.W.A., and Jones, D.T. (2019). The PSIPRED protein analysis workbench: 20 years on. Nucleic Acids Res. *47*, W402–W407.

Choi, M., Kipps, T., and Kurzrock, R. (2016). ATM mutations in cancer: therapeutic implications. Mol. Cancer Ther. *15*, 1781–1791.

Daniel, J.A., Pellegrini, M., Lee, J.H., Paull, T.T., Feigenbaum, L., and Nussenzweig, A. (2008). Multiple autophosphorylation sites are dispensable for murine ATM activation in vivo. J. Cell Biol. *183*, 777–783.

Dupre, A., Boyer-Chatenet, L., and Gautier, J. (2006). Two-step activation of ATM by DNA and the Mre11-Rad50-Nbs1 complex. Nat. Struct. Mol. Biol. *13*, 451–457.

Emsley, P., and Cowtan, K. (2004). Coot: model-building tools for molecular graphics. Acta Crystallogr. D Biol. Crystallogr. *60*, 2126–2132.

Falck, J., Coates, J., and Jackson, S.P. (2005). Conserved modes of recruitment of ATM, ATR and DNA-PKcs to sites of DNA damage. Nature *434*, 605–611.

Fernandes, N., Sun, Y., Chen, S., Paul, P., Shaw, R.J., Cantley, L.C., and Price, B.D. (2005). DNA damage-induced association of ATM with its target proteins requires a protein interaction domain in the N terminus of ATM. J. Biol. Chem. *280*, 15158–15164.

Gaciarz, A., Veijola, J., Uchida, Y., Saaranen, M.J., Wang, C., Hörkkö, S., and Ruddock, L.W. (2016). Systematic screening of soluble expression of antibody fragments in the cytoplasm of *E. coli*. Microb. Cell Fact. *15*, 1–10.

Goddard, T.D., Huang, C.C., Meng, E.C., Pettersen, E.F., Couch, G.S., Morris, J.H., and Ferrin, T.E. (2018). UCSF ChimeraX: meeting modern challenges in visualization and analysis. Protein Sci. *27*, 14–25.

Guo, Z., Kozlov, S., Lavin, M.F., Person, M.D., and Paull, T.T. (2010). ATM activation by oxidative stress. Science *330*, 517–521.

Hailemariam, S., Kumar, S., and Burgers, P.M. (2019). Activation of Tel1ATM kinase requires Rad50 ATPase and long nucleosome-free DNA but no DNA ends. J. Biol. Chem. *294*, 10120–10130.

Hanahan, D., and Weinberg, R.A. (2011). Hallmarks of cancer: the next generation. Cell *144*, 646–674.

Hoeijmakers, J.H.J. (2009). DNA damage, aging, and cancer. N. Engl. J. Med. *361*, 1475–1485.

Imseng, S., Aylett, C.H., and Maier, T. (2018). Architecture and activation of phosphatidylinositol 3-kinase related kinases. Curr. Opin. Struct. Biol. *49*, 177–189.

Jones, D.T. (1999). Protein secondary structure prediction based on position-specific scoring matrices. J. Mol. Biol. *292*, 195–202.

Katoh, K., Misawa, K., Kuma, K., and Miyata, T. (2002). MAFFT: a novel method for rapid multiple sequence alignment based on fast Fourier transform. Nucleic Acids Res. *30*, 3059–3066.

Katoh, K., Kuma, K., Toh, H., and Miyata, T. (2005). MAFFT version 5: improvement in accuracy of multiple sequence alignment. Nucleic Acids Res. *33*, 511–518.

Keith, C.T., and Schreiber, S.L. (1995). PIK-related kinases: DNA repair, recombination, and cell cycle checkpoints. Science *270*, 50–51.

Kellner, N., Schwarz, J., Sturm, M., Fernandez-Martinez, J., Griesel, S., Zhang, W., Chait, B.T., Rout, M.P., Kuck, U., and Hurt, E. (2016). Developing genetic tools to exploit *Chaetomium thermophilum* for biochemical analyses of eukaryotic macromolecular assemblies. Sci. Rep. *6*, 20937.

Kim, S.T., Lim, D.S., Canman, C.E., and Kastan, M.B. (1999). Substrate specificities and identification of putative substrates of ATM kinase family members. J. Biol. Chem. *274*, 37538–37543.

Knoll, K.R., Eustermann, S., Niebauer, V., Oberbeckmann, E., Stoehr, G., Schall, K., Tosi, A., Schwarz, M., Buchfellner, A., Korber, P., et al. (2018). The nuclear actin-containing Arp8 module is a linker DNA sensor driving INO80 chromatin remodeling. Nat. Struct. Mol. Biol. *25*, 823–832.

Krissinel, E., and Henrick, K. (2007). Inference of macromolecular assemblies from crystalline state. J. Mol. Biol. *372*, 774–797.

Lau, W.C., Li, Y., Liu, Z., Gao, Y., Zhang, Q., and Huen, M.S. (2016). Structure of the human dimeric ATM kinase. Cell Cycle *15*, 1117–1124.

Lee, J.H., and Paull, T.T. (2005). ATM activation by DNA double-strand breaks through the Mre11-Rad50-Nbs1 complex. Science *308*, 551–554.

Llorca, O., Rivera-Calzada, A., Grantham, J., and Willison, K.R. (2003). Electron microscopy and 3D reconstructions reveal that human ATM kinase uses an arm-like domain to clamp around double-stranded DNA. Oncogene *22*, 3867–3874.

Matsuoka, S., Ballif, B.A., Smogorzewska, A., McDonald, E.R., 3rd, Hurov, K.E., Luo, J., Bakalarski, C.E., Zhao, Z., Solimini, N., Lerenthal, Y., et al. (2007). ATM and ATR substrate analysis reveals extensive protein networks responsive to DNA damage. Science *316*, 1160–1166.

NCBI Resource Coordinators (2018). Database resources of the national center for biotechnology information. Nucleic Acids Res. *46*, D8–D13.

Nguyen, V.D., Hatahet, F., Salo, K.E.H., Enlund, E., Zhang, C., and Ruddock, L.W. (2011). Pre-expression of a sulfhydryl oxidase significantly increases the yields of eukaryotic disulfide bond containing proteins expressed in the cytoplasm of *E. coli*. Microb. Cell Fact. *10*, 1–13.

O'Neill, T., Dwyer, A.J., Ziv, Y., Chan, D.W., Lees-Miller, S.P., Abraham, R.H., Lai, J.H., Hill, D., Shiloh, Y., Cantley, L.C., et al. (2000). Utilization of oriented peptide libraries to identify substrate motifs selected by ATM. J. Biol. Chem. *275*, 22719–22727.

Pellegrini, M., Celeste, A., Difilippantonio, S., Guo, R., Wang, W., Feigenbaum, L., and Nussenzweig, A. (2006). Autophosphorylation at serine 1987 is dispensable for murine Atm activation in vivo. Nature *443*, 222–225.

Pettersen, E.F., Goddard, T.D., Huang, C.C., Couch, G.S., Greenblatt, D.M., Meng, E.C., and Ferrin, T.E. (2004). UCSF Chimera: a visualization system for exploratory research and analysis. J. Comput. Chem. *25*, 1605–1612.

Rohou, A., and Grigorieff, N. (2015). CTFFIND4: fast and accurate defocus estimation from electron micrographs. J. Struct. Biol. *192*, 216–221.

Rothbauer, U., Zolghadr, K., Tillib, S., Nowak, D., Schermelleh, L., Gahl, A., Backmann, N., Conrath, K., Muyldermans, S., Cardoso, M.C., et al. (2006). Targeting and tracing antigens in live cells with fluorescent nanobodies. Nat. Methods *3*, 887–889.

Sandoval, N., Platzer, M., Rosenthal, A., Dörk, T., Bendix, R., Skawran, B., Stuhrmann, M., Wegner, R.D., Sperling, K., Banin, S., et al. (1999). Characterization of ATM gene mutations in 66 ataxia telangiectasia families. Hum. Mol. Genet. *8*, 67–79.

Savitsky, K., Bar-Shira, A., Gilad, S., Rotman, G., Ziv, Y., Vanagaite, L., Tagle, D.A., Smith, S., Uziel, T., Sfez, S., et al. (1995). A single ataxia telangiectasia gene with a product similar to PI- 3 kinase. Science *268*, 1749–1753.

Sawicka, M., Wanrooij, P.H., Darbari, V.C., Tannous, E., Hailemariam, S., Bose, D., Makarova, A.V., Burgers, P.M., and Zhang, X. (2016). The dimeric architecture of checkpoint kinases Mec1ATR and Tel1ATM reveal a common structural organization. J. Biol. Chem. *291*, 13436–13447.

Schrödinger LLC (2015). The PyMOL Molecular Graphics System, Version 1.8 (Schrödinger).

Seidel, J.J., Anderson, C.M., and Blackburn, E.H. (2008). A novel Tel1/ATM N-terminal motif, TAN, is essential for telomere length maintenance and a DNA damage response. Mol. Cell. Biol. *28*, 5736–5746.

Shiloh, Y., and Ziv, Y. (2013). The ATM protein kinase: regulating the cellular response to genotoxic stress, and more. Nat. Rev. Mol. Cell. Biol. *14*, 197–210.

Stoppa-Lyonnet, D., Soulier, J., Laugé, A., Dastot, H., Garand, R., Sigaux, F., and Stern, M.H. (1998). Inactivation of the ATM gene in T-cell prolymphocytic leukemias. Blood *91*, 3920–3926.

Stothard, P. (2000). The sequence manipulation suite: JavaScript programs for analyzing and formatting protein and DNA sequences. Biotechniques *28*, 1102–1104.

Tate, J.G., Bamford, S., Jubb, H.C., Sondka, Z., Beare, D.M., Bindal, N., Boutselakis, H., Cole, C.G., Creatore, C., Dawson, E., et al. (2019). COSMIC: the catalogue of somatic mutations in cancer. Nucleic Acids Res. *47*, D941–D947.

The UniProt Consortium (2019). UniProt: a worldwide hub of protein knowledge. Nucleic Acids Res. *47*, D506–D515.

Wang, X., Chu, H., Lv, M., Zhang, Z., Qiu, S., Liu, H., Shen, X., Wang, W., and Cai, G. (2016). Structure of the intact ATM/Tel1 kinase. Nat. Commun. *7*, 1–8.

Waterhouse, A.M., Procter, J.B., Martin, D.M.A., Clamp, M., and Barton, G.J. (2009). Jalview Version 2—a multiple sequence alignment editor and analysis workbench. Bioinformatics *25*, 1189–1191.

Waterhouse, A., Bertoni, M., Bienert, S., Studer, G., Tauriello, G., Gumienny, R., Heer, F.T., De Beer, T.A.P., Rempfer, C., Bordoli, L., et al. (2018). SWISS-MODEL: homology modelling of protein structures and complexes. Nucleic Acids Res. *46*, 296–303.

Xiao, J., Liu, M., Qi, Y., Chaban, Y., Gao, C., Pan, B., Tian, Y., Yu, Z., Li, J., Zhang, P., et al. (2019). Structural insights into the activation of ATM kinase. Cell Res. *29*, 683–685.

Xin, J., Xu, Z., Wang, X., Tian, Y., Zhang, Z., and Cai, G. (2019). Structural basis of allosteric regulation of Tel1/ATM kinase. Cell Res. *29*, 655–665.

Yang, H., Rudge, D.G., Koos, J.D., Vaidialingam, B., Yang, H.J., and Pavletich, N.P. (2013). mTOR kinase structure, mechanism and regulation. Nature *497*, 217–223.

Yates, L.A., Williams, R.M., Hailemariam, S., Ayala, R., Burgers, P.M., and Zhang, X. (2019). Structure of nucleotide-bound Tel1^{ATM} reveals the molecular basis of inhibition and structural rationale for disease mutations. BioRxiv. https://doi.org/10.1101/696203.

You, Z., Chahwan, C., Bailis, J., Hunter, T., and Russell, P. (2005). ATM activation and its recruitment to damaged DNA require binding to the C terminus of Nbs1. Mol. Cell. Biol. *25*, 5363–5379.

Zheng, S.Q., Palovcak, E., Armache, J.P., Verba, K.A., Cheng, Y., and Agard, D.A. (2017). MotionCor2: anisotropic correction of beam-induced motion for improved cryo-electron microscopy. Nat. Methods *14*, 331–332.

Zivanov, J., Nakane, T., Forsberg, B.O., Kimanius, D., Hagen, W.J., Lindahl, E., and Scheres, S.H. (2018). New tools for automated high-resolution cryo-EM structure determination in RELION-3. Elife *7*, https://doi.org/10.7554/eLife.42166.

STAR★METHODS

KEY RESOURCES TABLE

REAGENT or RESOURCE	SOURCE	IDENTIFIER
Bacterial and Virus Strains		
E. coli Rosetta (DE3)	Sigma-Aldrich	Cat#70954
Chemicals, Peptides, and Recombinant Proteins		
BSA	New England Biolabs	Cat#B9000S
SIGMAFAST Protease Inhibitor Cocktail Tablet, EDTA free	Merck	Cat#S8830
2-Mercaptoethanol	Carl Roth	Cat#4227
TCEP	Sigma	Cat#646547
ATPγS	Sigma	Cat#A1388
MgCl2	Merck	Cat#7791-18-6
Imidazole	Carl Roth	Cat#3899
TWEEN-20	Carl Roth	Cat#9127.1
CHAPS	Carl Roth	Cat#1479.2
HEPES	Carl Roth	Cat#9105.3
TRIS	Carl Roth	Cat#HN95.2
NaCl	Merck	Cat#106404
Deposited Data		
CtTel1 FATKIN with C2 symmetry, coordinates	This paper	PDB: 6SKY
CtTel1 closed protomer, coordinates	This paper	PDB: 6SKZ
CtTel1 open protomer, coordinates	This paper	PDB: 6SL1
CtTel1 closed dimer with C2 symmetry, coordinates	This paper	PDB: 6SL0
CtTel1 FATKIN with C2 symmetry, EM map	This paper	EMDB: EMD-10231
CtTel1 closed protomer, EM map	This paper	EMDB: EMD-10232
CtTel1 open protomer, EM map	This paper	EMDB: EMD-10234
CtTel1 closed dimer with C2 symmetry, EM map	This paper	EMDB: EMD-10233
CtTel1 DNA sequence	This paper	MN255498
Experimental Models: Organisms/Strains		
Chaetomium thermophilum var. DSM 1495	DSMZ	Cat#759272
Oligonucleotides		
60 bp oligo for fluorescence anisotropy: 6-FAM - 5'-AAGGGAACATCGGGTAGTTGAACAGCATAGGCCCGGTCTTGCCTTAACCTCTAATTCTCG-3'	Metabion	N/A
30 bp oligo for fluorescence anisotropy: 5'-CGAGAATTAGAGGTTAAGGCAAGACCGGGCCTATGCTGTTCAACTACCCGATGTTCCCTT-3'	Metabion	N/A
60 bp oligo for fluorescein anisotropy: 6-FAM-5'-ACCGTAGGTTTACTGTCACGATATCAGTGC-3'	Metabion	N/A
30 bp oligo for fluorescein anisotropy: 5'-GCACTGATATCGTGACAGTAAACCTACGGT-3'	Metabion	N/A
25 bp oligo for fluorescein anisotropy: 6-FAM-5'-GAGATCCGTATGCCTACTGACATTG-3'	Metabion	N/A
25 bp oligo for fluorescence anisotropy: 5'-CAATGTCAGTAGGCATACGGATCTC-3'	Metabion	N/A
20 bp oligo for fluorescence anisotropy: 6-FAM-5'-CCTATATGAAGCTGAGTGCC-3'	Metabion	N/A

(*Continued on next page*)

Continued

REAGENT or RESOURCE	SOURCE	IDENTIFIER
20 bp oligo for fluorescence anisotropy: 5'-GGCACTCAGCTTCATATAGG-3'	Metabion	N/A
Recombinant DNA		
pET28-*CtTel1*(*1-1864*)	This Paper	N/A
pHEN4-nanobody	This Paper	N/A
pMJS187-nanobody	This Paper	N/A
Software and Algorithms		
EPU	FEI	https://www.fei.com/software/epu-automated-single-particles-software-for-life-sciences/
MotionCor2	(Zheng et al., 2017)	http://msg.ucsf.edu/em/software/motioncor2.html
CTFFind4.1	(Rohou and Grigorieff, 2015)	http://grigoriefflab.janelia.org/ctffind4 ; RRID: SCR_016732
Relion 3.0	(Zivanov et al., 2018)	https://www3.mrc-lmb.cam.ac.uk/relion/index.php?title=Main_Page ; RRID: SCR_016274
PHENIX	(Adams et al., 2010)	https://www.phenix-online.org/ ; RRID: SCR_014224
UCSF Chimera	(Pettersen et al., 2004)	https://www.cgl.ucsf.edu/chimera/; RRID: SCR_004097
UCSF ChimeraX	(Goddard et al., 2018)	https://www.rbvi.ucsf.edu/chimerax/; RRID: SCR_015872
PyMOL	Schrödinger LLC	https://pymol.org/2/; RRID: SCR_000305
COOT	(Emsley et al., 2004)	https://www2.mrc-lmb.cam.ac.uk/Personal/pemsley/coot/; RRID: SCR_014222
JalView	(Waterhouse et al., 2009)	https://www.jalview.org/; RRID: SCR_006459
MAFFT	(Katoh et al., 2002, 2005)	https://mafft.cbrc.jp/alignment/software/; RRID: SCR_011811
Sequence Manipulation Suite	(Stothard, 2000)	https://www.bioinformatics.org/sms2/
Prism	GraphPad	https://www.graphpad.com/; RRID: SCR_002798
SWISS-MODEL server	(Bienert et al., 2017; Waterhouse et al., 2018)	https://swissmodel.expasy.org/
Other		
Columns (Affinity, IEX, SEC)	GE Healthcare Life Sciences	http://www3.gehealthcare.de/de-de/produkte/kategorien/life_sciences
Anti-FLAG M2 Affinity Gel	Sigma	Cat#A2220 ; RRID: AB_10063035
StrepTactin Sepharose	IBA Lifesciences	Cat#2-1201-025
Amicon Ultra spin concentrators	Merck Millipore	Cat#UFC505096
Quantifoil R2/1 200 mesh + 2 nm C EM grids	Plano GmbH	Cat#S174-1-2C

LEAD CONTACT AND MATERIALS AVAILABILITY

Further information and requests for resources and reagents should be directed to and will be fulfilled by the Lead Contact Karl-Peter Hopfner (hopfner@genzentrum.lmu.de).

All plasmids generated in this study are available from the Lead Contact without restriction.

EXPERIMENTAL MODEL AND SUBJECT DETAILS

E. coli Rosetta was used for recombinant protein expression. *E. coli* Rosetta was grown in LB medium at 37°C for overnight cultures and for large cultures until induction of protein expression. During protein expression, the temperature was lowered to 18°C. *Chaetomium thermophilum* var. DSM 1495 was used for the purification of endogenous ctTel1 and was grown in CCM medium at 55°C (Kellner et al., 2016).

METHOD DETAILS

Cloning of ctTel1

Using a BLAST search (Altschul et al., 1990; NCBI Resource Coordinators, 2018), we identified GeneBank entry CTHT_0023400 (hereafter called ctTel1) as a *Chaetomium thermophilum* homolog of human ATM. Direct PCR amplification of the coding sequence

for full-length ctTel1 from a cDNA library from *C. thermophilum* was unsuccessful. Thus, we amplified the intron-rich 5' (1.9 kb) and 3' (0.3 kb) regions of ctTel1 from a cDNA library from *C. thermophilum* var DSM1495 and the intron-free middle region (6.7 kb) from *C. thermophilum* genomic DNA. These fragments were assembled using overlap-PCR and cloned into the vector pUC19 (Takara) using the In-Fusion system (Takara). All PCR reactions were performed using Phusion High-Fidelity PCR Master Mix with HF Buffer (New England Biolabs). We observed that the GeneBank entry incorrectly defines parts of the coding sequence as an intron and deposited our revised ctTel1 sequence as NCBI MN255498. This revised sequence was later confirmed by our structural data on endogenous ctTel1 (see below).

Purification of ctTel1(1-1864)

Expression trials for recombinant full-length ctTel1 in *E. coli*, *Saccharomyces cerevisiae*, *Drosophila melanogaster* S2 cells, *Trichoplusia ni* HighFive cells and HEK cells yielded small amounts of insoluble protein at most. Interestingly, however, the IMAC purification of ctTel1, fused to an N-terminal $(His)_6$-tag and a TEV protease recognition site in a pET28 vector and expressed in *E. coli* BL21 Rosetta, led to distinct fragments in the range of 40-200 kDa. These fragments were identified as fragments of ctTel1 using liquid chromatography-tandem mass spectrometry (LC-MS/MS) finger printing performed at the Protein Analysis Unit (ZfP) of the Ludwig-Maximilians-University of Munich, a registered research infrastructure of the Deutsche Forschungsgemeinschaft (DFG, RI-00089). Based on the boundaries of these fragments as defined by LC-MS/MS, several truncation constructs of ctTel1 were cloned into a pET21a vector containing a C-terminal TEV protease cleavage site followed by a $(His)_6$-tag. One construct, ctTel1 (1-1864), could be expressed solubly and at high yields in *Escherichia coli* Rosetta (DE3) cells.

Cells were grown overnight at 18°C in LB medium after induction with 0.5 mM IPTG. Cells were resuspended and lysed by sonication in lysis buffer (50 mM TRIS-HCl pH 8.0, 300 mM NaCl, 5% (v/v) glycerol, 30 mM imidazole and 1 mM β-mercaptoethanol) with protease inhibitor (Sigma). Lysate was cleared by centrifugation and loaded on to an immobilised metal affinity chromatography column (HisTrap, GE Healthcare), preequilibrated in lysis buffer. The column was washed with lysis buffer prior to elution in elution buffer (50 mM TRIS-HCl pH 8.0, 300 mM NaCl, 5% (v/v) glycerol, 500 mM imidazole and 1 mM β-mercaptoethanol). TEV protease was added to the peak fractions in order to cleave the $(His)_6$-tag overnight while dialysing against Dialysis buffer (50 mM TRIS-HCl pH 8.0, 200 mM NaCl, 5% (v/v) glycerol, 10 mM imidazole and 1 mM β-mercaptoethanol). After proteolytic cleavage of the $(His)_6$-tag, the tag was removed by a second round of Ni^{2+} chromatography, and the protein was further purified using size exclusion chromatography (HiLoad 16/60 Superdex 200, GE Healthcare). Protein was spin-concentrated (Amicon Ultra) to ca. 10 mg/mL in 25 mM HEPES-NaOH pH 8.0, 300 mM NaCl, 2 mM imidazole and 2 mM TCEP, and stored at −80°C after flash freezing.

Right Angle Light Scattering

In order to determine the molecular weight in solution and the oligomerization state of CtTel1(1-1864), size-exclusion chromatography coupled to right angle light scattering (SEC-RALS) was done on a S200 increase 10/300 column coupled to a micro AKTA system (GE Healthcare) and a right-angle light scattering device and refractive index detector (Malvern/Viscotek). The column was preequilibrated in a buffer containing 25 mM HEPES-NaOH pH 8.0, 300 mM NaCl, 2 mM imidazole and 2 mM TCEP. BSA (66 kDa) was used for calibration. Results were displayed and evaluated using OmniSEC (Malvern/Viscotek) and GraphPad Prism.

Generation of Nanobodies

Nanobodies against ctTel1 were generated using alpaca immunisation and phage display by ChromoTek GmbH (Martinsried, Germany) according to published protocols (Rothbauer et al., 2006). Briefly, an alpaca (*Vicugna pacos*) was immunised using ctTel1(1-1864) followed by several rounds of booster immunisations and a final bleed to enable the isolation of peripheral blood mononuclear cells (PBMCs). RNA was purified from PBMCs and transcribed into a cDNA library, which was cloned into vector pHEN4. Anti-ctTel1 nanobodies were enriched in one round of solid-phase panning using phage display, identified using ELISA and sequenced.

Purification and Analysis of Nanobodies

Sequences of candidate anti-ctTel1 nanobodies were cloned into a pHEN6 vector encoding a C-terminal Twin-Strep-tag and expressed in *Escherichia coli* Rosetta cells as described in (Knoll et al., 2018). Nanobodies were tested for binding to ctTel1 using immunoprecipitation. Purified nanobodies (0.05 mg/ml) were incubated with purified ctTel1(1-1864) (0.5 mg/ml) or with lysate of *C. thermophilum* in 50 mM Tris-HCl pH 8.0, 300 mM NaCl for 1 h, followed by pull-down using StrepTactin sepharose (IBA Lifesciences, Göttingen, Germany) and SDS-PAGE analysis. The sequences of all confirmed anti-ctTel1 nanobodies are summarised in Figure S1.

Fluorescence Polarisation Anisotropy

Oligonucleotides (Key Resources) with lengths of 20, 25, 30 and 60 bp were purchased from Metabion and were annealed in annealing buffer (25 mM TRIS pH 7.5, 50 mM NaCl and 10 mM $MgCl_2$) with a molar excess of 1.1 of the unlabelled oligo over the labelled oligo, which had a 6-FAM label on the 5′ terminus.

Dilutions of ctTel1(1-1864) were made in assay buffer (HEPES-NAOH pH 8.0, 100 mM NaCl and 5 mM β-mercaptoethanol) and mixed with the DNA substrate, which was at a final concentration of 5 nM. The reaction was incubated for 30 minutes at 25°C. The fluorescence anisotropy was measured at an excitation wavelength of 470 nm and an emission wavelength of 520 nm using

a Tecan plate reader. The resulting data were analysed using GraphPad Prism and K_D values were determined by fitting the data to a Hill equation, assuming a one binding site model. All experiments were performed in triplicates.

The influence of the nanobodies on the DNA binding properties of ctTel1(1-1864) was assayed using a ds60mer.

Nanobody-Based Purification of ctTel1

Nanobodies were cloned into a pMJS187 vector to increase expression levels (Gaciarz et al., 2016; Nguyen et al., 2011) (Key Resources), with a C-terminal G4S-PreScission-G4S-triple FLAG – $(His)_6$, the G4S linkers being introduced to facilitate proteolytic cleavage. Protein was expressed in *E. coli* Rosetta (DE3) cells. Nanobodies were purified using Ni2+-NTA agarose (supplier) and size exclusion chromatography (HiLoad 75 16/60, GE Healthcare). Protein was spin-concentrated to 20 mg/mL (Amicon Ultra) and stored in 25 mM Tris-HCl pH 8.0 and 150 mM NaCl at −80°C after flash freezing in liquid nitrogen.

Endogenous ctTel1 was purified from *Chaetomium thermophilum* var DSM1495, which cultured as described previously (Kellner et al., 2016). Briefly, *Chaetomium* mycelium was grown on CCM agar plates, which were then cut into pieces and used to inoculate a liquid CCM overnight culture, which was grown overnight at 55°C. The mycelium in the overnight culture was shredded in a blender and used to inoculate larger cultures, which were again grown at 55°C. *Chaetomium* was lysed by cryo milling (SPEX 6970 EFM freezer mill) and the powder was stored at −80°C until further use.

Of the *Chaetomium* powder, 100 g was resuspended in Resuspension buffer (25 mM HEPES-NaOH pH 7.5, 150 mM NaCl, 5% glycerol, 0.1% CHAPS) supplemented with protease inhibitor tablets (Sigma). The lysate was cleared by centrifugation at 30600 g for 45 min at 4°C. M2 FLAG affinity resin (150 μl, Sigma Aldrich) was preequilibrated in Resuspension buffer and incubated with a nanobody – G4S – PreScission – G4S – triple FLAG – $(His)_6$ for 1 hour at 10°C under rotation. Excess nanobody was washed off using 4 times 1 mL Resuspension buffer. Nanobody-loaded beads were incubated with the cleared *C. thermophilum* lysate overnight at 10°C, harvested by centrifugation, and washed using 4 times 15 mL washing buffer (25 mM HEPES-NaOH pH 7.5, 150 mM NaCl). The ctTel1:nanobody complex was eluted by proteolytic cleavage using PreScission protease. ATPγS and $MgCl_2$ was added to ATM eluate to a final concentration of 0.1mM and 1mM, respectively.

Grid Preparation

Holey carbon grids R2/1, with 2 nm continuous amorphous carbon (Quantifoil) were glow discharged using a GloQube glow discharger. Grids were prepared on a Leica EM GP (Leica). Directly before applying the ATM eluate (0.15mg/ml) to the grid, TWEEN-20 was added to the sample to a final concentration of 0.05%. The sample was subsequently pre-incubated 45 seconds on the grid at 15°C and 95% humidity and blotted for 2 seconds before flash freezing the grid in liquid ethane.

EM Data Acquisition

Three datasets were collected on an FEI Titan Krios transmission electron microscope operated at 300 kV, with a GIF quantum energy filter (slit width 40 eV) and a Gatan K2 Summit direct electron detector operated in counting mode. EPU (FEI) was used for automated data acquisition, with a defocus ranging from -1.2 um to -3.5 um at a calibrated pixel size 1.059 Å /pixel and a dose rate of 1.34 e/$Å^2$ frame, 8 seconds exposure over 40 frames.

Image Processing

All data processing was done using Relion 3.0 (Zivanov et al., 2018) and resolutions reported are based on the gold standard FSC 0.143 correlation. Motioncor2 as implemented within Relion 3.0 was used for beam induced motion correction of the Video frames (Zheng et al., 2017) and CTFFind 4.1, was used to determine the CTF parameters of the motion corrected micrographs (Rohou and Grigorieff, 2015). Micrographs that showed abnormal Fourier patterns and did not show any information beyond 4.5 Å were discarded.

Particles were picked automatically using a 3D reference, which was obtained from a previous test dataset and filtered to 20 Å to avoid model bias. After particle extraction, particles were sorted according to their autopicking figure of merit to remove contaminants. After initial 3D classifications, using a reference filtered to 60 Å, 286,284 particles from dataset 1, 269,295 particles from dataset 2 and 308,368 particles of dataset 3 were selected for initial 3D refinement, using a reference obtained from an earlier dataset that was filtered to 40 Å, resulting for all three datasets in a 3.9 Å map. The particles were subjected to Bayesian polishing and CTF refinement and another round of 3D refinement, resulting in three maps of 3.5 Å. The datasets were merged and the combined 863,937 particles were used for another round of 3D refinement, resulting in a 3.2 Å map. Further 3D classification with a mask for the kinase domain and fixed angles yielded a class of 613,262 particles that provided a 3.0 Å map of the kinase domain after 3D refinement, and a 2.8 Å map when applying C2 symmetry, which allowed for de novo model building (see next section).

Using a mask for one of the α-solenoids (corresponding to the Spiral and Pincer) we performed another 3D classification using fixed angles derived from the previous autorefinement. This yielded a class of 111,910 particles of the α-solenoid in an open conformation, and a class of 132,127 particles displaying a closed conformation. 3D refinement yielded a map of 3.6 E for the open conformation and 3.4 E for the closed conformation.

Using a mask for the α-solenoid of the other protomer, the 132,127 particles for the closed conformation were subjected to another round of 3D classification with fixed angles. This resulted in a class with 51,116 particles in which the other α-solenoid is also in a closed conformation. Autorefinement of these particles with C1 symmetry yielded a 4.0 Å map of the entire particle in a closed conformation, and applying C2 symmetry yielded a map of 3.8 Å.

In order to improve the overall map of the dimer further, as the density of the Spiral was still less well defined than the FATKIN domain density, a mask was made encompassing both α-solenoids in a closed conformation. Using this mask and a 3D classification with fixed angles, a class with 32,764 particles was identified in which both α-solenoids are in a closed conformation. Autorefinement while applying C2 symmetry yielded a more uniform density for the entire particle at an overall resolution of 3.7 Å.

Model Building

We generated a homology model of the ctTel1 kinase domain based on the kinase domain of hsATM (5NP0) using SwissServer (Bienert et al., 2017; Waterhouse et al., 2018) and performed rigid body docking into the density of the FATKIN domain using UCSF Chimera (Pettersen et al., 2004). Further rigid body fitting was performed in PHENIX (Adams et al., 2010). All other residues beyond the kinase domain were built manually in Coot (Emsley and Cowtan, 2004), guided by secondary structure predictions from PsiPred (Buchan and Jones, 2019; Jones, 1999). Since ctTel1 is predominantly α-helical and side chains were visible throughout the density, we were able to find the register for most of the protein and could build an atomic model for 2652 residues out of 2944 residues. We did not observe density for loops connecting helices in flexible parts of the α-solenoid, such as the first two HEAT repeats and the N-terminal helices of the Pincer, which we thus did not model. The density for the first 200 N-terminal residues was very weak in all 3D reconstructions. We placed α-helices with tentative registers into this region, based on secondary structure predictions.

To model the open conformation, a rigid body fit of the Spiral domain of the α-solenoid, as it was built in the closed conformation, was performed in Coot and PHENIX, since we could not observe any significant conformational changes within the Spiral at this resolution.

After initial fitting of all residues, further refinement and model building was performed using PHENIX. The structure for the FATKIN and the structure for the closed conformation were refined against their corresponding maps with real space refinement in PHENIX, using Ramachandran and Cβ restraints and further restraints for secondary structure. For modelling the closed and open conformation, we included self-restraints on the initial coordinates for the Pincer and the FATKIN.

To generate a model of the full dimer in the closed conformation, we generated the other protomer by applying C2 symmetry and then performed a rigid body fit of both protomers the corresponding map for the entire particle in PHENIX.

Model Interpretation and Analysis

All figures containing models were prepared with PyMOL (Schrödinger LLC, 2015) and EM maps were visualised with Chimera and ChimeraX, which was also used for the creation of the Video (Pettersen et al., 2004; Goddard et al., 2018). Alignments were done using MAFFTS (Katoh et al., 2002, 2005) in Jalview (Waterhouse et al., 2009). Percentages of identity and similarity were calculated using the Sequence Manipulation Suite (Stothard, 2000).

QUANTIFICATION AND STATISTICAL ANALYSIS

GraphPad Prism was used for plotting the technical triplicates (n=3) of the fluorescence anisotropy DNA binding assay (Figures 3 and S1). Error bars are given as the standard deviation of the mean.

DATA AND CODE AVAILABILITY

The DNA and protein sequence of CtTel1 is available at NCBI GenBank under MN255498.

The coordinates of the models described in this paper are available at the Protein Data Bank (https://www.rcsb.org/). The accession number for the coordinates of the FATKIN with C2 symmetry is PDB: 6SKY , for the closed conformation of one protomer PDB: 6SKZ , for the open conformation of one protomer PDB: 6SL1 and for the dimer with C2 symmetry in a closed conformation PDB: 6SL0.

The calculated density maps obtained in this study are available at the Electron Microscopy Data Bank (https://www.ebi.ac.uk/pdbe/emdb/). The accession number for the map of the FATKIN with C2 symmetry is EMDB: EMD-10231, for the closed conformation of one protomer EMDB:EMD-10232, for the open conformation of one protomer EMDB:EMD-10234 and for the dimer with C2 symmetry in a closed conformation EMDB: EMD-10233.

2.2 Molecular basis of human ATM kinase inhibition

Stakyte K.*, Rotheneder M.*, Lammens K.*, Bartho J.D*, Grädler U., Fuchß T., Pehl U., Alt A., van de Logt E. and Hopfner K.P. 2021. Molecular basis of human ATM kinase inhibition. **Nature Structure & Molecular Biology**. 2021 Oct;28(10):789-798.

* These authors contributed equally.

Summary

In this publication we report the first high-resolution cryo-EM structures of inhibitor-bound human ATM kinase. The overall structure of dimeric human ATM is consistent with previously published human and fungal ATM, but provides new insights due to significantly improved resolution. The quality of maps allowed us to build a near-complete atomic model of human ATM including the more flexible N-terminal spiral and pincer domains. This led to identification of previously unseen zinc-binding motifs. Mutation of the two zinc-coordinating cysteines did not affect kinase activity, but addition of zinc-specific chelating agents decreased the thermal stability of ATM. These results suggest a structure stabilizing function of zinc-coordinating motifs. We also observed different conformations of HEAT repeat domains, but they showed no effect on the state of the kinase domain. Cancer associated mutations were mapped onto the structure indicating functionally important elements of ATM. The kinase domain structures bound to ATPγS and the inhibitors KU-55933 and M4076 were determined at 2.8 Å, 2.8 Å and 3.0 Å resolution, respectively. In agreement to published ATM/Tel1 structures, all of our structures show the PIKK regulatory domain (PRD) blocking the active site access. This confirms the autoinhibitory function of the PRD. The comparison of ATPγS and inhibitor bound active site residue conformations explains the ~35-fold stronger enzymatic potency of M4076 towards ATM compared to KU-55933. In addition, structural comparisons of M4076 bound ATM active site with related kinases revealed several non-conserved ATM residues involved in M4076 binding. This explains the observed selectivity profile of M4076. Taken together, our atomic models of inhibitor bound human ATM provide a tool for the evaluation and development of specific and potent therapeutics.

Author contribution

I expressed and purified human ATM. Together with Mathias Rotheneder, I made grids for cryo-EM. I did cryo-EM data collection and processing, as well as model building together with Matthias Rotheneder, Katja Lammens and Joseph Bartho. Together with Erik van de Logt, I did kinase assays. I contributed to manuscript preparation together with other authors.

nature structural & molecular biology

ARTICLES

https://doi.org/10.1038/s41594-021-00654-x

Check for updates

Molecular basis of human ATM kinase inhibition

K. Stakyte[1,4], M. Rotheneder[1,4], K. Lammens[1,4]✉, J. D. Bartho[1,4], U. Grädler[2], T. Fuchß[2], U. Pehl[2], A. Alt[1,3], E. van de Logt[1] and K. P. Hopfner[1]✉

Human checkpoint kinase ataxia telangiectasia-mutated (ATM) plays a key role in initiation of the DNA damage response following DNA double-strand breaks. ATM inhibition is a promising approach in cancer therapy, but, so far, detailed insights into the binding modes of known ATM inhibitors have been hampered due to the lack of high-resolution ATM structures. Using cryo-EM, we have determined the structure of human ATM to an overall resolution sufficient to build a near-complete atomic model and identify two hitherto unknown zinc-binding motifs. We determined the structure of the kinase domain bound to ATPγS and to the ATM inhibitors KU-55933 and M4076 at 2.8 Å, 2.8 Å and 3.0 Å resolution, respectively. The mode of action and selectivity of the ATM inhibitors can be explained by structural comparison and provide a framework for structure-based drug design.

Cells rely on an efficient DNA damage response (DDR) to maintain genomic stability. Cancer cells, on the other hand, acquire defects in DDR genes to increase the genomic instability and mutation rate while ensuring cancer cell survival. The DDR comprises complex chains of events that result in the efficient repair of various types of DNA damage, including DNA double-strand breaks (DSBs)[1]. DSBs are a hallmark of cancer and particularly harmful to the cell if left unrepaired. Initiation of the DDR leads to activation of checkpoint responses, cell-cycle arrest, recruitment of the DNA repair machinery and chromatin remodeling[2–4]. Persistent DSBs and DDR trigger cellular senescence or apoptosis, thereby helping to remove potentially abnormal cells. However, misrepaired DSBs can result in gross chromosomal aberrations, aneuploidy or loss of genetic information and are linked to cancer development[1,5–7].

Ataxia telangiectasia-mutated (ATM) is a ~350-kDa Ser/Thr kinase that initiates a DDR following DSB formation. On activation, ATM phosphorylates a multitude of downstream transducers and effector proteins at SQ/TQ motifs. Target proteins include the DSB repair factor CtIP, histone variant H2AX, tumor suppressors BRCA1 and p53, and the checkpoint transducing kinase CHK2[4]. ATM belongs to a family of related surveillance kinases known as phosphatidylinositol 3-kinase-related protein kinases (PIKKs). Members of this kinase family also include ATR, the DNA-dependent protein kinase catalytic subunit (DNA-PKcs), mTOR, SMG1 and TRRAP[8,9]. ATM, ATR and DNA-PKcs monitor the cell for DNA damage by sensing DSBs (ATM and DNA-PKcs) or single-stranded DNA (ssDNA; ATR). SMG1 triggers nonsense-mediated messenger RNA (mRNA) decay. TRRAP is involved in epigenetic control of transcription regulation, while mTOR is part of distinct complexes that regulate metabolism, translation and cell growth[10–13]. PIKKs share a fairly conserved domain structure[14–16]. The N-terminal parts of the polypeptide chains are generally composed of HEAT repeats and form 100–300-kDa α-solenoid structures, which are interaction modules for nucleic acids and/or protein cofactors[17]. The C-terminal region known as FATKIN contains the kinase (KIN) domain along with regulatory domains. The latter are denoted as FAT (FRAP, ATM and TRRAP) domain, PRD (PIKK regulatory domain) and FATC (C-terminal part of the FAT domain). The FAT, PRD and FATC wrap around the kinase, regulating substrate recognition.

Cryo-EM provided the first structures of human ATM along with its fungal homologs at low to medium resolution[16,18–21]. ATM resides in the cell as an autoinhibited dimer in all organisms studied. The FATKIN is tightly associated through a fairly hydrophobic interface and keeps the kinase domains side by side in an inactive state[16,18–21]. The structure of human ATM at 4.7 Å showed how the PRD restricts kinase active site access by acting as a pseudo-substrate[16]. More highly resolved fungal Tel1 (ATM ortholog) structures showed details of the kinase active site[19,21]. They also revealed that Tel1 can bind ATP and possesses a properly folded active site geometry, even in the absence of activating ligands[19,21]. Current models of active site access postulate either ligand-induced conformational changes in the ATM dimer, or a dimer-to-monomer transition[22–24].

Although the DDR is important for genome integrity maintenance of healthy cells, it also helps cancer cells to cope with increasing amounts of replication and genotoxic stress, and to develop resistance against DNA-damaging chemo- and/or radiotherapy, thereby favoring tumor growth and survival[25]. Consequently, targeting of proteins involved in the DDR has shown promising effects in cancer therapy[26,27]. Owing to its prominent role in DDR signaling, ATM represents an auspicious target for drug development, predominately as an anticancer therapeutic. Inhibition of ATM increases the sensitivity of cancer cells to DNA-damaging agents and/or ionizing radiation[28–31]. DSB repair is crucial for the survival of malignant tumor cells, especially under DNA-damaging conditions. Thus, the rationale for transient pharmacological ATM inhibition is to impair DSB repair and maintain the extent of unrepaired tumor DNA damage for several hours so as to drive tumor cells ultimately to cell death[27,32,33]. Moreover, based on genetic and pharmacological evidence, inhibition of ATM kinase activity is considered to ameliorate mutant huntingtin (mHTT) toxicity as a potentially novel clinical intervention to treat Huntington's disease[34]. ATM deficiency or reduced expression levels have been identified as a biomarker of sensitivity for selective poly adenosine diphosphate-ribose polymerase (PARP) or ATR inhibition in the treatment of solid tumors[35–38]. ATM inhibitors in combination with ATR or PARP inhibitors induce synthetic lethality in proliferating cancer cell lines as a result of mitotic

[1]Gene Center, Department of Biochemistry, Ludwig-Maximilians-Universität, Munich, Germany. [2]Merck KGaA, Darmstadt, Germany. [3]Present address: Proteros Biostructures GmbH, Martinsried, Germany. [4]These authors contributed equally: K. Stakyte, M. Rotheneder, K. Lammens, J. D. Bartho. ✉e-mail: klammens@genzentrum.lmu.de; hopfner@genzentrum.lmu.de

replication stress and unrepaired DSBs[39]. Initial high-affinity ATM inhibitors (KU-55933 and CP466722) were identified by compound library screens and served as lead structures for the development of compounds with improved pharmacokinetic properties (KU-60019 and KU-59403)[28,29,40,41]. More recently, next generations of inhibitors (AZ31, AZ32, AZD0156 and AZD1390) with up to subnanomolar half-maximum inhibitory concentration (IC_{50}) potencies and suitable pharmacokinetic profiles were identified, demonstrating preclinical in vivo efficacy in rodent cancer models[42–44]. Both ATM inhibitors, AZD0156 and AZD1390, had been selected to enter clinical trials either in combination with cytotoxic chemotherapy, as well as targeted anticancer agents such as the PARP1/2 inhibitor olaparib (Lynparza, AZD2281) for the treatment of solid tumors, or with radiotherapy in the treatment of brain cancers[43–45]. M4076, a subnanomolar potent, ATP-competitive and orally bioavailable ATM inhibitor with excellent human kinase selectivity and physicochemical and pharmacokinetic properties was developed at Merck KGaA[46]. Currently, M4076 is in a phase I clinical trial for the treatment of cancer (ClinicalTrials.gov ID NCT04882917)[31].

Structure-based approaches are an important source of information for the optimization of selective inhibitors, and progress in the resolution capabilities of cryo-EM has opened up this technique to structure-based drug design[47]. Despite the fact that several cryo-EM structures of eukaryotic ATM/Tel1 have been published, high-resolution structures of human ATM enabling structure-based drug design are not yet available[16,18–21]. In this Article, we use cryo-EM to investigate the detailed binding modes of ATM-specific kinase inhibitors KU-55933 and M4076 comprising chemically diverse scaffolds. We present cryo-EM structures of human ATM in complex with KU-55933, M4076 and the non-hydrolysable ATP analog ATPγS at resolution below 3 Å, permitting the distinct fitting of all three compounds. The protein structures provide a detailed view of the kinase domain and the active site conformation in its inhibited state, and clearly explain the distinct ATM kinase inhibition and selectivity profiles of KU-55933 and M4076 based on their binding modes. The quality of the maps allowed us to generate a near-complete atomic model of human ATM, including the more flexible spiral and pincer domains, where we identified two zinc-binding motifs.

Results

Near-complete atomic structure of human ATM. Human ATM was expressed in Expi293F cells and purified using FLAG affinity followed by anion exchange chromatography. Biochemical analysis indicates that the purified protein is an enzymatically active kinase that is capable of phosphorylating its natural substrate, the C-terminal fragment of human CtIP (Fig. 1a). Basal kinase activity was reduced in the presence of the widely used ATM inhibitor KU-55933 (Fig. 1a). To reduce protein flexibility within the kinase domain of human ATM, we incubated the protein sample with KU-55933 before cryo-EM grid preparation[1]. Consistent with the published human ATM cryo-EM structure, which showed distinct dimeric states, we still observed conformational flexibility in the N-terminal α-solenoid domain, but, in contrast, did not observe conformationally 'open' C-terminal domains or monomers in the micrographs (Extended Data Fig. 1a and Supplementary Video 2)[2]. We reconstructed a full-length human ATM structure by using a 2.8-Å-resolution pincer-FATKIN map in combination with 3.0–3.3-Å maps for the spiral and pincer domains (Supplementary Figs. 1 and 2 and Table 1). The overall domain organization is illustrated in Fig. 1b. The quality of the map enabled us to build full side chain models for all secondary structural elements, along with large parts of the loop regions within the FATKIN and pincer domains. We also corrected the sequence assignments at the N-terminal 1,932 residues of earlier structures that were modeled based on lower-resolution maps (Fig. 1b, insets and Extended Data Fig. 1e)[2,3].

Intriguingly, analysis of the sequence and EM density revealed the presence of a zinc-binding motif in the pincer domain (Fig. 1b, top inset and Supplementary Video 1). This motif also validates a newly assigned registry. The zinc-binding site belongs to the classical Cys2 His2 motif zinc finger type and consists of residues H1876, H1895, C1899 and C1900 in a loop region at the C-terminal end of the pincer domain. The zinc-binding motif is pointing towards the spiral domain, which mediates the recruitment of DNA, binding partners such as NBS1 and substrates such as p53[4,5]. The loop stabilized by this motif contains the important cancer mutation T1880R[48]. Because all four zinc coordinating residues are only conserved in certain mammals, an essential, evolutionarily conserved role of this motif for kinase activity is not likely, but it could play an important function in mammalian-specific regulation and ligand or substrate recognition (Extended Data Fig. 1b)[24]. Mutation of the two zinc coordinating cysteine residues did not diminish kinase activity (Extended Data Fig. 1c). However, addition of zinc-specific chelating agents decreased the thermal stability of the ATM (Extended Data Fig. 1d).

To model the N-terminal α-solenoid structure, this region of the density was processed independently by subtracting the density for the C-terminal domains and the other protomer of the dimer to create a map of the N terminus alone (Supplementary Fig. 2). This workflow permitted classification of the structural variation within the N terminus, resulting in a map with an overall resolution of 3.15 Å that allowed atomic modeling of the N terminus. The map displays defined side chain densities until the two most N-terminal helices and indicates a different sequence assignment than previously published (Fig. 1c). This area is of particular interest because the HEAT repeats are believed to provide an interaction hub for components of the DNA repair machinery, such as NBS1, and substrates like p53[49,50]. In the center of the solenoid structure, the HEAT repeat pattern is broken where the loop (amino acids 549–570) between helices 24 and 25 extends to interact with the FATKIN domain loops (residues 2084–2092 and 2107–2123; Extended Data Fig. 2a,d). We note the direct contact between the N-terminal region of the α-solenoid and the FATKIN domain that was not observed in the previously published human ATM structures. However, the equivalent inter-domain interaction was observed in ctTel1[19]. After this FATKIN interacting loop, three short helices 25–28 break the HEAT repeat pattern in the center of the solenoid ring, followed by the 'plug' loop (residues 630–643) which bridges through the center of the solenoid (Extended Data Fig. 2c). This loop is tethered to the edge of the solenoid in a structure that may represent a second zinc-binding motif (Fig. 1c and Supplementary Video 1). The local resolution is insufficient to resolve all residues with confidence, but the density represents a turn-like structure bringing in close proximity two histidines (H635 and H636) with two cysteines (C633 and C790), with an additional density sufficient for a zinc atom. Helix 29 then sits on the opposite side of the solenoid, running nearly parallel to the junction between the N- and C-terminal sections of the solenoid structure, before loop 657–683 passes back across the bottom of the solenoid ring, connecting to helix 30 on the far outer side of the solenoid (Extended Data Fig. 2c). The solenoid then continues with regular HEAT repeats until the hinge region.

The functionally important Tel1/ATM N-terminal (TAN) motif (residues 15–27) and essential residues 91–97 form a continuous interaction site on the solenoid-facing side of the N terminus[48,49]. The proline and hydrophobic residues within this interaction site are more probably conserved for their role in protein folding rather than for ligand interaction. P37 caps helix 3, while the hydrophobic residues form internal contacts between HEAT repeats. The long, unstructured loop (residues 825–879) interacts with R35 of helix 2, directly neighboring the TAN motif. This loop contains the cancer-associated mutation F858L and may be involved in signal transduction or ligand binding at the N terminus (Extended Data Fig. 3)[48].

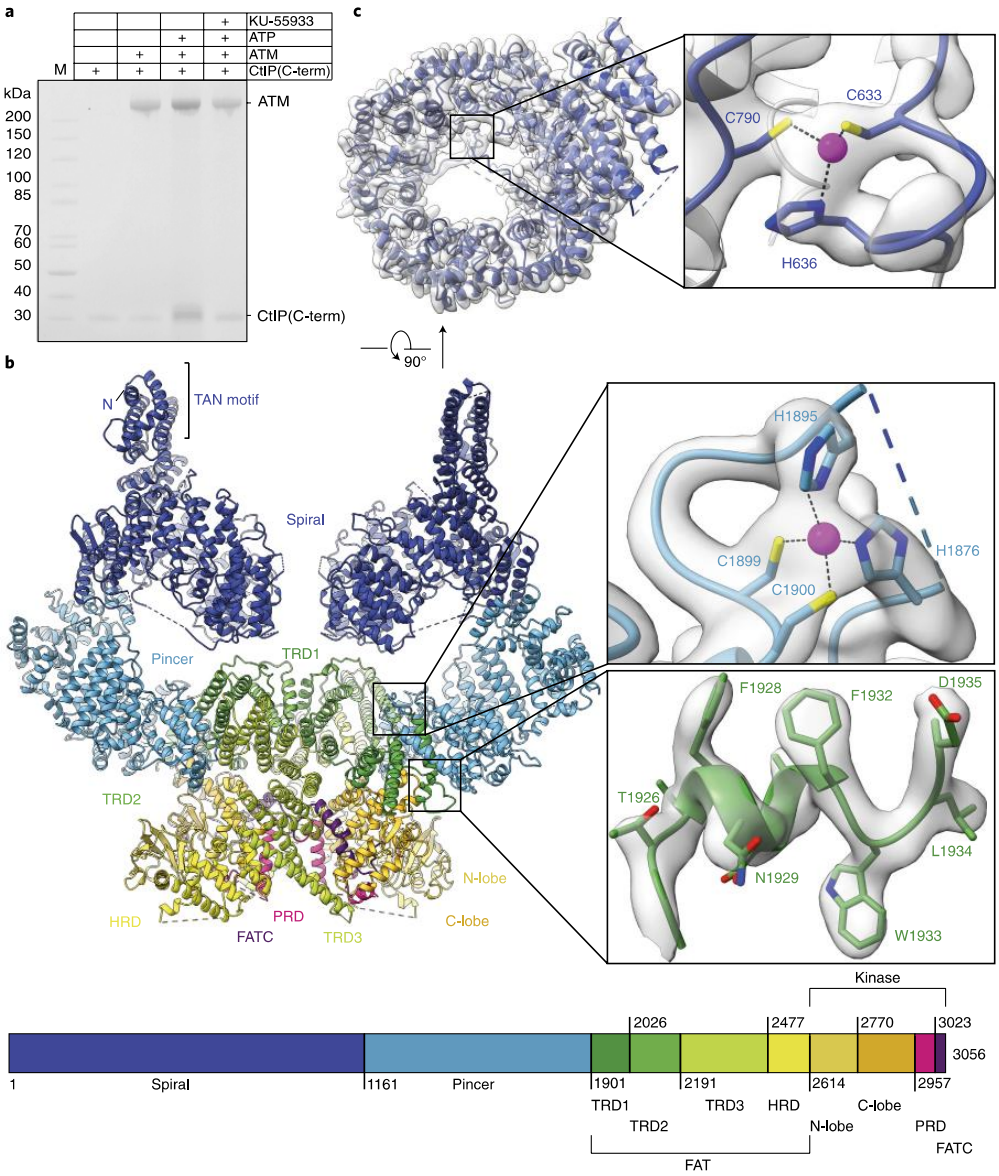

Fig. 1 | Cryo-EM structure and activity of dimeric human ATM. a, Inhibition of basal ATM kinase activity by KU-55933. Phosphorylation of human CtIP C terminus (650–897, phosphomimetic mutant T847E) visualized by phosphoprotein SDS–PAGE staining. The experiment was repeated twice with similar results. The uncropped gel image is available as source data. **b**, Model of KU-55933-bound human ATM. The structural domains are colored according to the schematic shown below the model. This domain color coding will be used throughout this Article. Top inset: pincer zinc-binding motif and map quality in the region. Bottom inset: map quality of the representative region (residues 1926–1935) in TRD1. **c**, Cryo-EM density map of the N-terminal spiral domain at 3.06 Å resolution (contoured at 0.017) with the fitted model in top view. Inset: spiral zinc-binding motif and map quality in the region.

To analyze the orientation of the region N-terminal to the FATKIN domain, we conducted focused three-dimensional (3D) classification on the spiral and pincer domain of all ATM particles (Supplementary Fig. 1). This indicated the presence of three different dimeric classes of ATM (Extended Data Fig. 1a and Supplementary Video 2). The main class, comprising 45% of the particles, belongs to a symmetrically related dimer with a small gap between the two opposing spiral domains, while 31% of the particles show a symmetrically related dimer with the spiral domains in close contact. Only 13% of the data resulted in one flexibly detached spiral domain. The best resolved N-terminal structure with closed spiral domains was refined to a final resolution of 3.41 Å. In addition to the spiral–FATKIN contact described above, we identified a second interface between the spiral domains of the two protomers. The N-terminal inter-domain contact was not seen in other human structures, in which the kinase and FAT domains were exclusively

Table 1 | Cryo-EM data collection and refinement statistics

	#1 ATM (kinase, KU-55933-bound state) (EMD-12343)	#2 ATM (hinge/pincer, KU-55933-bound state) (EMD-12345)	#3 ATM (N-term. spiral/pincer, KU-55933-bound state) (EMD-12346)	#4 ATM (focused N-term. spiral, KU-55933-bound state) (EMD-12347)	#5 ATM (composite map, KU-55933-bound state) (EMD-12351, PDB 7NI5)	#6 ATM (kinase, M4076-bound state) (EMD-12350, PDB 7NI4)	#7 ATM (kinase, ATPγS-bound state) (EMD-12352, PDB 7NI6)
Data collection and processing							
Magnification	130,000	130,000	130,000	130,000	130,000	130,000	130,000
Voltage (kV)	300	300	300	300	300	300	300
Electron exposure (e^-/Å^2)	45	45	45	45	45	45	43
Defocus range (μm)	−1.0 to −2.8	−1.0 to −2.8	−1.0 to −2.8	−1.0 to −2.8	−1.0 to −2.8	−1.0 to −2.8	−1.0 to −2.8
Pixel size (Å)	1.059	1.059	1.059	1.059	1.059	1.059	1.059
Symmetry imposed	*C*1	*C*1	*C*1	*C*1	*C*1	*C*2	*C*1
Initial particle images (no.)	2,679,787	2,679,787	2,679,787	2,679,787	2,679,787	2,346,822	709,013
Final particle images (no.)	826,510	807,127	1,035,906	977,752			
Map resolution (Å)	2.78	3.34	3.10	3.15	Composite Map (#1–4)	3.03	2.78
FSC threshold	0.143	0.143	0.143	0.143		0.143	0.143
Map resolution range (Å)	2.49–8.52	3.14–5.61	2.93–4.71	2.91–4.27		2.57–9.75	2.62–9.75
Refinement							
Initial model used					PDB 6K9L	PDB 7NI5	PDB 7NI5
Model resolution (Å)					2.79	3.3	2.9
FSC threshold					0.5	0.5	0.5
Model resolution range (Å)					2.49–4.27	2.57–4.80	2.62–3.90
Map sharpening *B* factor (Å^2)					0 (LAFTER filtered)	0 (LAFTER filtered)	0 (LAFTER filtered)
Model composition							
Nonhydrogen atoms					45,052	23,236	23,079
Protein residues					5,581	2,864	2,847
Ligands					4 Zn, 2 KU-55933	2 Zn, 2 M4076	2 Zn, 2 Mg, 2 AGS
B factors (Å^2)					22.49/138.51/70.38	59.66/184.03/106.29	24.39/131.44/65.67
Protein					39.77/167.58/48.67	74.15/205.96/78.84	50.79/143.71/69.28
Ligand							
R.m.s. deviations					0.003	0.005	0.003
Bond lengths (Å)					0.500	0.859	0.467
Bond angles (°)							
Validation							
MolProbity score					1.42	1.35	1.15
Clashscore					4.88	6.07	3.60
Poor rotamers (%)					0.02	0.08	0.08
Ramachandran plot							
Favored (%)					97.06	97.95	98.04
Allowed (%)					2.94	2.05	1.96
Disallowed (%)					0.00	0.00	0.00

Different datasets are described.

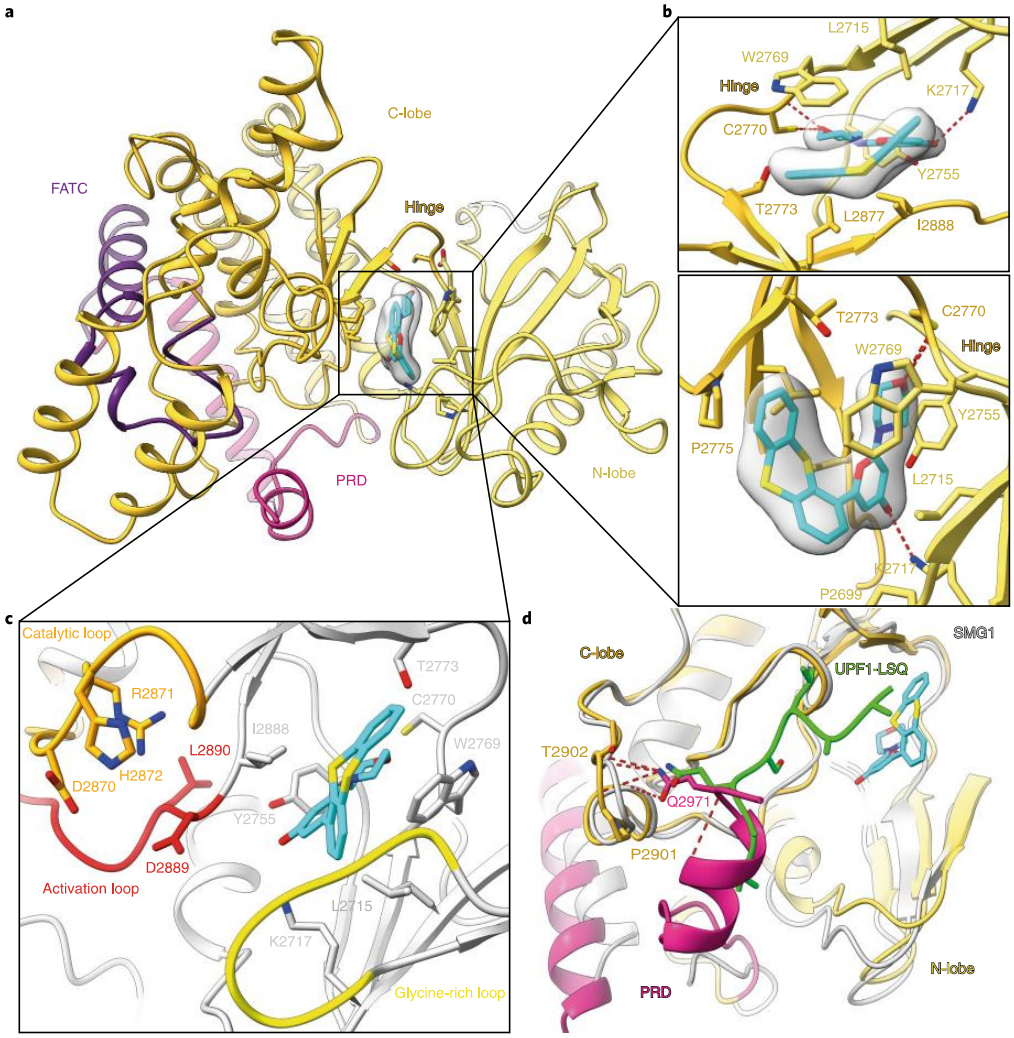

Fig. 2 | Human ATM active site conformation in the KU-55933 bound state. a, KU-55933 (cyan) in 2.8-Å density (contoured at 0.032) bound to the kinase active site. **b**, Detailed binding mode of KU-55933 inhibitor in side and top views. Side chains of inhibitor-proximal residues are shown. Interactions were calculated with ViewContacts and hydrogen bonds are indicated as red dotted lines[57]. **c**, Conformations of the kinase catalytic loop (orange), activation loop (red) and glycine-rich loop (yellow) surrounding the bound inhibitor. **d**, Detailed view of the superimposed substrate-bound (UPF1 substrate in green) SMG1 (PDB ID 6Z3R; gray) and KU-55933-bound ATM (color) kinase domain. Substrate-mimicking Q2971 of PRD (magenta) and its hydrogen bonds (red dotted lines) to the kinase C-lobe residues T2902 and P2901 are indicated.

involved in dimerization[21]. This observation supports the assumption that the inhibitor-bound ATM structure is in a more stable dimeric state (Extended Data Fig. 1a,e). The resolution of the spiral–FATKIN interface loops does not permit unambiguous identification of the interacting residues, but the opposing loops carry charge complementarity, suggesting they may mediate salt bridge formation.

Cancer-associated human ATM mutations. The prevalence of mutations that result in ATM functional deficiency is generally below 5%, but is enhanced for colon adenocarcinoma (11%), cholangiocarcinoma (8.8%) and uterine corpus endometrial carcinoma (6.9%). Other mutations that do not compromise ATM kinase function represent the majority of ATM alterations. (The results published here are in whole or part based upon data generated by the TCGA Research Network at https://www.cancer.gov/tcga.) We mapped the locations of common ATM mutations that were reported more than five times in the COSMIC database (Extended Data Fig. 3)[51]. Although mutations are distributed throughout the entire length of the protein, some mutations cluster in surface regions and may indicate important functional sites. For example, a highly conserved R23, frequently mutated to Q (count of 9), is located in the substrate-binding TAN motif. The very frequent F858L (count of 31) mutation maps to a loop that interacts with the TAN motif, supporting the functional role of this apical region in ATM signaling. R337C/H (count of 93), S707P and S333F (count of 9) mutations affect adjacent solvent-exposed loops of the spiral near the TAN motif, which may be an important interaction site.

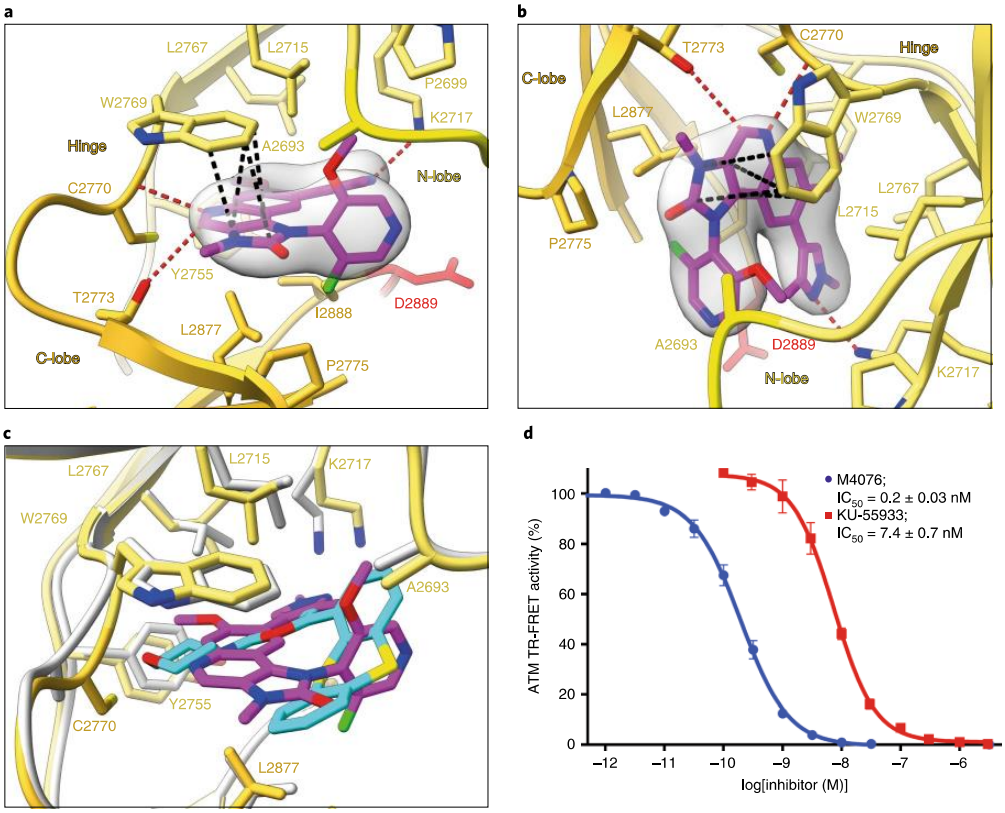

Fig. 3 | Human ATM active site conformation in the M4076-bound state. a, Detailed binding mode of the M4076 inhibitor at a resolution of 3.0 Å (contoured at 0.038). Side chains of inhibitor-proximal residues are shown. Interactions were calculated with ViewContacts[57]. Hydrogen bonds are indicated by red dotted lines and π-stacking interactions are highlighted as black dotted lines. The kinase activation loop is shown in red. **b**, Same as in **a**, but as a side view. **c**, Superimposition of M4076 (magenta, colored model) and KU-55933 (cyan, gray model) bound ATM active sites. **d**, Dose–response curves of enzymatic ATM kinase inhibition by M4076 and KU-55933. Data represent the mean ± s.e.m. from $n = 15$ independent experiments performed in duplicate for M4076 ($IC_{50} = 0.20 \pm 0.03$ nM) and from one experiment performed in duplicate for KU-55933 ($IC_{50} = 7.4 \pm 0.7$ nM). Data for **d** are available as source data.

R337C/H was identified as a 'hotspot' cancer mutation common in colorectal cancer and associated with an ATM loss-of-function phenotype[52]. V410A (count of 20) forms an internal hydrophobic contact with I339 that may influence the stability of the spiral, or may lead to conformational changes. T1880R (count of 7) affects a loop stabilized by the pincer zinc-binding motif and thus could be a substrate/ligand interaction site. Q2442P (count of 7) and R2443Q (count of 21) are located in the helix of the TRD3 that contacts the PRD across a dimer interface. R3008H/C (count of 64) contributes to this interaction from the PRD side. This TRD3–PRD interaction would need to break to enable the conformational change into the open dimer, as reported by Baretic and colleagues[16]. It has been proposed that R3008H substitution impairs the conformational change of PRD-I required for substrate interactions with the catalytic loop[53]. The following disease-associated mutations are located directly within the ATP-binding site: R2691C (count of 11), G2695S (count of 8), R2832C (count of 15), N2875S (count of 8), I2888T (count of 6) and L2890V (count of 7).

ATM active site and KU-55933 binding mode. The overall architecture of the FAT and kinase domains largely resembles the apoenzyme structure reported by Xiao et al. (Extended Data Fig. 4a,c)[22], but the reduced structural flexibility of ATM due to inhibitor binding as compared with the apoenzyme structures allowed for model building of virtually all amino acid side chains in the active site (Extended Data Fig. 4d). Briefly, the catalytic cleft is formed by the N- and C-terminal lobes (N-lobe and C-lobe) which are connected via a hinge region (Fig. 2a). In general, the N-lobe of PIKKs is responsible for nucleotide binding and coordination, and contains the glycine-rich loop (P-loop). The C-lobe of ATM and related kinases includes the catalytic loop with the DRH residues (D2870, R2871, H2872) required for substrate phosphorylation. The catalytic loop is held in place by the activation loop, which contains a DLG motif composed of D2889, L2890 and G2891. This motif plays an important role in substrate recognition and Mg^{2+} coordination, and hence in the regulation of catalysis (Fig. 2c)[54]. In the related kinases DNA-PK, mTOR, ATR and Mec1, the motif consists of DFG, DFN or DFD (see "Understanding of kinase inhibitor selectivity" below). Recently, it was shown that the conserved phenylalanine residue is critical for autoinhibition and activation of Mec1[55]. Mutation to leucine, the amino acid present in ATM and Tel1, leads to a constitutively active Mec1[55]. Consequently, the F-to-L substitution in ATM/Tel1 may explain why no additional activator protein is needed for their basal phosphorylation activity. However, in the

Table 2 | Kinase selectivity of KU-55933 and M4076 inhibitors

Inhibitor	On-target	Primary downstream target	Kinase selectivity						
	ATM IC_{50} (nM)[a]	Cellular pCHK^{Thr68} HCT116 IC_{50} (nM)[b]	DNA-PK IC_{50} (nM)[a]	mTOR IC_{50} (nM)[c]	ATR IC_{50} (nM)[a]	PI3Kα IC_{50} (nM)[a]	PI3Kβ IC_{50} (nM)[a]	PI3Kγ IC_{50} (nM)[a]	PI3Kδ IC_{50} (nM)[a]
KU-55933	7.4	1,100[d]	1,400	9,300[e]	>100,000[e]	2,000	1,900	14,000	1,500
M4076	0.2	10[f]	600	>30,000[c,g]	10,000[a]	8,500[g]	>30,000[g]	>30,000[g]	15,000[g]

Shown are KU-55933 and M4076 biochemical IC_{50} values against kinases ATM, DNA-PK, mTOR, ATR and PI3Ks and cellular IC_{50} values for inhibition of bleomycin- or 2 Gy-induced phosphorylation of CHK2 (pThr68) in HCT116 cells. Source data for Table 2 are presented in Supplementary Data 1. [a]Determined by time-resolved FRET assays with recombinant proteins. [b]In vitro cell-based IC_{50} for inhibition of bleomycin- or 2 Gy-induced phosphorylation of CHK2 (pThr68) in the human colon carcinoma cell line HCT116. [c]Determined by enzymatic mTOR assay. [d]ELISA, bleomycin-induced. [e]As determined by Hicksson et al.[40]. [f]Luminex assay, 2 Gy-induced (Methods). [g]IC_{50} obtained for racemate of M4076.

KU-55933 complex structure, the PRD blocks active site access, as seen in other ATM/Tel1 structures, confirming the autoinhibitory function of the ATM PRD domain in the inhibitor-bound form[19,21]. The PRD is firmly locked in position by interactions with the activation loop of the kinase via hydrogen-bond interactions of Q2971 with the backbone oxygens of P2901 and T2902 and hydrophobic contacts of L2970 (Fig. 2d). Superimposition with the substrate-bound SMG1-8-9 kinase UPF-1 complex structure shows that residue Q2971 occupies the substrate glutamine binding site of the kinase, thus mimicking the glutamine in the substrate SQ/TQ selectivity motifs and precluding substrate access to the catalytic center (Fig. 2d)[19,21,56]. Sequence alignment of the PRD region indicates that the substrate-mimicking inhibitory mechanism is conserved among most ATM orthologs (Extended Data Fig. 4b). Combined structural and sequence analysis of the human ATM C terminus with other human PIKKs suggests that DNA-PK may use a similar substrate-mimicking mechanism. However, the map quality of the other kinases, as well as the low level of sequence conservation in this region, precludes more definitive statements regarding a conserved PRD inhibition mechanism for other PIKK family members (Extended Data Fig. 4b).

A more detailed comparison of the KU-55933-bound and apoenzyme structures reveals that the ATM kinase N-lobe is shifted outwards to accommodate the inhibitor (Extended Data Fig. 4c). KU-55933 is well ordered, which facilitates fitting of the small-molecule inhibitor and all interacting residues within this area (Fig. 2b and Extended Data Fig. 4d). The chemical description of the inhibitor is shown in Extended Data Fig. 4e. KU-55933 forms two distinct hydrogen bonds via the morpholine O atom with C2770 of the hinge region and via the pyran-4-one carbonyl O atom with the catalytically important residue K2717 in the N-lobe (Fig. 2b,c). The non-planar thianthrene ring is involved in extensive van der Waals (vdW) contacts with residues P2699 in the P-loop, L2715, L2767, W2769 in the N-lobe, P2775, L2877 and I2888 in the C-lobe and activation loop, respectively (Extended Data Fig. 4f). We next examined the binding and inhibitory mechanism of a second inhibitor, M4076, with a chemically distinct scaffold to KU-55933.

Towards a more selective and potent ATM inhibitor. KU-55933 is a potent ATM inhibitor (IC_{50} = 7.4 nM) with selectivity towards ATR, mTOR (IC_{50} values above 10 μM) and other kinases, but with residual micromolar potencies on DNA-PK (IC_{50} = 1.4 μM), phosphoinositide 3-kinase (PIK3) isoforms α, β and δ (IC_{50} values ~2 μM) and PI3Kγ (IC_{50} = 14 μM) corresponding to IC_{50} splits above 180-fold towards ATM (Fig. 3d, Table 2 and Extended Data Figs. 5d and 6f)[40]. The ATM inhibitor M4076 is a result of advanced optimization efforts that led to the identification of a candidate drug being evaluated in a phase I trial[31]. In comparison to KU-55933, M4076 is a potent, subnanomolar ATM kinase inhibitor (IC_{50} = 0.2 nM) with strong enzymatic selectivity against ATM's close kinase family members, that is, ~3,000-fold selectivity towards DNA-PK (IC_{50} = 600 nM) and more than 40,000-fold selectivity towards ATR, mTOR and PIK3 isoforms α, β, γ and δ (IC_{50} values above 8.5 μM) (Fig. 3d, Table 2 and Extended Data Figs. 5d and 6c–e). Broader kinase profiling of M4076 revealed a strong overall human kinome selectivity. In a panel of 583 human kinases, no interaction had been observed below an IC_{50} of ~700-fold compared to the on-target enzymatic ATM IC_{50} of 0.2 nM for M4076 (Extended Data Fig. 6g,h and Supplementary Notes)[42,43]. M4076 also showed low nanomolar cellular inhibition of checkpoint kinase 2 (CHK2) Thr68 phosphorylation in HCT116 cells (IC_{50} = 10 nM) as the primary downstream target of ATM, while KU-55933 was only weakly potent (IC_{50} = 1,100 nM) in this readout (Extended Data Fig. 6a,b).

To understand the enhanced biochemical ATM potency of M4076, we determined the cryo-EM structure of human ATM in complex with M4076 to 3.0 Å resolution in the kinase domain (Fig. 3a,b and Extended Data Fig. 5c). Before solving the structure, the inhibitory effect on the purified human ATM sample was verified by a CtIP kinase assay (Extended Data Fig. 5a). The EM density allowed clear binding mode assignment of the inhibitor in the ATM active site cleft. The chemical description of the inhibitor is provided in Extended Data Fig. 5b. The 1,3-dihydro-imidazo[4,5-*c*]quinolin-2-one moiety binds towards the hinge region, indicating a classical hydrogen bond between the N5 atom and C2770, as well as non-classical hydrogen bonds of the 4-CH group to C2770 and T2773 (Fig. 3a,b). Remarkably, the imidazolone ring forms extensive π–π and amide–π stacking interactions towards the W2769 side chain of the hinge region (Fig. 3a,b), as calculated from the atomic coordinates by the software tool ViewContacts[57]. The 7-methoxy group attached to the quinoline ring interacts with the gatekeeper residue L2767 and with L2715 via vdW contacts (Extended Data Fig. 5c). The M4076 1,3-dimethyl-1*H*-pyrazole substituent is in vdW contact with I2888 next to the DLG motif of the activation loop and in hydrogen bond distance to K2717 via the unsubstituted N atom. Cryo-EM density fitting of the 3-fluoro-5-methoxypyridine ring was based on the S_a atropisomeric configuration of this moiety identified by small-molecule X-ray crystallography of M4076[46]. In this orientation, the 3-fluoro-5-methoxypyridine ring indicates vdW contacts of the fluorine atom with P2775 and L2877 on one side and of the methoxy group towards W2769 and A2693 on the other side (Extended Data Fig. 5c).

Understanding of kinase inhibitor selectivity. To understand the inhibitory mechanism and to compare the inhibited structure with the catalytic states of ATM, we also determined the cryo-EM structure of human ATM bound to the non-hydrolysable ATP analog ATPγS to a resolution of 2.8 Å (Extended Data Fig. 7c,d,h). Structural superimposition of all three human ATM structures in complex with compounds KU-55933, M4076 and ATPγS indicate a similar overall ATM conformation, including N-terminal domains, and an almost identical active site cleft geometry (Supplementary Video 3 and Extended Data Figs. 7 and 8). However, one major conformational difference involves residue C2770 of the hinge region, which is shifted by 1.2 Å based on αC-atom distance

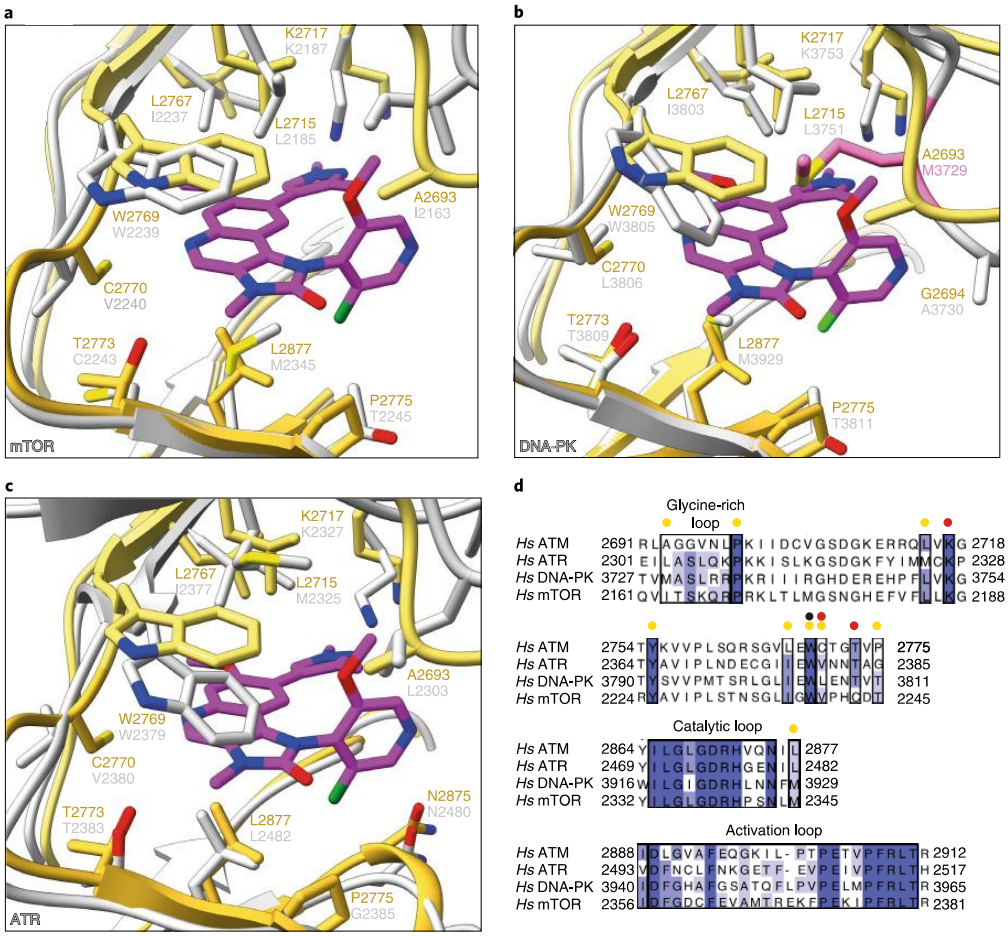

Fig. 4 | Specificity of the inhibitor M4076 towards human ATM kinase over other PIKKs. a, Superimposition of the M4076-bound human ATM active site (color) and apo human mTOR (PDB 4JSN; gray). Residues surrounding the inhibitor are labeled accordingly. **b**, Same as in **a** but with apo DNA-PK (PDB 6ZFP; gray). DNA-PK M3729 is shown in pink. **c**, Same as in **a** but with apo ATR (PDB 5YZ0; gray). **d**, Sequence alignment of the human (*Hs*) ATM, ATR, DNA-PK and mTOR active sites, colored by conservation. Glycine-rich, catalytic and activation loops are labeled. ATM residues forming hydrogen interactions with the inhibitor are marked with red circles, vdW interactions with yellow circles and π-stacking interactions with a black circle.

and 2.2 Å based on the S-atom distance towards the nucleotide binding site in the M4076 and ATPγS structures. This shift is induced by hydrogen bond formation between the C2770 backbone amide NH donor and the 1,3-dihydro-imidazo[4,5-*c*]quinolin-2-one N5 atom of M4076 or with the ATPγS N1 atom, respectively (Fig. 3a and Extended Data Fig. 7c,e,g). Furthermore, the 1,3-dihydro-imidazo[4,5-*c*]quinolin-2-one ring of M4076 overlaps well with the position of the purine ring in the ATPγS structure, creating additional aromatic stacking interactions to the adjacent W2769. The induced fit observed for C2770 together with π–π and amide–π stacking interactions towards the hinge tryptophane might explain the ~35-fold improved biochemical ATM potency as well as the improved selectivity of M4076 towards DNA-PK compared with KU-55933 (Extended Data Fig. 5d). Thus, M4076 perfectly mimics the ATPγS-bound pre-catalysis state of human ATM. Moreover, M4076 adopts additional vdW contacts to the C-lobe and the glycine-rich loop via both the 1,3-dimethyl-1*H*-pyrazole and 3-fluoro-5-methoxypyridine substituents, respectively. Another structural difference exclusively seen in the M4076-bound protein structure is an altered side chain rotamer of residue L2767 to accommodate the 7-methoxy substituent (Fig. 3c).

Structural analysis together with sequence alignment revealed several residues involved in M4076 binding interactions, which are not conserved within the structurally most related kinases ATR, mTOR, DNA-PK and PI3K isoforms: A2693, L2715, L2767, C2770, T2773, P2775 and L2877 (Fig. 4a–d and Extended Data Fig. 6i). The superimposition of ATM cryo-EM structures in complex with KU-55933 and M4076 shows overall similar conformations of these non-conserved residues with few exceptions, including L2767 and C2770 (Fig. 3c). Structural comparison of the M4076-bound ATM with the apoenzyme structures of mTOR, DNA-PK and ATR uncover a rational basis to understand the high selectivity of this inhibitor (Fig. 4a–c). These overlays highlight an important role of the M4076-specific 5-methoxypyridine group in selectivity, which is in vdW contact with A2693 in ATM[58]. This alanine is replaced by the bulkier residues isoleucine, methionine and leucine in mTOR, DNA-PK/PI3Ks and ATR, respectively (Fig. 4a–d and Extended Data Fig. 6i). These larger amino acids might sterically hinder the scaffold of M4076 to obtain an optimal binding position towards

π–π stacking interactions with W2769 as well as hydrogen-bond interactions with C2770 in the hinge region. Sequence variations impairing optimal hinge-binding interactions are also in line with the observed M4076 selectivity against PI3K isoforms, because both W2769 and C2770 are replaced by valines (PIK3α, β and δ) or isoleucine (PIK3γ) and valine, respectively. Additional contributions towards DNA-PK, mTOR and ATR selectivity might be due to second shell residues in ATM (I2701, R2713 and T2771) influencing W2769 side chain flexibility, which are different in DNA-PK (R3737, P3749, E3807), mTOR (K2171, V2183, P2241) and ATR (K2311, I2323, N2381). Finally, residue L2877 below the inhibitor in the C-lobe region is in vdW contact with the imidazolone ring of M4076. This leucine is conserved in ATR but replaced with methionine in DNA-PK, mTOR and PI3Ks, leaving less space for the inhibitor in these kinases.

Discussion

As a key regulator, nuclear ATM kinase orchestrates cellular responses to DNA DSBs. Inhibition of ATM activity sensitizes different tumors to DNA DSB-inducing cancer treatments, such as chemo- and radiotherapy as well as targeted therapies (PARP or ATR inhibition), thereby impeding the ability of cancer cells to evade anticancer therapies[25,32,35,37,59]. A compelling medical need thus exists for the development of ATM inhibitors for anticancer therapies, prompting us to focus on structural studies of ATM. We provide three cryo-EM structures of the human ATM kinase with bound inhibitors and ATPγS. These structures reveal modes of action of small-molecule inhibition of ATM in therapeutic approaches, but also details of kinase active site autoinhibition, as well as an internal pseudo-substrate glutamine in human ATM. The increased conformational rigidity in the inhibited state allowed for atomic modeling of the nearly complete ATM protein. Careful evaluation of the spiral and pincer domain conformations of the KU-55933 inhibitor-bound ATM structure resulted in a cryo-EM density that allowed for a thorough model building of the entire solenoid region. This revealed—unexpectedly—two zinc-binding motifs in the spiral and pincer domains, respectively. These motifs are partially conserved in mammals and appear to either stabilize ATM or be involved in the interaction with other binding partners and/or DNA. Recently, a related zinc-finger motif was discovered in the N-terminal HEAT domain of $Mec1^{ATR}$ checkpoint kinase, which is involved in stabilization of the interface area with the $Mec1^{ATR}$ integral partner $Ddc2^{ATRIP}$ (ref. [55]). In all three structures, the PRD blocks the active site access, confirming the autoinhibitory function of this domain[19,21]. Thereby, the PRD gatekeeper helix is locked in its position by interaction of Q2971 with the activation loop. Overall, the active site cleft geometry of the presented ATM structures is nearly identical except for the hinge region residue C2770 and minor changes in the glycine-rich loop (P-loop) region (Extended Data Fig. 7 and Supplementary Video 3). Together, structures with the bound small-molecule inhibitors uncover the binding mechanisms of two different ATM inhibitor classes and provide further insights into the understanding of their selectivity profiles.

High-resolution ATM structures were not available at the time of discovery of the ATM inhibitor M4076, detailed insights into the binding modalities as well as selectivity determinants towards closely related kinases remained hypothetical[31]. The presented high-resolution cryo-EM structure of ATM now allows detailed insights into the binding mode of M4076. In this regard, we identified extensive π–π and amide–π stacking interactions between the central 1,3-dihydro-imidazo[4,5-*c*]quinolin-2-one scaffold of M4076 towards W2769 in the hinge region of ATM, which are not present in the complex with KU-55933 (Fig. 3a–c). A second major difference between the ATM structures of both inhibitors is the position of C2770, also in the hinge region, which is shifted towards the 1,3-dihydro-imidazo[4,5-*c*]quinolin-2-one moiety of M4076 with respect to the morpholine ring of KU-55933 (Fig. 3c and Supplementary Video 3). The same shifted position of C2770 was observed in the ATM structure with ATPγS, which is considered to correspond to the pre-catalytic state of ATM (Extended Data Fig. 7g). In comparison to KU-55933, M4076 forms additional vdW contacts within the ATP site via its 7-methoxy group as well as with the 3-fluoro-5-methoxypyridine substituent. Together, these additional contacts explain the ~35-fold stronger enzymatic ATM potency of M4076 compared to KU-55933. The enhanced ATM inhibitory potency of M4076 observed in vitro translates well into the in cellulo inhibition of CHK2 phosphorylation at low nanomolar concentrations in HCT116 cells. We note that this inhibitory effect on cellular CHK2 phosphorylation is ~100-fold increased with M4076 compared with KU-55933. Additionally, we identified several non-conserved ATM residues involved in M4076 binding interactions by structural comparison with the DNA-PK, mTOR, ATR and PI3K isoforms. These sequence differences include residues in direct contact with M4076, such as A2693, and in the case of PI3K isoforms also W2769 and C2770. Further sequence differences involve residues in the second shell around W2769, thereby affecting its side chain flexibility to adopt optimal π-stacking interactions with the inhibitor (Fig. 4d and Extended Data Fig. 6i). In this respect, the substitution of A2693 in ATM by bulkier residues in DNA-PK, mTOR, ATR and PI3Ks is considered to be a crucial factor that explains the observed selectivity profile of M4076 towards these closely related kinase family proteins (Table 2).

Taken together, our atomic models of human ATM provide a framework for the evaluation and development of highly specific and potent therapeutics, as well as analyzing the central role and function of human ATM in healthy and cancerogenic cells through structure-informed approaches.

Online content

Any methods, additional references, Nature Research reporting summaries, source data, extended data, supplementary information, acknowledgements, peer review information; details of author contributions and competing interests; and statements of data and code availability are available at https://doi.org/10.1038/s41594-021-00654-x.

Received: 3 February 2021; Accepted: 30 July 2021;
Published online: 23 September 2021

References

1. Hoeijmakers, J. H. Genome maintenance mechanisms for preventing cancer. *Nature* **411**, 366–374 (2001).
2. Matsuoka, S. et al. ATM and ATR substrate analysis reveals extensive protein networks responsive to DNA damage. *Science* **316**, 1160–1166 (2007).
3. Bartek, J. & Lukas, J. Chk1 and Chk2 kinases in checkpoint control and cancer. *Cancer Cell* **3**, 421–429 (2003).
4. Burma, S., Chen, B. P., Murphy, M., Kurimasa, A. & Chen, D. J. ATM phosphorylates histone H2AX in response to DNA double-strand breaks. *J. Biol. Chem.* **276**, 42462–42467 (2001).
5. Roos, W. P. & Kaina, B. DNA damage-induced cell death: from specific DNA lesions to the DNA damage response and apoptosis. *Cancer Lett.* **332**, 237–248 (2013).
6. Mills, K. D., Ferguson, D. O. & Alt, F. W. The role of DNA breaks in genomic instability and tumorigenesis. *Immunol. Rev.* **194**, 77–95 (2003).
7. Kastan, M. B. & Bartek, J. Cell-cycle checkpoints and cancer. *Nature* **432**, 316–323 (2004).
8. Lovejoy, C. A. & Cortez, D. Common mechanisms of PIKK regulation. *DNA Repair (Amst.)* **8**, 1004–1008 (2009).
9. Keith, C. T. & Schreiber, S. L. PIK-related kinases: DNA repair, recombination and cell cycle checkpoints. *Science* **270**, 50–51 (1995).
10. Shiloh, Y. & Ziv, Y. The ATM protein kinase: regulating the cellular response to genotoxic stress, and more. *Nat. Rev. Mol. Cell Biol.* **14**, 197–210 (2013).
11. Zou, L. & Elledge, S. J. Sensing DNA damage through ATRIP recognition of RPA–ssDNA complexes. *Science* **300**, 1542–1548 (2003).

12. Yamashita, A., Ohnishi, T., Kashima, I., Taya, Y. & Ohno, S. Human SMG-1, a novel phosphatidylinositol 3-kinase-related protein kinase, associates with components of the mRNA surveillance complex and is involved in the regulation of nonsense-mediated mRNA decay. *Genes Dev.* **15**, 2215–2228 (2001).
13. McMahon, S. B., Van Buskirk, H. A., Dugan, K. A., Copeland, T. D. & Cole, M. D. The novel ATM-related protein TRRAP is an essential cofactor for the c-Myc and E2F oncoproteins. *Cell* **94**, 363–374 (1998).
14. Yang, H. et al. mTOR kinase structure, mechanism and regulation. *Nature* **497**, 217–223 (2013).
15. Imseng, S., Aylett, C. H. & Maier, T. Architecture and activation of phosphatidylinositol 3-kinase related kinases. *Curr. Opin. Struct. Biol.* **49**, 177–189 (2018).
16. Baretic, D. et al. Structures of closed and open conformations of dimeric human ATM. *Sci. Adv.* **3**, e1700933 (2017).
17. Baretic, D. & Williams, R. L. PIKKs—the solenoid nest where partners and kinases meet. *Curr. Opin. Struct. Biol.* **29**, 134–142 (2014).
18. Sawicka, M. et al. The dimeric architecture of checkpoint kinases Mec1ATR and Tel1ATM reveal a common structural organization. *J. Biol. Chem.* **291**, 13436–13447 (2016).
19. Jansma, M. et al. Near-complete structure and model of Tel1ATM from *Chaetomium thermophilum* reveals a robust autoinhibited ATP state. *Structure* **28**, 83–95 (2020).
20. Xin, J. et al. Structural basis of allosteric regulation of Tel1/ATM kinase. *Cell Res.* **29**, 655–665 (2019).
21. Yates, L. A. et al. Cryo-EM structure of nucleotide-bound Tel1(ATM) unravels the molecular basis of inhibition and structural rationale for disease-associated mutations. *Structure* **28**, 96–104 (2020).
22. Xiao, J. et al. Structural insights into the activation of ATM kinase. *Cell Res.* **29**, 683–685 (2019).
23. Bakkenist, C. J. & Kastan, M. B. DNA damage activates ATM through intermolecular autophosphorylation and dimer dissociation. *Nature* **421**, 499–506 (2003).
24. Guo, Z., Kozlov, S., Lavin, M. F., Person, M. D. & Paull, T. T. ATM activation by oxidative stress. *Science* **330**, 517–521 (2010).
25. Lavin, M. F. & Yeo, A. J. Clinical potential of ATM inhibitors. *Mutat. Res.* **821**, 111695 (2020).
26. Jin, M. H. & Oh, D. Y. ATM in DNA repair in cancer. *Pharmacol. Ther.* **203**, 107391 (2019).
27. Weber, A. M. & Ryan, A. J. ATM and ATR as therapeutic targets in cancer. *Pharmacol. Ther.* **149**, 124–138 (2015).
28. Rainey, M. D., Charlton, M. E., Stanton, R. V. & Kastan, M. B. Transient inhibition of ATM kinase is sufficient to enhance cellular sensitivity to ionizing radiation. *Cancer Res.* **68**, 7466–7474 (2008).
29. Batey, M. A. et al. Preclinical evaluation of a novel ATM inhibitor, KU59403, in vitro and in vivo in p53 functional and dysfunctional models of human cancer. *Mol. Cancer Ther.* **12**, 959–967 (2013).
30. Riches, L. C. et al. Pharmacology of the ATM inhibitor AZD0156: potentiation of irradiation and olaparib responses preclinically. *Mol. Cancer Ther.* **19**, 13–25 (2020).
31. Fuchss, T. et al. Abstract 3500: highly potent and selective ATM kinase inhibitor M4076: a clinical candidate drug with strong anti-tumor activity in combination therapies. *Cancer Res.* **79**, 3500 (2019).
32. Choi, M., Kipps, T. & Kurzrock, R. ATM mutations in cancer: therapeutic implications. *Mol. Cancer Ther.* **15**, 1781–1791 (2016).
33. Dohmen, A. J. C. et al. Identification of a novel ATM inhibitor with cancer cell specific radiosensitization activity. *Oncotarget* **8**, 73925–73937 (2017).
34. Toledo-Sherman, L. et al. Optimization of potent and selective ataxia telangiectasia-mutated inhibitors suitable for a proof-of-concept study in Huntington's disease models. *J. Med. Chem.* **62**, 2988–3008 (2019).
35. Min, A. et al. AZD6738, a novel oral inhibitor of ATR, induces synthetic lethality with ATM deficiency in gastric cancer cells. *Mol. Cancer Ther.* **16**, 566–577 (2017).
36. Perkhofer, L. et al. ATM deficiency generating genomic instability sensitizes pancreatic ductal adenocarcinoma cells to therapy-induced DNA damage. *Cancer Res.* **77**, 5576–5590 (2017).
37. Schmitt, A. et al. ATM deficiency is associated with sensitivity to PARP1- and ATR inhibitors in lung adenocarcinoma. *Cancer Res.* **77**, 3040–3056 (2017).
38. Weston, V. J. et al. The PARP inhibitor olaparib induces significant killing of ATM-deficient lymphoid tumor cells in vitro and in vivo. *Blood* **116**, 4578–4587 (2010).
39. Kantidze, O. L., Velichko, A. K., Luzhin, A. V., Petrova, N. V. & Razin, S. V. Synthetically lethal interactions of ATM, ATR and DNA-PKcs. *Trends Cancer* **4**, 755–768 (2018).
40. Hickson, I. et al. Identification and characterization of a novel and specific inhibitor of the ataxia-telangiectasia mutated kinase ATM. *Cancer Res.* **64**, 9152–9159 (2004).
41. Golding, S. E. et al. Improved ATM kinase inhibitor KU-60019 radiosensitizes glioma cells, compromises insulin, AKT and ERK prosurvival signaling, and inhibits migration and invasion. *Mol. Cancer Ther.* **8**, 2894–2902 (2009).
42. Karlin, J. et al. Orally bioavailable and blood–brain barrier-penetrating ATM inhibitor (AZ32) radiosensitizes intracranial gliomas in mice. *Mol. Cancer Ther.* **17**, 1637–1647 (2018).
43. Pike, K. G. et al. The identification of potent, selective and orally available inhibitors of ataxiatelangiectasia mutated (ATM) kinase: the discovery of AZD0156(8-{6-[3-(dimethylamino)propoxy]pyridin-3-yl}-3-methyl-1-(tetrahydro-2*H*-pyran-4-yl)-1,3-dihydro-2*H*-imidazo[4,5-*c*]quinolin-2-one). *J. Med. Chem.* **61**, 3823–3841 (2018).
44. Durant, S. T. et al. The brain-penetrant clinical ATM inhibitor AZD1390 radiosensitizes and improves survival of preclinical brain tumor models. *Sci. Adv.* **4**, eaat1719 (2018).
45. Morgado-Palacin, I. et al. Targeting the kinase activities of ATR and ATM exhibits antitumoral activity in mouse models of MLL-rearranged AML. *Sci. Signal.* **9**, ra91 (2016).
46. Fuchss, T., Becker, A., Kubas, H. & Graedler, U. Imidazolonylquinoline compounds and therapeutic uses thereof. WO patent 2020/193660 (2020).
47. Boland, A., Chang, L. & Barford, D. The potential of cryo-electron microscopy for structure-based drug design. *Essays Biochem.* **61**, 543–560 (2017).
48. Seidel, J. J., Anderson, C. M. & Blackburn, E. H. A novel Tel1/ATM N-terminal motif, TAN, is essential for telomere length maintenance and a DNA damage response. *Mol. Cell. Biol.* **28**, 5736–5746 (2008).
49. Fernandes, N. et al. DNA damage-induced association of ATM with its target proteins requires a protein interaction domain in the N terminus of ATM. *J. Biol. Chem.* **280**, 15158–15164 (2005).
50. Falck, J., Coates, J. & Jackson, S. P. Conserved modes of recruitment of ATM, ATR and DNA-PKcs to sites of DNA damage. *Nature* **434**, 605–611 (2005).
51. Tate, J. G. et al. COSMIC: the Catalogue Of Somatic Mutations In Cancer. *Nucleic Acids Res.* **47**, D941–D947 (2019).
52. Weber, A. M. et al. Phenotypic consequences of somatic mutations in the ataxia-telangiectasia mutated gene in non-small cell lung cancer. *Oncotarget* **7**, 60807–60822 (2016).
53. Milanovic, M. et al. The cancer-associated ATM R3008H mutation reveals the link between ATM activation and its exchange. *Cancer Res.* **81**, 426–437 (2020).
54. Vivek, M., & Dunbrack, R. L. Defining a new nomenclature for the structures of active and inactive kinases. *Proc. Natl Acad. Sci. USA* **116**, 6818–6827 (2019).
55. Tannous, E. A., Yates, L. A., Zhang, X. & Burgers, P. M. Mechanism of auto-inhibition and activation of Mec1(ATR) checkpoint kinase. *Nat. Struct. Mol. Biol.* **28**, 50–61 (2021).
56. Langer, L. M., Gat, Y., Bonneau, F. & Conti, E. Structure of substrate-bound SMG1-8-9 kinase complex reveals molecular basis for phosphorylation specificity. *eLife* **9**, e57127 (2020).
57. Kuhn, B., Fuchs, J. E., Reutlinger, M., Stahl, M. & Taylor, N. R. Rationalizing tight ligand binding through cooperative interaction networks. *J. Chem. Inf. Model.* **51**, 3180–3198 (2011).
58. Chaplin, A. K. et al. Dimers of DNA-PK create a stage for DNA double-strand break repair. *Nat. Struct. Mol. Biol.* **28**, 13–19 (2021).
59. Armstrong, S. A., Schultz, C. W., Azimi-Sadjadi, A., Brody, J. R. & Pishvaian, M. J. ATM dysfunction in pancreatic adenocarcinoma and associated therapeutic implications. *Mol. Cancer Ther.* **18**, 1899–1908 (2019).

Publisher's note Springer Nature remains neutral with regard to jurisdictional claims in published maps and institutional affiliations.

© The Author(s), under exclusive licence to Springer Nature America, Inc. 2021

Methods

Expression of human ATM. The pCDNA3.1 vector containing the full-length (1–3056) human ATM gene was ordered from GenScript. Human ATM was designed to comprise an N-terminal FLAG tag (MDYKDDDDK) and codons optimized for protein expression in mammalian cells.

DNA required for transfections was obtained using GigaKit (Macherey-Nagel) and eluted in sterile deionized water. Human ATM was expressed in Expi293F cells (Thermo Fisher Scientific, A14527), as described previously[16].

Human ATM purification. Cell pellet from 500 ml of transfected Expi293F culture was resuspended in 50 ml of pre-cooled buffer A (50 mM HEPES (pH 7.5, 23 °C), 150 mM NaCl, 100 mM L-arginine, 5% (vol/vol) glycerol) supplemented with one tablet of EDTA-free protease inhibitor cocktail (Sigma-Aldrich) and 10 U of TURBO DNase (Thermo Fisher Scientific). The cells were gently lysed using a Dounce homogenizer, followed by sonication for 70 s (50% duty cycle, five-output control) on ice. The cell lysate was cleared by centrifugation at 16,000 r.p.m. for 40 min using an SS-34 rotor. All of the following steps were performed at 8 °C. The soluble fraction of the lysate was filtered using 0.45-µm PVDF membrane filters (Merck Millipore), then 3 ml of anti-FLAG affinity gel resin (Sigma-Aldrich) was equilibrated with buffer A. The cleared lysate was added to the equilibrated beads and incubated in a 2.5 cm × 10 cm glass Econo-Column (Bio-Rad) on a rocking platform for 2 h. After removal of the flow-through, the resin was washed with 50 ml of buffer B (50 mM HEPES (pH 7.5, 23 °C), 150 mM NaCl, 5% (vol/vol) glycerol, 0.5 mM DTT), then 5 ml of buffer B supplemented with 2 mM ATP and 5 mM $MgCl_2$ was added to the resin and incubated for 30 min with rocking. The ATP wash was repeated four times. The resin was washed with 50 ml of buffer B. Elution buffer was prepared by diluting 3× FLAG peptide stock solution (5 mg ml^{-1} 3× FLAG peptide in TBS (50 mM Tris-HCl at pH 7.4, 150 mM NaCl)) in buffer B to reach a final peptide concentration of 200 µg ml^{-1}. The resin was gently resuspended in 3 ml of elution buffer and incubated for 30 min while slowly rocking. In total, 5 × 3-ml elution fractions were obtained in this way. All elution fractions were combined and filtered through a 0.2-µm filter (Merck Millipore) before anion exchange chromatography (AEC). AEC was performed on an AKTA Pure system using a 15-ml loop and a MonoQ 5/50 GL column equilibrated in MonoQ-A buffer (50 mM HEPES (pH 7.5, 23 °C), 150 mM NaCl, 5% (vol/vol) glycerol, 2 mM tris(2-carboxyethyl) phosphine (TCEP)). The column was washed with MonoQ-A buffer following sample application and eluted with a NaCl gradient from 150 mM (MonoQ-A buffer) to 1 M (MonoQ-B buffer (50 mM HEPES (pH 7.5, 23 °C), 1 M NaCl, 5% (vol/vol) glycerol, 2 mM TCEP)). Elution fractions of 0.2 ml were collected. Purified protein was stored at 4 °C and used for cryo-EM grid preparation within 48 h of purification.

Cryo-electron microscopy grid preparation. Freshly purified human ATM was diluted in compensation buffer to obtain a protein concentration of 0.26 mg ml^{-1} in 20 mM HEPES (pH 7.5, 23 °C), 150 mM NaCl and 5 mM $MgCl_2$,. The human ATM sample (4 µl) was mixed with 1 µl of 21 µM inhibitor KU-55933 (Sigma-Aldrich) and incubated on ice for at least 5 min. Immediately before plunging, Tween-20 was added to the ATM sample to a final concentration of 0.01%. Grids were prepared using a Leica EM GP plunge freezer (Leica). Tween-20-containing sample (4.5 µl) was deposited onto a plasma-cleaned (GloQube, Quorum) gold grid with a carbon support (Au 200, R2/2, 2 nm C, UltrAufoil). Samples were pre-incubated on the grids for 20 s at 15 °C and 95% humidity and blotted for 2.5 s before plunge-freezing the grid in liquid ethane.

Cryo-electron microscopy data acquisition. Two datasets of ATM-KU-55933 (8,519 and 4,139 micrographs) were acquired on a Titan Krios transmission electron microscope (Thermo Fisher Scientific) operated at 300 kV, with a K2 summit direct electron detector (Gatan) operated in counting mode and an energy filter (Gatan). Data acquisition was automated with the EPU (Thermo Fisher Scientific) software package. Images were recorded at a nominal magnification of ×130,000 (1.059 Å per pixel) with a defocus range of 1.0 µm to 2.8 µm, and total dose of 45 $e^-/Å^2$ over 40 frames. Four datasets of ATM-M4076 (5,287, 1,372, 3,745 and 2,269 micrographs) were acquired using the same set-up as described above. A dataset of ATM-ATPγS containing 5,619 micrographs was collected using the same set-up as described above. Representative micrographs are provided in Supplementary Fig. 7.

Cryo-electron microscopy image processing. Motion correction with MotionCor2 and CTF estimation with CTFFind4 were performed on the fly for all datasets using an in-house-developed pipeline[60,61].

Further processing of ATM-KU-55933 data was carried out using RELION-3.0.7/3.1.0[62]. Particles were picked automatically using a previously obtained low-resolution map of human ATM filtered to 20 Å as a 3D reference (unpublished). A total of 5,333,298 particles were extracted using a box size of 320 × 320 pixels and binned four times to speed up the initial processing. Extracted particles were subjected to a few rounds of 2D classification followed by a selection of 'clean' 2D classes. The resulting 2,679,787 particles were used in 3D classification and another round of 'cleanup' selection was done. The best 3D class with 891,295 particles was selected and used for two rounds of 3D refinement, followed by CTF refinement and Bayesian polishing. A set of polished particles was cleaned by 2D classification. The remaining 826,510 particles were 3D-refined and post-processed with automatic *B*-factor determination. The final map showed an overall resolution of 2.78 Å according to the gold-standard Fourier shell correlation 0.143 criterion (used hereafter unless otherwise stated).

To better resolve the conformational flexibility of the N-terminal HEAT repeat region of ATM, we started by 3D-refining, CTF-refining and Bayesian-polishing all 2,679,787 particles. Polished particles were cleaned by 2D classification and further 3D-refined. The resulting 2,651,173 particles were subjected to a 3D classification, followed by a focused (N-terminal) 3D classification with fixed angles, selectively masking for the N-terminal domains. Masks for the regions of interest were created using UCSF Chimera[63]. Three distinct 3D classes with different N-terminal solenoid confirmation emerged. All three classes were processed individually by focused 3D classification with fixed angles and 3D refinement (for details see the processing scheme in Supplementary Fig. 1). An analogous approach was used to resolve the conformational flexibility of the N-terminal region of M4076- and ATPγS-bound ATM (Extended Data Fig. 8).

To improve the resolution of the N terminus and pincer regions, subtracted maps were prepared. Using the 3D refinement of all 2,679,787 CTF-refined and polished particles, one complete monomer of the ATM dimer and the C-terminal portion of the other were subtracted. Two particle sets were prepared with the pincer region either included or subtracted. The particles were re-centered on the remaining N-terminal density and cropped to 200 × 200 pixels. Maps from the subtracted particles were produced using relion_reconstruct, and used to prepare masks and as references for 3D classifications with local angular searches. Dominant classes appeared containing 1,075,217 particles (excluding pincer) and 1,117,056 particles (including pincer). These classes were refined and post-processed to overall resolutions of 3.06 Å (excluding pincer) and 3.15 Å (including pincer). The 3D classifications with fixed angles were performed using masks for the pincer region and very N-terminal HEAT repeats, and the best classes refined with local searches using the same targeted masks. This resulted in a map of the N-terminal HEAT repeats from 1,035,906 particles to a resolution of 3.10 Å, and a map of the pincer region from 807,127 particles to a resolution of 3.34 Å (Supplementary Fig. 3).

Processing of the ATM-M4076 dataset was continued in CryoSparc by using Topaz for automated particle picking on the motion-corrected micrographs[64,65]. After four rounds of Topaz training and 2D classification cleaning, 455,866 particles were used for ab initio reconstruction and homogeneous refinement. Local refinement masking for the C-terminal half of ATM resulted in a final map with a resolution of 2.99 Å (the processing scheme is depicted in Supplementary Fig. 4).

ATM-ATPγS particles were picked in CryoSparc by using Topaz (as described above) in combination with template-based automated particle picking performed in Relion using a previously obtained human ATM-KU-55933 map filtered to 20 Å as a 3D reference. Particle coordinates were transferred between CryoSPARC and Relion using UCSF pyEM, CryoSparc and Relion picked particles were combined in Relion, removing duplicates, and cleaned by 2D classification. The resulting 709,013 particles were subjected to 3D refinement, CTF refinement and Bayesian polishing. Polished particles were cleaned by 2D classification and the selected 701,857 particles were 3D-refined and 3D-classified using fixed angles, then 690,548 particles from the best 3D class were 3D-refined, masking for the C-terminal half and using local search angles, and post-processed with automatic *B* factor determination (Supplementary Fig. 5). The final map showed an overall resolution of 2.78 Å (Supplementary Fig. 6).

Some maps were filtered using LAFTER in the CCPEM interface[66,67]. Maps with different origins were aligned and resampled using UCSF Chimera where appropriate. Phenix combine-focused-maps was used to generate an overall map of ATM-KU-55933, combining the highest-resolution components of each focused map[63,68].

Model building and refinement. An existing model of *Hs*ATM (PDB 6K9L) was rigid-body-fitted to the ATM-KU-55933 map density using UCSF Chimera. Model building and refinement were performed using Coot[63,69]. The existing *Hs*ATM model was used as a template for building of the C-terminal region, from which sequences were fitted, corrected and extended. However, all existing models were shown to be incorrect for the N-terminal and pincer regions, so these regions were built manually, assisted by secondary-structure predictions from JPred 4[70]. The multiple maps with different focal positions were used to provide the highest resolution at each point in the protein sequence and ensure the model was built in the correct register, before fitting to individual maps. LAFTER filtered maps provided the clearest densities for model building[66]. Loops with poor density were only built where well-defined anchor points and traceable density limited positioning errors. Some side chains were omitted in poorly resolved loops.

For modeling the lower-resolution N-terminal regions of the overall maps, the spiral and hinge models from the high-resolution subtracted maps were rigid-body-fitted into the density, followed by real-space refinement with local restraints. All structures were refined by iterative rounds of model building with Coot and refinement using Phenix real-space refine[71]. Models were validated using Phenix comprehensive validation (cryo-EM)[68]. Figures were generated using UCSF ChimeraX[72].

Sequence alignments of the C-terminal 236 amino acids of human ATM with other PIKK family members and ATM orthologs were carried out using the program clustalW2.

Human CtIP fragment expression and purification for kinase assays. A truncated version of human CtIP consisting of the C-terminal residues 650–897 and the phosphomimetic mutant T847E was cloned into a pET47b vector together with an N-terminal 6× His tag, followed by an MBP tag and an HRV3C protease cleavage site. Transfected *Escherichia coli* Rosetta cells (Novagen) were cultured in Turbo medium at 37 °C, 140 r.p.m. until reaching an optical density at 600 nm of ~1.2. Recombinant protein expression was induced with 0.2 mM IPTG and carried out at 18 °C, 140 r.p.m. for 16 h. Cells were collected by centrifugation at 4,000*g*, 10 min, 4 °C. The cell pellet from a 2-l culture was resuspended in 50 ml of pre-cooled lysis buffer (50 mM HEPES, pH 7.5, 300 mM NaCl, 10% (vol/vol) glycerol, 0.5 mM TCEP, 10 μM $ZnCl_2$, 10 mM imidazole, 0.5% NP-40) supplemented with one tablet of EDTA-free protease inhibitor cocktail (Sigma-Aldrich). Lysis was performed by three rounds of sonication for 5 min each (50% duty cycle, eight-output control) on ice. The cell lysate was cleared by centrifugation at 17,000 r.p.m. for 1 h using an SS-34 rotor. The supernatant was further filtered using 0.45-μm PVDF membrane filters (MERCK Millipore). All of the following steps were performed at 8 °C. A 10 ml volume of Ni-NTA beads (Machery Nagel), equilibrated with buffer A (50 mM HEPES pH 7.5, 300 mM NaCl, 10% (vol/vol) glycerol, 0.5 mM TCEP, 10 μM $ZnCl_2$, 10 mM imidazole), was added to the cleared lysate and incubated in a 2.5 cm × 10 cm glass Econo-Column (Bio-Rad) on a rocking platform for 1 h. The flow-through was removed and the beads washed three times with buffer A, twice with 5% buffer B (buffer A, containing 500 mM imidazole), once with 10% buffer B and once with 15% buffer B. CtIP was eluted four times with 50% buffer B. The fractions were pooled and dialyzed against buffer containing 50 mM HEPES pH 7.5, 150 mM NaCl, 10% (vol/vol) glycerol, 0.5 mM TCEP, 10 μM $ZnCl_2$ and 5 mM imidazole overnight after self-made PreScission protease was added. The dialyzed sample was applied to the same amount of Ni-NTA beads, pre-equilibrated with dialysis buffer and incubated while rotating for 1 h. The flow-through, containing cleaved CtIP, was collected and excess protease removed with a glutathione bead (Thermo Scientific) pulldown. After concentrating the sample using a centrifugal filter (30-kDa molecular weight cutoff, Amicon) to ~8 mg ml^{-1}, 500 μl was injected onto a Superdex 75 10/300 column (GE Healthcare) connected to an ÄKTA Pure system, pre-equilibrated in SEC buffer (20 mM HEPES, pH 7.5, 150 mM NaCl, 10 μM $ZnCl_2$, 0.5 mM TCEP). CtIP was eluted at 1.5 mg ml^{-1} with some minor degradation products, aliquoted, flash-frozen in liquid nitrogen and stored at −80 °C.

Gel-based kinase assay. The kinase activity of freshly purified full-length human ATM (50 mM HEPES (pH 7.5, 23 °C), 160 mM NaCl, 5% (vol/vol) glycerol, 2 mM TCEP) was assessed using human CtIP peptide substrate at a final concentration of 2.4 μM. The final concentration of human ATM used was 0.35 μM. The reactions were carried out in buffer containing 20 mM HEPES (pH 7.5, 23 °C), 150 mM NaCl, 5 mM $MgCl_2$, 1 mM $MnCl_2$, 0.01 mM $ZnCl_2$, 5% (vol/vol) glycerol and 0.5 mM TCEP at a final volume of 15 μl. The ATM-specific inhibitors KU-55933 (Sigma-Aldrich) and M4076 (Merck) were dissolved in dimethyl sulfoxide and used in a final concentration of 10 μM. The reactions were started by the addition of 1 mM adenosine 5′-triphosphate (ATP) followed by 30-min incubation at 30 °C. The reactions were stopped by adding 4× sodium dodecyl sulfate polyacrylamide gel electrophoresis (SDS–PAGE) loading buffer. An aliquot of 15 μl from each reaction was loaded on a 4–20% RunBlue SDS gel (Expedion) and resolved by SDS–PAGE. The gel was stained using Pro-Q Diamond Phosphoprotein gel stain (Thermo Fisher Scientific) and analyzed using a Typhoon FLA 9000 laser scanner (GE Healthcare). In addition, gel was stained with Coomassie (InstantBlue, Expedion) to assure consistent sample loading.

Thermal shift assay. 1,10-Phenanthroline, *N,N,N′,N′*-tetrakis-(2-pyridylmethyl) ethylenediamine (TPEN) and EGTA (Sigma-Aldrich) were prepared by dissolving appropriate amounts of chelating agents in ethanol to reach 500 mM concentration, then further diluted with MonoQ-A buffer to generate 100 mM (100×) stock of chelating agents. The 100× stocks were further diluted with MonoQ-A buffer to 10× concentration before mixing chelating agents with protein.

A volume of 9 μl of freshly purified full-length human ATM at 0.6 μM concentration was mixed with 1 μl of 10× (10 mM) chelating agents. In the control reaction, the same amount of ATM was mixed with 1 μl of buffer prepared in the same way as chelating agents. Following a 10-min incubation of ATM with chelating agents, changes in the intrinsic fluorescence (at 330 nm and 350 nm) with respect to increasing temperature were measured using a Tycho NT.6 system (NanoTemper). The measurements were performed in standard capillaries (NanoTemper).

Recombinant proteins for biochemical kinase activity assays. The following recombinant proteins used in the biochemical kinase activity assays (except Fig. 1a and Extended Data Figs. 1c and 5a) were purchased from Eurofins: human full-length FLAG-tagged ATM (GenBank ID NM_000051; item no. 14-933-K, lot no. 2447914) expressed in a mammalian cell line; human full-length FLAG-tagged ATR (GenBank ID NM_001184.3) and human full-length ATRIP (GenBank ID AF451323.1) co-expressed in a mammalian cell line (item no. 14-953M, lot no. D14HP005NB); N-terminal FLAG-tagged human mTOR amino acids 1362-end (GenBank ID NM_004958.2; item nos. 14-769, 14-769-K and 14-769M, lot no. 1607837) expressed by baculovirus in Sf21 insect cells; PI3K p110α/p85α (complex of N-terminal 6His-tagged full-length p110α and untagged full-length p85α; GenBank U79143(PI3Ka)/GenBank XM_043865(p85a)) (item nos. 14-602, 14-602-K and 14-602M, lot no. WAB0319), expressed by baculovirus in Sf21 insect cells; PI3K p110β/p85α (complex of N-terminal 6His-tagged full-length p110β and untagged full-length p85α; GenBank NM_006219(PI3Kb)/GenBank XM_043865(p85a)) (item nos. 14-603, 14-603-K and 14-603M, lot no. WAD0867), expressed by baculovirus in Sf21 insect cells; PI3K p120γ (N-terminal 6His-tagged full-length PI3-kinase (p120γ); GenBank AF327656) (item nos. 14-558, 14-558-K and 14-558M, lot no. 2298365) and PI3K p110δ/p85α (complex of N-terminal 6His-tagged full-length p110δ and untagged full-length p85α; GenBank NM_005026(PI3Kδ)/GenBank XM_043865(p85α)) (item nos. 14-604, 14-604-K and 14-604M, lot no. WAE0320), expressed by baculovirus in Sf21 insect cells.

DNA-PK was prepared from HeLa nuclear cell extract (Cilbiotech) by Merck KGaA, which was diluted to a final concentration of 40 mM KCl and applied to ion exchange chromatography (AIEX Fractogel DEAE) in buffer A (40 mM KCl, 20 mM HEPES, 1 mM EDTA, 1 mM EGTA, 1 mM DTT, 10% glycerol, 0.02% Tween-20, pH 7.9). Increasing KCl concentrations were applied for a stepwise elution. Fractionation of active DNA-PK was achieved at 300 mM KCl. All steps were performed at 4 °C. Aliquots were frozen in liquid nitrogen and stored at −80 °C. Western blot analysis was used to confirm the DNA-PK catalytic subunit, Ku85 and Ku70. The final protein concentration was determined by Bradford assay (details are provided in the Supplementary Information).

Time-resolved FRET-based ATM kinase assay. The enzymatic ATM assay was carried out as a time-resolved FRET (TR-FRET; homogeneous time-resolved fluorescence (HTRF), Cisbio Bioassays) based 384-well assay. In the first step, purified human recombinant ATM (Eurofins) was incubated in assay buffer for 15 min with the ATM inhibitor at various concentrations and without test substance (as a negative or neutral control). The assay buffer comprised 25 mM HEPES pH 8.0, 10 mM $Mg(CH_3COO)_2$, 1 mM $MnCl_2$, 0.1% BSA, 0.01% Brij 35 and 5 mM DTT. The inhibitor solutions were dispensed into the microtiter plates using an ECHO 555 handler (Labcyte). In the second step, purified human recombinant c-myc-labeled p53 (human p53, full length, GenBank ID BC003596, expressed in Sf21 insect cells, Eurofins) and ATP were added, and the reaction mixture was incubated at 22 °C for 35 min. The final concentrations in the assay during incubation of the reaction mixture were 0.3 nM ATM, 75 nM p53 and 10 μM ATP (final reaction volume of 5 μl). The enzymatic reaction was stopped by the addition of EDTA. The formation of phosphorylated p53 as the result of the ATM-mediated reaction in the presence of ATP was detected via specific antibodies (labeled with the fluorophore europium (Eu) as donor and d2 as acceptor (Cisbio Bioassays)), which enabled FRET. A volume of 2 μl of antibody-containing stop solution (12.5 mM HEPES pH 8.0, 125 mM EDTA, 30 mM NaCl, 300 mM KF, 0.006% Tween-20, 0.005% Brij 35, 0.21 nM anti-phospho-p53(ser15)-Eu antibody and 15 nM anti-cmyc-d2 antibody) was added to the reaction mixture. After 2 h of incubation for signal development, the plates were analyzed in a plate reader (EnVision, PerkinElmer or Pherastar, BMG Labtech) using the TRF mode (and with laser excitation). After excitation of the donor Eu at a wavelength of 340 nm, the emitted fluorescence light both of the acceptor d2 at 665 nm and of the donor Eu at 615 nm was measured. The amount of phosphorylated p53 was directly proportional to the quotient of the amounts of light emitted, that is, the relative fluorescence units at 665 nm and 615 nm. The measurement data were processed by means of GraphPad Prism software. IC_{50} determinations were carried out by fitting a response curve to the data points by means of nonlinear regression analysis.

ATR–ATRIP kinase assay. The ATR–ATRIP enzymatic assay was performed as a TR-FRET (HTRF, Cisbio Bioassays) based 384-well assay. In a first step, purified human recombinant ATR–ATRIP (Eurofins) was incubated in assay buffer for 15 min at 22 °C with inhibitor at different concentrations or without test compound (as a negative control). The assay buffer contained 25 mM HEPES pH 8.0, 10 mM $Mg(CH_3COO)_2$, 1 mM $MnCl_2$, 0.1% BSA, 0.01% Brij 35 and 5 mM DTT. An ECHO 555 handler (Labcyte) was used to dispense compound solutions. In a second step, purified human recombinant cmyc-tagged p53 (human p53, full length, GenBank ID BC003596, expressed in Sf21 insect cells, Eurofins) and ATP were added, and the reaction mixture was incubated for 25–35 min, typically 25 min, at 22 °C. The pharmacologically relevant assay volume was 5 μl. The final concentrations in the assay during incubation of the reaction mixture were 0.3–0.5 nM (typically 0.3 nM) ATR–ATRIP, 50 nM p53 and 0.5 μM ATP. The enzymatic reaction was stopped by the addition of EDTA. The generation of phosphorylated p53 as a result of the ATR-mediated reaction in the presence of ATP was detected by using specific antibodies (labeled with the fluorophores Eu as donor and d2 as acceptor (Cisbio Bioassays)), enabling FRET. For this purpose, 2 μl of antibody-containing stop solution (12.5 mM HEPES pH 8.0, 125 mM EDTA, 30 mM NaCl, 300 mM KF, 0.006% Tween-20, 0.005% Brij 35, 0.21 nM anti-phospho-p53(Ser15)-Eu antibody,

15 nM anti-cmyc-d2 antibody) were added to the reaction mixture. Following signal development for 2 h, the plates were analyzed in an EnVision (PerkinElmer) microplate reader using the TRF mode with laser excitation. Following excitation of the donor Eu at 340 nm, the emitted fluorescence light of the acceptor d2 at 665 nm as well as from the donor Eu at 615 nm was measured. The amount of phosphorylated p53 was directly proportional to the ratio of the amounts of emitted light, that is, the ratio of the relative fluorescence units at 665 nm and 615 nm. Data were processed using GraphPad Prism software. IC_{50} values were determined in the usual manner by fitting a dose–response curve to the data points using nonlinear regression analysis.

DNA-PK assay. The DNA-PK kinase assay was performed as an HTRF (Cisbio Bioassays) based 384-well assay. In a first step, DNA-PK protein complex from HeLa nuclear extract pre-incubated with DNA from calf thymus and staurosporine was incubated with or without test compound for 15–20 min at 22 °C. After addition of the STK-substrate 1-biotin (Cisbio Bioassays) and Mg-ATP, the reaction mixture was incubated for 60–70 min (depending on the activity of the DNA-PK protein complex) at 22 °C. An ECHO 555 handler (Labcyte) or a Biomek FX handler (Beckman Coulter) was used for dispensing of compound solutions. The assay buffer consisted of 25 mM HEPES pH 7.4, 11 mM $MgCl_2$, 80 mM KCl, 0.45 mM EDTA and 0.5 mM EGTA, and contained 1 mM DTT, 0.17% BSA and 0.01% Tween-20. The pharmacologically relevant volume was 5 or 5.5 µl. The final concentrations in the assay during incubation of the reaction mixture were 100–235 ng DNA-PK protein complex per well (depending on the activity of the DNA-PK protein complex), 1 µM STK substrate 1-biotin (Cisbio Bioassays), 10 or 20 µM Mg-ATP, 80 ng DNA from calf thymus per well and 1 µM staurosporine. The enzymatic reaction was stopped by the addition of EDTA. The generation of phosphorylated STK-substrate 1-biotin as a result of the DNA-PK-mediated reaction was detected via a specific anti-phospho STK-antibody (Cisbio Bioassays) labeled with Eu as donor and streptavidin labeled with XL665 (Cisbio Bioassays) as acceptor, allowing FRET. For this purpose, 4 µl of antibody- and streptavidin-containing stop solution (50 mM HEPES pH 7.0, 800 mM KF, 20 mM EDTA, 0.1% BSA, 0.179 or 8.95 nM anti-phospho-STK antibody, 160 or 200 nM streptavidin-XL665) were added to the reaction mixture. Following signal development for 1 h, the plates were analyzed on a Rubystar or Pherastar (BMG Labtech) or on an Ultra Evolution (Tecan) microplate reader. The amount of phosphorylated substrate was directly proportional to the ratio of fluorescence units (excitation wavelength of 337 or 320 nm) at the emission wavelengths of 665 nm (phosphopeptide-sensitive wavelength/emission of XL665) to fluorescence units at 620 nm (reference wavelength Eu). IC_{50} values were calculated using GraphPad Prism software[73].

mTOR kinase assay. The DiscoveRx KINOMEscan assay (Eurofins) was used for mTOR selectivity profiling of inhibitors. Recombinant human mTOR protein (Eurofins) was incubated in assay buffer containing 50 mM HEPES pH 7.5, 1 mM EGTA, 0.01% Tween-20, 2 mg ml^{-1} substrate, 3 mM $MnCl_2$ and [γ-^{33}P-ATP] (specific activity ~500 c.p.m. $pmol^{-1}$, [ATP] = 70 µM in the assay). The reaction was initiated by the addition of Mn-ATP solution. The reaction was stopped by the addition of 3% phosphoric acid after 40-min incubation at room temperature. A volume of 10 µl of reaction solution was pipetted on P30 filters and washed three times for 5 min in 75 mM phosphoric acid and once in methanol, dried, and measured by scintillation counting. IC_{50} values were calculated using GraphPad Prism software.

PI3K HTRF-based assay. The DiscoveRx KINOMEscan assay (Eurofins) was used for PI3K selectivity profiling of inhibitors. The following human recombinant proteins expressed by baculovirus in Sf21 insect cells (Eurofins) were used: PI3K p110α/p85α, PI3K p110β/p85α, PI3K p120γ and PI3K p110δ/p85α. The following HTRF-based assay protocol was used for all PI3K isoforms with ATP concentrations at the respective K_m values (PI3K p110α/p85α, ATP K_m = 193 µM, [ATP] = 200 µM in assay; PI3K p110β/p85α ATP K_m = 235 µM, [ATP] = 200 µM in assay; PI3K p120γ ATP K_m = 109 µM, [ATP] = 100 µM in assay; p110δ/p85α ATP K_m = 321 µM, [ATP] = 200 µM in assay). Recombinant human PI3K protein was incubated in assay buffer containing 10 µM phosphatidylinositol-4,5-bisphosphate. The reaction was initiated by the addition of a Mg-ATP solution at K_m concentration (see above). After incubation for 30 min at room temperature, the reaction was stopped by the addition of EDTA and biotinylated phosphatidylinositol-3,4,5-trisphosphate. Finally, detection buffer was added, containing Eu-labeled anti-GST monoclonal antibody, GST-tagged GRP1 PH domain and streptavidin allophycocyanin. The plate was then read in time-resolved fluorescence mode and the HTRF signal was determined according to the formula HTRF = 10,000 × (Em 665 nm/Em 620 nm). Mg-ATP, magnesium 5′-*O*-[hydroxy[[(hydroxyphosphinato)oxy]-phosphinato]-oxy)-phosphoryl] adenosine; $MgCl_2$, magnesium dichloride; EGTA, ethylenglycole-bis(aminoeth ylether)-*N*,*N*,*N*′,*N*′-tetra acetic acid; Tween-20, Polysorbate 20.IC_{50} values were calculated using GraphPad Prism software.

In vitro kinase selectivity profiling assay for M4076. The Reaction Biology Corporation (RBC) HotSpot kinase profiling service (http://www.reactionbiology.com) was used for in vitro selectivity profiling of M4076 in single-dose singlicate mode at a concentration of 1 µM against 583 kinases. Dose–response curves of M4076 were determined for 10 kinases and their mutants (22 kinases in total), which showed activity values below 50% tested at 1 µM M4076 in the in vitro kinase selectivity profile against 583 kinases. For IC_{50} determination, M4076 was tested in duplicate in a 10-dose IC_{50} mode with three-fold serial dilution starting at 10 µM. Staurosporine was used as control compound and tested in 10-dose IC_{50} mode with four-fold serial dilution starting at 20 µM. Reactions were carried out at K_m ATP concentrations of individual kinases according to the RBC K_m binning structure. Kinases inhibitory activities were assessed by the HotSpot assay platform, which contained specific kinase/substrate pairs along with the required cofactors. Base reaction buffer: 20 mM HEPES (pH 7.5), 10 mM $MgCl_2$, 1 mM EGTA, 0.02% Brij 35, 0.02 mg ml^{-1} BSA, 0.1 mM Na_3VO_4, 2 mM DTT and 1% DMSO. M4076 was dissolved in 100% DMSO to a specific concentration. The serial dilution was conducted by Integra Viaflo Assist in DMSO. The reaction mixture containing the examined compound M4076 and ^{33}P-ATP (specific activity 0.01 µCi $µl^{-1}$ final) was incubated at room temperature for 2 h, and radioactivity was detected by the filter-binding method. In detail, reactions were spotted onto P81 ion exchange paper (Whatman cat. no. 3698-915) and filters were extensively washed in 0.75% phosphoric acid. Kinase activity data were expressed as the percent remaining kinase activity in test samples compared to vehicle (dimethyl sulfoxide) reactions. IC_{50} values and curve fits were obtained using GraphPad Prism software.

Cellular pCHK2 Thr68 Luminex. Cellular levels of pCHK2 were detected in a Luminex-based assay format. HCT116 cells (ATCC CCL-247, authenticated by STR analysis) were seeded in medium with 10% fetal calf serum (FCS) in 12-well plates. The next day, the medium was removed and 100 µl of fresh medium including a serial dilution of inhibitor M4076 was added per well 1 h prior to the irradiation of 2 Gy by the CellRad irradiator. The irradiation was performed by adjusting the tube voltage to 120 kV_p; 5 mA and positioning the plates inside circle 2 at plate height position 2. A copper filter was used to reduce the intensity of particular wavelengths from the beam. At 1 h after irradiation, the cells were washed once with PBS, and cell lysates were prepared by using HGNT lysis buffer (20 mM HEPES pH 7.4, 150 mM NaCl, 2 mM EDTA, 25 mM NaF, 10% glycerol and 1% Triton X-100; plus 1% phosphatase inhibitor Cocktail Set II and 0.2% protease inhibitor Cocktail Set III) and analyzed for the level of pCHK2 Thr68 applying a Luminex-based assay. After adding the diluted bead suspension (3,000 beads in BR (Roche 11112589001 + 0.1% Tween)) with coupled antibodies against total CHK2 (Chk2 (D9C6) XP rabbit mAb; Cell Signaling Technology cat. no. 6334BF) to 25 µg of total protein in HGNT, the plate was incubated overnight at 4 °C. The beads were washed three times with TBST (Pierce/Thermo 28358 + 0.05% Tween) and 25 µl of BR as well as 25 µl of antibody dilution of the detection antibody coupled to biotin were added in BR (tCHK2: Chk2 (1C12) mouse mAb; Cell Signaling Technology cat. no. 3440BF, pCHK2: pChk2 (Thr68) (C13C1) rabbit mAb; Cell Signaling Technology cat. no. 2197BF, final concentration 1.5 µg ml^{-1}). After 1 h of incubation at room temperature, the beads were washed again with TBST and 25 µl BR and the streptavidin-phycoerythrin dilution (25 µl, Moss cat. no. 001NB, 1:1,000 diluted in BR) were added for 45 min at room temperature. After washing and adding 100 µl of BR, the probes were analyzed in a Magpix instrument (Thermo Fisher Scientific) following the instruction manual. The instrument settings were as follows: sample volume, 35 µl; count, 50; unit, MFI. To control the Luminex assay, different concentrations of recombinant CHK2 protein (R&D cat. no. 1358-KS) were used as standard and were analyzed in parallel. After background correction, the signals for the phosphorylated proteins were normalized to signals of the total protein. Basal levels were set to 0% and irradiated samples without compound were set to 100%. Samples were measured in singlicate and the experiment was repeated three times. IC_{50} values were calculated using GraphPad Prism software.

Cellular pCHK2 Thr68 enzyme-linked immunosorbent assay. HCT116 cells (ATCC CCL-247) were seeded in 100 µl of culture medium (MEM Alpha, with 10% FCS) in the range of 5×10^4 cells per well in 96-well plates to achieve a defined cell density. The plates were then incubated for 24 h at 37 °C and 10% CO_2. The next day, the medium was removed and 100 µl of fresh medium containing KU-55933 inhibitor in various concentrations (10 nM to 25 µM) plus a constant concentration of 10 µM bleomycin and without test substance as DMSO and bleomycin controls was added per well and incubation was continued for a further 6 h. The medium was removed and cells were lysed using HGNT lysis buffer (20 mM HEPES pH 7.4, 150 mM NaCl, 2 mM EDTA, 25 mM NaF, 10% glycerol and 1% Triton X-100; plus 1% phosphatase inhibitor Cocktail Set II and 0.2% protease inhibitor Cocktail Set III) and incubated at 4 °C overnight. Levels of pCHK2 were determined by ELISA (all reagents from Cell Signaling, cat. no. 7037; PathScan kit) with capture antibody specific for pCHK2 (Thr68) and detection antibody against total CHK2 protein. Anti-mouse immunoglobulin-G, horseradish peroxidase-linked antibody was then used to recognize the bound detection antibody. Horseradish peroxidase substrate (TMB) was added to develop color. The magnitude of the absorbance for the developed color is proportional to the amount of CHK2 phosphorylated at Thr68. Absorbance was measured at 450 nm for 4 s using a Tecan Sunrise reader. IC_{50} values were calculated using GraphPad Prism software.

Reporting Summary. Further information on research design is available in the Nature Research Reporting Summary linked to this Article.

Data availability

The 3D cryo-EM density maps reported in this Article have been deposited in the EMD under accession nos. EMD-12352 (ATM-ATPyS), EMD-12350 (ATM-M4076), EMD-12343 (ATM-KU-55933, Kinase), EMD-12347 (ATM-KU-55933, Spiral), EMD-12345 (ATM-KU-55933, Pincer) and EMD-12346 (ATM-KU-55933, Spiral–Pincer). The corresponding models have been deposited in the Protein Data Bank under IDs 7NI6 (ATM-ATPyS), 7NI4 (ATM-M4076) and 7NI5 (ATM-KU-55933). Raw micrographs are archived at the LRZ of the Bavarian Academy of Science and Humanities and can be accessed for legitimate research purposes upon reasonable request to K.P.H. (hopfner@genzentrum.lmu.de). Any requests for additional data by qualified scientific and medical researchers for legitimate research purposes will be subject to the Merck KGaA, Darmstadt, Germany Data Sharing Policy. All requests should be submitted in writing to the Merck KGaA, Darmstadt, Germany data-sharing portal (https://www.emdgroup.com/en/research/our-approach-to-research-and-development/healthcare/clinical-trials/commitment-responsible-data-sharing.html). When Merck KGaA, Darmstadt, Germany has a co-research, co-development, or co-marketing or co-promotion agreement, or when the product has been out-licensed, the responsibility for disclosure might be dependent on the agreement between parties. Under these circumstances, Merck KGaA, Darmstadt, Germany, will endeavor to gain agreement to share data in response to requests. Source data are provided with this paper.

References

60. Zheng, S. Q. et al. MotionCor2: anisotropic correction of beam-induced motion for improved cryo-electron microscopy. *Nat. Methods* **14**, 331–332 (2017).
61. Rohou, A. & Grigorieff, N. CTFFIND4: fast and accurate defocus estimation from electron micrographs. *J. Struct. Biol.* **192**, 216–221 (2015).
62. Zivanov, J. et al. New tools for automated high-resolution cryo-EM structure determination in RELION-3. *eLife* **7**, e42166 (2018).
63. Pettersen, E. F. et al. UCSF Chimera—a visualization system for exploratory research and analysis. *J. Comput. Chem.* **25**, 1605–1612 (2004).
64. Punjani, A., Rubinstein, J. L., Fleet, D. J. & Brubaker, M. A. cryoSPARC: algorithms for rapid unsupervised cryo-EM structure determination. *Nat. Methods* **14**, 290–296 (2017).
65. Bepler, T. et al. Positive-unlabeled convolutional neural networks for particle picking in cryo-electron micrographs. *Nat. Methods* **16**, 1153–1160 (2019).
66. Ramlaul, K., Palmer, C. M. & Aylett, C. H. S. A local agreement filtering algorithm for transmission EM reconstructions. *J. Struct. Biol.* **205**, 30–40 (2019).
67. Wood, C. et al. Collaborative computational project for electron cryo-microscopy. *Acta Crystallogr. D Biol. Crystallogr.* **71**, 123–126 (2015).
68. Liebschner, D. et al. Macromolecular structure determination using X-rays, neutrons and electrons: recent developments in Phenix. *Acta Crystallogr. D Struct. Biol.* **75**, 861–877 (2019).
69. Emsley, P. & Cowtan, K. Coot: model-building tools for molecular graphics. *Acta Crystallogr. D Biol. Crystallogr.* **60**, 2126–2132 (2004).
70. Drozdetskiy, A., Cole, C., Procter, J. & Barton, G. J. JPred4: a protein secondary structure prediction server. *Nucleic Acids Res.* **43**, W389–W394 (2015).
71. Afonine, P. V. et al. Real-space refinement in PHENIX for cryo-EM and crystallography. *Acta Crystallogr. D Struct. Biol.* **74**, 531–544 (2018).
72. Pettersen, E. F. et al. UCSF ChimeraX: structure visualization for researchers, educators and developers. *Protein Sci.* **30**, 70–82 (2020).
73. Kashishian, A. et al. DNA-dependent protein kinase inhibitors as drug candidates for the treatment of cancer. *Mol. Cancer Ther.* **2**, 1257–1264 (2003).

Acknowledgements

EM data were collected at the Cryo-EM Core Facility of the Gene Center, Department of Biochemistry, LMU, Munich. B. Kessler, a technician at the Gene Center, LMU, provided support with cloning and protein purification. We are grateful for support from B. Blume and H. Dahmen, both employees of Merck KGaA, Darmstadt, Germany, for providing cellular pCHK2 results. Funding was provided by the Deutsche Forschungsgemeinschaft (CRC1054 to K.L.; CRC1361, CRC1064, Gottfried Wilhelm Leibniz-Prize and GRK1721 to K.P.H.) and a PhD fellowship from Boehringer Ingelheim Fonds (BIF) to E.v.d.L. This research was supported by the healthcare business of Merck KGaA, Darmstadt, Germany (CrossRef Funder ID 10.13039/100009945), which provided solid material of inhibitor M4076, free of charge.

Author contributions

J.D.B., K.S., M.R., A.A. and E.v.d.L. were involved in protein production and kinase assays. K.S., M.R., K.L. and J.D.B. carried out structural studies. T.F. was the project leader and principal inventor of M4076 at Merck KGaA, Darmstadt, Germany. U.G. was involved in the structure-based design of M4076 and cryo-EM structural refinement efforts. T.F. and U.P. contributed biochemical assay and kinase selectivity results and graphs. Together with K.L., K.S., M.R., J.D.B., T.F. and U.G. contributed to manuscript preparation. K.P.H. and all authors were involved in the interpretation of data, final manuscript preparation and approval.

Competing interests

K.S., M.R., K.L., J.D.B., E.v.d.L. and K.-P.H. declare no competing interests. A.A. contributed as an employee at the Gene Center, Department of Biochemistry, LMU at the time of the study and is currently an employee of Proteros Biostructures. U.G., T.F. and U.P. are employees of Merck KGaA, Darmstadt, Germany. Proteros Biostructures was contracted by Merck KGaA, Darmstadt, Germany, to determine the cryo-EM structure of ATM in complex with M4076.

Additional information

Extended data is available for this paper at https://doi.org/10.1038/s41594-021-00654-x.

Supplementary information The online version contains supplementary material available at https://doi.org/10.1038/s41594-021-00654-x.

Correspondence and requests for materials should be addressed to K. Lammens or K. P. Hopfner.

Peer reveiw information *Nature Structural & Molecular Biology* thanks Xiaodong Zhang and the other, anonymous, reviewer(s) for their contribution to the peer review of this work. Peer reviewer reports are available. Anke Sparmann and Beth Moorefield were the primary editors on this article and managed its editorial process and peer review in collaboration with the rest of the editorial team.

Reprints and permissions information is available at www.nature.com/reprints.

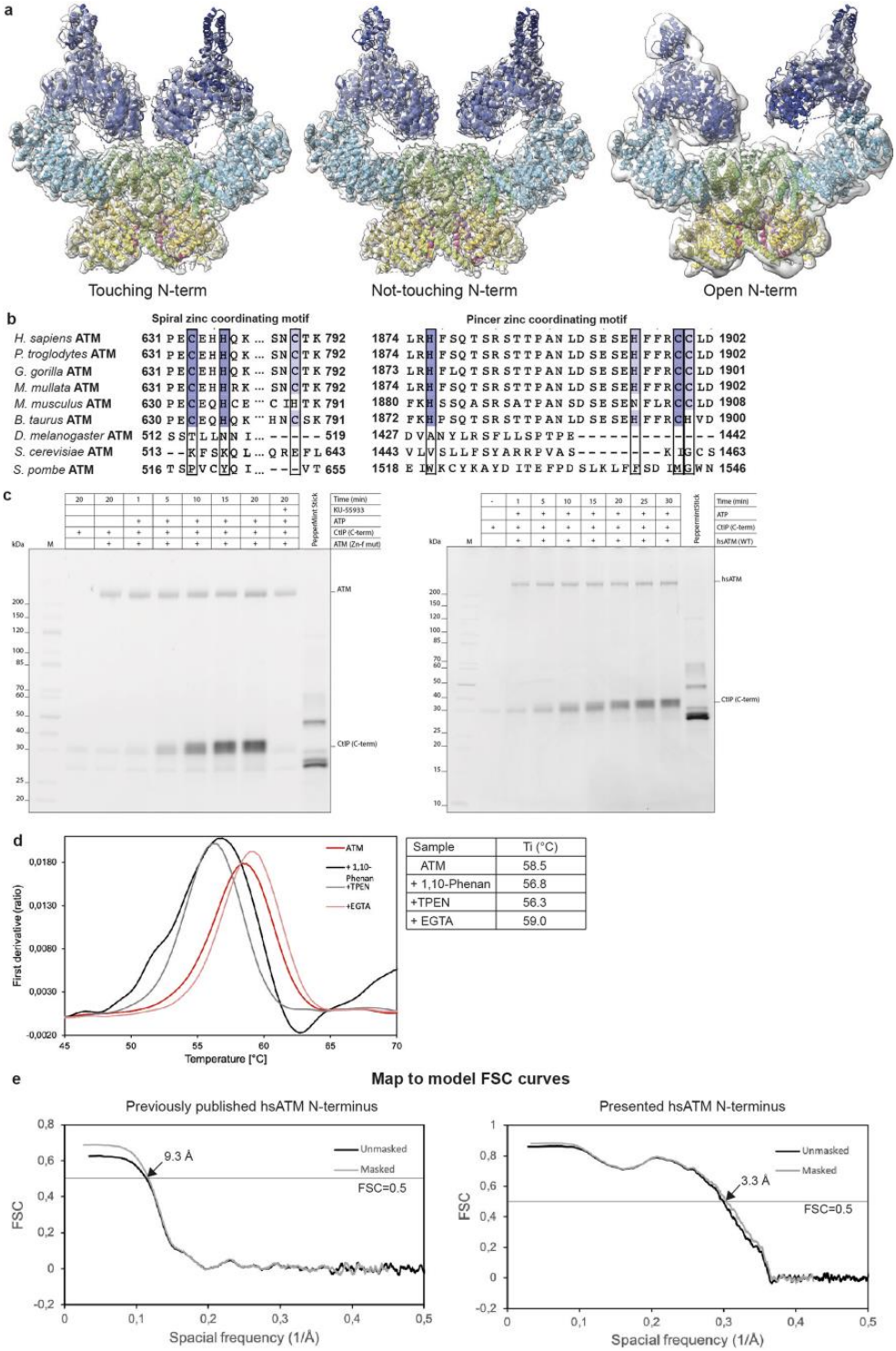

Extended Data Fig. 1 | See next page for caption.

Extended Data Fig. 1 | Features of the N-terminal Spiral domain of human ATM. (**a**) Cryo-EM density maps and models representing three conformational states of N-terminal Spiral-Pincer domains. Left: N-terminal Spiral domains are touching. Middle: N-terminal Spiral domains are not touching. Right: One N-terminal Spiral domain is resolved, the other one is more flexible. (**b**) Sequence alignment of zinc-binding motifs of ATM from different species. ATM residues involved in zinc coordination are highlighted and coloured by conservation. (**c**) Kinase activity time-course of zinc-binding motif mutant (C1899A, C1900A, left) and WT (right) ATM. Kinase activity on CtIP C-terminus (650–897, phosphomimic mutation T847E) visualized by phosphoprotein SDS-PAGE staining. Uncropeed gel image is available in Source Data: Extended Data Fig. 1. (**d**)Effects of chelating agents on the thermal stability of ATM. 1,10-phenanthroline (black) and TPEN (grey) are more specific to Zn2+. ATM only (red) and EGTA (pink) were used as controls. (**e**) Comparison of map to model FSC curves of previously published Spiral (PDB ID: 5NP0) and here presented Spiral domain model.

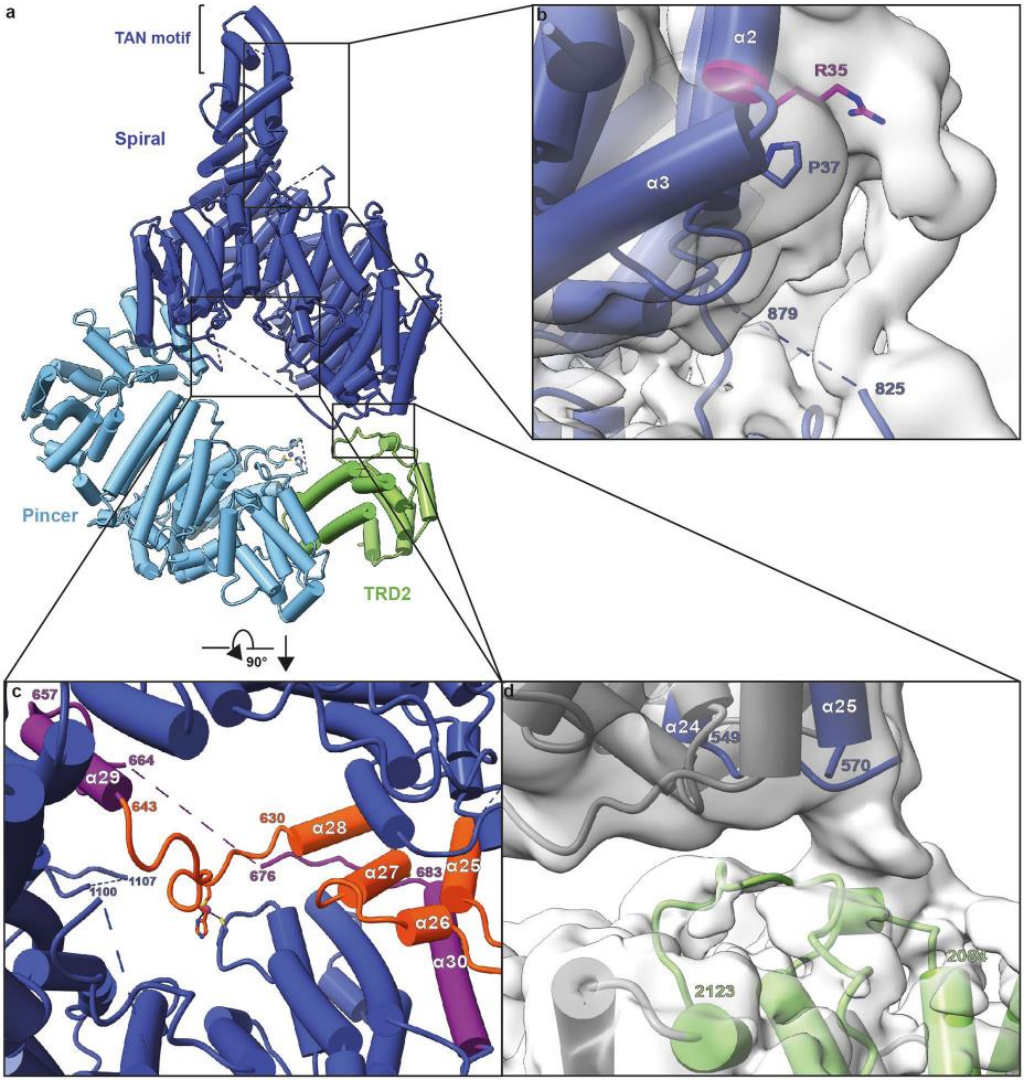

Extended Data Fig. 2 | N-terminal alpha-solenoid structure of human ATM. (**a**) Overview of organization of N-terminal spiral, pincer and TRD2 domains, helices depicted as cylinders. TAN motif labelled. (**b**) Interaction between unstructured loop 825–879 and R35 (helix 2). Density map contoured at 0.0034 and R35 colored in magenta. (**c**)Top view of spiral solenoid ring. Helices 25–28 and ring-crossing loop (630–643) colored in orange. Helices 29–30 and partially resolved loop (657–683) colored in purple. (**d**) Interaction between Spiral loop (549–570) joining helices 24 and 25 (blue), and TRD2 loops 2084–2092 and 2107–2123 (green). Density map contoured at 0.0032.

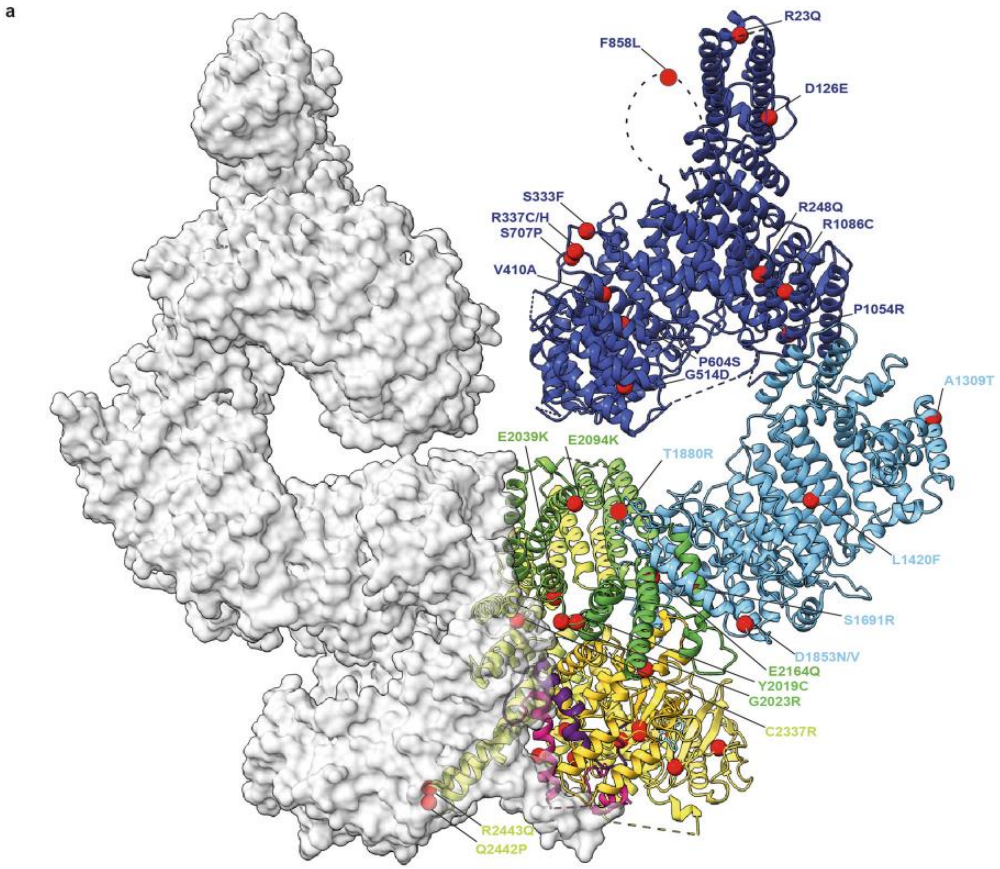

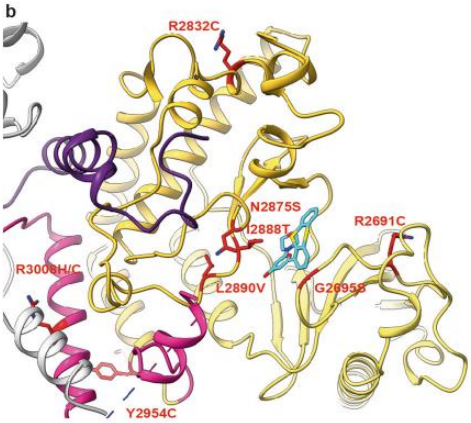

c

Domain	Mutations	Potential effects
Spiral	R23Q	Stabilisation of TAN motif
	D126E, R248Q, S333F, R337C/H, V410A, G514D, P604S, S707P, F858L, P1054R, R1086C	Stabilisation and charge distribution at Spiral interaction hub
Pincer	A1309T, L1420F, S1691R, D1853N/V, T1880R	Flexibility and folding of the N-terminus
FAT	Y2019C, G2023R, E2039K	Contact to kinase domain: might have an effect on a kinase activity
	E2094K, E2164Q	Folding of TRD2
	C2337R	Dimerisation
	Q2442P, R2443Q	Position of the PRD, kinase activity
	S2489F	HRD - kinase C-lobe connection
Kinase	R2691C, G2695S, N2875S, I2888T, L2890V	ATP binding
	R2832C	Kinase interaction with TRD1
	Y2954C	Kinase - PRD interaction, kinase regulation
	R3008H/C	PRD - TRD3 (opposite protomer) interaction

Extended Data Fig. 3 | Mapping of cancer-associated human ATM missense mutations. (**a**) Positions of commonly reported (count > 5) cancer mutations from COSMIC database depicted on to the ATM protomer. Approximate locations of F858L and T1880R mutations are shown based on unmodelled density. One ATM protomer coloured using domain colour-code, another–shown as a grey surface. Mutated residues are shown as red spheres with mutations indicated. (**b**) Model of KU-55933-bound ATM kinase with commonly (count > 5) mutated amino acid side chains coloured in red. Opposite protomer shown in grey. (**c**) Table summarising cancer-associated human ATM missense mutations. Mutations grouped based on their locations and coloured using domain colour-code.

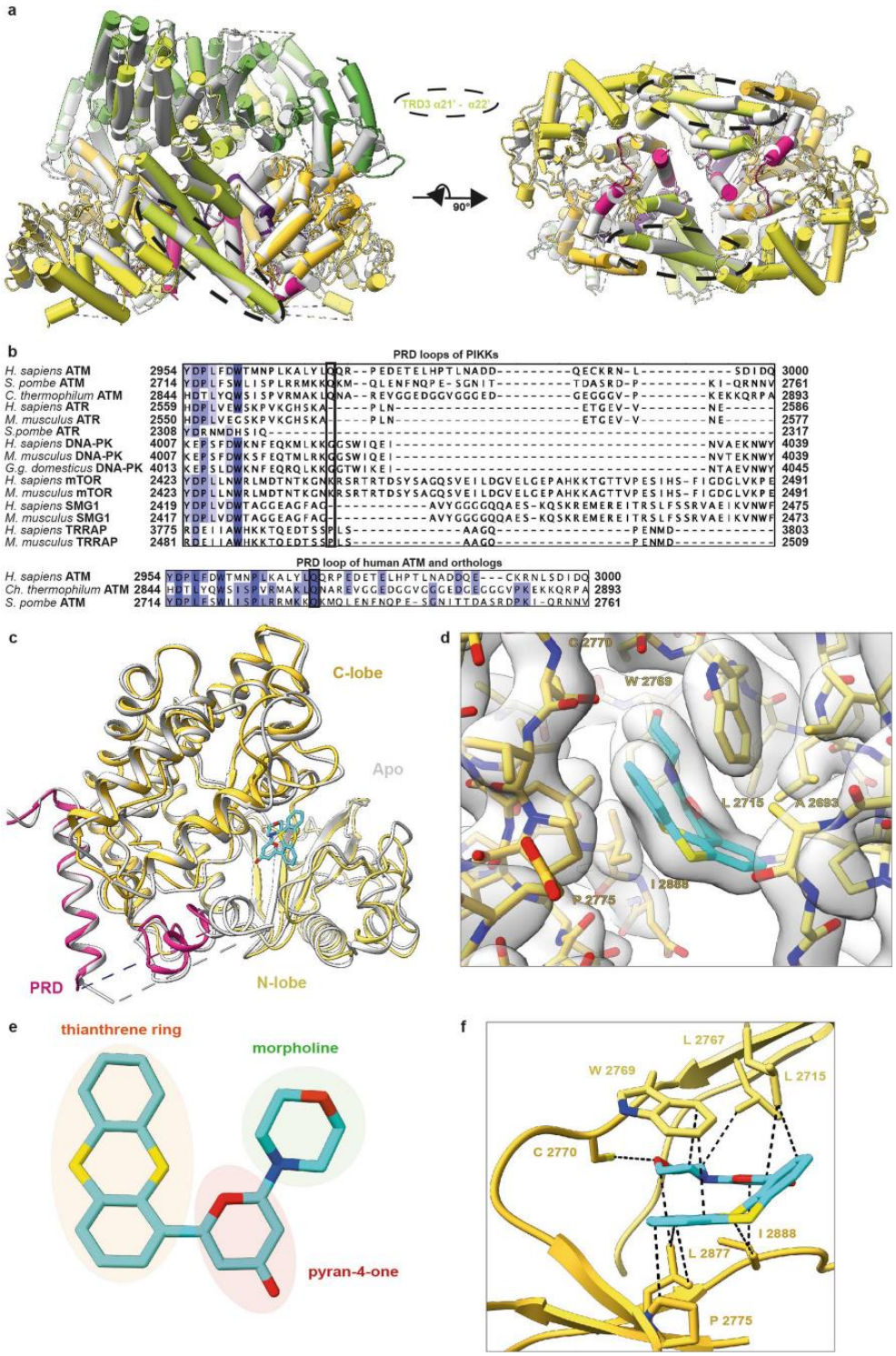

Extended Data Fig. 4 | See next page for caption.

Extended Data Fig. 4 | Conformation of KU-55933-bound human ATM. (**a**) Superimposition of KU-55933-bound human ATM dimer (color) and 'closed dimer' of human ATM (PDB ID: 5NP0; grey). Side and bottom views of C-terminal halves shown, helices depicted as cylinders. TRD3 α21-α22 indicated by black dotted line. (**b**) Sequence alignments of PRD loops from PIKKs from different organisms (top) and PRD loops of human ATM and its orthologs (bottom). PRD loops are colored by conservation and substrate-mimicking Q2971 of human PRD is highlighted. (**c**) Superimposition of kinase and PRD domains of inhibitor-bound (color) and apo human ATM (PDB ID: 6K9L; grey) models. (**d**) Cryo-EM density (grey, contoured at 0.0346) and model of the KU-55933 inhibited ATM active site. Clearly visible inhibitor proximal side chains labelled. (**e**) KU-55933 consists of three different ring systems: Thianthrene (orange), Pyran-4-one (red), Morpholine (green). (**f**) Detailed view of ATM active site with KU-55933. Van der Waals interactions indicated by dotted lines and interacting residues labelled.

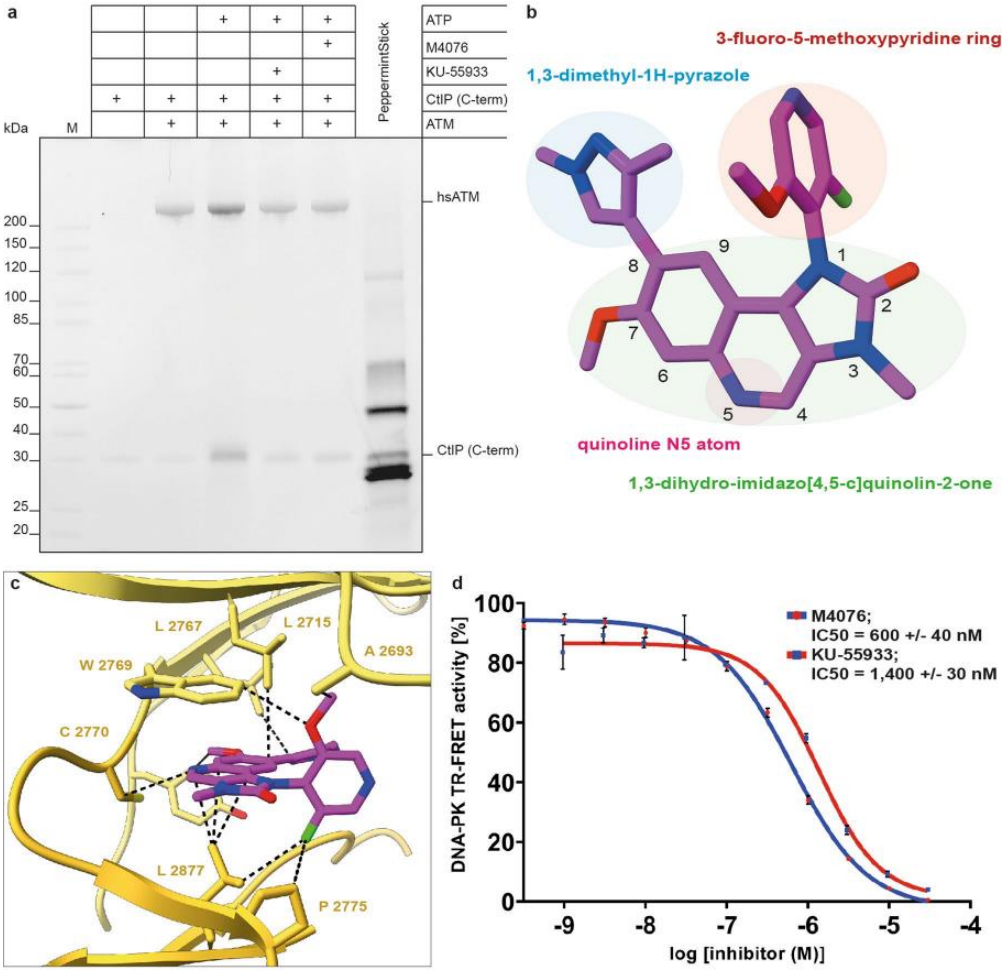

Extended Data Fig. 5 | Inhibition of ATM by M4076. (**a**) Inhibition of basal ATM kinase activity by M4076. Phosphorylation of CtIP C terminus (650–897, phosphomimetic mutation T847E) visualized by phosphoprotein SDS-PAGE staining, same gel as in Fig. 1a. The experiment was repeated twice with similar results. Uncropped gel image is presented in Source Data Fig. 1. (**b**) M4076 chemical structure and assignment of functional groups. (**c**) Detailed view of M4076 (magenta) bound ATM active site. Van der Waals interactions illustrated as black dotted lines and interacting residues labelled. (**d**) Dose-response curves of enzymatic DNA-PK kinase inhibition by M4076 and KU-55933. Data represent the mean ± s.e.m. from n = 16 independent experiments performed in duplicates for M4076 (IC50 = 600 ± 40 nM) and from one experiment performed in duplicates for KU-55933 (IC50 = 1,400 ± 30 nM). Data behind graph in panel d are available in Source Data Extended Data Fig. 5d.

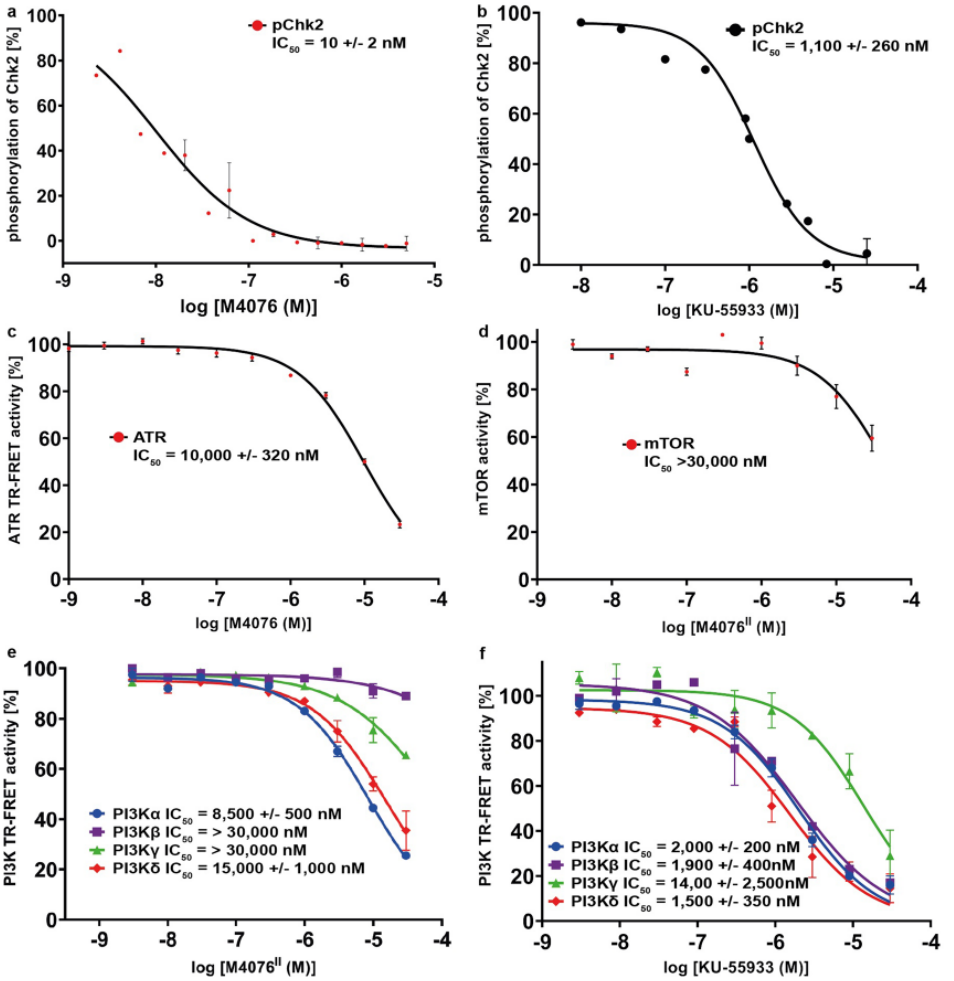

g

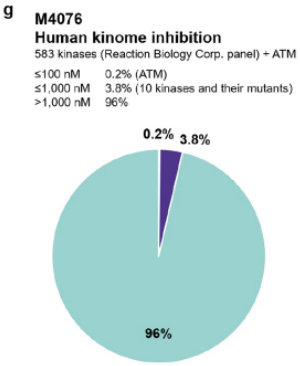

h

Kinase	Biochemical IC_{50} (nM)[1]	IC_{50}-splits vs. M4076 ATM IC_{50}[2]
Aurora A	1,025	>1,000
c-Kit (D820Y)	552	>1,000
FGFR2 (K526E)	777	>1,000
FGFR2 (R612T)	442	>1,000
FGFR2 (V564F)	136	~700
FGFR3 (V555M)	755	>1,000
FLT3	411	>1,000
FLT3 (D835Y)	241	>1,000
JAK2	684	>1,000
JAK3	405	>1,000
LRRK2	488	>1,000
RET(A883F)	574	>1,000
RET(L790F)	254	>1,000
RET(R749T)	537	>1,000
RET(S891A)	233	>1,000
RET(S904F)	615	>1,000
RET(V804E)	274	>1,000
RET(Y791F)	884	>1,000
RET-CCDC6 (PTC1)	741	>1,000
RET-NCOA4 (PTC3)	1,003	>1,000
RET-PRKAR1A (PTC2)	868	>1,000
RSK4	1,010	>1,000

i

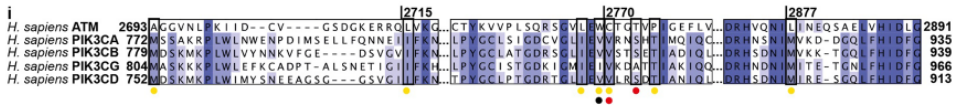

Extended Data Fig. 6 | See next page for caption.

Extended Data Fig. 6 | Kinase specificity of KU-55933 and M4076 inhibitors. (**a**)In vitro cell-based IC50 for inhibition of 2 Gy-induced phosphorylation of CHK2 (pThr68) in the human colon carcinoma cell line HCT116 for M4076 (IC50 = 10 ± 2 nM) from a Luminex assay. Data represent the mean ± s.e.m. from n = 3 independent experiments performed in singlicates. (**b**) In vitro cell-based IC50 for inhibition of bleomycin-induced phosphorylation of CHK2 (pThr68) in the human colon carcinoma cell line HCT116 for KU-55933 (IC50 = 1,100 ± 260 nM) from an ELISA. Data represent the mean ± s.e.m. from n = 2 independent experiments performed in singlicates. (**c**) Dose-response curves of enzymatic ATR kinase inhibition by M4076. Data represent the mean ± s.e.m. from n = 7 independent experiments performed in duplicates for M4076 (IC50 = 10,000 ± 320 nM). (**d**) Dose-response curves of enzymatic mTOR kinase inhibition by the racemate of M4076. Data represent the mean ± s.e.m. from n = 1 experiment performed in duplicate for the racemate of M4076 (IC50 > 30,000 nM). (**e**)Dose-response curves of enzymatic inhibition of recombinant PIK3 kinases p110α/p85α, p110β/p85α, p120γ, and p110δ/p85α by the racemate of M4076. Data represent the mean ± s.e.m. from n = 1 experiment performed in duplicates for the racemate of M4076 (IC50 values above 8.5 μM). (**f**)Dose-response curves of enzymatic inhibition of recombinant PIK3 kinases p110α/p85α, p110β/p85α, p120γ, and p110δ/p85α by KU-55933. Data represent the mean ± s.e.m. from n = 1 experiment performed in duplicates (PIK3 isoforms α, β and δ: IC50 values ~2 μM; PI3Kγ: IC50 = 14 μM). (**g**) Reaction Biology Corporation (RBC) kinase selectivity profiles of 583 kinases for M4076 tested at 1 μM. Segment sizes of pie chart represent numbers of 583 kinases from RBC panel and ATM in addition with IC50 ranges (cyan: 96% of the tested 583 kinases showed kinase activity values above 50% corresponding to IC50 values above 1,000 nM; dark blue: 10 kinases and their mutants, 22 kinases in total (3.8% out of 583 kinases tested) showed kinase activity values below 50% corresponding to IC50 values between 100–1000 nM). ATM is the only kinase with an IC50 value below 100 nM (0.2%). (**h**) IC50 values of M4076 determined for 10 kinases and their mutants, which showed kinase activity values below 50% tested at 1 μM M4076 in the RBC kinase selectivity profile against 583 kinases (22 kinases in total, corresponding to the dark blue segment in the Reaction Biology kinase selectivity pie chart in Extended Data Fig. 6g). 1: M4076 was tested in duplicate in a 10-dose IC50 mode with 3-fold serial dilution starting at 10 μM. Reactions were carried out at Km ATP concentrations of individual kinases according to the RBC Km binning structure. 2: The biochemical ATM IC50 value of 0.2 nM for M4076 was used for IC50-split calculation of individual kinases. (**i**) Sequence alignment of human ATM and PIK3 kinases p110α/p85α, p110β/p85α, p120γ, and p110δ/p85α active sites, coloured by conservation. Glycine-rich, catalytic and activation loops labelled. ATM residues forming hydrogen interactions with the inhibitor are marked with red dots, van der Waals interactions - yellow dots, and π-stacking interactions - black dot. Data for panels a-h are available as Source Data (Source Data Extended Data Fig. 6a-h).

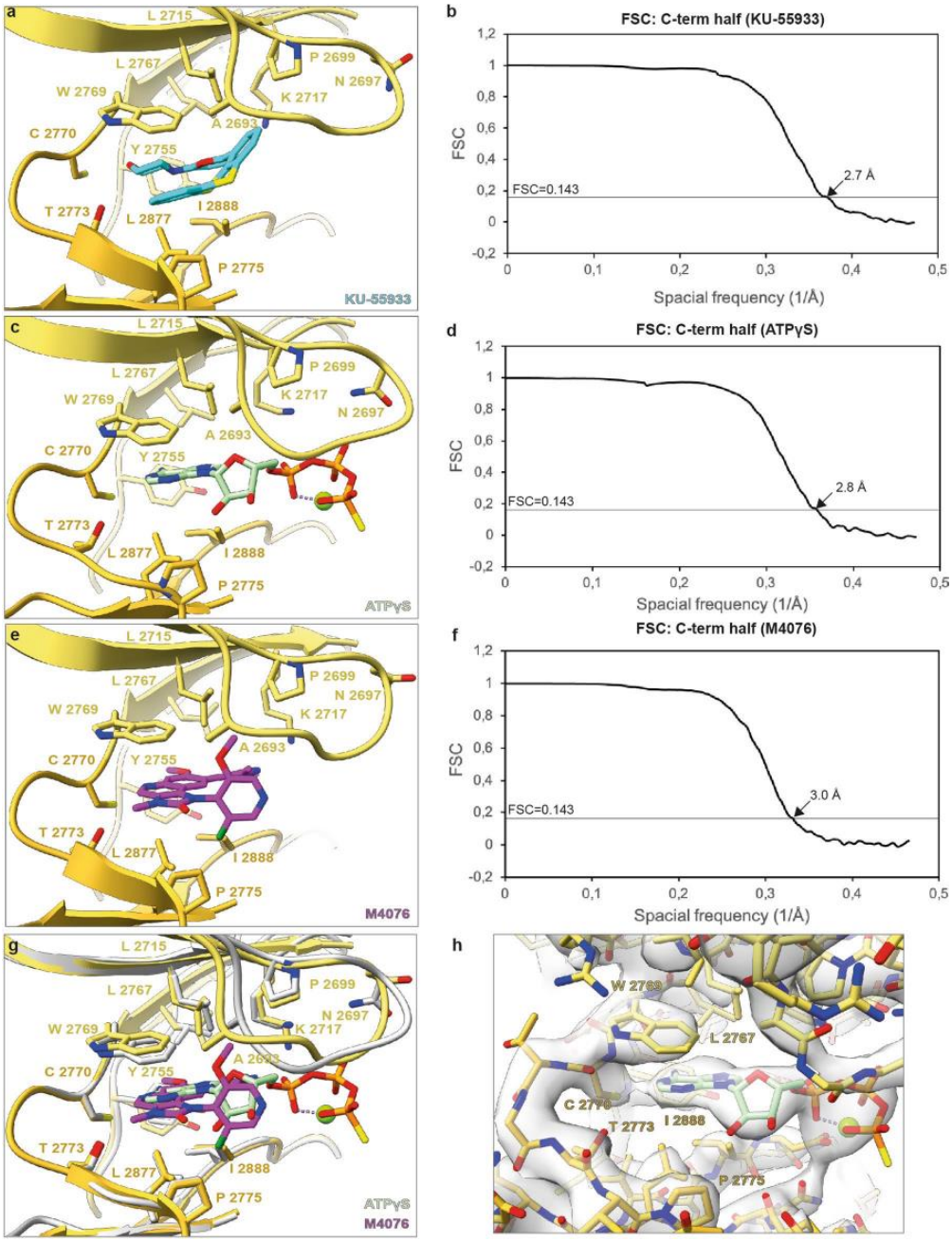

Extended Data Fig. 7 | Comparison of ATPγS-bound to KU-55933 and M4076 inhibited ATM kinase active sites. (**a**) Active site of KU-55933 (cyan) bound ATM (yellow) with highlighted surrounding residues. (**b**) Gold-standard Fourier shell correlation (FSC) curve from RELION-3.0 of the KU-55933 full ATM map. (**c**)Same as (A) with ATPγS (green, orange). (**d**) FSC curve from RELION-3.0 of the ATPγS bound ATM FATKIN map. (**e**)Same as (A) with M4076 (magenta). (**f**) FSC curve from CryoSPARC-2.14 of the M4076-bound ATM FATKIN map. (**g**) Superimposition of ATPγS (ATM in grey) and M4076 inhibitor (ATM in yellow) bound ATM active sites. (**h**) ATM active site density (grey, contoured at 0.0169) at 2.8 Å resolution with a fitted ATM model and ATPγS (orange, green).

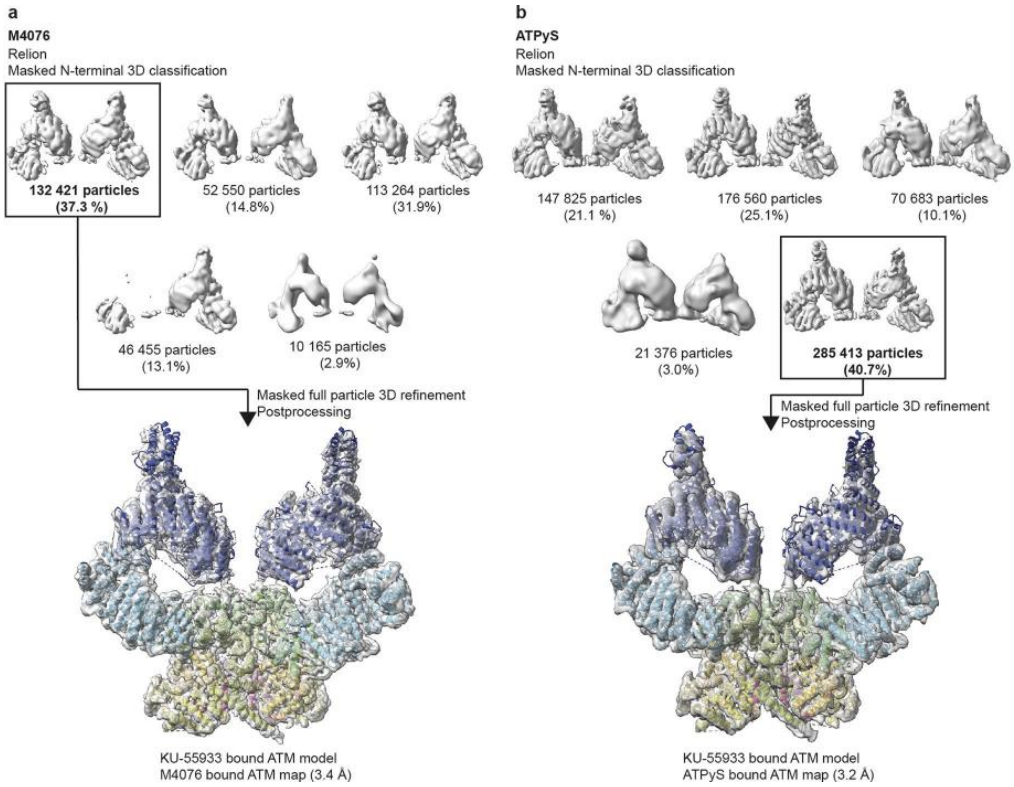

Extended Data Fig. 8 | N-terminal conformations of M4076 and ATPγS bound ATM. (**a**) Masked N-terminal 3D classification of M4076-bound ATM followed by further processing of dominant class and comparison to KU-55933 bound ATM conformation. (**b**) Masked N-terminal 3D classification of ATPγS bound ATM followed by further processing of dominant class and comparison to KU-55933 bound ATM conformation.

2.3 Cryo-EM structure of the Mre11-Rad50-Nbs1 complex reveals the molecular mechanism of scaffolding functions

Summary

In this manuscript we present the cryo-EM structure of the full-length eukaryotic MRN complex. The globular part of *Chaetomium thermophilum* (*ct*) MRN complex adopts a compact conformation with ATPγS sandwiched between Rad50 nucleotide binding domains (NBDs) and closed Rad50 coiled-coils. A single Nbs1 wraps around the Mre11 nuclease domain dimer and continues towards Rad50 NBDs revealing 2:2:1 stoichiometry of the MRN complex. Nbs1 is anchored across the Mre11 dimer via a highly conserved KNFKxFxx motif, as previously indicated by a *S. pombe* structure. The biochemical investigation of *ct*MRN DNA binding activities revealed two DNA binding modes. The C-terminus of Mre11 binds intact DNA in an ATP-independent manner, while the evolutionarily conserved Rad50 DNA binding site shows ATP dependency and preference to DNA ends. We also solved cryo-EM and crystal structures of Rad50 zinc-hook tetramer. These structures explain how MRN-MRN inter-complex can be formed and hints to a model for the mechanism of MRN-mediated DNA tethering. Taken together, our results reveal an architecture of full-length eukaryotic MRN complex and propose a mechanism for integration of catalytic and tethering functions of the complex.

Author contribution

I produced MRN complex together with Matthias Rotheneder, Aaron Alt, Brigitte Keßler and Erik van de Logt. Together with Matthias Rotheneder I performed biochemical assays and prepared grids for cryo-EM. I collected and processed data, built MRN structure together with Matthias Rotheneder, Katja Lammens and Joseph Bartho. MRN zinc-hook was crystallized by me, Matthias Rotheneder and Brigitte Keßler. X-ray crystallography data was collected and processed and model was built by me, Matthias Rotheneder and Katja Lammens. I was involved in manuscript preparation together with all authors.

Cryo-EM structure of the Mre11-Rad50-Nbs1 complex reveals the molecular mechanism of scaffolding functions

Matthias Rotheneder[1,+], Kristina Stakyte [1,+], Katja Lammens[1], Joseph D. Bartho[1], Erik van de Logt[1], Aaron Alt[1,2], Brigitte Kessler[1], Christophe Jung[1], Wynand P. Roos[4], Barbara Steigenberger[3], Karl-Peter Hopfner[1,*]

[1] Gene Center, Ludwig-Maximilians-Universität, Munich, Germany, Department of Biochemistry,

[2] Present address: CureVac AG, Tübingen, Germany

[3] Mass Spectrometry Core Facility, Max-Planck-Institute of Biochemistry, Martinsried, Germany

[4] Institute for Toxicology, Johannes-Gutenberg-Universität, Mainz, Germany

[+] These authors contributed equally

* Correspondence:
Prof. Dr. Karl-Peter Hopfner
Gene Center
Feodor-Lynen-Str. 25
81377 Munich, Germany
Tel: +49(0)89 2180 76953
Email: hopfner@genzentrum.lmu.de

Summary

The MRN (Mre11-Rad50-Nbs1) complex is a central DNA double-strand break repair factor that detects and nucleolytically processes DNA ends, activates the ATM kinase, and tethers DNA at break sites. The integrative mechanism how MRN can act both as nuclease and scaffold protein is not well understood. Here we provide a cryo-EM structure of MRN from *Chaetomium thermophilum* which takes shape as a 2:2:1 complex with a single Nbs1 wrapping around the autoinhibited Mre11 nuclease dimer. MRN has two DNA binding modes, one ATP independent for binding intact DNA through Mre11's C-terminus, along with an ATP dependent mode for loading onto DNA ends, suggesting how it may interact with DSBs and intact DNA. MRNs two 60 nm long segmented coiled coil domains protrude from the catalytic head as a linear rod, the apex of which is assembled by the two joined zinc-hook motifs. Apices from two MRN complexes can further dimerize through a new interface, forming 120 nm spanning MRN-MRN structures. Our results provide a near-atomic resolution architecture of MRN and suggest how it mechanistically integrates catalytic and tethering functions.

Introduction

DNA double-strand breaks (DSBs) are a threat to genomic integrity throughout life. Un- or misrepaired DSBs can lead to cell death, gross chromosomal aberrations, aneuploidy, and tumorigenesis (Carbone et al., 2020). DSBs can be caused by ionizing radiation and genotoxic chemicals, and frequently arise during DNA replication (Tubbs and Nussenzweig, 2017). In addition, "programmed" DSBs are physiological intermediates in immunoglobulin gene rearrangements and meiotic chromosome recombination (Johnson et al., 2021; Zhang et al., 2022). To maintain genomic stability, cells have evolved potent DSB sensing, signaling and repair pathways, which are generally grouped into two major branches. In end-joining reactions, such as non-homologous end joining (NHEJ) or microhomology-mediated end joining (MMEJ), broken DNA ends are ligated without or with various amounts of limited processing, a procedure that can be potentially mutagenic (Chaplin et al., 2021; Zhao et al., 2020). In homologous recombination (HR), DNA ends are resected into long 3' single strand overhangs, which pair with the homologous template for template-dependent DNA synthesis (Chen et al., 2018; Haber, 2018; Wright et al., 2018). In eukaryotic cells, the usage of the different pathways is tightly regulated in the cell cycle (Scully et al., 2019).

DSBs can be structurally very diverse and feature chemical alterations, hairpins or covalently attached proteins. The latter arises during abortive type II topoisomerase reactions and is the physiological source of DSBs in meiosis (Johnson *et al.*, 2021; Morimoto et al., 2019). Detection and repair of chemically diverse and obstructed DNA ends, in particular protein-blocked DNA ends, requires the Mre11-Rad50-Nbs1 (MRN, Mre11-Rad50-Xrs2 in yeast) complex (Cejka, 2015; Paull, 2018; Syed and Tainer, 2018). Current models suggest that MRN cuts the 5’ strand in the vicinity of the DNA end, followed by exonucleolytic back-resection in the 3’ to 5’ direction (Deshpande et al., 2016; Garcia et al., 2011). The resulting ssDNA can act in strand annealing in end-joining reactions or can be further extended by 5’ to 3’ long-range resection in HR. MRN or bacterial MR homologs can also cleave the second strand, thereby inducing a DSB near the blocked end, which will clip off the blocked DNA termini (Connelly et al., 2003; Deshpande *et al.*, 2016; Myler et al., 2017). The evolutionary conserved core complex consists of two copies of each Mre11 and Rad50. It takes shape as a globular ATP-dependent DNA binding and nuclease module (head module) with two protruding, up to 60 nm long flexible coiled coil (CC) domains (de Jager et al., 2001; Hopfner et al., 2001; Lammens et al., 2011; Lim et al., 2011). The two Rad50 CC domains of an MR or MRN complex are apically linked together via a zinc-hook dimerization motif (Hohl et al., 2015; Hopfner et al., 2002; Park et al., 2017). Recent structural data on *E. coli* Mre11-Rad50 (*Ec*MR, also denoted SbcCD) suggest that the linked CC domains act as gate and chemo-mechanical sensor via ring to rod transitions to promote ATP dependent loading and cleavage of linear but not circular DNA (Kashammer et al., 2019).

In eukaryotes, Mre11 and Rad50 bind a third protein, Nijmegen breakage syndrome 1 (Nbs1, denoted Xrs2 in yeast) (Carney et al., 1998), which regulates MRs nuclease activity and acts as a scaffold for interactions with chromatin and DNA repair and signaling factors. Genetic inactivation of Mre11, Rad50 or Nbs1 is lethal in mammals, while hypomorphic mutations lead to several genome instability syndromes, like Nijmegen breakage syndrome and Ataxia-telangiectasia-like disorder, characterized by cancer predisposition, neurodegeneration and/or immunological defects (Bian et al., 2019; Buis et al., 2008; Luo et al., 1999; Zhu et al., 2001). The eukaryotic MRN complex has both enzymatic and structural functions in DSB repair. It is involved in HR and end-joining pathways, meiotic and replication-associated recombination, chromatin architecture as well as telomere maintenance (Marie and Symington, 2022; Paull, 2018; Syed and Tainer, 2018). The various activities of MRN/X are tightly orchestrated and regulated by the cell cycle state and additional factors, such as ATM/Tel1, CtIP/Sae2 and Rif2 (Cejka and Symington, 2021). CtIP/Sae2 functions as a DNA scaffold protein (Andres et al., 2019) and MRN/X coactivator (Cannavo and Cejka, 2014; Deshpande *et al.*, 2016; Reginato et al., 2017; Wang et al., 2017) and is critical for DSB processing (Mimitou and Symington, 2008; Sartori et al., 2007). At *S. cerevisiae* telomeres, on the contrary, Sae2's coactivator function is counteracted by telomeric factor Rif2, which prevents endonucleolytic cleavage by MRX (Khayat et al., 2021; Martina et al., 2012; McGee et al., 2010; Roisne-Hamelin et al., 2021).

MRN/X also recruits and activates the Ataxia telangiectasia mutated (ATM, Tel1 in yeast) at DSBs (Cassani et al., 2019; Lee and Paull, 2005; You et al., 2005). ATM/Tel1 phosphorylates a large number of target proteins, thereby orchestrating the DNA damage response, a complex set of events that involves chromatin reorganization, DNA repair, cell cycle arrest, transcriptional responses and apoptosis (Lee and Paull, 2021). An important but particularly poorly understood function of MRN/X is the tethering of DNA (Cassani et al., 2018; Mojumdar et al., 2019; Seeber et al., 2016), and more generally chromatin organization (Delamarre et al., 2020; Forey et al., 2021; Salifou et al., 2021). MRN/X forms large clusters in vitro and repair foci in vivo, and both catalytic head complexes, as well as CC domains, are observed in low resolution EM or atomic force microscopy (AFM) to engage in cluster formation (Frame et al., 2006; Hopfner *et al.*, 2002; Vera et al., 2022; Zabolotnaya et al., 2020). Such clusters might also be involved in generating multiple cleavage events at DSBs as well (Cannavo et al., 2019). The mechanism of how MRN integrates enzymatic and structural tethering functions and the molecular basis for the roles of the CCs in clustering has not been established and remains unclear. A particular conundrum is how the CC domain and zinc-hook can be involved in both intra-complex and inter-complex interactions, to act as gate in DSB sensing on one hand, or bridge MRN complexes in tethering functions on the other hand.

Here we report the cryo-electron microscopy (cryo-EM) structure of *Chaetomium thermophilum* (*Ct*)MRN complex bound to ATPγS. Our structure not only clarifies the atomic architecture of eukaryotic MRN but reveals several unexpected features that rationalize enzymatic and tethering

functions in a single framework. A 3.8 Å reconstruction of MRN's catalytic head shows that 75 amino acids of Nbs1 wrap as an extended chain around both Mre11 subunits. This portion of Nbs1 agrees well with that of the minimal core of murine Nbs1 necessary to maintain embryonic viability (Bian *et al.*, 2019). Our data thus clarify *Ct*MRN as a $M_2R_2N_1$ complex and suggest that a key function of Nbs1 is to stabilize the Mre11 dimer. The Rad50 CC domains are in a rod configuration, stabilized by several points of interactions along their entire lengths. Unexpectedly, we not only observe zinc-hook mediated dimerization of the two CC domains in a rod configuration, but the apices of two MRN CC domains further dimerize to form joined MRN-MRN assemblies. Supported by cell-based and biochemical studies, the structure provides a molecular basis for the transient tethering of DNA ends and/or chromatids by MRN.

Results

Cryo-EM structure of the Mre11-Rad50-Nbs1 complex

Recombinant expression of the MRN proteins from *Chaetomium thermophilum* (*Ct*) in insect cells resulted in a homogeneous MRN complex with a 2:2:1 stoichiometry (**Figure S1A**). We vitrified the protein in the presence of ATPγS, which we found to stabilize the complex for cryo-EM. Since *Ct*MRN's ATPase is 10-fold stimulated by DNA (see below), similar to human (*Hs*)MRN and *Escherichia coli* (*Ec)*MR (Deshpande et al., 2017; Saathoff et al., 2018), the resulting ATPγS bound structure resembles an autoinhibited "resting" state of the complex between occasional ATP hydrolysis events.

In the micrographs, we observed homogenous particles along with large, clustered oligomers, entangled Rad50 coiled coils (CCs), and partially dissociated complexes (**Figure S1B**). For structure determination, we focused on isolated particles that typically showed a globular head module (i.e., Rad50NBDs bound to the Mre11 dimer and Nbs1) along with straight or curved protruding CCs. The highly elongated, flexible nature of the particles prevented us to obtain a cryo-EM map of the entire complex, however, we could reconstruct a structure covering the head and approx. 50% of the proximal CCs, and another structure covering 25% of the distal CCs around the zinc-hook.

We first focused on the head module and adjacent CCs. Several rounds of automated particle picking, 2D classification, training of the TOPAZ neural network-based particle picker, followed by extensive 3D classification, refinement, and polishing led to a 4.0 Å C1-reconstruction of the catalytic head module (**Figure 1A, Figure S1C, D, Figure S2, Table 1**). By further selecting for straight CCs and re-extracting the particles with bigger box sizes, we obtained a C2-symmetrical density with 4.8 Å overall resolution in which around 30 nm of the Rad50 CCs were resolved (**Figure 1A, Figure S2, S3A-E**). Different regions of the C1 map were improved by further classification through variability analysis,

masking, and focused refinement, which brought out features like the path of Nbs1 around the Mre11 dimer and parts of the Mre11 extended C-terminus. We generated a composite map by combining the higher resolution maps of different regions, using the C2-map with long CCs as a reference and scaffold (**Figure S1D**). The EM density maps enabled us to build an atomic model for the catalytic head domain and 30 nm of the Rad50 CCs, using various crystal structures and AlphaFold2 models for subunits as starting models (**Figure 1A, Figure S3F**).

The catalytic head model consists of two Mre11, the two Rad50NBD subunits and an extended portion of Nbs1 that wraps around both Mre11 protomers (**Figure 1A**). The Mre11 nuclease domain, composed of the phosphodiesterase and capping domains (CD), forms the characteristic dimer structure with a prominent DNA binding cleft. The Mre11 nuclease active sites are blocked by both Rad50NBDs, which are situated in the DNA binding cleft to prevent unspecific DNA degradation. Following the nuclease domain, the helix-bundle Rad50-binding domain (RBD) attaches Mre11 to the Rad50 CCs. Overall, the architecture of the M_2R_2 head module is related to that of *Ec*MR bound to ATPγS, showing the autoinhibited "resting" state (Kashammer *et al.*, 2019).

The CC domains have a highly segmented nature with interspersed loops (CC segment joints). *Ct*MRN-ATPγS CCs are parallel and tightly engaged (rod configuration), in contrast to the *Ec*MR-ATPγS "resting" state complex, where the CCs protrude at an angle of approx. 60° from the head (ring configuration) **(Figure S4A**). Both CCs interact with each other predominantly via contacts at the segment joints. Additionally, the CCs are held together by a bridge element formed by Mre11 that spans the CCs in the vicinity of the Rad50NBDs and is absent in the prokaryotic MR complex (**Figure 1A, Figure S4A**). Imaging *Ct*MRN in the presence of ATP, we observed a small fraction of particles that showed open CCs, similar to the structure observed in the *Ec*MR-ATPγS "resting" state complex (**Figure S4B**) (Kashammer *et al.*, 2019). This indicates that ATP, like in the bacterial complex, can induce CC opening.

To generally validate the structural model and obtain additional architectural information, we performed lysine-specific chemical cross-linking followed by LC-MS/MS (XL-MS), which provides in-solution distance restraints of <30 Å between Cα atoms **(Figure 1B, Figure S4C)**. In general, the obtained crosslinks are highly consistent with the model and especially validate the low-resolution parts of the map in the CCs and the fitting of the AlphaFold2 predicted CC segments **(Figure 1A)**. The crosslinks also agree well with a highly extended conformation of the CCs as observed in the micrographs. Out of 40 crosslinks mapped to our model, 35 fulfill the distance restraints. The remaining crosslinks are all located within the catalytic head and could be explained by its flexibility **(Video S1)**. This does not argue for elbow elements and folding of the CCs as observed for the structurally related class of SMC proteins (Burmann et al., 2019).

A single Nbs1 wraps around the Mre11 dimer

A single Nbs1 polypeptide binds asymmetrically to both Mre11 phosphodiesterase domains with an S-shaped double turn across the Mre11 dimerization interface (**Figure 1C**). In total the Mre11 interacting region of *Ct*Nbs1 comprises 75 residues. Binding is centered on the highly conserved KNFKxFxx motif (K659-F664), which binds right across the two-fold symmetry axis of the M_2R_2 head module with the pseudo-symmetric KxFxR region **(Figure 1C, Figure S5A)**. This interaction was previously observed in a crystal structure of *S. pombe* (*Sp*)Mre11 catalytic domain bound to a small fragment of *Sp*Nbs1, showing high structural conservation of this central interaction mode **(Figure S5B)** (Schiller et al., 2012). However, the cryo-EM map, in conjunction with AlphaFold2 multimer analysis, enables us to trace the entire interaction region of Nbs1 around the Mre11 dimer **(Figure 1A top view, Figure S3E)**.

A series of coordinated turns, N-terminal of the KNFKxFxx motif form a small, compact central domain that further bridges the Mre11:Mre11 interface **(Figure 1C)**. The central domain is reasonably well ordered with many contacts to Mre11, and has a predicted local resolution range from 3.8 Å to 4.3 Å. The size of the central domain structure appears to be a species-specific feature of Nbs1 homologs, as alignment with other species shows a significantly shorter sequence neighboring the KNFKxFxx motif (**Figure S5A**). The N- and C-terminal chains of *Ct*Nbs1 turn and extend back past this central domain in both directions to wrap across the entire Mre11 phosphodiesterase dimer **(Figure 1C, insets).** Both extensions bind with reverse polarity to equivalent regions of the two Mre11 phosphodiesterase domains. This extended part of a single Nbs1 polypeptide interacts with and breaks the symmetry of the Mre11 dimer**.** Beyond this core Mre11 interaction region, the Nbs1 C-terminal chain branches away into the solvent, while the N-terminal chain forms a short helix, overall resulting not only in an asymmetric Mre11-Nbs1 complex, but also asymmetries in the interactions between Mre11 and Rad50 **(Figure S5C).** The asymmetric elements of Mre11 and Rad50 directly correlate with the orientation of Nbs1, suggesting the symmetry breaking orientation of Nbs1 influences the behavior of the entire MRN complex. This may be driven by the Mre11 loop H213-L225, which alternatively interacts with N-terminal strand of Nbs1 in a conformation matching the crystal structure **(Figure S5C, left)**, or swings 15 Å to interact with Rad50 **(Figure S5C, right).** One Rad50 appears stabilized by this interaction, while the other shows a more flexible conformation, deviating up to 8 Å from the symmetry related position **(Video S1).**

The strong interactions of the central domain are present in most observed particles, while the weaker interactions of the N- and C-terminal chains with Mre11 allow their release into the solvent. 3D classification of the Mre11-Nbs1 interaction showed that particles could be divided into 5 classes: central domain with N-terminal chain bound (27%), central domain with C-terminal chain bound (27%), central domain with both chains bound (25%), central domain with neither chain bound (13%), and no

Nbs1 bound (8%) (**Figure S5D**). This indicates that the interaction of Nbs1 with MR could be locally quite dynamic, perhaps to allow for conformational changes or response to interaction partners. Finally, we note that the 75-residue long Mre11 interaction region of Nbs1 more or less precisely corresponds to the minimal fragment of Nbs1 required to maintain embryonic viability. This highlights the importance of the asymmetric wrapping of the Mre11 dimer by Nbs1 as revealed by work for MRN core functionality in mammals (Kim et al., 2017).

Rad50 is in a pre-engaged ATP state

Closer inspection of the head module reveals one Mg^{2+}-ATPγS moiety bound to each of the two Walker A motif regions of the Rad50 dimer **(Figure 2A, B).** Mg^{2+} is properly coordinated by Walker B and Q-loop residues. However, the signature motifs, a conserved motif characteristic for the ABC-type ATPase family, are approx. 10 Å away from the γ-(thio)phosphate of ATPγS. In the fully engaged state of ABC-type ATPases, the signature motif binds the γ-(thio)phosphate of the "trans" ATP, inducing a "power stroke" in the ABC-type ATPase dimer when transiting from apo to ATP-bound states (**Figure 2C**). We took advantage of two crystal structures of the isolated *Ct*Rad50NBD, bound to ATPγS and either DNA or the Mre11 RBD, respectively, to compare with the cryo-EM structure of CtMRN and reveal structural differences (Seifert et al., 2016). Both structures show the same conformation with the signature motifs fully engaged with the trans γ-(thio) phosphates (**Figure 2C**). Comparison with the cryo-EM structure reveals a approx. 30° rotation of each of the two NBDs, driven via signature motif γ-(thio)phosphate interactions. Accompanying are corresponding movements of the CC domains (truncated in the crystal structures) **(Video S2)**. Thus, in the full-length *Ct*MRN cryo-EM structure, the adhesion of the CC domains and possibly the Mre11 bridge, likely prevents full engagement of the Rad50NBDs, by obstructing the necessary rotation of the NBDs, which remain in a partially engaged state. Even in the presence of ATP, only a subset of particles showed an open CC conformation, altogether pointing to a tighter autoinhibition of MRN as compared to MR in the absence of DNA **(Figure S4B).**

ATP dependent and independent DNA binding by MRN

The rod structure of the CCs raises the question of whether the canonical DNA binding site on the Rad50NBDs remains accessible to DNA **(Figure 2C, crystal structure)** and what role ATP plays in DNA binding. To assay ATP-dependent and independent DNA binding, we used a fluorescence polarization anisotropy (FA)-based assay (Materials and Methods). Wild-type *Ct*MRN complex binds to 80-mer dsDNA oligonucleotide with K_d's of 53±5 nM and 30±2 nM in the presence of ATP and

ATPγS, respectively (**Figure 3A**). We attribute the higher K_d for ATP to hydrolysis-dependent turnover since DNA robustly stimulates ATP hydrolysis (see below). Surprisingly, MRN also binds DNA in absence of ATP with a somewhat higher K_d of 73±7 nM (**Figure 3A**). Robust DNA binding in the absence of ATP was also seen for human MRN and appears to be a preserved feature of eukaryotic MRN/X, which is in contrast to the strictly ATP dependent DNA binding of prokaryotic MR (Hopfner et al., 2000; Lammens *et al.*, 2011; Paull and Gellert, 1999; Rojowska et al., 2014).

Interestingly, the binding curves converge to higher FA plateau values than in presence of ATP and ATPγS (97 mP and 92 mP, respectively) compared to the curve with no nucleotide (56 mP) (**Figure 3A**). This approx. 2-fold FA increase in presence of ATP and ATPγS is a strong hint for the binding of a second DNA molecule to the MRN complex. Apart from the canonical binding site at the Rad50NBDs, we hypothesized that the eukaryote-specific Mre11 C-terminal extension could bind an additional DNA molecule (Usui et al., 1998). We generated a mutant MRN complex ($M^{\Delta C}RN$), where this Mre11 extension (568-730) was removed (**Figure 3B, top**). The truncation still retains the bridge, as removal of the bridge resulted in an unstable complex that was not characterized further. Our truncation site coincides with a recently described SPARTN protease cleavage site in human Mre11 in certain cancers cells that reduced the affinity of *Hs*Mre11 to DNA (Na et al., 2021). *Ct*$M^{\Delta C}RN$'s ability to bind DNA in the absence of ATP/ATPyS was nearly abolished, confirming both binding caused by the Mre11 C-terminal tail and ATP dependence for binding to Rad50NBD. **(Figure 3B)** As expected, DNA binding to Rad50NBDs in the presence of ATP/ATPyS remained nearly unaltered (K_d values 51±5 nM, 28±2 nM, respectively). Moreover, the levels of the FA plateaus (50 mP and 27 mP) are consistent with FA increase caused by one DNA oligomer, as seen above for the wt *Ct*MRN. In addition, sigmoidal DNA binding curves for *Ct*MRN and *Ct*$M^{\Delta C}RN$ with and without ATP with Hill coefficients >1 (ranging from 1.3 to 3.0, see Material and Methods) indicate cooperative binding modes possibly arising from protein oligomerization, similar to what was observed for *S. cerevisiae* MRX (Vera *et al.*, 2022). In support for this interpretation, we noticed that DNA-bound *Ct*$M^{\Delta C}RN$ complexes were significantly less prone to oligomer formation than *Ct*MRN, observed by visualization of fluorescently labeled DNA **(Figure S6A, B).**

Next, to investigate the preference of *Ct*MRN and *Ct*$M^{\Delta C}RN$ for DNA ends, we performed competition assays by adding increasing amounts of unlabeled circular or linearized plasmid DNA to the solution containing a fixed amount of protein and labeled 80-mer dsDNA. For *Ct*MRN, the linearized DNA competed approx. 3-fold better than the circular DNA, showing an only moderate preference for DNA ends (**Figure 3C**). This could be due to the presence of the Mre11's C-terminal tail containing the second binding site exhibiting no preference for DNA ends. However, for *Ct*$M^{\Delta C}RN$, linear DNA competed ~35-fold better than circular DNA (**Figure 3D**), demonstrating the strong dependence for DNA ends of the Rad50NBDs.

Finally, to test the effect of DNA stimulated ATP hydrolysis on DNA binding properties, we performed ATPase assays. Similar to studies on human MRN, we find that linear DNA stimulated *Ct*MRNs ATPase approx. 10-fold, while circular DNA stimulated MRN only 2-fold (**Figure 3E**) (Deshpande *et al.*, 2017). ATPase rates of *Ct*M$^{\Delta C}$RN were generally reduced to 2/3 of wt MRN's ATPase levels but showed a similar 10-fold (linear) and 2-fold (circular) stimulation by DNA (**Figure 3F**). The lower ATPase rate might be caused by a less stable protein. However, the strong increase of M$^{\Delta C}$RN's preference for ATP-dependent binding of linear vs circular DNA is unlikely caused by the moderate reduction in ATPase activity, especially because the same increase in preference for linear over circular DNA is observed in the presence of ATPyS.

We conclude that MRN possesses two DNA binding components. The first binds DNA in an ATP-dependent manner via the evolutionary conserved head module. Much like bacterial MR, a strong preference for specific binding at DNA ends is exhibited through this mode. The second DNA binding mode is ATP-independent and lies within the *Ct*Mre11 C-terminal tail. These additional interactions further increase binding of internal DNA elements.

MRN-MRN tethering via zinc-hook tetramerization

During cryo-EM data processing we noted 2D classes that resembled Rad50 zinc-hook dimers in the "closed" rod configuration **(Figure S1C)**. We denote the tips of the dimerized CCs of a single MRN complex as CC apex. 2D class averages did not show single apices but depicted apex dimers: two Rad50 zinc-hooks, joined via Zn^{2+} coordination to form the canonical apex in rod configuration, further dimerize in an antiparallel fashion. As a result, these apex-apex interactions tether two MRN complexes. Selecting and training for those particles enabled us to reconstruct a cryo-EM density at an overall resolution of 4.9 Å, which resolved another 14 nm of the total CCs (**Figure 4A, Figure S7, Table 1**). To obtain a higher resolution and independently verify this apex-apex interaction, we crystallized a fragment of the CC region around the zinc-hook (*Ct*Rad50$^{589-782}$). We obtained crystals in space group P1 and determined a structure to 2.5 Å resolution by molecular replacement, using a corresponding *Ct*Rad50 AlphaFold2 model **(Figure 4B)** (Jumper et al., 2021). Data collection and model statistics are listed in **Table 2.** The asymmetric unit of the crystal consists of a dimer of zinc-hook dimers, i.e., two tethered apices, in the same arrangement as observed by cryo-EM **(Figure 4B)**.

Zooming in, we find that the primary interface between the CCs of a single $M_2R_2N_1$ complex through joint coordination of a Zn^{2+} ion is very similar to that observed in crystal structures of archaeal and human Rad50 zinc-hook regions (Hopfner *et al.*, 2002; Park *et al.*, 2017; Soh et al., 2021). Conserved C691 and C694 from each of the two protomers jointly bind Zn^{2+} in a tetrahedral fashion (**Figure 4C**).

In both cryo-EM and crystal structure, the two CCs are arranged in the same rod configuration, stabilized by small confined, hydrophobic contact points along the two CC protomers.

The rod state, as opposed to the originally observed open state, enables an antiparallel interaction of two apices through formation of a secondary interface (**Figure 4D**) (Hopfner *et al.*, 2002). Hereby, F688 of one Rad50 dimer binds into a hydrophobic pocket (I651 and L654) at the last CC segment joint of the other Rad50 dimer. Flanking this hydrophobic interaction are salt bridges between R684 and E655, R687 and E658, and K686 and D736. Altogether, these contacts are formed twice in the secondary interface. Furthermore, due to the dimeric nature of the CC rods, the tethering interactions can form on both sides of a given apex, thus leading to formation of two-dimensional sheets of antiparallel tethered apices in the crystal lattice (**Figure S8A**). Interestingly, we observe apex multimers in cryo-EM, supporting the idea of higher-order apex interactions (**Figure S8B**). Due to the low number of particles, we could not obtain higher resolved 3D maps at this stage. Nevertheless, crystal packing and the cryo-EM classes raise the possibility that CC apex tethering might go beyond MRN-MRN dimer interactions towards higher-order oligomerization.

Since the *Ct*Rad50 zinc-hook shows structural conservation to the previously published crystal structure of the *Hs*Rad50 zinc-hook (Park *et al.*, 2017), we wondered whether *Hs*Rad50 could also form these antiparallel tethering interactions and inspected the underlying crystal lattice (PDB: 5GOX). Intriguingly, the *Hs*Rad50 apices adopt related, compared to *Ct*Rad50 longitudinally shifted, tethered structures within the crystal lattice (**Figure 5A**). Like in *Ct*Rad50, the same region at the tip of the CC helix mediates this interaction with the neighboring apex and we denote this region as an apex tethering element. The apex tethering element does not interact with the first loop insertion element of the CCs, as observed for *Ct*Rad50, but with a CC segment just beyond (**Figure 5A, inset**). Nevertheless, the overall mode of antiparallel interactions of both human and *C. thermophilum* CC apices suggest that apex-apex interactions might be a conserved feature to tether two or more MRN complexes.

Zinc-hook tetramerization is required for efficient DNA repair in human cells

To assess the functional significance of MRN-MRN tethering on recombinational DNA damage repair in living cells, we mutated the *Hs*Rad50 apex tethering element (DENQS675-679AAAAA; Rad50^{apex}). Purified *Hs*MR^{apex}N complex has an $M_2R_2N_1$ stoichiometry and a thermal stability profile similar to that of the wt *Hs*MRN complex, suggesting that the overall complex formation and folding are not affected by the mutations (**Figure S9A, B).** We analyzed the capability of *Hs*MR^{apex}N to repair reactive oxygen species (ROS) mediated DNA damage through comet assays in U2OS cells. Endogenous Rad50 was knocked down via siRNAs and the cells were transfected with wt or mutated Rad50, along with wtMre11 and wtNbs1 to have all components expressed at the same level. Knockdown of endogenous

Rad50 without supplementing plasmid expressed MRN caused impaired DNA repair upon ROS-induced stress **(Figure 5B)**. Residual repair capacity may be attributed to remaining levels of endogenous Rad50 after siRNA knockdown. Transfection with wt MRN fully rescued the repair deficiency **(Figure 5B).** Transfection with $MR^{apex}N$ only led to a partial rescue, despite robust overexpression of the proteins **(Figure S9C)**. The rescue level is in a similar range, slightly better than in the absence of MRN transfection, indicating that the mutant has a residual but substantially affected repair capacity. Taken together, these data suggest that the apex tethering element mutation compromises MRN function in DSB repair and that the structurally observed tethering interaction is an important feature of MRN in human cells.

Discussion

The MRN complex is a tightly regulated, multifunctional DNA double-strand break (DSB) repair factor that senses and processes DSBs (Cejka, 2015; Paull, 2018; Syed and Tainer, 2018). In addition to its nuclease activity, MRN has functions in DNA damage signaling (via ATM recruitment and activation), DNA tethering, telomere maintenance and chromatin organization (Cannavo and Cejka, 2014; de Jager *et al.*, 2001; Deshpande *et al.*, 2016; Khayat *et al.*, 2021; Lamarche et al., 2010; Lee and Dunphy, 2013; Lee and Paull, 2005; Salifou *et al.*, 2021; You *et al.*, 2005). Many mechanistic aspects of the activation and regulation, but especially also the scaffold functions remain unclear to date. Using cryo-EM analysis and crystallography, we determined the structure of the MRN complex in a “resting” state, providing an architectural framework and mechanism for the unresolved question of how MRN combines catalytic and structural tethering functions.

Our structure of the full-length MRN clarifies the complex stoichiometry as $M_2R_2N_1$ and provides a molecular basis for the symmetry breaking by Nbs1. Parts of Nbs1 wrap as an elongated chain around the Mre11 nuclease domain dimer, binding to the same surface regions of both Mre11 protomers via different Nbs1 elements. The observed wrapping mode argues that an essential function of Nbs1 is to stabilize the Mre11 dimer and head architecture, which might be critical for ATM activation and other functions of the complex. For instance, the *S. cerevisiae* Nbs1/Xrs2 provides nuclear localization, is required for ATM/Tel1 recruitment and canonical end-joining activities, while it is dispensable for nuclease associated functions of MRN/X (Oh et al., 2016). In mice, Nbs1 deletions cause embryonic lethality, however a minimal Mre11 binding fragment that more or less precisely correlates with the portion of Nbs1 that we visualize here, was shown to restore viability and enable ATM activation (Kim *et al.*, 2017). These data indicate that the observed wrapping of the Mre11 dimer by Nbs1 would be particularly important for roles in DNA tethering and Tel1 activation.

An unexpected observation was that the *Ct*MRN-ATPγS CCs adopt a closed rod state, rather than the open, flexible ring structure that was observed for the *Ec*MR-ATPγS complex (Kashammer *et al.*, 2019). We attributed the open state to loading onto DNA ends, especially those that carry a proteinaceous block. The relatively narrow opening between the CC domains at the head complex could help clamp down DNA once it is loaded, as observed in the EcMR "cutting" state, but it is difficult to envision how a blocked DNA end could enter between the CCs in this configuration. The structure may indicate that eukaryotic MRN is more autoinhibited than bacterial MR, which makes sense considering the much more complex functional spectrum of eukaryotic MRN and the perhaps even greater cytotoxic threat that unregulated DNA cleavage by MRN might pose on eukaryotic genomes. However, the CCs might also be more dynamic than presented by the cryo-EM analysis. For instance, atomic force microscopy (AFM) studies generally show a more dynamic nature of the CC domains (Moreno-Herrero et al., 2005; Tatebe et al., 2020; Zabolotnaya *et al.*, 2020). We also observe a subpopulation of open CC domains exclusively in the presence of ATP, in line with the idea that ATP binding is needed to open the CCs (Lee et al., 2013). Comparison with the crystal structures of *Ct*Rad50NBD in complex with ATPγS reveals that a full engagement of the NBDs with the signature motif binding to the y-phosphate of ATP needs an approx. 60° rotation of NBDs with respect to the other, a movement that would pry the CCs open (**Figure 2C, Video S2)** (Seifert *et al.*, 2016). A switch between a semi-engaged NBD (this study) and engaged NBD (Rad50NBD crystal structures) would be consistent with studies that show partially open and closed conformations of NBDs on archaeal MR (Canny and Latham, 2022). It is likely that cooperative ATP and DNA binding may help to stabilize the open CC conformation with fully engaged NBDs since linear DNA triggers ATP hydrolysis approx. 10-fold in both *C. thermophilum* (**Figure 3F**) and human MRN (Deshpande *et al.*, 2017). Thus, it is reasonable to assume that DNA interacts with MRN after ATP dependent loading on DSBs such that DNA is bound at Rad50's NBDs between the CC, consistent with a prior crystallographic analysis of *Ct*Rad50 and crystal as well as cryo-EM structures of prokaryotic MR in complex with DNA (Kashammer *et al.*, 2019; Liu et al., 2016; Seifert *et al.*, 2016).

However, the spectrum of DNA binding activities by MRN is arguable more complex than for bacterial MR, which only displayed DNA binding activities that were highly specific for DNA ends and fully dependent on ATP (Saathoff *et al.*, 2018). Here we identify the C-terminal extension of eukaryotic Mre11 as responsible for the additional nucleotide independent DNA binding activity, as well as the increased capacity to bind circular compared to linear DNA. A DNA binding site in the C-terminus of *S. cerevisiae* Mre11 has been identified early on and found to be specifically important for the formation of meiotic breaks and chromatin organization at DSBs, but otherwise showed almost wt phenotypes in meiosis (Furuse et al., 1998). Thus, our identified separation of DNA binding modes into one that involves the core head complex and is highly specific for DNA ends and ATP, and another that is ATP independent and extends DNA binding also to undamaged DNA regions could be particularly useful to

dissect the pleiotropic enzymatic and scaffolding functions of MRN in genome biology. We envision that MRN, like bacterial MR, is loaded onto DBSs in a configuration where the DNA end passes through the CCs, while internal DNA is recognized in a more peripheral fashion via the Mre11's C-terminus **(Figure 5C).** However, the molecular details of the different modes of DNA binding to MRN must await future studies.

The separation of binding modes is consistent with and useful to interpret several recent studies. The presence of two modes fits very well with the DNA binding dynamics observed in single-molecule DNA curtain experiments (Myler *et al.*, 2017). The canonical, ATP-dependent Rad50 DNA binding site seems to be responsible for binding to DNA ends, where *Hs*MRN was observed to cleave Ku and itself off in a process that requires ATP. However, before DNA end recognition, MRN was observed to diffuse along linear DNA in an ATP independent fashion. These and our data suggest that MRN binds to internal DNA via a mechanism that involves the Mre11 C-terminus that allows sliding along DNA. Upon engagement of DNA ends MRN is then properly loaded in an ATP-dependent process to form a "cutting" state.

Furthermore, a physiologically occurring truncation of the *Hs*Mre11 C-terminus at a site that matches the one analyzed biochemically by us in *Ct*MRN was identified in human cancer cells and attributed to cleavage by the SPRTN protease (Na *et al.*, 2021). The biochemical analysis showed loss of DNA binding and nuclease activities of MRN *in vitro*, consistent with our work. However, in that study *in vitro* nuclease and DNA binding activities were only assessed in the absence of ATP. As a result, the conclusion that truncation of the Mre11 C-terminus benefits these cancer cells due to loss of all MRN DNA binding should be further studied, as MRNs ATP dependent interaction with DNA ends might still be intact. For instance, the Mre11 truncation could be beneficial to cancer cells because some DSB sensing capacity might still be present, while MRNs poorly understood role in chromosome organization or transcription, a process that could require specifically interaction with intact DNA, could be affected (Forey *et al.*, 2021; Salifou *et al.*, 2021).

Perhaps the most important result of our work is the discovery of the apex dimerization, since this provides an integrated mechanistic framework for both head-associated DNA binding, nuclease, and zinc-hook associated tethering. Numerous studies, starting from early low-resolution negative stain electron microscopy to AFM and cell-based studies show that CC apices from different MR/MRN complexes can associate to form large DNA tethering assemblies *in vitro* and that MRN has functions in tethering or cohesion of different DNA elements (de Jager *et al.*, 2001; He et al., 2012; Hohl *et al.*, 2015; Hopfner *et al.*, 2002; Moreno-Herrero *et al.*, 2005; Park *et al.*, 2017; Seeber *et al.*, 2016; Vera *et al.*, 2022; Zabolotnaya *et al.*, 2020). Based on structural work on the zinc-hook regions, which showed nearly antiparallel (Hopfner *et al.*, 2002) and parallel (Park *et al.*, 2017; Soh *et al.*, 2021) conformations, to date, it was assumed that the dimerization of two zinc-hooks can occur between the CCs of a single

MRN complex (intra-complex) or between the CCs from different MRN complexes (inter-complex), thus tethering MRN. However, the stability of the zinc-hook dimers, the emerging role of the CC domains as a critical chemo-mechanical element, rather than a mere linker element, made it unlikely that zinc-hooks switch from intra- to inter-complex interaction modes. Rather they act as stably associated hinges that can switch between ring and rod states of the CCs of a single MRN complex.

Our cryo-EM data now resolves this prevailing conundrum, showing that two apex regions in the rod configuration can further dimerize to join two MRN-MRN complexes **(Figure 5D).** We believe this clarifies the mode how MRN-MRN dimers are tethered generating large structures spanning up to approx. 120 nm (**Figure 5D**). Apparently, the tethering interaction requires the CC domain to be in the rod configuration. Thus, it is possible that ATP-dependent dynamics and DNA loading at the head have a functional crosstalk with the state of tethering.

The mode of this tether, with a very small hydrophobic anchor surrounded by salt bridges, might be quite transient on a single MRN-MRN level. Since, MRN complexes have the property to form large clusters at DNA ends, likely through head-head interactions (Vera *et al.*, 2022), multiple protruding CC rods from those clusters could form a molecular Velcro through multivalent interactions (de Jager *et al.*, 2001; Zabolotnaya *et al.*, 2020), which could be an interesting way to regulate tethering strength through the size of such clusters **(Figure 5C)**. Likewise, such a cluster could interact with MRN complexes on the sister-chromatid, providing a possible mechanism for the role of MRX in sister-chromatid cohesion at DSBs in *S. cerevisiae* (Seeber *et al.*, 2016). Of note, the type of interface with small hydrophobic parts and ion pairs is characteristic of the types of interactions found in liquid-liquid phase-separated condensates (Banani et al., 2017). Furthermore, an inspection of the crystal lattice of *Ct*Rad50^{apex} shows that even 1D-lattice-like interactions between multiple apices might form, which fit very well with the 1D-lattice geometry of the Rad50NBD dimers bound to DNA. It is therefore possible that DNA tethering by MRN proceeds via multivalent interactions much like those proposed for phase-separated condensates.

The *Hs*Rad50^{hook} crystal lattice revealed a similar tetrameric arrangement with predominantly ionic interactions (**Figure 5A)** (Park *et al.*, 2017). Mutating the apex tethering interface impaired the repair of ROS-mediated DNA damage in human cells, showing its functional significance. Part of the apex-apex interface is also a loop insertion element in the segmented CC that carries an SQ-motif (S635, Q636). This site has been noticed and studied before and it was found to be phosphorylated by both ATM and ATR (Gatei et al., 2011; Gatei et al., 2014). Mutations in S635 affected DSB repair, checkpoint activation and survival, as well as cohesin loading at sites of replication restart (Gatei *et al.*, 2011; Gatei *et al.*, 2014). These phenotypes were not caused by defects in the nuclease activity, since *Hs*MRN^{S635G} had unaltered nuclease activity *in vitro* (Gatei *et al.*, 2011) and indicate that tethering may be subject to regulation by ATM and ATR in human cells. From a structural point of view,

phosphorylation could increase the stability of the tethering through interactions with nearby basic amino acids on the opposing apex protomer, but it could also alter the geometry of the apex and reduce tethering through geometric issues. However, the functional importance of MRN-MRN tethering and its regulation probably differs in different species, since the replacement of the zinc-hook region with the hinge domain of the bacterial SMC protein MukB did not result in increased camptothecin and hydroxyurea sensitivity in *S. pombe* (Tatebe *et al.*, 2020).

In summary, we provide the framework for the molecular architecture of the eukaryotic MRN complex. We reveal an unexpected, closed conformation of the MRN CCs that enables topology-sensitive binding of DNA ends as well as DNA end tethering.

STAR METHODS

LEAD CONTACT AND MATERIALS AVAILABILITY

Further information and requests for resources and reagents should be directed to and will be fulfilled by the Lead Contact Karl-Peter Hopfner (hopfner@genzentrum.lmu.de).

EXPERIMENTAL MODEL AND SUBJECT DETAILS

Organisms as source for materials used in experiments

E. coli XL1 Blue cells were used for amplification of plasmid DNA.

Spodoptera frugiperda sf21 insect cells were used for virus production.

E. coli Rosetta2, *Trichoplusia ni* insect cells and *Homo sapiens* HEK293T were used for recombinant protein expression.

Homo sapiens U2OS cells were used for Comet assays.

METHOD DETAILS

Expression and purification of the *Ct*MRN complex

Codon-optimized synthetic genes (Genscript, Piscataway, USA) encoding *Ct*Mre11, *Ct*Rad50, *Ct*Nbs1 were PCR amplified and cloned into pACEBac1 (*Ct*Mre11, *Ct*Rad50) and pIDK (*Ct*Nbs1) using MultiBac expression system (Berger et al., 2004). Recombination steps were carried out in *Escherichia*

coli XL1Blue cells (Stratagene) under the addition of Cre-recombinase (NEB). Baculoviruses were generated in *Spodoptera frugiperda* (SF21) insect cells (IPLB-Sf21AE) and virus titers were determined by small-scale test expression. 1 L of *Trichoplusia ni* High Five cells (Invitrogen), seeded to 1 mio/mL, were infected with 1:1000 of baculovirus and cultured for 72 h at 27°C. Cells were harvested by centrifugation.

The fresh cell pellet was suspended in 50 mL of Lysis buffer (50 mM HEPES pH 7.0, 250 mM NaCl, 10% glycerol, 0.5 mM TCEP, 5 µL TURBO DNase (Thermo-Fisher Scientific), supplemented with a SIGMAFAST Protease Inhibitor Cocktail Tablet, EDTA free (Merck) on ice. All further purification steps were performed on ice or in an 8°C cold room. The cells were lysed using a Dounce homogenizer followed by sonication for 1 min (50% duty cycle, 5 output control). The lysate was cleared by centrifugation at 17000 rpm for at least 1 h using an SS-34 rotor. The soluble supernatant was prefiltered with a Millex fiber-glass filter (Roth) and filtered using 0.45 µm PVDF membrane filters (Merck Millipore).

The lysate was applied onto a 5 mL HiTrap Heparin HP column (GE Healthcare) attached to an AKTA Pure system (GE Healthcare) and equilibrated in Buffer A (50 mM HEPES pH 7.0, 250 mM NaCl, 10% glycerol, 0.5 mM TCEP). The column was washed with 5 CV Buffer A, 5 CV of 7% Buffer B (50 mM HEPES pH 7.0, 1 M NaCl, 10% glycerol, 0.5 mM TCEP). Protein was eluted with 33% Buffer B, pooled, and dialyzed for 8 h in SEC buffer (20 mM HEPES 7.0, 200 mM NaCl, 10% Glycerol, 0.5 mM TCEP). 1 g (dry mass) cellulose phosphate (CP) fine mesh resin (Merck) was prepared according to protocol and equilibrated in SEC buffer. The dialyzed protein was applied to CP resin, which was washed until no DNA eluted anymore. Protein was eluted by the addition of CP elution buffer (20 mM HEPES 7.0, 400 mM NaCl, 10% glycerol, 0.5 mM TCEP) to a total of 10 CV. The CP eluate was concentrated and applied to size exclusion chromatography (SEC; Superose 6, 10/300, GE Healthcare) in SEC buffer (No glycerol was added for cryo-EM grid preparation). Stoichiometric *Ct*MRN complex eluted at 0.4 CV.

Crosslinking mass spectrometry

Freshly purified MRN complex was diluted in compensation buffer to obtain a protein concentration of 0.25 mg/mL in 20 mM HEPES (pH 7.0), 200 mM NaCl, 5 mM $MgCl_2$, 1 mM $MnCl_2$, 0.2 mM TCEP, 1 mM ATPγS. The complex was incubated for 15 min at 21°C, then a 6.2 mM solution of bis sulfosuccinimidyl suberate (BS3), dissolved in 20 mM HEPES (pH 8.5) buffer, was added to obtain a final concentration of 31.1 µM BS3. The protein was crosslinked for 30 min @ 35°C before it was quenched by the addition of 1 M Tris-HCl (pH 8.0) to a final concentration of 62 mM.

To the crosslinked proteins, 4 M Urea and 50 mM Tris (pH 8.0) were added. The mixture was sonicated using a Bioruptor Plus sonication system (Diogenode) for 10x 30 s at high intensity. Thereafter, 40 mM 2-chloroacetamide (CAA, Sigma-Aldrich) and 10 mM tris(2-carboxyethyl) phosphine (TCEP; Thermo Fisher Scientific) were added for the reduction and alkylation of disulfide bonds. After incubation for 20 min at 37°C, the samples were diluted 1:2 with MS grade water (VWR). Crosslinked proteins were digested overnight at 37°C by addition of 0.5 µg of LysC and 1 µg of trypsin (Promega). Afterward, the mixture was acidified with 10% trifluoroacetic acid (TFA; Merck) in water to a final concentration of 1%, followed by desalting of the peptides using Sep-Pak C18 1cc vacuum cartridges (Waters). Desalted peptides were vacuum-dried.

Vacuum-dried peptides were dissolved in buffer A (0.1% formic acid). For nano-LC separation of the peptides at a flow rate of 250 nL/min, the Thermo Easy-nLC 1000 (Thermo Fisher Scientific) equipped with a 30-cm analytical column (inner diameter: 75 microns; packed in-house with ReproSil-Pur C18-AQ 1.9-micron beads, Dr. Maisch GmbH) was used. Through the nanoelectrospray interface, eluting peptides were sprayed into the benchtop Orbitrap Q Exactive HF (Thermo Fisher Scientific)(Scheltema et al., 2014). As gradient, the following steps were programmed with increasing addition of buffer B (80% acetonitrile, 0.1% formic acid): linear increase from 8 to 30% over 60 minutes, followed by a linear increase to 60% over 5 minutes, a linear increase to 95% over the next 5 minutes, and finally maintenance at 95% for another 5 minutes. The mass spectrometer was operated in data-dependent mode with survey scans from m/z 300 to 1650 Th (resolution of 60k at m/z = 200 Th), and up to 15 of the most abundant precursors were selected and fragmented using stepped Higher-energy collisional Dissociation (HCD with a normalized collision energy of value of 19, 27, 35). The MS2 spectra were recorded with a dynamic m/z range (resolution of 30k at m/z = 200 Th). AGC targets for MS1 and MS2 scans were set to 3×10^6 and 10^5, respectively, within a maximum injection time of 100 and 60 ms for the MS1 and MS2 scans, respectively. Charge state 2 was excluded from fragmentation to enrich the fragmentation scans for cross-linked peptide precursors.

The acquired raw data were processed using Proteome Discoverer (version 2.5.0.400) with the XlinkX/PD nodes integrated (Klykov et al., 2018). To identify the crosslinked peptide pairs, a database search was performed against a FASTA containing the sequences of the proteins under investigation as well as a contaminant database. DSS was set as a crosslinkers. Cysteine carbamidomethylation was set as fixed modification and methionine oxidation and protein N-term acetylation were set as dynamic modifications. Trypsin/P was specified as protease and up to two missed cleavages were allowed. Furthermore, identifications were only accepted with a minimum score of 40 and a minimal delta score of 4. Otherwise, standard settings were applied. Filtering at a 1% false discovery rate (FDR) at peptide level was applied through the XlinkX Validator node with setting simple.

The crosslinks were analyzed and visualized using the xVis Crosslink Analyzer Webserver and the Xlink Analyser software for UCSF Chimera(Grimm et al., 2015; Kosinski et al., 2015; Pettersen et al., 2004).

Cryo-EM grid preparation

Freshly purified MRN complex was diluted in compensation buffer to obtain a protein concentration of 0.27 mg/mL in 20 mM HEPES (pH 7.6), 200 mM NaCl, 5 mM $MgCl_2$, 1 mM $MnCl_2$, 20 µM $ZnCl_2$, 0.2 mM TCEP, 2 mM ATPγS. The complex was incubated for at least 10 min at 21°C to bind ions and nucleotide. Just before plunging, Octyl β-D-glucopyranoside (β-OG) was added to a final concentration of 0.05%. Grids were prepared using a Leica EM GP plunge freezer (Leica). β-OG containing sample (4.5 µl) was deposited onto plasma cleaned (GloQube, Quorum) copper grid (Cu 200, R2/1, Quantifoil). The sample was applied to the grids at 15°C and 95% humidity and blotted for 2.7 s before plunge-freezing the grid in liquid ethane.

Cryo-EM data acquisition

Six datasets of *Ct*MRN-ATPγS (a total of 29349 micrographs) were acquired on a Titan Krios transmission electron microscope (Thermo Fisher Scientific) operated at 300 kV, with a K2 summit direct electron detector (Gatan) operated in counting mode and energy filter (Gatan). Data acquisition was automated with the EPU (Thermo Fisher Scientific) software package. Images were recorded at a nominal magnification of 130,000x (1.059 Å/pix) with a defocus range of 1.0 µm to 2.8 µm, and a total dose of 45 $e^{-}/Å^2$ over 40 frames.

Cryo-EM image processing

Motion correction with MotionCor2 and CTF estimation with CTFFind4 were performed on the fly for all datasets using an in-house developed pipeline (Rohou and Grigorieff, 2015; Zheng et al., 2017). Further processing was performed using Relion v3.0 (Zivanov et al., 2018) and CryoSPARC v3.2.0 (Punjani et al., 2017), and older versions. Initially, particles were picked in CryoSPARC using the implemented blob picker. After 2D classification, selected particles were used to train the TOPAZ deep picker(Bepler et al., 2020). TOPAZ was trained iteratively until no further increase in particle numbers and particles were extracted using box sizes of 768 pix (Long CC map), 352 pix (Catalytic head map), 352 pix (ZH tetramer).

Initial models were generated using CryoSPARC ab-initio reconstruction. The particles for the Catalytic head map were transferred to Relion, further sorted by 2D classification and subjected to focused 3D refinement by masking the catalytic head. This resulted in the C1 map of the catalytic head at 4.0 Å. Further, focused 3D classification resulted in five different classes that showed different degrees of Nbs1 binding to the catalytic head. Non-uniform (NU) refinement of the Long CC particles in CryoSPARC led to a C2 map with 4.8 Å overall resolution. Further local refinements of the C2 maps led to two maps of the CCs with 6.8 Å and 7.6 Å, respectively. Maps were LAFTER filtered (ref) in the CCP-EM software suite (ref). The full compliment of picked particles were additionally processed independently in CryoSparc. Particles were initially sorted by rounds of 2D classification and heterogeneous refinement. 3D variability was used to divide the particles by Rad50 orientation. The classes corresponding to the extremes of Rad50 motion were used for heterogeneous refinement. The most stable class further processed by non-uniform refinement producing a map of the catalytic head with extended Rad50 coiled coils and the Mre11 bridge at an overall resolution of 3.92 Å. Local refinement with a mask for Nbs1 and the Mre11 phosphodiesterase domains produced a map of Nbs1 interactions at 3.75 Å.

The ZH particles were processed in CryoSPARC. An ab-initio reconstruction was created from the particles picked in TOPAZ. Particles were repicked and sorted via heterogeneous refinement with 5 references from a ZH tetramer, ZH octamer, Mre11, MRN catalytic head, and a part of the CCs. The ZH particles were pooled and sorted via iterative rounds of 2D classification. From NU refinement, followed by local refinement a 4.9 Å C2 map of the ZH was calculated. To avoid over-refining, the map was eventually filtered to 7 Å.

Model building

The MRN head and coiled coils model was prepared using a combination of crystal structure templates, AlphaFold predictions, and *de novo* building. Initial models were rigid body fitted in Chimera (ref), using 4KYE (ref) for the Mre11 phosphodiesterase and capping domains, and 5DA9 (ref) for the Mre11 RBDs and Rad50 nuclease domains and coiled coils until residues 214 and 1107. Alphafold2 predictions were used as templates for Nbs1 (606 to 689) bound to the Mre11 phosphodiesterase dimer, Rad50 DNA binding site loops (1176 to 1187) and coiled coils (215 to 1106), and Mre11 bridge (523 to 557) (Figure S3F). Further model building and refinement was performed in Coot 0.9 (ref). Initial models were morphed into EM density by real space refinement with local restrains, then further refined with optional restraints based on local resolution. Regions not matching the initial models, in particular the non-symmetric loops, were manually built. The model was refined against several focused maps, and LAFTER filtered maps were used for poorly resolved and partially flexible regions. The Mre11-Rad50 head module was refined against EMD-14880. Nbs1 and interacting residues of Mre11 were

refined against EMD-14877. Mre11 RBD and bridge, and the neighbouring Rad50 coiled coils and loops were refined against EMD-14876. The remaining Rad50 coiled coils were refined against EMD-14878 and EMD-14879. Real space refinement and validation were performed in Phenix 1.20.1 (ref).

DNA stimulated ATPase assays

We used an NADH-coupled assay to monitor the rate of ATP hydrolysis by *Ct*MRN. The ATPase rate was assayed in reaction buffers containing 250 nM MRN complex, 20 mM HEPES pH 7.0, 80 mM NaCl; 5 mM MgCl2, 1 mM MnCl2, 0.1 mg/mL BSA, 0.2 mM TCEP, 0.25 mM NADH, 20 U/ml PK, 30 U/ml LDH, 2 mM Phosphoenolpyruvate (PEP), the reaction was started by addition of 1 mM ATP and 52 ng/µL DNA. The measurements were started immediately after ATP addition for 2 h at 37 °C. The oxidation rate of NADH was assayed fluorometrically by measuring the fluorescence at 460 nm (excitation 340 nm) on a Tecan microplate reader (Infinite M1000).

Direct fluorescence polarization anisotropy (nucleotide dependence)

Fluorescence polarization anisotropy was used to monitor *Ct*MRN and *Ct*M$^{\Delta C}$RN binding to 80 bp dsDNA. 5 nM of 3' 6-FAM-labeled DNA was incubated with increasing amounts of MRN in ATP (20 mM HEPES pH 7.0, 100 mM NaCl, 5 mM $MgCl_2$, 0.2 mg/ml BSA, 1 mM ATP, 0.5 mM TCEP), ATPyS (20 mM HEPES pH 7.0, 100 mM NaCl, 5 mM $MgCl_2$, 0.2 mg/ml BSA, 1 mM ATPyS, 0.5 mM TCEP) and no nucleotide (20 mM HEPES pH 7.0, 100 mM NaCl, 5 mM $MgCl_2$, 0.2 mg/ml BSA, 0.5 mM TCEP) assay buffers. All DNA binding reactions were done without the addition of $MnCl_2$ to avoid DNA degradation. After 15 min incubation at 37 °C, the fluorescence anisotropy was measured at an excitation wavelength of 488 nm and an emission wavelength of 520 nm using an automated polarization microscope(Jung et al., 2018; Jung et al., 2019). Each sample was measured at twelve different z-planes to reduce the effect of potential fluorescing protein-DNA aggregates that could lead to erroneous FA values, these measurements were repeated three times for each of the 3-4 replicates. The FA values were calculated for each image using the following formula, requiring the parallel ($I^{=}$) and perpendicular (I^{+}) fluorescence intensities and the instrumental G-factor (G = 1.15 for our setup, as determined by measuring free dye in solution). Regions of interest (ROI) were defined as equal-sized regions around the maxima in the respective channels.

$$FA(z,t) = \frac{I^{=}(z,t) - GI^{+}(z,t)}{I^{=}(z,t) + 2I^{+}(z,t)}$$

Finally, we calculated for each sample the median FA value of all images acquired from a given well to reduce variability, namely the contribution to FA of images containing potential Protein-DNA aggregates.

Competitive fluorescence polarization anisotropy (topology dependence)

Fluorescence polarization anisotropy was used to monitor *Ct*MRN and *Ct*M$^{\Delta C}$RN binding to linear and circular DNA. 5 nM of 3' 6-FAM-labeled 80 bp dsDNA was incubated with 45 nM MRN in ATPyS containing assay buffer (20 mM HEPES pH 7.0, 100 mM NaCl, 5 mM $MgCl_2$, 0.2 mg/ml BSA, 1 mM ATP, 0.5 mM TCEP). After 10 min incubation, increasing amount of either circular or linear (obtained by digesting of circular DNA with PvuII-HF NEB) pUC19 plasmid DNA was added. After 15 min incubation at 37 °C, the fluorescence anisotropy was measured using the same setup as described above.

Fluorescence imaging and segmentation of protein-DNA aggregates

To characterize the relative amount of aggregates between samples, we acquired for each sample z-stacks of widefield fluorescence images. Image segmentation of the aggregates was performed using a custom-written Definiens XD 2.0 script (Munich, Germany). The image analysis procedure was the following. The individual aggregates appear in bright, relatively round objects within a heterogeneous background arising from the inhomogeneous widefield illumination. To facilitate the detection of the contour of the objects, we applied a 3D-Gaussian filter with a kernel size of 5 × 5 × 3 pixels, followed by a second 3D-Gaussian filter with the same kernel size. We then subtracted the latter image from the previous one. This procedure resulted in a background-subtracted image. Then, we applied a global threshold and carried out segmentation using an algorithm implemented in the Definiens XD 2.0 software platform. Briefly, the Multi-Threshold Segmentation algorithm splits the image domain and classifies the resulting image objects based on a defined pixel value threshold. This results in segmented patterns classified as "aggregates" or "background". We then extracted for each frame the total number of aggregate particles, their size (in a 2D projection within our optical resolution of about approx. 0.5 µm), and their average fluorescence intensity. The latest parameter can be assumed to be proportional to the number of protein-DNA aggregating in a single particle.

Crystallization and structure determination of the *Ct*Rad50 Zn-hook domain

Codon-optimized synthetic DNA (Genscript, Piscataway, USA) encoding *Ct*Rad50$^{598\text{-}782}$ was PCR amplified and cloned into pET47b (6xHis-HRV3C-*Ct*Rad50$^{598\text{-}782}$). The construct was expressed in

Escherichia coli BL21 Rosetta cells (Novagen). 0.5 L of *E. coli* culture were grown in TURBO Broth™ medium (Molecular Dimensions) containing Kanamycin (50 µg/mL) and Chloramphenicol (34 µg/mL) at 37°C to an OD_{600} of 2.0 before induction with 0.4 mM IPTG. Upon induction, further cultivation was performed at 18°C, until the cells reached an OD_{600} of 7.0.

The cells were harvested via centrifugation (10 min, 3000 g, 4°C) and resuspended in 150 mL lysis buffer (50 mM HEPES 7.5, 250 mM NaCl, 10 % Glycerol, 5 mM β-Mercaptoethanol, 2 µL TURBO DNase (Thermo-Fisher Scientific), supplemented with a SIGMAFAST Protease Inhibitor Cocktail Tablet, EDTA free (Merck). The cells were lysed via sonication for 3x 3 min (50% duty cycle, 5 output control), and cleared lysate was prepared by centrifugation at 17 000 rpm for 1 h using an SS-34 rotor.

5 mL Ni-NTA beads (Macherey-Nagel) were equilibrated in Buffer A (50 mM HEPES 7.5, 250 mM NaCl, 10 % Glycerol, 5 mM β-mercaptoethanol) and incubated with cleared lysate for 1h at 8°C on a rolling incubator. The beads were washed with 3 CV of Buffer A, 3 CV Buffer A and 20 mM Imidazole, followed by 3 CV Buffer A. 5 mL of Buffer A containing 50 µL HRV3C protease (Cytiva) were added, and the beads were incubated over night at 8°C on a rolling incubator. On the next day the eluate was applied to a fresh 5 mL of Ni-NTA, equilibrated in Buffer A and the flow-through was collected. EDTA was added to a final concentration of 1 mM and the protein was concentrated to 30 mg/ml. A Superose 200 16/60 HiLoad column (Cytiva) was equilibrated in SEC buffer (20 mM HEPES 7.5, 150 mM NaCl, 1 mM EDTA, 5% Glycerol, 0.5 mM TCEP) and 3 mL of the concentrated protein sample was injected. The eluate was fractionated and analyzed on SDS PAGE.

Crystals of *Ct*Rad50$^{598\text{-}782}$ were grown in hanging drops by mixing 1.5 µl protein at 4.5 mg/mL and 1.5 µl reservoir solution (0.1 M MES pH 6.8, 0.6 M NaCl, 18% PEG4000). The crystals were soaked in a reservoir solution supplemented with 10% 1,4-butanediol and frozen in liquid Nitrogen. X-ray data to a resolution of 2.5 Å were collected at EMBL Hamburg P14 beamline at PETRA III storage ring (DESY Hamburg) at 100K. Data were indexed, integrated and scaled with XDS/XSCALE in space group P1 (Kabsch et al.). The structure was solved by molecular replacement with the program Phaser using a Rad50 Zn-hook search model calculated by AlphaFold2 (Phaser, Jumper et al. 2022). Model building was done in COOT and refinement was performed with PHENIX (Coot Phenix). Prior to model building and refinement, we randomly omitted 10% of the reflections for monitoring the free R value. Data collection and model statistics are stated in Supplementary table 2. All figures were prepared using Chimera or ChimeraX (Chimera).

Comet assay

Cells and culture conditions: The human osteosarcoma cell line U2OS (RRID:CVCL_0042) was cultivated in DMEM containing 10% fetal bovine serum (FBS) and penicillin/streptomycin at 37°C in a humidified 5% CO_2 atmosphere.

Protein extracts and Western blot analysis: Whole-cell protein extracts were prepared by disrupting cell pellets in Lysis Buffer (20 mM tris, 1 mM EDTA, 1 mM β-mercaptoethanol, 5% glycerine, pH 8.5) supplemented with various protease and phosphatase inhibitors (0.02 M β-glycerophosphate, 1 mM Na_3VO_4, 0.1 mM phenylmethylsulfonyl fluoride, 0.01 mM MG-132, 0.01 M dithiothreitol, 0.01 M NaF and cOmplete^{TM}) using sonification. The protein concentration was determined using the Bradford method as described (Bradford, 1976). 30 µg of protein were separated by sodium dodecyl sulfate-polyacrylamide gel electrophoresis (SDS-PAGE) and transferred overnight at 100 mA in blotting buffer (0.025 M tris, 0.192 M glycine, 20% methanol) onto a nitrocellulose membrane. All primary antibodies were used at 1:1000 dilution in 5% BSA in tris buffered saline (TBS) containing 0.1% Tween and 1% Na-Azide. The antibodies used were anti-RAD50 (Cell Signalling, #3427) and anti-Vinculin (Santa Cruz, sc-73614). The secondary antibodies (Li-COR Bioscience) were diluted (1:10000) in TBS containing 0.1% Tween and the proteins were visualized using the Odyssey® Infrared Imaging System (LI-COR Biotechnology).

Transfections: For RAD50 knockdown, U2OS cells were transfected with siRNA targeting RAD50 (s792, Silencer®Select, ThermoFisher Scientific) and negative control siRNA (#AM4611; Life Technologies) using Lipofectamine RNAiMAX (Invitrogen), according to the manufacturer's instructions. The siRNA-mediated knockdown of RAD50 was confirmed at the protein level using Western blot analysis.

For RAD50 wild-type and mutant expression, the plasmids pACEMam1_pMDC_*Hs*MRN and pACEMam1_pMDC_*Hs*MR^{apex}N were transfected into U2OS cells using Polyethylenimine Hydrochloride (PEI) (#24765; Polysciences). 1 µg plasmid DNA was mixed with 4 µg PEI in 200 µl serum and antibiotic-free DMEM medium, 45 min later the DNA/PEI complex was added to the cells dropwise. The RAD50 expression was confirmed by Western blot analysis.

Neutral comet assay: DNA double-strand breaks (DSBs) and their repair was monitored by single-cell gel electrophoresis under neutral conditions. RAD50 was knocked down in U2OS cells, 8 hours later the cells were transfected with the MR123, MR132, or MR133 expression plasmids. 16 h later the knockdown and transfected cells were reseeded into three Petri dishes, designated untreated, tert-Butyl hydroperoxide (t-BuOOH) treated, and t-BuOOH treated with 2 h repair. The next day, the cells were exposed to 150 µM t-BuOOH for 1 h. The comet assays were performed, as described (Nikolova et al., 2017). Shortly, cells were embedded in 0.5 % low melting point agarose in PBS and spread onto glass

slides coated with 1.2 % agarose. All following steps were performed at 4°C unless stated otherwise. Cells were lysed in lysing solution (2.5 M NaCl, 100 mM EDTA, 10 mM Tris, 1% Na-Laurylsarcosinate, 1% Tryton X-100) at a pH of 7.5. Slides were electrophoresed for 25 min in electrophoresis buffer (90 mM Tris, 90 mM boric acid, 2 mM EDTA, pH= 7.5) at 7.4 V/cm, fixed in 100% methanol, and then dried. All following steps were performed at room temperature. DNA was stained using propidium iodide (50 µg/ml) and 50 cells per slide were evaluated using a fluorescence microscope and the Comet IV software (Perceptive Imaging, Liverpool, UK).

Quantification and statistical analysis

For ATPase assay, the linear decrease in fluorescence between 200 s and 800 s was fitted to a linear regression in GraphPad Prism and the slope was used to calculate the ATPase rate using the following formula (Figure 3E, F). The NADH slope was calculated using a calibration curve which was recorded by titrating ADP to a constant NADH solution in a reaction buffer without MRN/DNA.

$$ATPase\ rate\ [ATP\ complex^{-1}s^{-1}] = \frac{slope\ [FU\ s^{-1}]}{NADH\ slope\ \left[-587.9\ \frac{FU}{\mu M\ ATP}\right] c_{MRN}\ [\mu M\ complex]}$$

Direct fluorescence anisotropy data were analyzed using Prism (GraphPad) and K_D values derived by fitting the anisotropy data to a Specific binding with Hill slope model, using the following formula (Figure 3A, B):

$$FU = \frac{B_{max}\ [MRN\ in\ nM]^h}{{K_D}^h\ [MRN\ in\ nM]^h}$$

Competitive fluorescence anisotropy data were analyzed using Prism (GraphPad) by fitting the anisotropy data to a One phase decay model, using the following formula, K_D was calculated as ln(2)/K (Figure 3C, D).

$$FU = (FU_{max} - FU_{min})\ e^{-K\left[DNA\ in\ {}^{ng}/_{\mu l}\right]} + FU_{min}$$

Data of fluorescence imaging and segmentation of protein-DNA aggregates were plotted using Prism (GraphPad) (Figure S6B).

Neutral comet assay data are expressed as tail intensity, which denotes the percentage of DNA in the tail multiplied by the length between the center of the head and tail and plotted using GraphPad Prism (Figure 5B).

Data and code availability

The coordinate files generated during this study are available at the Protein Data Bank (https://www.rcsb.org/) with the accession codes PDB: 7ZR1 (*Ct*MRN head & coiled coils) and PDB: 7ZQY (*Ct*Rad50 zinc-hook tetramer). The cryo-EM reconstructions generated during this study are available at the Electron Microscopy Data Bank (https://www.ebi.ac.uk/pdbe/emdb/) with the accession codes EMDB: EMD-14881 (Composite map of *Ct*MRN head & coiled coils), EMDB: EMD-14880 (*Ct*MRN catalytic head), EMDB: EMD-14876 (*Ct*MRN RBD & bridge), EMDB: EMD-14877 (*Ct*MRN catalytic head & Nbs1), EMDB: EMD-14878 (*Ct*MRN long coiled coils), EMDB: EMD-14879 (*Ct*MRN distant coiled coils), EMDB: EMD-14882 (*Ct*Rad50 zinc-hook tetramer). Custom-written script for fluorescence anisotropy analysis is made available (https://github.com/GeneCenterMunich/HiP-FA). Any additional information required to reanalyse the data reported in this paper is available from the lead contact upon request.

Acknowledgements

EM data were collected at the Cryo-EM Core Facility of the Gene Center, Department of Biochemistry, LMU, Munich. We are grateful for the support by G. Witte for help in the collection of X-ray diffraction data. Funding was provided by the Deutsche Forschungsgemeinschaft (CRC1361, Gottfried Wilhelm Leibniz-Prize, SFB1361 and GRK1721 to K.P.H., CRC1054 to K.L.) and a PhD fellowship from Boehringer Ingelheim Fonds (BIF) to E.v.d.L.

Author contributions

M.R., K.S., E.v.d.L., A.A., B.K., were involved in protein production, crystallization, and *in vitro* assays. M.R., K.S., K.L., J.D.B, A.A., and K.P.H. carried out structural studies. C.J. performed fluorescence anisotropy measurements and segmentation of protein-DNA aggregates. W.P.R. contributed the *in cellulo* comet assays to quantify the DNA repair efficiency. B.S. processed crosslinked complexes and performed mass spectrometry analysis. K-P.H designed overall research and

provided funding. All authors were involved in the interpretation of data, final manuscript preparation, and approval.

Declaration of interests

None of the authors declares competing interests. A.A. contributed as an employee at the Gene Center, Department of Biochemistry, LMU at the time of the study and is currently an employee of CureVac, Tübingen, Germany.

Main Figures:

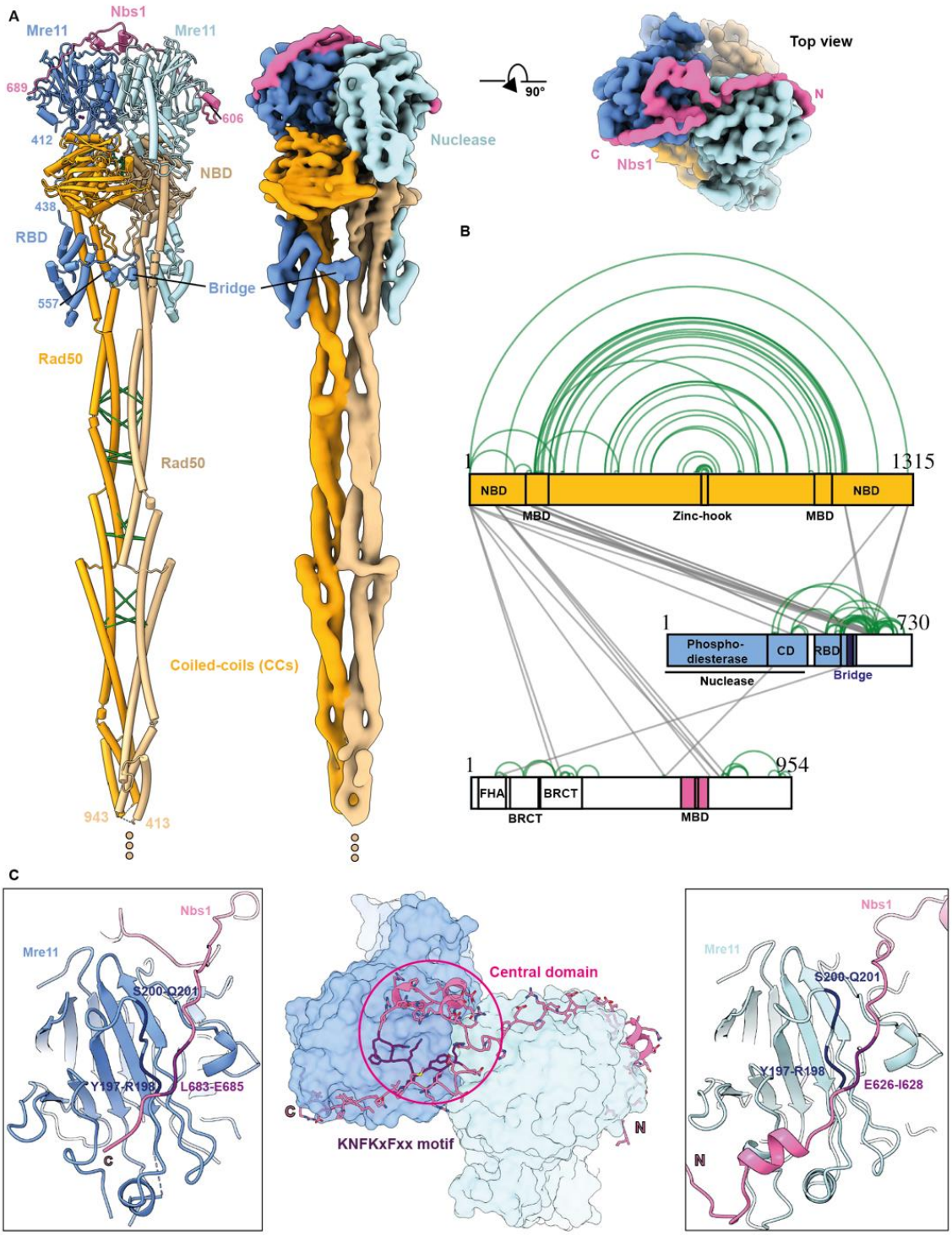

Figure 1: Structure of the MRN complex in resting state

(A) CryoEM structure and composite map of the MRN complex with CCs in a closed conformation. The map was created by combining the higher resolution maps of different regions. The atomic model of the catalytic head domain and 30 nm of the Rad50 CCs region is shown, whereas Mre11 is colored blue, Rad50 orange, and NBS1 pink, respectively. Crosslink restraints obtained by CX-MS are labeled green in the Coiled coil domain.

(B) Graphical overview of the Lysine-specific chemical cross-linking mass spectrometry results (CX-MS). The crosslinks are highly consistent with the model and validate the fitting of the AlphaFold2 predicted CC part. Colored portions indicate structurally characterized parts of each protein.

(C) A single Nbs1 polypeptide (colored pink) binds asymmetrically across both Mre11 phosphodiesterase domains (colored blue). The interfaces of the N- and C-terminal region, which bind with reverse polarity to equivalent regions on Mre11, as well as the central core region harboring the conserved KNFKxF motif, are shown.

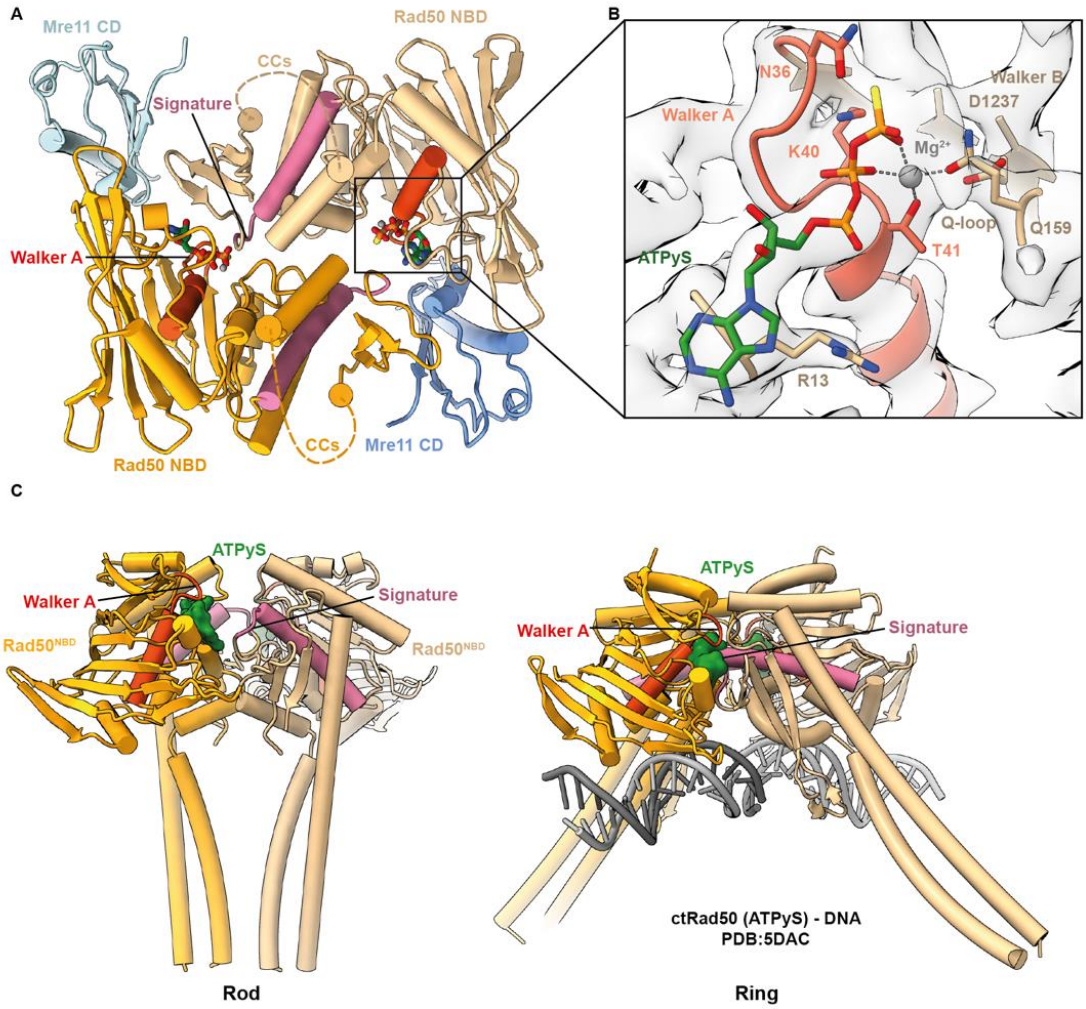

Figure 2: Rad50 in a pre-engaged ATP state

(A) Bottom view of Rad50 NBDs with ATPγS bound. Enzymatically important elements are highlighted.

(B) Close-up view of the coordinated Mg^{2+} and ATPγS in the NBD of Rad50. The Mg^{2+} ion is depicted in gray and enzymatically important residues are annotated and illustrated as sticks. The atomic model is overlaid by the cryoEM map.

(C) A comparison of the cryoEM structure with the ATPγS bound Rad50 crystal structure (PDB code: 5DAC) illustrates the differences in Rad50NBD dimerization and the pre-engaged state of Rad50 in the MRN complex. In the cryoEM structure, the signature motifs are ~10Å away from the γ-(thio)phosphate of ATPγS. In the fully engaged crystal structure, the signature motif interacts with the γ-(thio)phosphate of the "trans" ATP inducing a "power stroke" to the Rad50 and the CC domain.

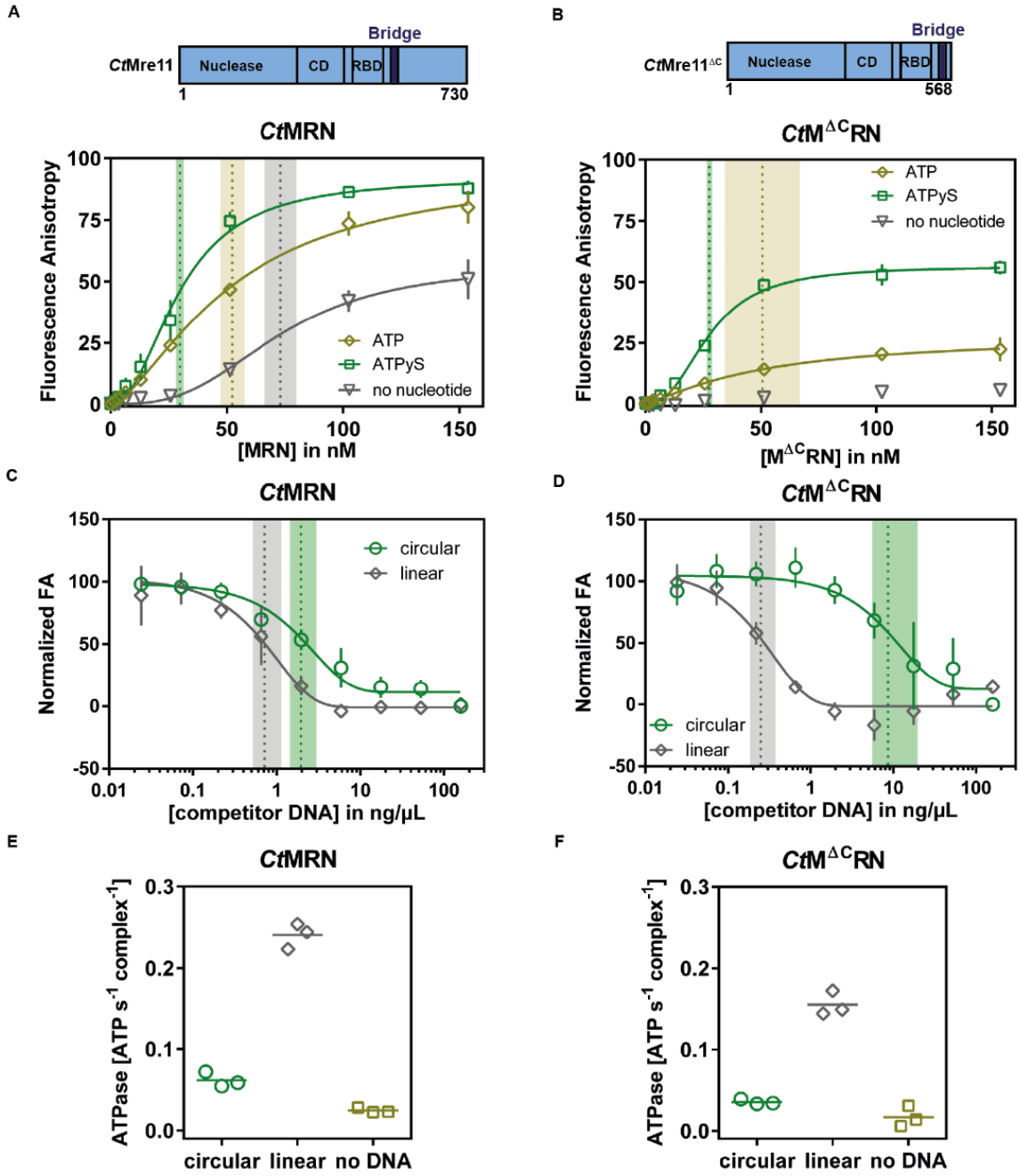

Figure 3: ATP dependent and independent DNA binding by MRN

(A) Top, depiction of full-length *Ct*Mre11 construct used in the DNA binding and ATPase assays. Fluorescence anisotropy-based assay documenting the effect of ATP and ATPγS on *Ct*MRN binding towards 80-mer dsDNA. The wild-type complex binds cooperatively to dsDNA also in the absence of ATP.

(B) Depiction of *Ct*Mre11$^{\Delta C}$ construct used in the DNA binding and ATPase assays. Similar Fluorescence anisotropy assay as in (A) using the C-terminal truncated *Ct*M$^{\Delta C}$RN complex. *Ct*M$^{\Delta C}$RN binding to DNA was nearly abolished in the absence of ATP/ATPyS, while it retained DNA binding in the presence of ATP or ATPyS.

(C) DNA binding competition assay utilizing the FA-based experiment as in (A and B) and adding increasing amounts of unlabeled circular or linearized plasmid DNA to the experiment. The results reveal that *Ct*MRN binds linear and circular DNA with a similar affinity.

(D) DNA binding competition assay as in (C) showing that *Ct*M$^{\Delta C}$RN complex has a strong preference for linear DNA.

(E) ATPase assays of *Ct*MRN showing the stimulation of the ATP hydrolysis rate by the addition of linearized DNA.

(F) ATPase assays of *Ct*M$^{\Delta C}$RN showing the stimulation of the ATP hydrolysis rate by the addition of linearized DNA, as for *Ct*MRN.

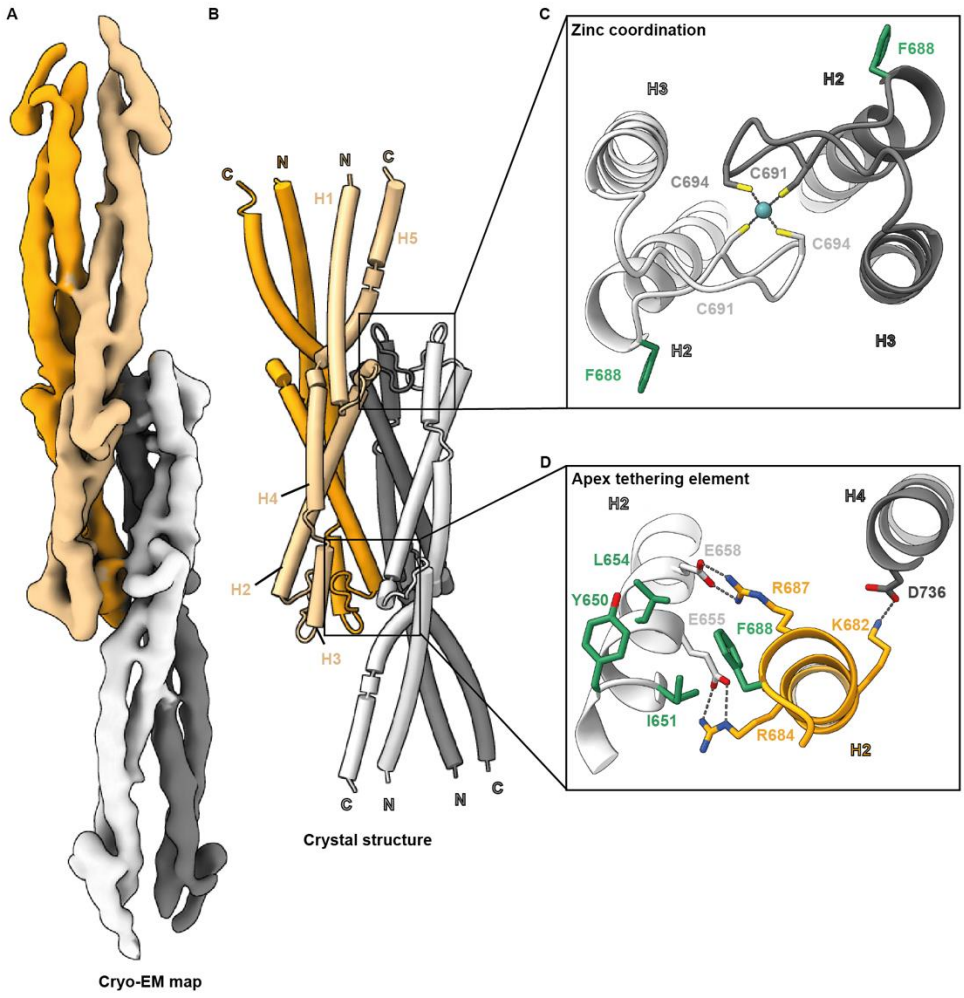

Figure 4: Structure of the *Ct*Rad50 zinc-hook tetramer

(A) CryoEM map of zinc-hook tetramer at 4.9 Å resolution, where each Rad50 monomer belonging to one MRN complex is depicted in related color.

(B) Atomic model of the zinc-hook tetramer crystal structure shown in comparison to the cryoEM map.

(C) Close-up view of the Zn^{2+} binding site.

(D) Rad50 apex tethering element with the residues involved in the interaction are shown in stick representation.

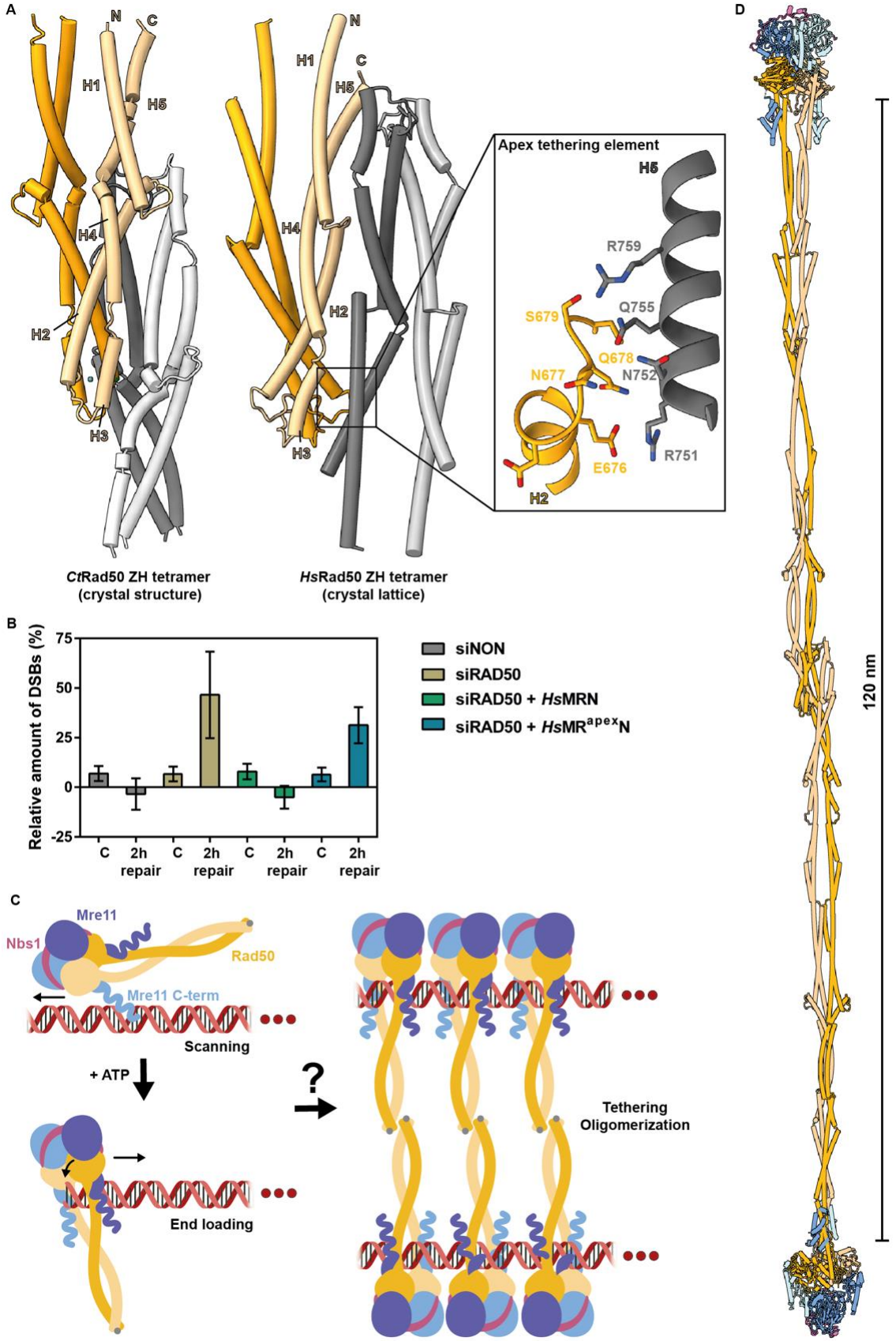
A
N
C
H1
H5
H4
H2
H3
CtRad50 ZH tetramer
(crystal structure)
HsRad50 ZH tetramer
(crystal lattice)
Apex tethering element
R759
Q755
S679
Q678
N677
N752
E676
R751
B
Relative amount of DSBs (%)
75
50
25
0
-25
C
2h repair
siNON
siRAD50
siRAD50 + HsMRN
siRAD50 + HsMRapexN
C
Mre11
Nbs1
Rad50
Mre11 C-term
Scanning
+ ATP
End loading
?
Tethering
Oligomerization
D
120 nm

Figure 5: Zinc-hook mediated MRN-MRN tethering.

(A) Comparison of *Ct*Rad50 and *Hs*Rad50 zinc-hook tetramers. Crystal structure of *Ct*Rad50 zinc-hook tetramer and crystal lattice of *Hs*Rad50 zinc-hook (PDB:5GOX) tetramer indicates conserved zinc-hook tethering mechanism. Inset illustrates the apex tethering element (orange Rad50 side chains) and its interactions.

(B) Mutation of apex tethering element in human MRN impairs DNA repair *in cellulo*. DNA comet assay shows the relative amount of DNA double-strand breaks (DSBs) after 2h following the treatment (or control without the treatment) of U2OS cells with tert-Butyl hydroperoxide. Cells treated with siRAD50 show high levels of DNA damage. Transfection with wild-type human MRN decreases DNA damage to control levels, while transfection with $MR^{apex}N$ does not.

(C) Proposed model of DNA scanning, end detection and DNA tethering by eukaryotic MRN. MRN complex scans DNA via the C-terminus of Mre11. Upon DNA end detection, MRN loads onto DNA in an ATP-dependent mechanism and binds DNA via the canonical Rad50 binding site. Further oligomerization may occur via Rad50 NBDs and zinc-hook leading to DNA end tethering. Details of DNA binding in the tethering mode need to be addressed in future work.

(D) Model of Rad50 zinc-hook mediated MRN dimer. This structure could bridge DNA ends that are up to 120 nm apart.

Table 1. Cryo-EM Data Collection, 3D Reconstruction and Model Refinement Statistics

	Composite (EMD-14881 PDB-7ZR1)	Head (EMD-14880)	long coiled-coils (EMD-14878)	Distant coiled-coils (EMD-14879)	RBD &bridge (EMD-14876)	Nbs1 (EMD-14877)	Zn hook (EMD-14882)
Data collection and Processing							
Magnification	130,000						
Voltage (kV)	300						
Electron exposure (e-/ Å^2)	44.68 44.90 45.27 37.92						
Defocus range (µm)	-1.2 to -2.8						
Pixel size (Å)	1.059						
Symmetry imposed	C1/C2	C1	C2	C2	C1	C1	C2
Initial particle images (no.)	-	288,443	211,134	211,134	1,841,184	1,841,184	995,751
Final particle images (no.)	-	288,443	71,734	71,734	137,843	137,843	32,603
Map resolution (Å)	-	4.0	4.8	7.6	3.9	3.8	4.9
FSC threshold	-	0.143	0.143	0.143	0.143	0.143	0.143
Map resolution range (Å)	-	3.7-5.6	3.1-12.5	6.3-11.5	3.2-8.5	3.2-8.2	4.5-10.7
Refinement							
Initial model	4YKE, 5DA9, Alphafold						
Model resolution (Å)*	6.0	4.2	8.4	10.0	7.7	4.0	
FSC threshold	0.5	0.5	0.5	0.5	0.5	0.5	
Map sharpening B factor (Å^2)	-	-140	0	0	-186	-171	
Model Composition							
Non-hydrogen atoms	21793						
Protein residues	2686						
Ligand	4 Mn 2 Mg 2 ATPyS						
B factors (Å^2)							
Protein	7.38/349.16/164.49						
Ligand	107.84/252.96/178.22						
R.m.s. deviations							
Bond lengths (Å)	0.007						
Bond angles (°)	1.161						
Validation							
MolProbity score	0.99						
Clashscore	1.13						
Poor rotamer (%)	0.59						
Ramachandran plot							
Favored (%)	97.03						
Allowed (%)	2.97						
Disallowed (%)	0						

***Model resolution refers only to the average resolution of region the of composite model refined within that map.**

Table 2. Data collection and refinement statistics (molecular replacement)

	Zinc-hook (PDB:7ZQY)
Data collection	
Space group	P1
Cell dimensions	
a, *b*, *c* (Å)	43,49 53,97 110,42
α, β, γ (°)	75,847 78,742 89,996
Resolution (Å)	2,5 *
R_{sym} or R_{merge}	7,8 (67,4)
$I / \sigma I$	7,86 (1,72)
Completeness (%)	97,4 (91,3)
Redundancy	3,55
Refinement	
Resolution (Å)	2,5
No. reflections	63 401
R_{work} / R_{free}	26,42 /28,30
No. atoms	
Protein	5801
Ligand/ion	2 Zn
Water	3
B-factors (Å^2)	
Protein	81
Ligand/ion	79,5
Water	75,55
R.m.s. deviations	

Bond lengths (Å)	0,012
Bond angles (°)	1,779

*Values in parentheses are for highest-resolution shell.

Supplementary Figures:

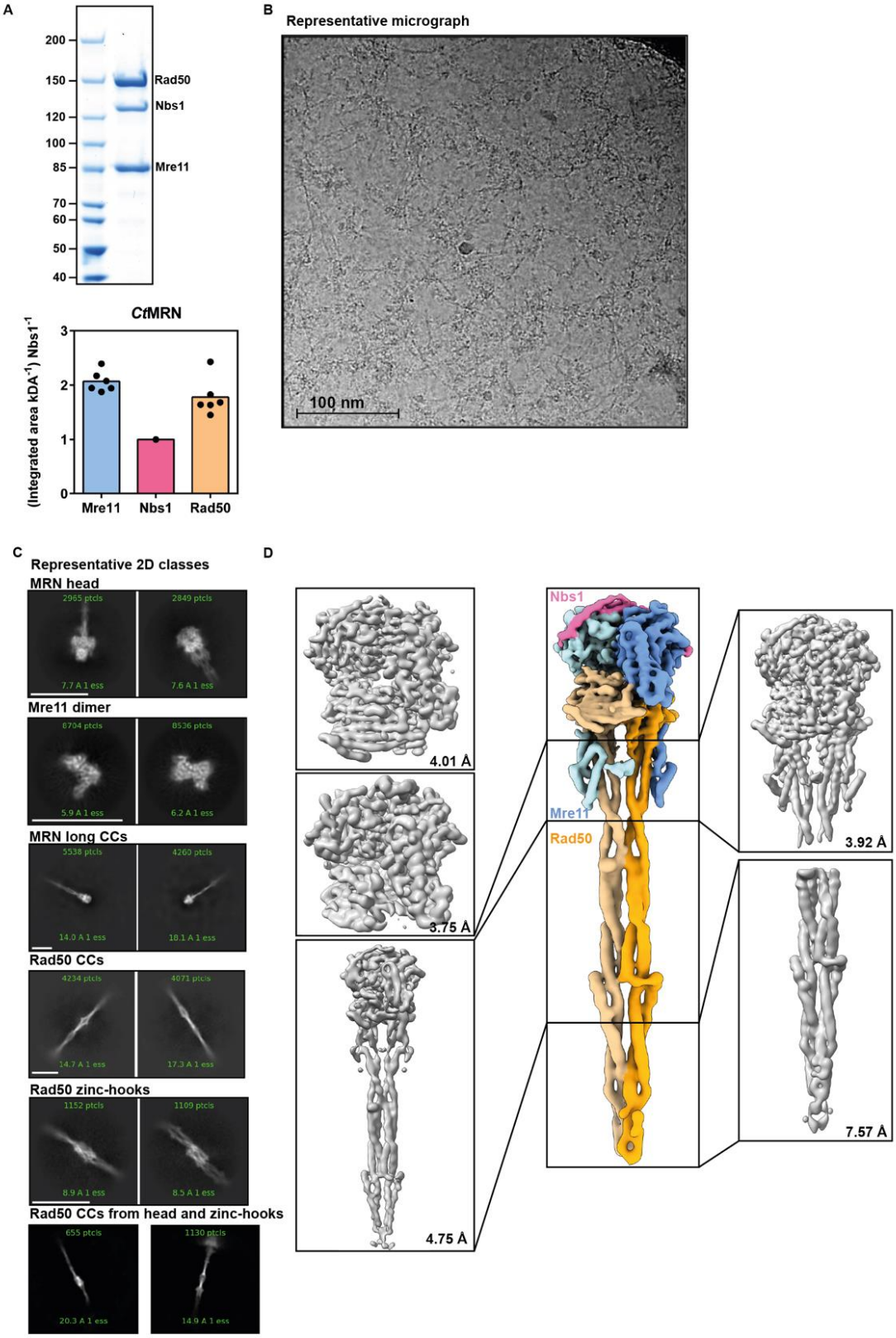

Figure S1: *Ct*MRN complex cryo-EM preparation

(A) Representative SDS-PAGE of purified *Ct*MRN complex and gel quantification (N=6).

(B) Representative Micrograph of *Ct*MRN-ATPγS.

(C) Representative 2D classes of particles picked within the *Ct*MRN-ATPγS datasets.

(D) Composite map (colored) composition. The highest resolved areas from the depicted LAFTER filtered maps were used to generate a composite map.

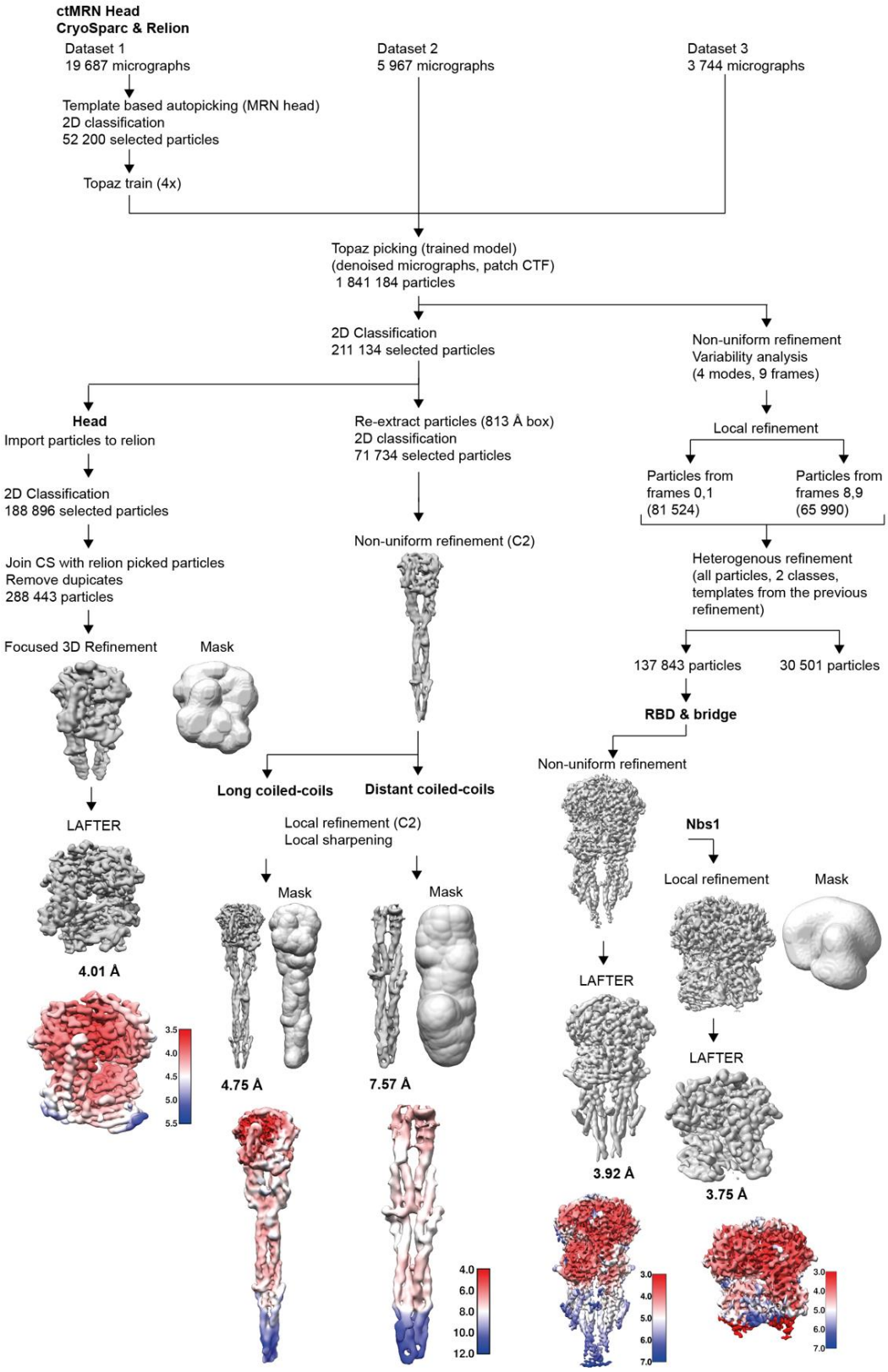

Figure S2: Processing schemes for the *Ct*MRN catalytic head and CC maps. Processing schemes of *Ct*MRN-ATPys head, long coiled coils, distant coiled coils and RBD & bridge with local resolution estimates at the end of each processing branch.

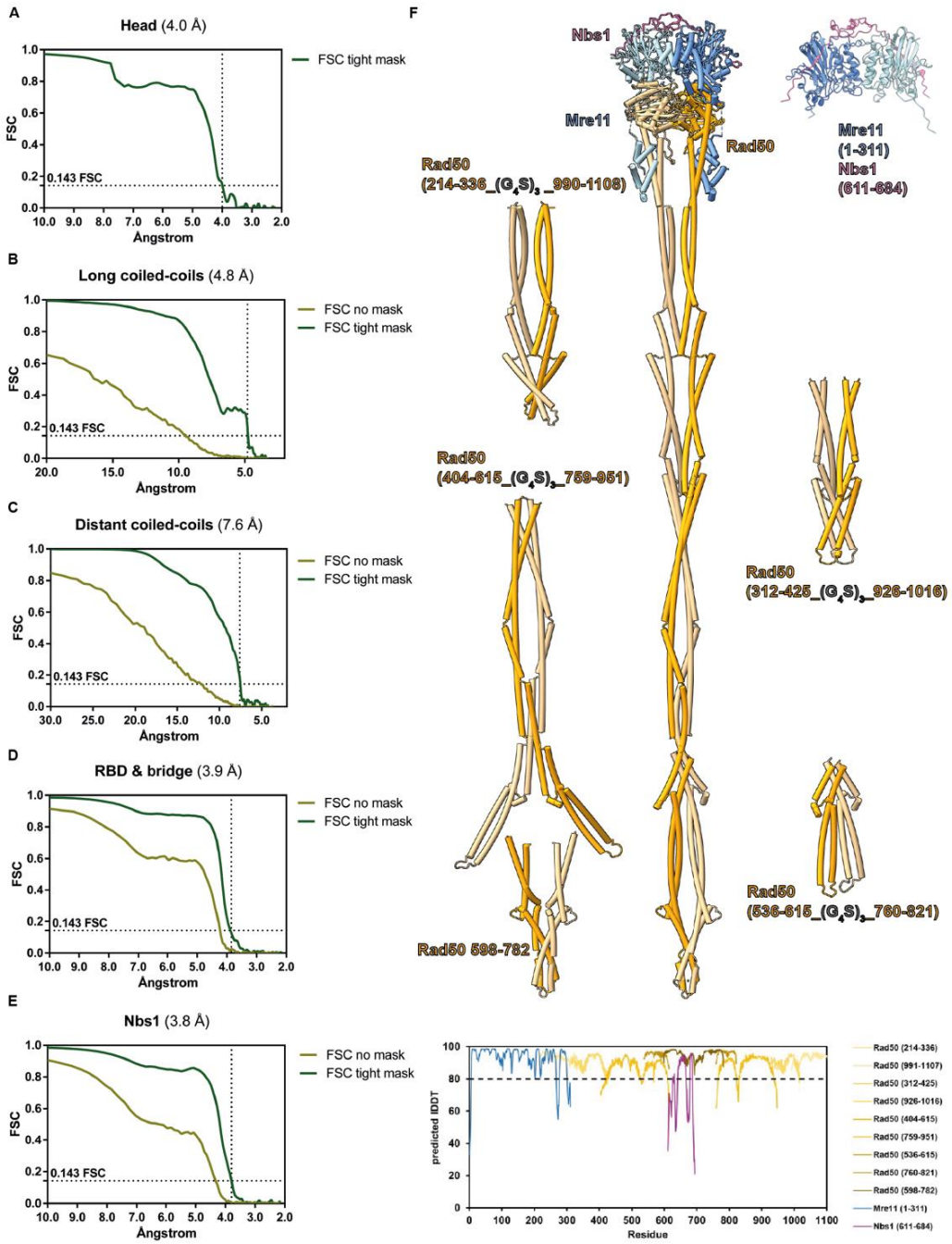

Figure S3: FSC curves and AlphaFold2 models.

A) FSC curves of the Head maps (Relion v3.0).

B) FSC curves of the long coiled coils map (CryoSPARC v3.2.0).

C) FSC curves of the distant coiled coils map (CryoSPARC v3.2.0).

D) FSC curves of the RBD & bridge map (CryoSPARC v3.2.0).

E) FSC curves of the Nbs1 map (CryoSPARC v3.2.0).

F) AlphaFold2 models used to build a full-length MRN model and the predicted IDDT scores (>80 indicates high confidence models)

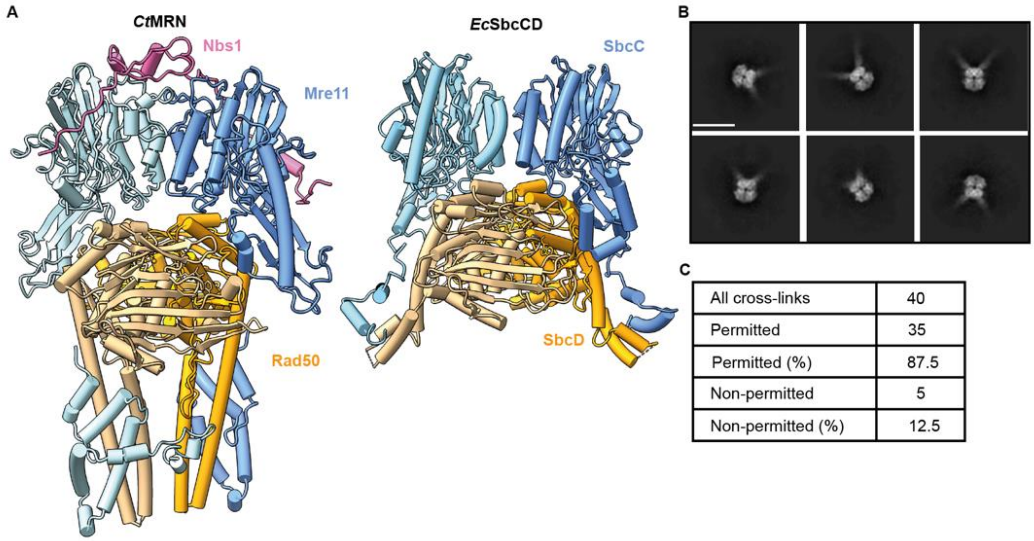

All cross-links	40
Permitted	35
Permitted (%)	87.5
Non-permitted	5
Non-permitted (%)	12.5

Figure S4: Conformations of Rad50 CCs and crosslinking MS statistics.

A) Comparison of the Cryo-EM structures of the eukaryotic *Ct*MRN complex and the prokaryotic *Ec*MR/SbcCD complex bound to ATPγS. Mre11/SbcD colored in blue, Rad50/SbcC colored orange, Nbs1 colored pink.

B) 2D classes of *Ct*MRN particles bound to ATP showing open coiled coils. Scale bar 10 nm.

C) Statistics of XL-MS restraints fitted to the cryo-EM model.

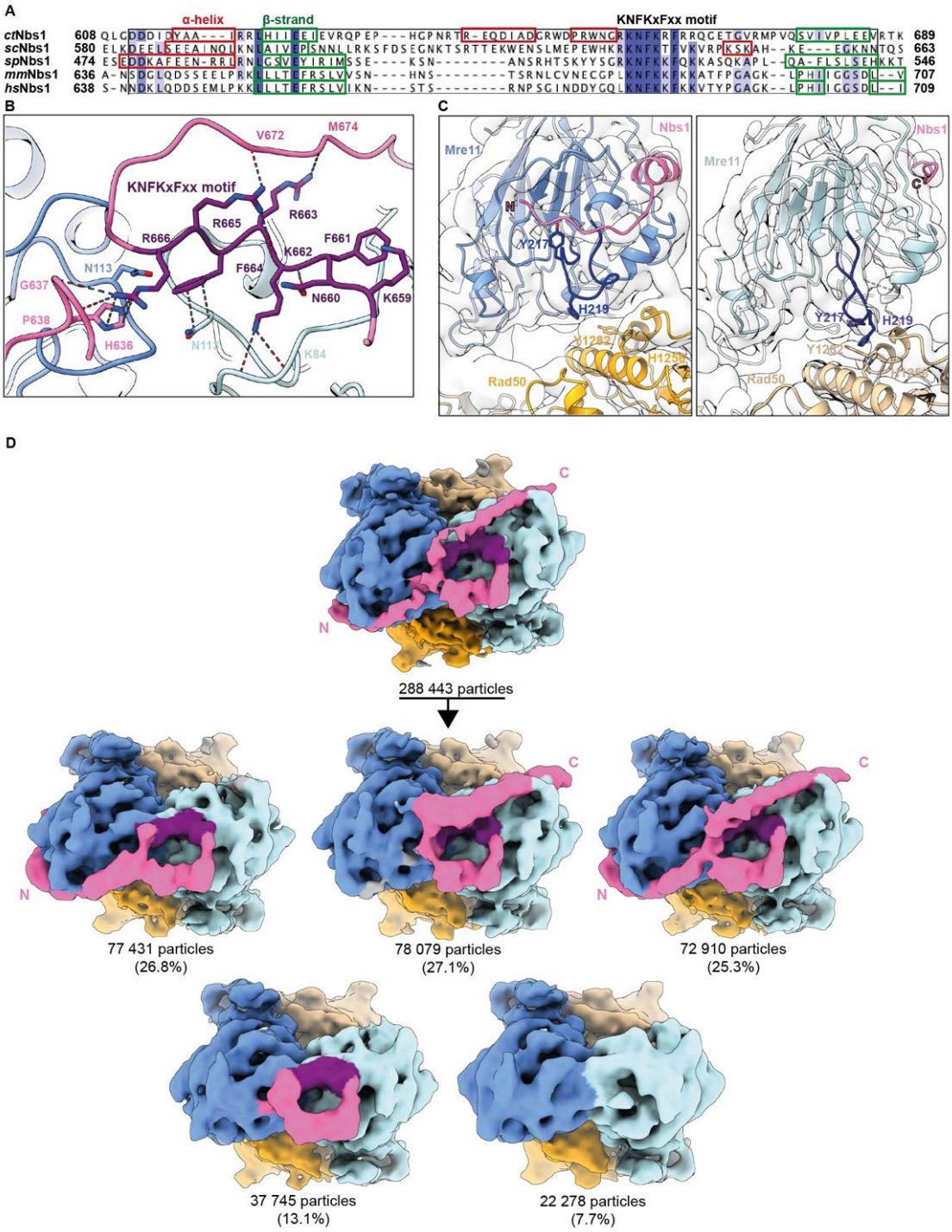
A
α-helix
β-strand
KNFKxFxx motif
ctNbs1 608 689
scNbs1 580 663
spNbs1 474 546
mmNbs1 636 707
hsNbs1 638 709
B
KNFKxFxx motif
V672
M674
R663
R665
R666
F661
K662
F664
N660
K659
N113
G637
P638
H636
K84
C
Nbs1
Mre11
Y217
H219
Y1282
H1258
Rad50
D
C
N
288 443 particles
77 431 particles
(26.8%)
78 079 particles
(27.1%)
72 910 particles
(25.3%)
37 745 particles
(13.1%)
22 278 particles
(7.7%)

Figure S5: Structural characterization of Nbs1

(A) Sequence alignment of Nbs1 from different species. Conserved residues were highlighted in shades of blue, predicted α-helices were framed in red and predicted β-strands were framed in green. Alignments were calculated with ClustalΩ, secondary structure predictions with JPred4.

(B) Side view of the KNFKxFxx motif (purple) interactions with Mre11 (shades of blue).

(C) Side-by-side comparison of N- and C-termini of resolved Nbs1 peptide interacting with Mre11. Longer N-terminus of Nbs1 interacts with Mre11 loop containing Y217 and H219 residues affecting Mre11-Rad50 interaction at this site.

(D) Heterogeneity of Nbs1-Mre11/Rad50 interactions. 3D classification revealed full interaction (25.3%), CD/N-terminal interaction (26.8%), CD/C-terminal interaction (27.1%), CD interaction (13%), no Nbs1 present (7.7%). Rad50 highlighted in shades of orange, Mre11 in shades of blue, Nbs1 in pink, KNFKxFxx motif in purple.

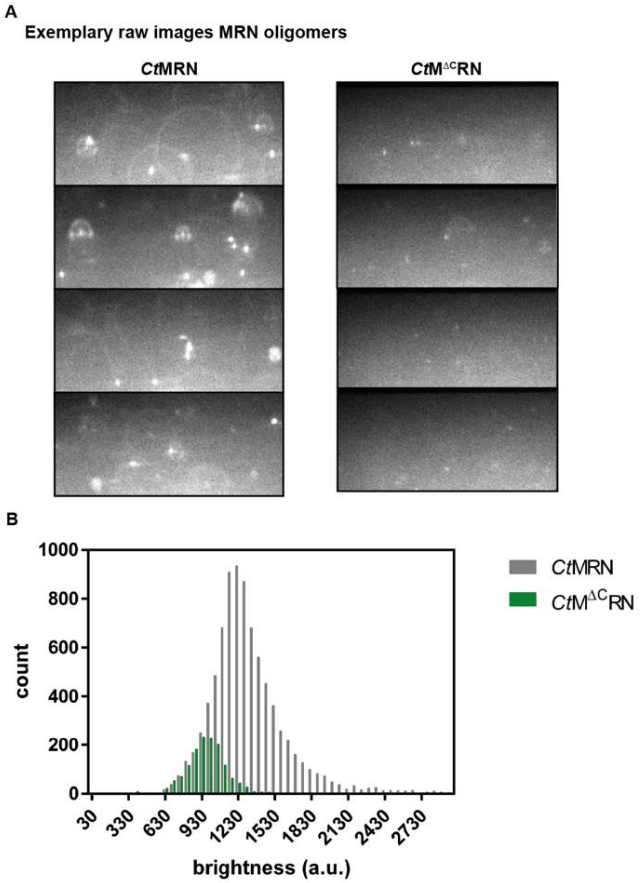

Figure S6: Quantification of *Ct*MRN clustering

(A) Exemplary fluorescence images of *Ct*MRN/ *Ct*M$^{\Delta C}$RN with FAM-labeled DNA.

(B) Histogram of *Ct*MRN-DNA and *Ct*M$^{\Delta C}$ RN-DNA cluster formation. Fluorescence images were collected and clusters grouped based on their size.

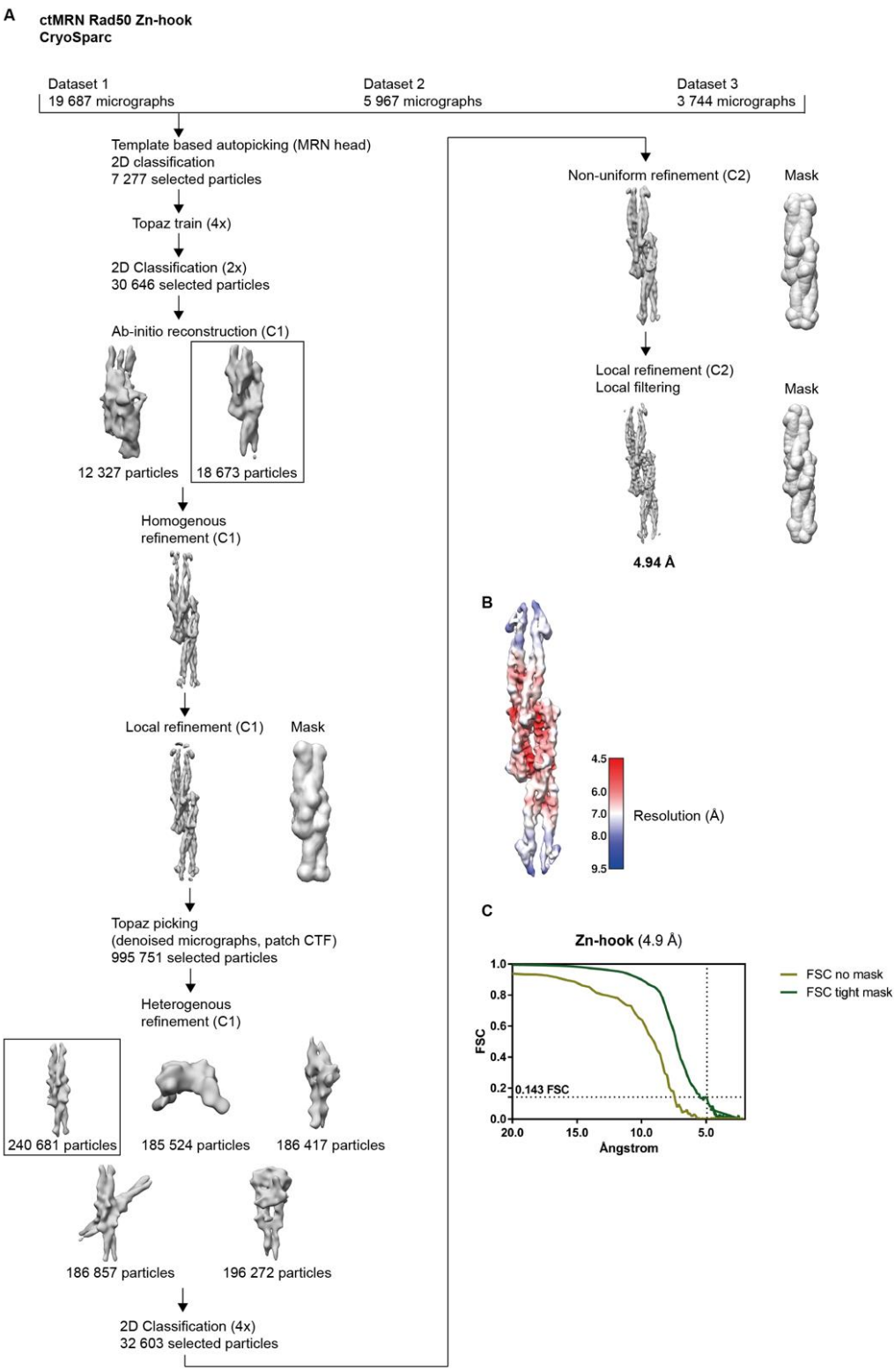

Figure S7: Processing schemes for the *Ct*MRN zinc-hook map.

(A) Cryo-EM processing scheme for the *Ct*Rad50 zinc-hook in CryoSPARC v3.2.0.

(B) Local resolution estimation of the *Ct*Rad50 zinc-hook Cryo-EM map.

(C) FSC curve of the Cryo-EM zinc-hook map (CryoSPARC v3.2.0).

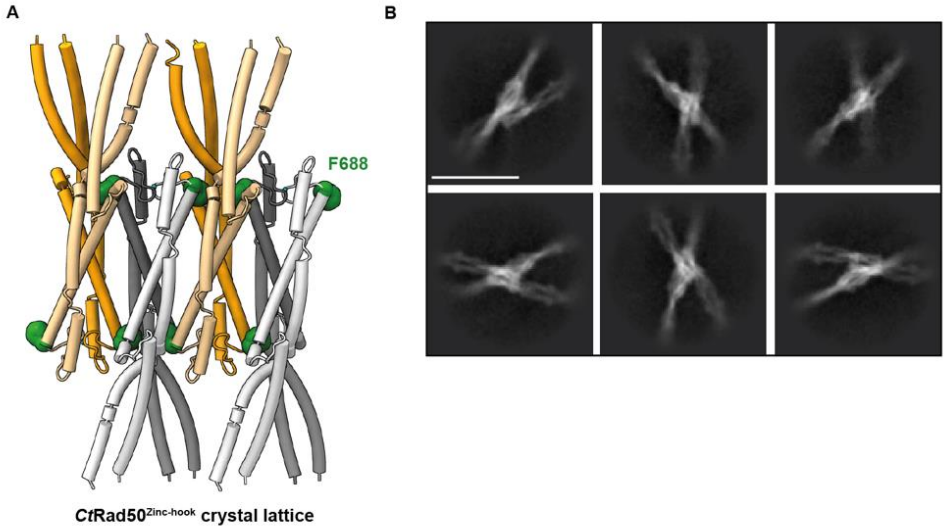

Figure S8: Higher order *Ct*MRN zinc-hook structures.

(A) Crystal lattice of *Ct*Rad50$^{\text{zinc-hook}}$ with F688 residue hidden in the lattice arrangement.

(B) 2D classes of *Ct*Rad50 zinc-hook octamers. Scale bar 10 nm.

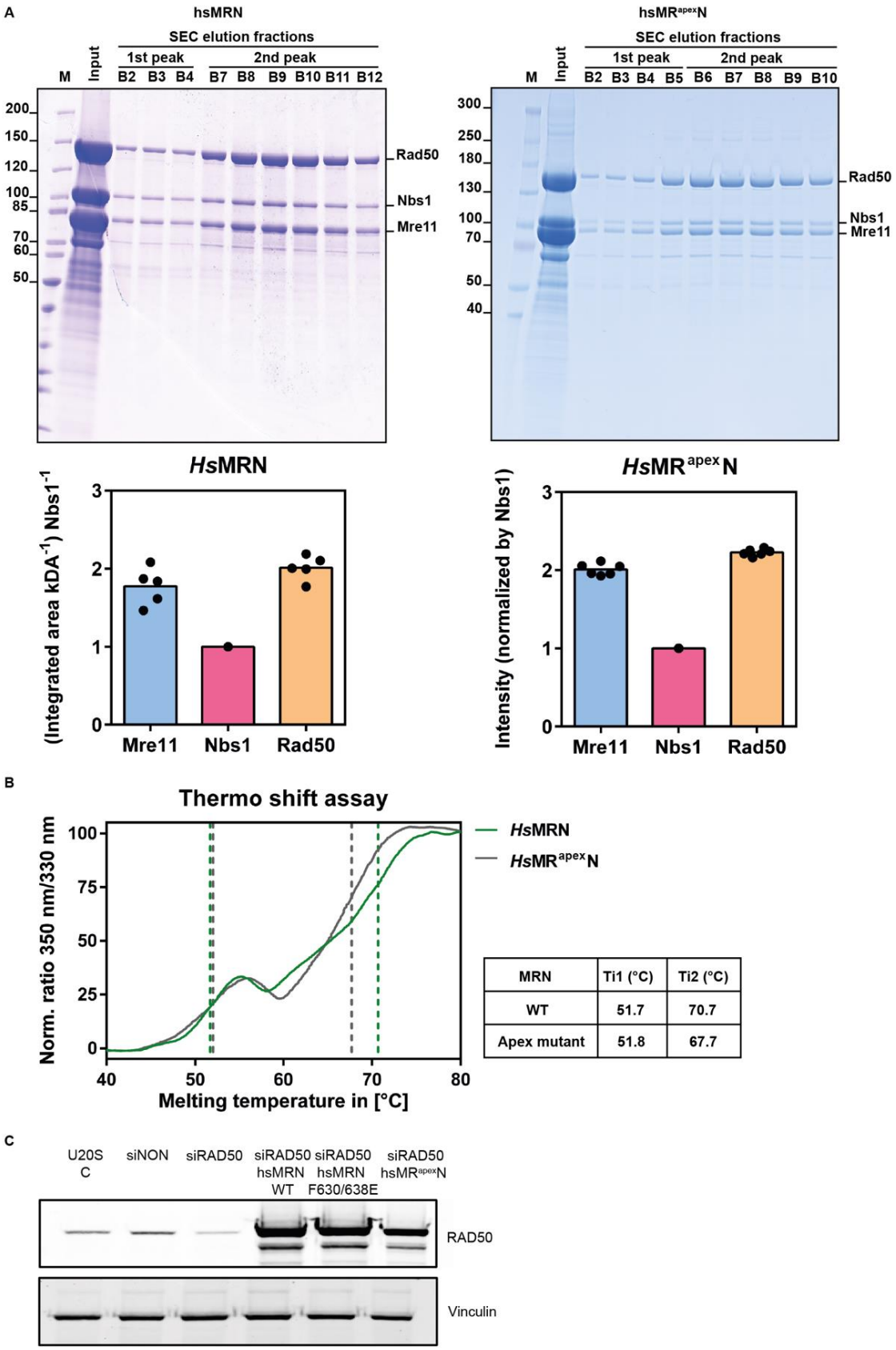

MRN	Ti1 (°C)	Ti2 (°C)
WT	51.7	70.7
Apex mutant	51.8	67.7

Figure S9: Quality assessment of purified *Hs*MRN and *Hs*MR^{loop}N complexes and siRNA knock-down of *Hs*Rad50

(A) Representative SDS-PAGE of purified *Hs*MRN and *Hs*MR^{loop}N complexes. Below, normalized gel quantification of complex stoichiometry (N = 5).

(B) Microscale thermophoresis thermal shift assay with purified *Hs*MRN and *Hs*MR^{loop}N complexes. Melting points are indicated.

(C) Knock-down of Rad50 and overexpression of mutated *Hs*MRN complex. Western blot stained with anti-Rad50 antibody and Vinculin loading control. U2OS C: untreated cells, siNON: non-targeting siRNA; siRad50: siRNA targeting Rad50; siRad50 *Hs*MRN WT: siRNA targeting Rad50, transfection with codon-optimized WT *MRN* genes; siRad50 *Hs*MRN F630/638E: siRNA targeting Rad50, transfection with codon-optimized mutant *MRN* genes; siRad50 *Hs*MR^{loop}N: siRNA targeting Rad50, transfection with codon-optimized mutant *MRN* genes.

Video S1: Flexibility within the CtMRN catalytic head.

Morphing of outputs from 3D variability analysis (CryoSPARC) illustrates increased flexibility of one Rad50 subunit (orange) compared to the the other Rad50 subunit (beige). Mre11 subunits colored blue, Nbs1 colored pink.

Video S2: Conformational change of Rad50 coiled coils

The binding of the signature coupling helix (R1204) to the ATP-phosphates leads to the opening of the Rad50 coiled coils. The video shows an overview of the MRN head bound to ATPγS, with the closed conformation of the coiled coils. The ATPyS nucleotides are colored green, the Walker A motif and the adjacent helix (Rad50$^{35-53}$) are colored red, and the signature coupling helix (Rad50$^{1206-1227}$) is colored violet. The models of the closed structure were morphed with the crystal structure of open, DNA-bound *Ct*Rad50 (PDB: 5DA9) using ChimeraX.

References

Andres, S.N., Li, Z.M., Erie, D.A., and Williams, R.S. (2019). Ctp1 protein-DNA filaments promote DNA bridging and DNA double-strand break repair. The Journal of biological chemistry *294*, 3312-3320. 10.1074/jbc.RA118.006759.

Banani, S.F., Lee, H.O., Hyman, A.A., and Rosen, M.K. (2017). Biomolecular condensates: organizers of cellular biochemistry. Nature reviews. Molecular cell biology *18*, 285-298. 10.1038/nrm.2017.7.

Bepler, T., Kelley, K., Noble, A.J., and Berger, B. (2020). Topaz-Denoise: general deep denoising models for cryoEM and cryoET. Nature communications *11*, 5208. 10.1038/s41467-020-18952-1.

Berger, I., Fitzgerald, D.J., and Richmond, T.J. (2004). Baculovirus expression system for heterologous multiprotein complexes. Nature biotechnology *22*, 1583-1587. 10.1038/nbt1036.

Bian, L., Meng, Y., Zhang, M., and Li, D. (2019). MRE11-RAD50-NBS1 complex alterations and DNA damage response: implications for cancer treatment. Molecular cancer *18*, 169. 10.1186/s12943-019-1100-5.

Bradford, M.M. (1976). A rapid and sensitive method for the quantitation of microgram quantities of protein utilizing the principle of protein-dye binding. Analytical biochemistry *72*, 248-254. 10.1006/abio.1976.9999.

Buis, J., Wu, Y., Deng, Y., Leddon, J., Westfield, G., Eckersdorff, M., Sekiguchi, J.M., Chang, S., and Ferguson, D.O. (2008). Mre11 Nuclease Activity Has Essential Roles in DNA Repair and Genomic Stability Distinct from ATM Activation. Cell *135*, 85-96. 10.1016/j.cell.2008.08.015.

Burmann, F., Lee, B.G., Than, T., Sinn, L., O'Reilly, F.J., Yatskevich, S., Rappsilber, J., Hu, B., Nasmyth, K., and Lowe, J. (2019). A folded conformation of MukBEF and cohesin. Nature structural & molecular biology *26*, 227-236. 10.1038/s41594-019-0196-z.

Cannavo, E., and Cejka, P. (2014). Sae2 promotes dsDNA endonuclease activity within Mre11-Rad50-Xrs2 to resect DNA breaks. Nature *514*, 122-125. 10.1038/nature13771.

Cannavo, E., Reginato, G., and Cejka, P. (2019). Stepwise 5' DNA end-specific resection of DNA breaks by the Mre11-Rad50-Xrs2 and Sae2 nuclease ensemble. Proc Natl Acad Sci U S A *116*, 5505-5513. 10.1073/pnas.1820157116.

Canny, M.D., and Latham, M.P. (2022). LRET-derived HADDOCK structural models describe the conformational heterogeneity required for DNA cleavage by the Mre11-Rad50 DNA damage repair complex. Elife *11*. 10.7554/eLife.69579.

Carbone, M., Arron, S.T., Beutler, B., Bononi, A., Cavenee, W., Cleaver, J.E., Croce, C.M., D'Andrea, A., Foulkes, W.D., Gaudino, G., et al. (2020). Tumour predisposition and cancer syndromes as models to study gene-environment interactions. Nature reviews. Cancer *20*, 533-549. 10.1038/s41568-020-0265-y.

Carney, J.P., Maser, R.S., Olivares, H., Davis, E.M., Le Beau, M., Yates, J.R., 3rd, Hays, L., Morgan, W.F., and Petrini, J.H. (1998). The hMre11/hRad50 protein complex and Nijmegen breakage syndrome: linkage of double-strand break repair to the cellular DNA damage response. Cell *93*, 477-486. 10.1016/s0092-8674(00)81175-7.

Cassani, C., Gobbini, E., Vertemara, J., Wang, W., Marsella, A., Sung, P., Tisi, R., Zampella, G., and Longhese, M.P. (2018). Structurally distinct Mre11 domains mediate MRX functions in resection, end-tethering and DNA damage resistance. Nucleic acids research *46*, 2990-3008. 10.1093/nar/gky086.

Cassani, C., Vertemara, J., Bassani, M., Marsella, A., Tisi, R., Zampella, G., and Longhese, M.P. (2019). The ATP-bound conformation of the Mre11-Rad50 complex is essential for Tel1/ATM activation. Nucleic acids research *47*, 3550-3567. 10.1093/nar/gkz038.

Cejka, P. (2015). DNA End Resection: Nucleases Team Up with the Right Partners to Initiate Homologous Recombination. The Journal of biological chemistry *290*, 22931-22938. 10.1074/jbc.R115.675942.

Cejka, P., and Symington, L.S. (2021). DNA End Resection: Mechanism and Control. Annual review of genetics *55*, 285-307. 10.1146/annurev-genet-071719-020312.

Chaplin, A.K., Hardwick, S.W., Liang, S., Kefala Stavridi, A., Hnizda, A., Cooper, L.R., De Oliveira, T.M., Chirgadze, D.Y., and Blundell, T.L. (2021). Dimers of DNA-PK create a stage for DNA double-strand break repair. Nature structural & molecular biology *28*, 13-19. 10.1038/s41594-020-00517-x.

Chen, C.C., Feng, W., Lim, P.X., Kass, E.M., and Jasin, M. (2018). Homology-Directed Repair and the Role of BRCA1, BRCA2, and Related Proteins in Genome Integrity and Cancer. Annu Rev Cancer Biol *2*, 313-336. 10.1146/annurev-cancerbio-030617-050502.

Connelly, J.C., de Leau, E.S., and Leach, D.R. (2003). Nucleolytic processing of a protein-bound DNA end by the E. coli SbcCD (MR) complex. DNA Repair (Amst) *2*, 795-807.

de Jager, M., van Noort, J., van Gent, D.C., Dekker, C., Kanaar, R., and Wyman, C. (2001). Human Rad50/Mre11 Is a Flexible Complex that Can Tether DNA Ends. Molecular Cell *8*, 1129-1135. 10.1016/s1097-2765(01)00381-1.

Delamarre, A., Barthe, A., de la Roche Saint-Andre, C., Luciano, P., Forey, R., Padioleau, I., Skrzypczak, M., Ginalski, K., Geli, V., Pasero, P., and Lengronne, A. (2020). MRX Increases Chromatin Accessibility at Stalled Replication Forks to Promote Nascent DNA Resection and Cohesin Loading. Mol Cell *77*, 395-410 e393. 10.1016/j.molcel.2019.10.029.

Deshpande, R.A., Lee, J.H., Arora, S., and Paull, T.T. (2016). Nbs1 Converts the Human Mre11/Rad50 Nuclease Complex into an Endo/Exonuclease Machine Specific for Protein-DNA Adducts. Mol Cell *64*, 593-606. 10.1016/j.molcel.2016.10.010.

Deshpande, R.A., Lee, J.H., and Paull, T.T. (2017). Rad50 ATPase activity is regulated by DNA ends and requires coordination of both active sites. Nucleic acids research *45*, 5255-5268. 10.1093/nar/gkx173.

Forey, R., Barthe, A., Tittel-Elmer, M., Wery, M., Barrault, M.B., Ducrot, C., Seeber, A., Krietenstein, N., Szachnowski, U., Skrzypczak, M., et al. (2021). A Role for the Mre11-Rad50-Xrs2 Complex in Gene Expression and Chromosome Organization. Mol Cell *81*, 183-197 e186. 10.1016/j.molcel.2020.11.010.

Frame, F.M., Rogoff, H.A., Pickering, M.T., Cress, W.D., and Kowalik, T.F. (2006). E2F1 induces MRN foci formation and a cell cycle checkpoint response in human fibroblasts. Oncogene *25*, 3258-3266. 10.1038/sj.onc.1209352.

Furuse, M., Nagase, Y., Tsubouchi, H., Murakami-Murofushi, K., Shibata, T., and Ohta, K. (1998). Distinct roles of two separable in vitro activities of yeast Mre11 in mitotic and meiotic recombination. The EMBO journal *17*, 6412-6425. 10.1093/emboj/17.21.6412.

Garcia, V., Phelps, S.E.L., Gray, S., and Neale, M.J. (2011). Bidirectional resection of DNA double-strand breaks by Mre11 and Exo1. Nature *479*, 241-244.

Gatei, M., Jakob, B., Chen, P., Kijas, A.W., Becherel, O.J., Gueven, N., Birrell, G., Lee, J.H., Paull, T.T., Lerenthal, Y., et al. (2011). ATM protein-dependent phosphorylation of Rad50 protein regulates DNA repair and cell cycle control. The Journal of biological chemistry *286*, 31542-31556. 10.1074/jbc.M111.258152.

Gatei, M., Kijas, A.W., Biard, D., Dork, T., and Lavin, M.F. (2014). RAD50 phosphorylation promotes ATR downstream signaling and DNA restart following replication stress. Human molecular genetics *23*, 4232-4248. 10.1093/hmg/ddu141.

Grimm, M., Zimniak, T., Kahraman, A., and Herzog, F. (2015). xVis: a web server for the schematic visualization and interpretation of crosslink-derived spatial restraints. Nucleic acids research *43*, W362-369. 10.1093/nar/gkv463.

Haber, J.E. (2018). DNA Repair: The Search for Homology. BioEssays : news and reviews in molecular, cellular and developmental biology *40*, e1700229. 10.1002/bies.201700229.

He, J., Shi, L.Z., Truong, L.N., Lu, C.S., Razavian, N., Li, Y., Negrete, A., Shiloach, J., Berns, M.W., and Wu, X. (2012). Rad50 zinc hook is important for the Mre11 complex to bind chromosomal DNA double-stranded breaks and initiate various DNA damage responses. The Journal of biological chemistry *287*, 31747-31756. 10.1074/jbc.M112.384750.

Hohl, M., Kochanczyk, T., Tous, C., Aguilera, A., Krezel, A., and Petrini, J.H. (2015). Interdependence of the rad50 hook and globular domain functions. Mol Cell *57*, 479-491. 10.1016/j.molcel.2014.12.018.

Hopfner, K.P., Craig, L., Moncalian, G., Zinkel, R.A., Usui, T., Owen, B.A., Karcher, A., Henderson, B., Bodmer, J.L., McMurray, C.T., et al. (2002). The Rad50 zinc-hook is a structure joining Mre11 complexes in DNA recombination and repair. Nature *418*, 562-566. 10.1038/nature00922.

Hopfner, K.P., Karcher, A., Craig, L., Woo, T.T., Carney, J.P., and Tainer, J.A. (2001). Structural biochemistry and interaction architecture of the DNA double-strand break repair Mre11 nuclease and Rad50-ATPase. Cell *105*, 473-485.

Hopfner, K.P., Karcher, A., Shin, D.S., Craig, L., Arthur, L.M., Carney, J.P., and Tainer, J.A. (2000). Structural biology of Rad50 ATPase: ATP-driven conformational control in DNA double-strand break repair and the ABC-ATPase superfamily. Cell *101*, 789-800.

Johnson, D., Crawford, M., Cooper, T., Claeys Bouuaert, C., Keeney, S., Llorente, B., Garcia, V., and Neale, M.J. (2021). Concerted cutting by Spo11 illuminates meiotic DNA break mechanics. Nature *594*, 572-576. 10.1038/s41586-021-03389-3.

Jumper, J., Evans, R., Pritzel, A., Green, T., Figurnov, M., Ronneberger, O., Tunyasuvunakool, K., Bates, R., Zidek, A., Potapenko, A., et al. (2021). Highly accurate protein structure prediction with AlphaFold. Nature *596*, 583-589. 10.1038/s41586-021-03819-2.

Jung, C., Bandilla, P., von Reutern, M., Schnepf, M., Rieder, S., Unnerstall, U., and Gaul, U. (2018). True equilibrium measurement of transcription factor-DNA binding affinities using automated polarization microscopy. Nature communications *9*, 1605. 10.1038/s41467-018-03977-4.

Jung, C., Schnepf, M., Bandilla, P., Unnerstall, U., and Gaul, U. (2019). High Sensitivity Measurement of Transcription Factor-DNA Binding Affinities by Competitive Titration Using Fluorescence Microscopy. J Vis Exp. 10.3791/58763.

Kashammer, L., Saathoff, J.H., Lammens, K., Gut, F., Bartho, J., Alt, A., Kessler, B., and Hopfner, K.P. (2019). Mechanism of DNA End Sensing and Processing by the Mre11-Rad50 Complex. Mol Cell *76*, 382-394 e386. 10.1016/j.molcel.2019.07.035.

Khayat, F., Cannavo, E., Alshmery, M., Foster, W.R., Chahwan, C., Maddalena, M., Smith, C., Oliver, A.W., Watson, A.T., Carr, A.M., et al. (2021). Inhibition of MRN activity by a telomere protein motif. Nature communications *12*, 3856. 10.1038/s41467-021-24047-2.

Kim, J.H., Grosbart, M., Anand, R., Wyman, C., Cejka, P., and Petrini, J.H.J. (2017). The Mre11-Nbs1 Interface Is Essential for Viability and Tumor Suppression. Cell reports *18*, 496-507. 10.1016/j.celrep.2016.12.035.

Klykov, O., Steigenberger, B., Pektas, S., Fasci, D., Heck, A.J.R., and Scheltema, R.A. (2018). Efficient and robust proteome-wide approaches for cross-linking mass spectrometry. Nature protocols *13*, 2964-2990. 10.1038/s41596-018-0074-x.

Kosinski, J., von Appen, A., Ori, A., Karius, K., Muller, C.W., and Beck, M. (2015). Xlink Analyzer: software for analysis and visualization of cross-linking data in the context of three-dimensional structures. Journal of structural biology *189*, 177-183. 10.1016/j.jsb.2015.01.014.

Lamarche, B.J., Orazio, N.I., and Weitzman, M.D. (2010). The MRN complex in double-strand break repair and telomere maintenance. FEBS letters *584*, 3682-3695. 10.1016/j.febslet.2010.07.029.

Lammens, K., Bemeleit, D.J., Mockel, C., Clausing, E., Schele, A., Hartung, S., Schiller, C.B., Lucas, M., Angermuller, C., Soding, J., et al. (2011). The Mre11:Rad50 structure shows an ATP-dependent molecular clamp in DNA double-strand break repair. Cell *145*, 54-66. 10.1016/j.cell.2011.02.038.

Lee, J., and Dunphy, W.G. (2013). The Mre11-Rad50-Nbs1 (MRN) complex has a specific role in the activation of Chk1 in response to stalled replication forks. Mol Biol Cell *24*, 1343-1353. 10.1091/mbc.E13-01-0025.

Lee, J.H., Mand, M.R., Deshpande, R.A., Kinoshita, E., Yang, S.H., Wyman, C., and Paull, T.T. (2013). Ataxia telangiectasia-mutated (ATM) kinase activity is regulated by ATP-driven conformational changes in the Mre11/Rad50/Nbs1 (MRN) complex. The Journal of biological chemistry *288*, 12840-12851. 10.1074/jbc.M113.460378.

Lee, J.H., and Paull, T.T. (2005). ATM activation by DNA double-strand breaks through the Mre11-Rad50-Nbs1 complex. Science *308*, 551-554. 10.1126/science.1108297.

Lee, J.H., and Paull, T.T. (2021). Cellular functions of the protein kinase ATM and their relevance to human disease. Nature reviews. Molecular cell biology *22*, 796-814. 10.1038/s41580-021-00394-2.

Lim, H.S., Kim, J.S., Park, Y.B., Gwon, G.H., and Cho, Y. (2011). Crystal structure of the Mre11-Rad50-ATPgammaS complex: understanding the interplay between Mre11 and Rad50. Genes & development *25*, 1091-1104. 10.1101/gad.2037811.

Liu, Y., Sung, S., Kim, Y., Li, F., Gwon, G., Jo, A., Kim, A.K., Kim, T., Song, O.K., Lee, S.E., and Cho, Y. (2016). ATP-dependent DNA binding, unwinding, and resection by the Mre11/Rad50 complex. The EMBO journal *35*, 743-758. 10.15252/embj.201592462.

Luo, G., Yao, M.S., Bender, C.F., Mills, M., Bladl, A.R., Bradley, A., and Petrini, J.H. (1999). Disruption of *mRad50* causes embryonic stem cell lethality, abnormal embryonic development, and sensitivity to ionizing radiation. Proc Natl Acad Sci U S A *96*, 7376-7381.

Marie, L., and Symington, L.S. (2022). Mechanism for inverted-repeat recombination induced by a replication fork barrier. Nature communications *13*, 32. 10.1038/s41467-021-27443-w.

Martina, M., Clerici, M., Baldo, V., Bonetti, D., Lucchini, G., and Longhese, M.P. (2012). A balance between Tel1 and Rif2 activities regulates nucleolytic processing and elongation at telomeres. Molecular and cellular biology *32*, 1604-1617. 10.1128/MCB.06547-11.

McGee, J.S., Phillips, J.A., Chan, A., Sabourin, M., Paeschke, K., and Zakian, V.A. (2010). Reduced Rif2 and lack of Mec1 target short telomeres for elongation rather than double-strand break repair. Nature structural & molecular biology *17*, 1438-1445. 10.1038/nsmb.1947.

Mimitou, E.P., and Symington, L.S. (2008). Sae2, Exo1 and Sgs1 collaborate in DNA double-strand break processing. Nature *455*, 770-774. 10.1038/nature07312.

Mojumdar, A., Sorenson, K., Hohl, M., Toulouze, M., Lees-Miller, S.P., Dubrana, K., Petrini, J.H.J., and Cobb, J.A. (2019). Nej1 Interacts with Mre11 to Regulate Tethering and Dna2 Binding at DNA Double-Strand Breaks. Cell reports *28*, 1564-1573 e1563. 10.1016/j.celrep.2019.07.018.

Moreno-Herrero, F., de Jager, M., Dekker, N.H., Kanaar, R., Wyman, C., and Dekker, C. (2005). Mesoscale conformational changes in the DNA-repair complex Rad50/Mre11/Nbs1 upon binding DNA. Nature *437*, 440-443. 10.1038/nature03927.

Morimoto, S., Tsuda, M., Bunch, H., Sasanuma, H., Austin, C., and Takeda, S. (2019). Type II DNA Topoisomerases Cause Spontaneous Double-Strand Breaks in Genomic DNA. Genes (Basel) *10*. 10.3390/genes10110868.

Myler, L.R., Gallardo, I.F., Soniat, M.M., Deshpande, R.A., Gonzalez, X.B., Kim, Y., Paull, T.T., and Finkelstein, I.J. (2017). Single-Molecule Imaging Reveals How Mre11-Rad50-Nbs1 Initiates DNA Break Repair. Mol Cell *67*, 891-898 e894. 10.1016/j.molcel.2017.08.002.

Na, J., Newman, J.A., Then, C.K., Syed, J., Vendrell, I., Torrecilla, I., Ellermann, S., Ramadan, K., Fischer, R., and Kiltie, A.E. (2021). SPRTN protease-cleaved MRE11 decreases DNA repair and radiosensitises cancer cells. Cell death & disease *12*, 165. 10.1038/s41419-021-03437-w.

Nikolova, T., Marini, F., and Kaina, B. (2017). Genotoxicity testing: Comparison of the gammaH2AX focus assay with the alkaline and neutral comet assays. Mutat Res Genet Toxicol Environ Mutagen *822*, 10-18. 10.1016/j.mrgentox.2017.07.004.

Oh, J., Al-Zain, A., Cannavo, E., Cejka, P., and Symington, L.S. (2016). Xrs2 Dependent and Independent Functions of the Mre11-Rad50 Complex. Mol Cell *64*, 405-415. 10.1016/j.molcel.2016.09.011.

Park, Y.B., Hohl, M., Padjasek, M., Jeong, E., Jin, K.S., Krezel, A., Petrini, J.H., and Cho, Y. (2017). Eukaryotic Rad50 functions as a rod-shaped dimer. Nature structural & molecular biology *24*, 248-257. 10.1038/nsmb.3369.

Paull, T.T. (2018). 20 Years of Mre11 Biology: No End in Sight. Mol Cell *71*, 419-427. 10.1016/j.molcel.2018.06.033.

Paull, T.T., and Gellert, M. (1999). Nbs1 potentiates ATP-driven DNA unwinding and endonuclease cleavage by the Mre11/Rad50 complex. Genes & development *13*, 1276-1288.

Pettersen, E.F., Goddard, T.D., Huang, C.C., Couch, G.S., Greenblatt, D.M., Meng, E.C., and Ferrin, T.E. (2004). UCSF Chimera--a visualization system for exploratory research and analysis. J Comput Chem *25*, 1605-1612. 10.1002/jcc.20084.

Punjani, A., Rubinstein, J.L., Fleet, D.J., and Brubaker, M.A. (2017). cryoSPARC: algorithms for rapid unsupervised cryo-EM structure determination. Nature methods *14*, 290-296. 10.1038/nmeth.4169.

Reginato, G., Cannavo, E., and Cejka, P. (2017). Physiological protein blocks direct the Mre11-Rad50-Xrs2 and Sae2 nuclease complex to initiate DNA end resection. Genes & development *31*, 2325-2330. 10.1101/gad.308254.117.

Rohou, A., and Grigorieff, N. (2015). CTFFIND4: Fast and accurate defocus estimation from electron micrographs. Journal of structural biology *192*, 216-221. 10.1016/j.jsb.2015.08.008.

Roisne-Hamelin, F., Pobiega, S., Jezequel, K., Miron, S., Depagne, J., Veaute, X., Busso, D., Du, M.L., Callebaut, I., Charbonnier, J.B., et al. (2021). Mechanism of MRX inhibition by Rif2 at telomeres. Nature communications *12*, 2763. 10.1038/s41467-021-23035-w.

Rojowska, A., Lammens, K., Seifert, F.U., Direnberger, C., Feldmann, H., and Hopfner, K.P. (2014). Structure of the Rad50 DNA double-strand break repair protein in complex with DNA. The EMBO journal *33*, 2847-2859. 10.15252/embj.201488889.

Saathoff, J.H., Kashammer, L., Lammens, K., Byrne, R.T., and Hopfner, K.P. (2018). The bacterial Mre11-Rad50 homolog SbcCD cleaves opposing strands of DNA by two chemically distinct nuclease reactions. Nucleic acids research *46*, 11303-11314. 10.1093/nar/gky878.

Salifou, K., Burnard, C., Basavarajaiah, P., Grasso, G., Helsmoortel, M., Mac, V., Depierre, D., Franckhauser, C., Beyne, E., Contreras, X., et al. (2021). Chromatin-associated MRN complex protects highly transcribing genes from genomic instability. Sci Adv *7*. 10.1126/sciadv.abb2947.

Sartori, A.A., Lukas, C., Coates, J., Mistrik, M., Fu, S., Bartek, J., Baer, R., Lukas, J., and Jackson, S.P. (2007). Human CtIP promotes DNA end resection. Nature *450*, 509-514. 10.1038/nature06337.

Scheltema, R.A., Hauschild, J.P., Lange, O., Hornburg, D., Denisov, E., Damoc, E., Kuehn, A., Makarov, A., and Mann, M. (2014). The Q Exactive HF, a Benchtop mass spectrometer with a pre-filter, high-performance quadrupole and an ultra-high-field Orbitrap analyzer. Mol Cell Proteomics *13*, 3698-3708. 10.1074/mcp.M114.043489.

Schiller, C.B., Lammens, K., Guerini, I., Coordes, B., Feldmann, H., Schlauderer, F., Mockel, C., Schele, A., Strasser, K., Jackson, S.P., and Hopfner, K.P. (2012). Structure of Mre11-Nbs1 complex

yields insights into ataxia-telangiectasia-like disease mutations and DNA damage signaling. Nature structural & molecular biology *19*, 693-700. 10.1038/nsmb.2323.

Scully, R., Panday, A., Elango, R., and Willis, N.A. (2019). DNA double-strand break repair-pathway choice in somatic mammalian cells. Nature reviews. Molecular cell biology *20*, 698-714. 10.1038/s41580-019-0152-0.

Seeber, A., Hegnauer, A.M., Hustedt, N., Deshpande, I., Poli, J., Eglinger, J., Pasero, P., Gut, H., Shinohara, M., Hopfner, K.P., et al. (2016). RPA Mediates Recruitment of MRX to Forks and Double-Strand Breaks to Hold Sister Chromatids Together. Mol Cell *64*, 951-966. 10.1016/j.molcel.2016.10.032.

Seifert, F.U., Lammens, K., Stoehr, G., Kessler, B., and Hopfner, K.P. (2016). Structural mechanism of ATP-dependent DNA binding and DNA end bridging by eukaryotic Rad50. The EMBO journal *35*, 759-772. 10.15252/embj.201592934.

Soh, Y.M., Basquin, J., and Gruber, S. (2021). A rod conformation of the Pyrococcus furiosus Rad50 coiled coil. Proteins *89*, 251-255. 10.1002/prot.26005.

Syed, A., and Tainer, J.A. (2018). The MRE11-RAD50-NBS1 Complex Conducts the Orchestration of Damage Signaling and Outcomes to Stress in DNA Replication and Repair. Annual review of biochemistry *87*, 263-294. 10.1146/annurev-biochem-062917-012415.

Tatebe, H., Lim, C.T., Konno, H., Shiozaki, K., Shinohara, A., Uchihashi, T., and Furukohri, A. (2020). Rad50 zinc hook functions as a constitutive dimerization module interchangeable with SMC hinge. Nature communications *11*, 370. 10.1038/s41467-019-14025-0.

Tubbs, A., and Nussenzweig, A. (2017). Endogenous DNA Damage as a Source of Genomic Instability in Cancer. Cell *168*, 644-656. 10.1016/j.cell.2017.01.002.

Usui, T., Ohta, T., Oshiumi, H., Tomizawa, J., Ogawa, H., and Ogawa, T. (1998). Complex formation and functional versatility of Mre11 of budding yeast in recombination. Cell *95*, 705-716.

Vera, K., Giordano, R., Eliana, B., Kristina, K., Janny, T., Gea, C., Sung Sik, L., Raphaël, G., Ralf, S., Petr, C., and Matthias, P. (2022). Nature Portfolio. 10.21203/rs.3.rs-811984/v1.

Wang, W., Daley, J.M., Kwon, Y., Krasner, D.S., and Sung, P. (2017). Plasticity of the Mre11-Rad50-Xrs2-Sae2 nuclease ensemble in the processing of DNA-bound obstacles. Genes & development *31*, 2331-2336. 10.1101/gad.307900.117.

Wright, W.D., Shah, S.S., and Heyer, W.D. (2018). Homologous recombination and the repair of DNA double-strand breaks. The Journal of biological chemistry *293*, 10524-10535. 10.1074/jbc.TM118.000372.

You, Z., Chahwan, C., Bailis, J., Hunter, T., and Russell, P. (2005). ATM activation and its recruitment to damaged DNA require binding to the C terminus of Nbs1. Molecular and cellular biology *25*, 5363-5379. 10.1128/MCB.25.13.5363-5379.2005.

Zabolotnaya, E., Mela, I., Williamson, M.J., Bray, S.M., Yau, S.K., Papatziamou, D., Edwardson, J.M., Robinson, N.P., and Henderson, R.M. (2020). Modes of action of the archaeal Mre11/Rad50 DNA-repair complex revealed by fast-scan atomic force microscopy. Proceedings of the National Academy of Sciences *117*, 14936-14947.

Zhang, Y., Zhang, X., Dai, H.Q., Hu, H., and Alt, F.W. (2022). The role of chromatin loop extrusion in antibody diversification. Nature reviews. Immunology. 10.1038/s41577-022-00679-3.

Zhao, B., Rothenberg, E., Ramsden, D.A., and Lieber, M.R. (2020). The molecular basis and disease relevance of non-homologous DNA end joining. Nature reviews. Molecular cell biology *21*, 765-781. 10.1038/s41580-020-00297-8.

Zheng, S.Q., Palovcak, E., Armache, J.P., Verba, K.A., Cheng, Y., and Agard, D.A. (2017). MotionCor2: anisotropic correction of beam-induced motion for improved cryo-electron microscopy. Nature methods *14*, 331-332. 10.1038/nmeth.4193.

Zhu, J., Petersen, S., Tessarollo, L., and Nussenzweig, A. (2001). Targeted disruption of the Nijmegen breakage syndrome gene NBS1 leads to early embryonic lethality in mice. Current biology : CB *11*, 105-109.

Zivanov, J., Nakane, T., Forsberg, B.O., Kimanius, D., Hagen, W.J., Lindahl, E., and Scheres, S.H. (2018). New tools for automated high-resolution cryo-EM structure determination in RELION-3. Elife *7*. 10.7554/eLife.42166.

3. Discussion

3.1 The auto-inhibited conformation of *ct*MRN

The flexible nature of Rad50 coiled-coils frequently eliminated them from structural studies, but recent cryo-EM work on the full-length bacterial MR complex shed some light on coiled-coil dynamics[100]. A flexible ring structure of coiled-coils was observed for the *Escherichia coli* (*ec*) MR-ATPγS complex and was interpreted as an open state conformation for loading onto DNA ends, especially those that have protein blocks. Then upon DNA binding, Rad50 coiled-coils zip-up into a rod conformation clamping a single DNA duplex and allowing movement of Mre11 dimer into a "cutting" state. This transition was illustrated by the structure of *ec*MR-ADP-DNA complex[100].

Interestingly, the cryo-EM structure of *Chaetomium thermophilum* (*ct*) MRN-ATPγS revealed a closed state of Rad50 coiled-coils, where blocked DNA ends could not enter between the coiled-coils (Figure 16 A). In addition, the *ct*Rad50 coiled-coils are held together by a bridge element formed by the Mre11 in the proximity of Rad50 NBDs keeping DNA binding site relatively inaccessible (Figure 16 A). The bridge element of Mre11 is absent in the prokaryotic MR complex. These findings suggest that eukaryotic MRN might be under a stricter control than bacterial MR and adopt an autoinhibited state. This tight regulation of MRN activity could be explained by a broader functional spectrum of eukaryotic MRN and more severe consequences of a poorly regulated nuclease complex on eukaryotic genomes. It is also important to point out that coiled-coils in solution have a more dynamic behavior than presented by the cryo-EM analysis. This is well illustrated by the atomic force microscopy (AFM) studies of the MRN complex by other research groups and our unpublished AFM data (Figure 16 B)[244,245].

We noticed that in the cryo-EM sample with ATP a portion of full-length *ct*MRN complexes adopt an open coiled-coil conformation (Section 2.3 Figure S4 B). This observation hints towards ATP hydrolysis being required for the opening of coiled-coils as in the presence of ATPγS coiled-coils are completely closed. On the other hand, a crystal structure of *ct*Rad50 NBDs in complex with ATPγS shows that a full engagement of NBDs, where the signature motif contacts γ-phosphate of ATP, involves a positioning of NBDs with respect to one another in a way that proximal coiled-coils should be split open[104]. It is worth noting that coiled-coils are severely truncated in this case and might not represent a full-length coiled-coil conformation. Also, the Mre11 bridge motif, which might play a role in keeping Rad50 coiled-coils in a rod arrangement, is absent in the crystalized construct. Hence, further investigation is needed in order to fully understand effects of ATP binding and hydrolysis on conformations of the Rad50 coiled-coils.

Comparison of *ct*Rad50 NBDs from the full-length *ct*MRN-ATPγS cryo-EM structure with the ATPγS-bound crystal structure of *ct*Rad50 NBDs shows that NBDs in *ct*MRN-ATPγS structure are in pre-engaged ATP state (Figure 16 C)[104]. Here, a signature motif, responsible for binding to the γ-(thio) phosphate of the "trans" ATP in a fully engaged state, is approximately 10 Å away from the γ-(thio) phosphate. Also, NBDs require a further 30° rotation to achieve signature motif binding to the γ-(thio) phosphate and transition to a fully engaged state. The presence of the pre-engaged ATP state is supported by studies on the archaeal MR complex, which identified three in solution conformations of NBDs: fully engaged, pre-engaged and disengaged[246].

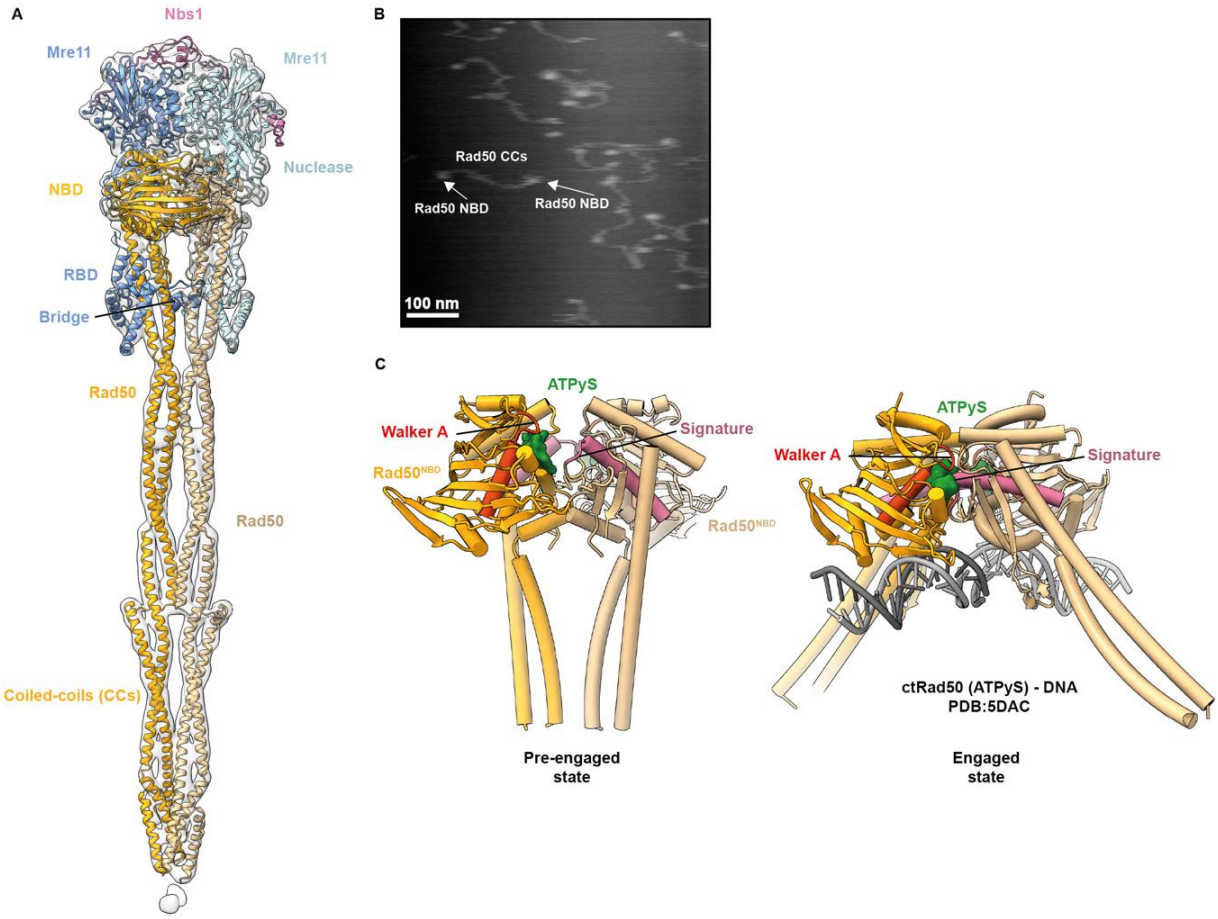

Figure 16. Auto-inhibited conformation of *ct*MRN. A, CryoEM structure and composite map of the MRN complex with coiled-coils in a closed conformation. The map was created by combining the higher resolution maps of different regions. The atomic model of the catalytic head domain and 30 nm of the Rad50 coiled-coils region is shown. Mre11 is colored blue, Rad50 orange and NBS1 pink. **B,** flexible nature of Rad50 coiled-coils illustrated by AFM image. NBD and coiled-coils (CCs) of Rad50 are labeled. **C,** A side-by-side comparison of our cryoEM structure with the ATPγS bound Rad50 crystal structure (PDB code: 5DAC) illustrates

the differences in Rad50NBD dimerization and the pre-engaged state of Rad50 in the *ct*MRN complex. In the cryoEM structure, the signature motifs are ~10Å away from the γ-(thio)phosphate of ATPγS. In the fully engaged crystal structure, the signature motif interacts with the γ-(thio)phosphate of the "trans" ATP.

3.2 DNA binding modes of eukaryotic MRN complex

All of the MRN functions in DNA damage repair pathways depend on DNA binding and nucleolytic activities of the complex. An investigation of DNA binding activities by a bacterial MR complex revealed a high specificity to DNA ends and a full dependency on ATP[247]. However, eukaryotic MRN complex seems to have a more complex DNA binding profile. It is known from earlier studies in *S. cerevisiae* that, in addition to a well-characterized DNA binding platform along the two Rad50 NBDs, the C-terminus of Mre11 can bind DNA. This binding site functions distinctly in the formation of meiotic breaks and chromatin organization at DSBs (Figure 17 A)[248].

We further investigated the influence of eukaryote-specific C-terminal extension of Mre11 on DNA binding[100,104,105]. The data on *ct*MRN revealed a nucleotide-independent DNA binding and increased capacity to bind circular compared to linear DNA (Section 2.3 Figure 3 A-D). Hence, we separated two DNA binding modes of the eukaryotic MRN with the first one being DNA end-specific, ATP-dependent and performed by the catalytic head, while the second one is nucleotide-independent, not limited to DNA DSBs and executed by the C-terminus of Mre11. In light of these findings, we anticipate that the MRN complex could interact with an intact DNA in a more peripheral fashion via the C-terminus of Mre11 and, once DNA DSB is encountered, MRN can get loaded onto the DNA end in a conformation similar to bacterial MR complex where DNA passes through the Rad50 coiled-coils (Figure 17 B)[100]. The molecular details of different DNA binding modes by eukaryotic MRN remain to be investigated in future studies. In addition, separation of DNA binding modes can be used in the future to independently study enzymatic and scaffolding functions of MRN.

The separation of binding modes is consistent with and useful to interpret several recent studies. A publication using single-molecule DNA curtain approach determined that *Homo sapiens* (*hs*) MRN uses a combination of 3D collision through space and 1D sliding along the DNA to detect DSBs[249]. The canonical, ATP-dependent DNA binding via the Rad50 site seems to be responsible for the DNA end binding, where *hs*MRN generated an endo-nucleolytic cut at approximately 30 nt upstream of Ku-blocked DNA end and cleaved Ku and itself off. However, before the end recognition *hs*MRN was diffusing along a linear homoduplex DNA in an ATP independent manner. In addition, *hs*MRN could diffuse past multiple nucleosome obstacles in a scanning mode[249]. These results are in a perfect agreement with our findings and together they suggest that MRN performs a 1D sliding along an intact nucleosomal DNA via

the Mre11 C-terminus. Once DNA ends are encountered, MRN is then properly loaded in an ATP-dependent process to form a “cutting” state (Figure 17 B).

Another study identified a C-terminally truncated form of human Mre11 (TR-Mre11), which was naturally produced by the SPRTN protease and detected in bladder cancer cells[250]. The biochemical analysis indicated that TR-Mre11 can still interact with its MRN partners and form a complex, but showed a loss of DNA binding and nuclease activity *in vitro*. However, it is important to note that *in vitro* DNA binding and nuclease assays were performed only in the absence of ATP[250]. Our biochemically characterized *ct*M$^{\Delta C}$RN construct precisely matched the cancer-associated Mre11 truncation and we observed that removal of Mre11’s C-terminus did not eliminate ATP dependent interaction with DNA ends (Figure 17 C, Section 2.3 Figure 3 B). Hence, an interpretation that C-terminal truncation of Mre11 benefits cancer cells due to loss of DNA binding by the MRN complex should be further investigated. Alternatively, the Mre11 truncation could benefit cancer cells not because of inability to bind DNA ends at a damage site, but rather lack of efficient scanning for DSBs. In addition, this SPRTN mediated truncation can have an effect on non-repair roles of MRN that might require interaction with undamaged DNA, like chromosome organization or transcription[251,252].

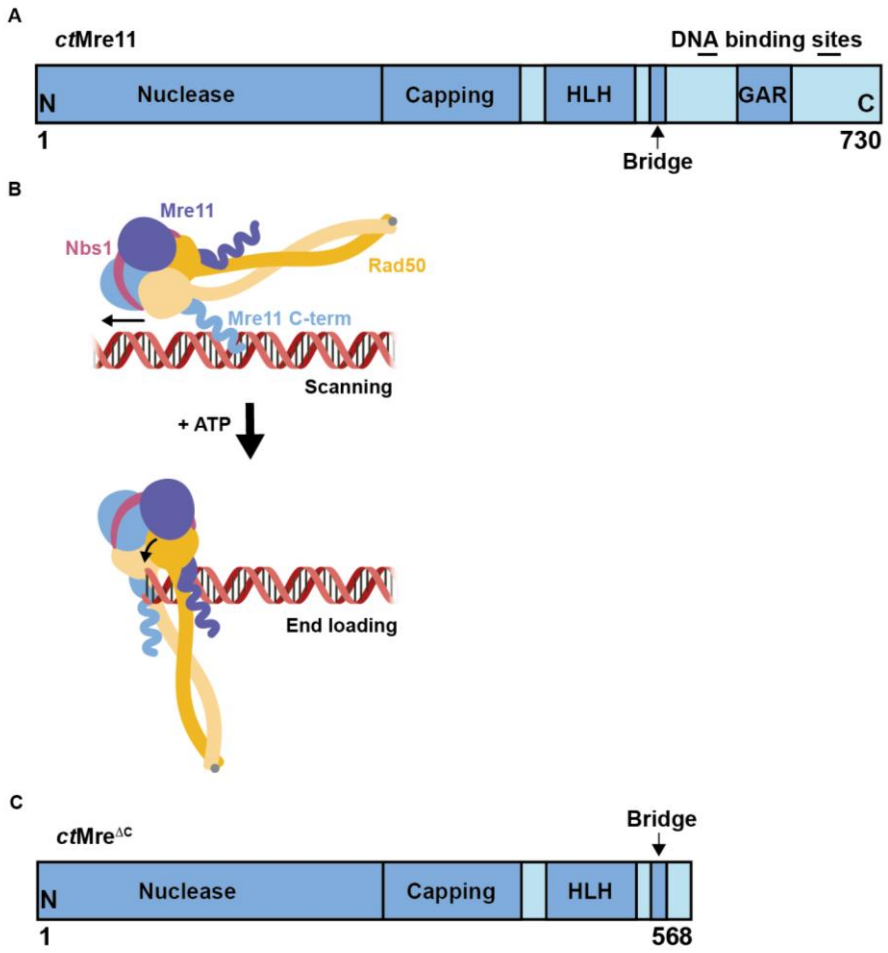

Figure 17. Two distinct modes of DNA binding by *ct*MRN. A, domain map of eukaryotic Mre11 with newly identified bridge motif and C-terminal DNA binding sites indicated. **B,** proposed model of DNA scanning and end detection by eukaryotic MRN. MRN complex scans DNA via the C-terminus of Mre11. Upon DNA end detection, MRN loads onto DNA in an ATP-dependent mechanism and binds DNA via the canonical Rad50 binding site. **C,** domain map of C-terminally truncated eukaryotic Mre11.

3.3 The structural and functional roles of Nbs1 in the MRN complex

Despite extensive structural and functional studies of MRN/X complex, eukaryote-specific and highly unstructured Nbs1/Xrs2 remains the least characterized component of the complex. Multiple crystal structures of *S. pombe* Nbs1/Xrs2 N-terminal FHA-BRCT1-BRCT2 domains with and without binding partners, like CtIP/Sae2, are available[121,253]. This structured N-terminal region is known to bind phosphorylated substrates and be involved in organization of

repair foci, but it spans less than half of the Nbs1 protein[254]. The flexible C-terminal half of Nbs1 contains functionally critical and highly conserved motifs. The FxF/Y motif and the acidic patch are located at the very C-terminus of Nbs1/Xrs2 and function in recruitment and activation of ATM/Tel1 kinase[125]. Structural and functional studies have mapped Nbs1 binding site to the N-terminal HEAT repeat domains of ATM/Tel1, which is in a similar location to mTORC1 and DNA-PKcs activator binding sites[125,255,256]. However, the cryo-EM structure of human ATM bound to an Nbs1 peptide containing the FxF/Y motif revealed an inactive conformation of the kinase[256]. Also, addition of high concentrations of this peptide to the steady-state kinase assays showed no effect on the ATM catalytic activity[256]. Taken together, the Nbs1/Xrs2 alone is not sufficient to activate ATM/Tel1 kinase. This is in agreement with observations that all components of the MRN/X complex and dsDNA are needed for a full activation of ATM/Tel1[137,257].

The C-terminus of Nbs1/Xrs2 also contains a highly conserved KNFKxFxx motif, which is responsible for mediating interaction with the Mre11 dimer. A crystal structure of *S. pombe* Mre11 in complex with Nbs1 revealed this complex stoichiometry as M_2N_2 with one Nbs1 binding to each side of Mre11 dimer as an extended chain. However, only one of the two interacting Nbs1 molecules bound across the Mre11 dimer interface via the KNFKxFxx motif providing an asymmetric bridging[86]. In contrast to these findings, our structure of full-length *ct*MRN complex defines complex stoichiometry to be $M_2R_2N_1$ (Section 2.3 Figure 1 C). We also observe Nbs1 that wrap around the Mre11 nuclease domain dimer as an elongated chain and binds the Mre11 dimer interface via the conserved KNFKxFxx motif as seen in the *S. pombe* structure (Figure 18 A)[86]. In the *ct*MRN complex, it is a single Nbs1 protein that bridges the Mre11 dimer and binds to the same surface areas of both Mre11 protomers via different elements (Figure 18 B). The mode of a single Nbs1 interacting with the dimeric Mre11 suggests that the essential function of Nbs1 is to stabilize the dimeric state of Mre11 and the architecture of MR catalytic head. This is also supported by our observation that asymmetric features of Mre11 and Rad50 correlate with the orientation of Nbs1 indicating that Nbs1 influences the behavior of the entire MRN complex (Figure 18 C). In addition, CtIP/Sae2 promotes the endonuclease activity of the Mre11 component via binding to the N-terminus of Nbs1/Xrs2[67,121]. Hence, the stabilizing function of Nbs1 might play an important role in the regulation of MRN activity as major conformational changes are known to be needed for complex transition from a “resting” to a “cutting” state[100].

Recent studies in mice showed that Nbs1 deletion leads to the embryonic lethality and identified a minimal Nbs1 fragment that rescues Nbs1 deficiency. This fragment was shown to be sufficient for the ATM activation, Mre11 dimerization and DNA binding, and CtIP-mediated activation of Mre11 endonuclease activity[258]. Interestingly, the minimal murine Nbs1 almost precisely matches the fragment of Nbs1 that we observe in our *ct*MRN structure (Figure 18 D). Taken together, these findings suggest that wrapping around the Mre11 dimer by Nbs1

is essential for structural integrity and functional roles of the MRN complex in endo-nucleolytic DNA processing and ATM activation.

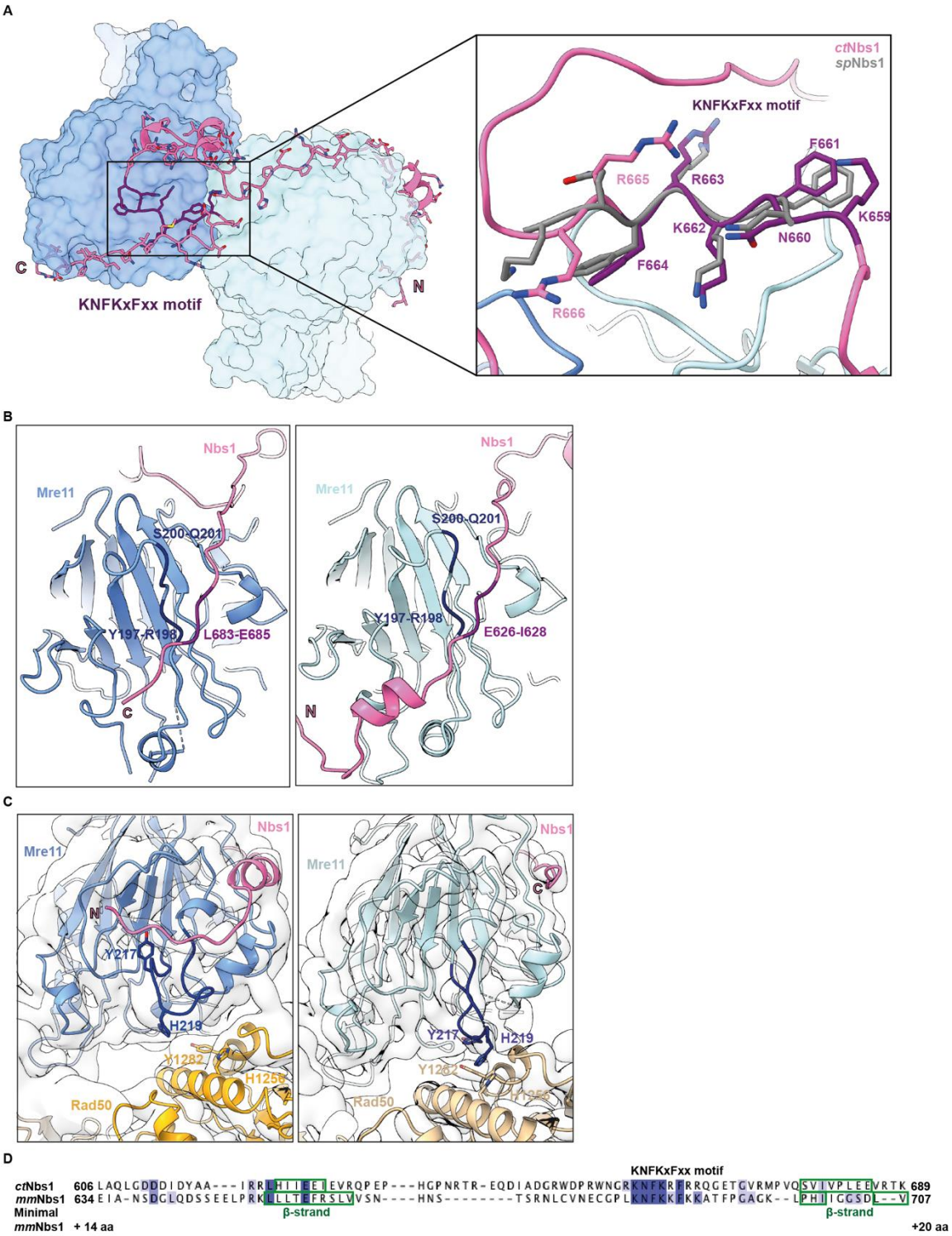

Figure 18. Structural features of *ct*Nbs1 peptide. A, a single Nbs1 polypeptide (colored pink) binds asymmetrically across both Mre11 phosphodiesterase domains (colored blue). Inset, comparison of *ct*Nbs1 and *sp*Nbs1 KNFKxFxx motif. **B,** the interfaces of the N- and C-terminal region of resolved *ct*Nbs1 peptide, which bind with reverse polarity to equivalent regions on Mre11are shown. **C,** side-by-side comparison of N- and C-termini of resolved Nbs1 peptide interacting with Mre11. Longer N-terminus of Nbs1 interacts with Mre11 loop containing Y217 and H219 residues affecting Mre11-Rad50 interaction at this site. **D,** sequence alignment of *ct* and *mm*Nbs1. Conserved residues were highlighted in shades of blue, predicted conserved β-strands were framed in green. Minimal mouse Nbs1 is indicated with a number of additional amino acids at each side of the fragment used for the alignment. Alignments were calculated with ClustalΩ, secondary structure predictions with JPred4[259,260].

3.4 Rad50 zinc-hook mediated MRN dimerization

The Rad50 zinc-hook is critical for an assembly and various functions of the MRN complex since deletion of the zinc-hook domain leads to phenocopying of the Rad50 knockdown[116,261]. Numerous studies, that include negative stain electron microscopy, AFM, X-ray crystallography and *in cellulo* assays, have shown that multiple MR/MRN complexes can interact with one another via apices of Rad50 coiled-coils, forming large assemblies and tethering different DNA fragments[113,114,244,245,262]. Crystal structures of zinc-hook fragments showed two different arrangements: nearly anti-parallel and parallel conformations (Figure 8)[113,114,263]. Thus, it was interpreted that dimerization of two zinc-hooks can happen within a single MR/MRN complex in a closed rod or an open ring conformation (intra-complex), or between the coiled-coils of different MR/MRN complexes (inter-complex) resulting in the DNA tethering. More recently, the understanding of the role of Rad50 coiled-coils has shifted from linker elements connecting two MR/MRN catalytic heads to being functionally critical chemo-mechanical elements[100]. This made it less feasible that zinc-hooks switch from intra- to inter-complex interaction conformations. They rather act as stably associated hinges that can switch between open and closed states of the coiled-coils within a single MR/MRN complex.

The cryo-EM structure of the *ct*Rad50 zinc-hook tetramer revealed how the rod-shaped zinc-hook dimer can further dimerize forming an interaction between two MRN complexes. This explains how MRN complexes can perform the tethering function and hold together DNA regions that are up to 120 nm apart (Figure 19 A). It seems that the tethering interaction between two MRN complexes requires Rad50 coiled-coils to adopt a closed rod conformation. Therefore, zinc-hook mediated tethering might be influenced by ATP- and DNA-binding determined conformational changes of the catalytic head and proximal coiled-coils.

The crystal lattice of the *hs*Rad50 zinc-hook revealed a similar tetrameric arrangement that was determined for the *ct*Rad50 and mainly had ionic interactions between the zinc-hook dimers (Figure 19 B, C)[114]. The functional significance of the observed MRN-MRN interaction via the

zinc-hook was evident after the mutation of the apex tethering loop impaired the repair of ROS-induced DNA damage in human cells (Section 2.3 Figure 5 B). An observation that a SQ-motif is present in the proximity of the apex tethering loop suggests a potential role of phosphorylation in the regulation of the MRN mediated tethering (Figure 19 D). Earlier studies have noticed and investigated this SQ site showing that it gets phosphorylated by both ATM and ATR kinases[264,265]. In addition, mutating the serine residue of the SQ site affected DSB repair, checkpoint activation, survival and loading of cohesion at the sites of replication restart. As *hs*MRN^{S635G} mutant retained a fully functional nuclease, phenotypes observed are not caused by defects in the nuclease activity[264]. This indicates that MRN tethering function is regulated by ATM and ATR activity in human cells. Structurally, phosphorylation could increase stability of tethering via interactions with basic amino acids on the connecting apex protomer. On the other hand, phosphorylation could change conformation of the apex tethering loop and reduce tethering potential.

It is important to note that the functional importance of the zinc-hook mediated MRN inter-complex dimerization might not be conserved throughout different species as the exchange of the *S. pombe* Rad50 zinc-hook with the hinge element of the MukB (bacterial SMC protein) did not lead to changes affecting DNA repair[266]. This suggests that in some organisms, like *S. pombe*, the Rad50 zinc-hook might function as a rather stable dimerization interface.

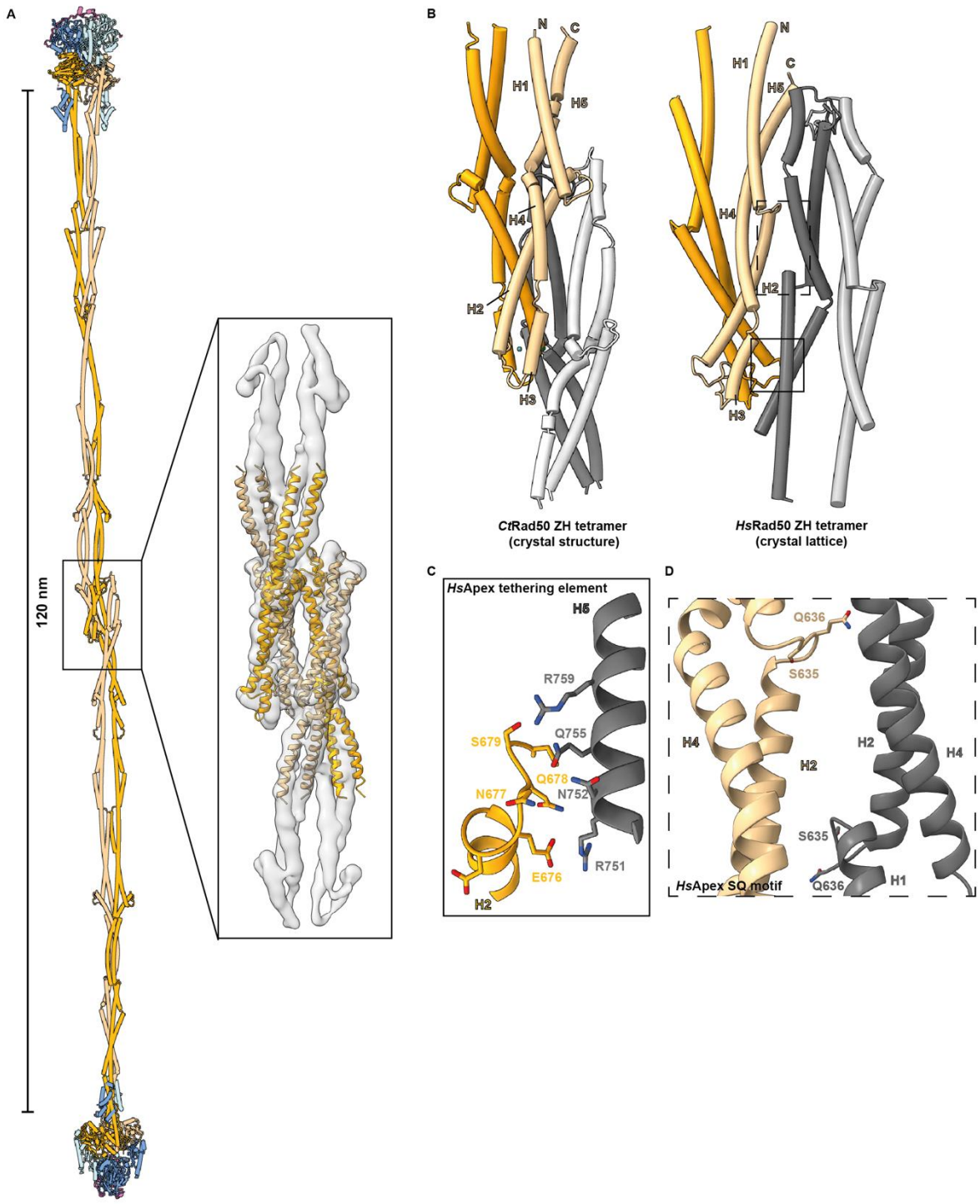

Figure 19. Dimerization of MRN via Rad50 zinc-hook. A, model of Rad50 zinc-hook mediated MRN dimer. This structure could bridge DNA ends that are up to 120 nm apart. Inset, crystal structure of *ct*Rad50 zinc-hook tetramer fitted into cryoEM density. **B,** comparison of *Ct*Rad50 and *Hs*Rad50 zinc-hook tetramers. Crystal structure of *Ct*Rad50 zinc-hook tetramer and crystal lattice of *Hs*Rad50 zinc-hook (PDB:5GOX) tetramer indicates conserved zinc-hook tethering mechanism. **C,** the apex tethering element of *Hs*Rad50 and its interactions. Side chains of residues involved in the interaction are shown. **D,** SQ motif proximal to apex tethering element.

3.5 Functional clustering of MRN complexes

Clustering of the MRN/X complex has been observed in numerous studies using different techniques, like AFM, electron microscopy, mass photometry and cell-based experiments[113,114,262,267–269]. A recent article reveals that *S. cerevisiae* MRX can oligomerize via the conserved beta-sheet motif in the Rad50 head domain and form nucleolytically active assemblies at DNA ends[269]. *In vivo* experiments using Rad50 mutants with altered head-mediated oligomerization capabilities showed the importance of higher-order MRX assemblies for its cellular functions in DNA repair, signaling and telomere maintenance[269].

The Rad50 zinc-hook mediated MRN-MRN interaction is composed of a small hydrophobic element surrounded by salt bridges and, therefore, can be relatively transient on a single MRN dimer scale (Figure 19 C). However, head-mediated MRN clustering can lead to multiple protruding Rad50 coiled-coils and bring numerous zinc-hooks in proximity generating a molecular Velcro through multivalent interactions (Figure 20)[269]. In this case, the extent of tethering could be regulated via the cluster size by the head of the complex. Combination of DNA end binding activity with head-to-head and zinc-hook-to-zinc-hook interactions can explain the mechanism by which MRN/X complex can bridge DNA ends and sister chromatids at double-strand breaks as observed in *S. cerevisiae*[268].

Interestingly, the nature of zinc-hook mediated interactions that combine small hydrophobic parts and ionic bonds are characteristic for the types of interactions seen in liquid-liquid phase separation (LLPS), or condensates[270]. These structures create separated membranelles compartments that execute specific cellular functions. For instance, the process of DNA damage response creates transient repair compartments to increase local concentration of repair proteins and activate signaling pathways. In the recent years, numerous DNA repair proteins, like 53BP1, Rad52 and TopBP1, have been shown to form LLPS[271–273]. In addition, MRN interacting protein (MRNIP) undergoes condensation *in vitro* and *in vivo* concentrating the MRN complex into liquid-like droplets in the nucleus[274]. MRNIP condensates have been shown to accelerate MRN loading, enhance DNA end resection, promote DNA damage repair and amplify ATM signaling[274]. Currently there is no experimental evidence confirming that MRN/X clusters form condensates on their own. Thus, it could be that Rad50 zinc-hook mediated interactions have a secondary function in further promoting MRNIP initiated LLPS.

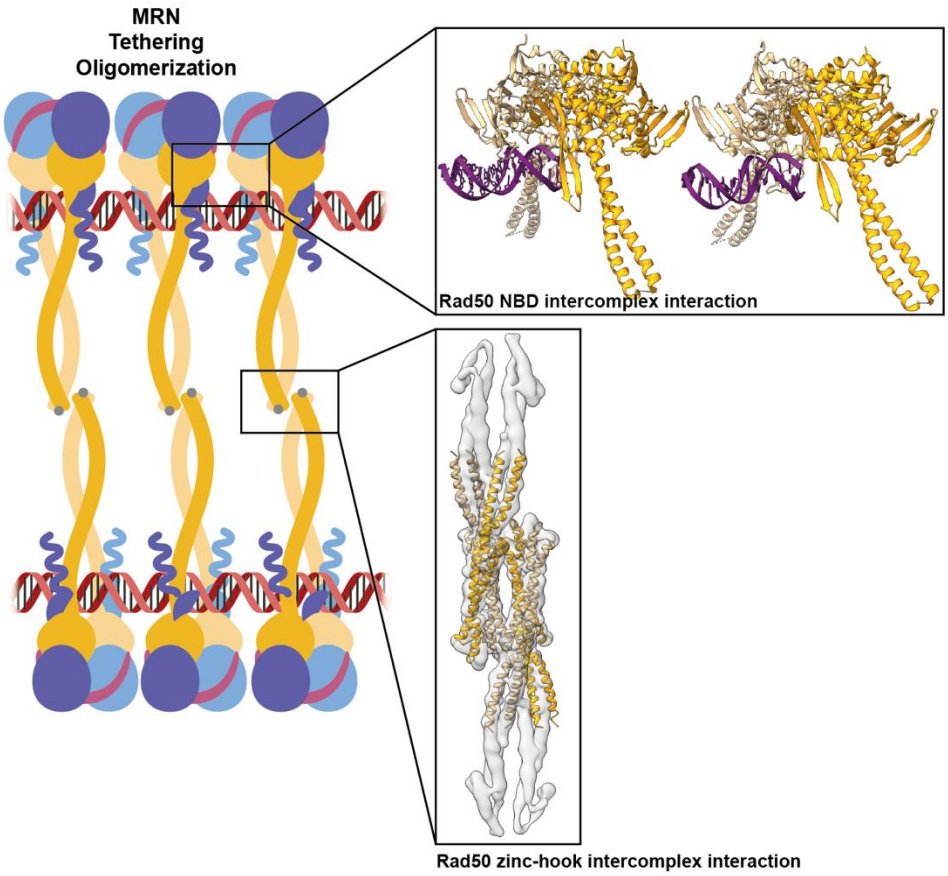

Figure 20. Tethering oligomerization model of MRN complexes. Proposed model of DNA tethering by eukaryotic MRN. Oligomerization may occur via Rad50 NBDs and zinc-hook leading to DNA end tethering. Insets show crystal structure of two *Ct*Rad50 dimers bound to one oligonucleotide molecule each (PDB: 5DAC) (top) and crystal and cryoEM structures of *Ct*Rad50 zinc-hook tetramer (bottom).

3.6 DNA binding activity of ATM/Tel1 kinase

Multiple studies using yeast and mammalian systems have confirmed that ATM/Tel1 kinase has DNA binding properties[137,257,275,276]. This finding does not come as a surprise since ATM/Tel1 gets recruited directly to DNA damage sites by the MRN/X complex and its kinase activity is stimulated by DNA. In *S. cerevisiae*, the presence of both MRX and DNA has a synergistic effect on Tel1 activation[137].

We have used the N-terminal fragment of *Chaetomium thermophilum* (*ct*) Tel1, containing the spiral and the pincer HEAT-repeat domains, which have been previously suggested to be involved in interaction with DNA, to further investigate DNA binding[277]. Our findings confirmed, that N-terminal domains of *ct*Tel1 interact with DNA and revealed a higher binding

affinity to longer DNA oligomers, in agreement with other studies (Section 2.1 Figure 3B)[137,257,276]. In addition, a much stronger binding to a 60-mer duplex DNA than 30-mer DNA suggests that *ct*Tel1 does not bind DNA by primarily recognizing the ends. This is in agreement with findings on *S. cerevisiae* (*sc*) Tel1, where no significant difference was observed comparing linear, supercoiled and nicked circular DNA stimulatory effect on kinase activity[137]. Thus, DNA ends are not required for Tel1 kinase activity. When it comes to a human system, ATM kinase activity is stimulated about 100-fold in the presence of MRN and 1000 bp long DNA, and has an absolute requirement for double-stranded DNA ends[257]. This hints to the fundamental difference between the yeast and human systems. Work on *sc*Tel1 also showed that at least 60 base-pair (bp) double-stranded DNA was necessary for kinase activation with longer DNA having an even stronger effect[137]. It is worth noting that the longest dimensions of dimeric *ct*Tel1 are in the range of 200 Å, which roughly corresponds to the length of 60 bp of linear B-DNA. One possible interpretation of this DNA length dependency could be that dimeric, or even multimeric, form of Tel1 functions in high-affinity DNA binding and kinase activation.

The atomic model of *ct*Tel1 allowed calculation of surface charge map, which revealed a few positively charged patches on N-terminal HEAT repeat domains that could be involved in DNA binding (Section 2.1 Figure 3A). One of the promising DNA binding sites is a highly conserved RKKR motif located in the loop between helices H7 and H8. Another potential site for DNA interaction is in a highly conserved TAN motif located at the very N-terminus of the protein and involved in DNA damage signaling and telomere maintenance[278]. A high sequence conservation level, in otherwise not sequence conserved HEAT repeats, as well as occurrence of human cancer associated mutations in these positively charged patches highlight their proposed functional significance, which could be connected to DNA binding roles. One potential explanation for the DNA length dependency seen in our binding assay could also be that multiple positively charged patches on the Tel1 surface contribute to stable DNA binding (Section 2.1 Figure 3). In this case, a longer DNA would be needed to bind across all of the Tel1 patches. However, this would not explain the minimal requirement of 200 bp DNA for ATM activation in *Xenopus* extract[279].

Currently the DNA binding activity of ATM/Tel1 seems to be fully conserved and have a clear activating function, but the details of interaction and mechanism of activation remain to be elucidated by combination of structural and biochemical approaches.

3.7 Auto-inhibited state of ATM/Tel1 kinase and potential activation mechanisms

All medium to high-resolution structures of ATM/Tel1 kinase to date have a dimeric form, which is considered to be an inactive state[255,256,280–282]. Detailed structural information that we and others obtained on fungal and human ATM/Tel1 consistently explained the molecular mechanism of kinase active site inhibition[255,280,282]. The active site cleft of the kinase domain is blocked for potential substrates by the PIKK regulatory domain (PRD) (Figure 21 A, Section 2.1 Figure 6 B). The PRD makes multiple interactions firmly keeping it in a position. In the human structure, these interactions include hydrogen bonding of Q2971 and hydrophobic contact of L2970 with residues in the activation loop. Comparison of human ATM structure with PIKK SMG1-8-9 in complex with its substrate UPF1 showed that PRD residue Q2971 is positioned at the site of substrate glutamine from the SQ/TQ kinase selectivity motif (Figure 21 A, inset) [283]. Hence, PRD mimics SQ/TQ site and acts as a pseudo-substrate. It has been suggested that the obstruction of the active site by the PRD is the main mechanism of kinase inhibition as the ATM/Tel1 active site residues are in a catalytically competent conformation[171,255,280,284]. However, structural studies on mTOR, another member of PIKK family, showed that kinase activation involves conformational rearrangements in the FAT domain that influence the positioning of N- and C-lobes of the kinase domain. This results in the adjustment of catalytic residues into the optimal conformation for efficient catalysis (Figure 21 B)[285]. In addition, a recent structure of DNA-PKcs in an active-state showed a similar conformational change of kinase domain lobes upon activation as seen for mTOR (Figure 21 C)[286]. This hints to a common activation mechanism of PIKKs that involves conformational changes in the active site.

However, the exact activation mechanism of ATM/Tel1 kinase as well as factors involved remain poorly understood. It is known that kinase activity of ATM/Tel1 is stimulated by the MRN/X complex and DNA, both of which interact with N-terminal domains located far away from the active site[137,256,276]. This mode of action seems to be conserved as some activators of other PIKKs, like ATRIP of ATR, Ku70/80 of DNA-PKcs and RHEB of mTOR, also interact with N-terminal HEAT-repeat portions of kinases and promote activity by relay of conformational changes that reach the active site[285,287–289]. In order to unambiguously confirm this mechanism of ATM/Tel1 activation by MRN/X, a structure of ATM-MRN complex is required.

Another important factor in ATM/Tel1 activation is post-translational modifications (PTMs). In human cells, a full ATM activation is thought to involve auto-phosphorylation of five sites and acetylation[290–292]. Even though we obtained the most complete structures of *ct*Tel1 and human ATM to date, the mapping of phosphorylation sites was not possible as they are all located in the flexible loop regions. The observation that these sites are not located at any

important dimer interfaces or known regulatory motifs questions the ability of phosphorylation to directly induce conformational changes and activate ATM/Tel1. Phosphorylation of exposed flexible loops might allow binding of additional factors that promote the transition of ATM/Tel1 to the active state. However, further studies are needed to investigate this theory. On the contrary to phosphorylation, acetylation site could be mapped on the human ATM structure and K3016, which gets modified by histone acetyltransferase Tip60, is located at one of the conserved PRD helices. This residue forms a salt bridge with E2895, which belongs to the C-lobe of the kinase domain (Figure 21 D)[293]. Neutralization of positive charge would directly affect this salt bridge and could lead to a larger scale rearrangement potentially resulting in kinase activation.

Initial models suggested that dissociation of ATM/Tel1 into monomers is required for enzymatic activation[294]. There is evidence supporting the existence of ATM monomers *in vitro* and *in vivo*[173,257,276]. However, in the light of dimeric ATM/Tel1 structures, monomerization seems unlikely as it is energetically unfavorable due to the large and hydrophobic dimer interface (Section 2.1 Figure 5)[255,280]. Structures of asymmetric dimers for human ATM and *sc*Tel1 have been solved showing distorted PRD and, therefore, are proposed to be an active form of dimer[280,284]. Thus, dimer-to-monomer transition might be unnecessary to activate ATM/Tel1 kinase. A low-resolution cryo-EM structure of monomeric human ATM is available, but it does not show any major conformational changes that would shield hydrophobic dimer interface and explain an active monomer state[282].

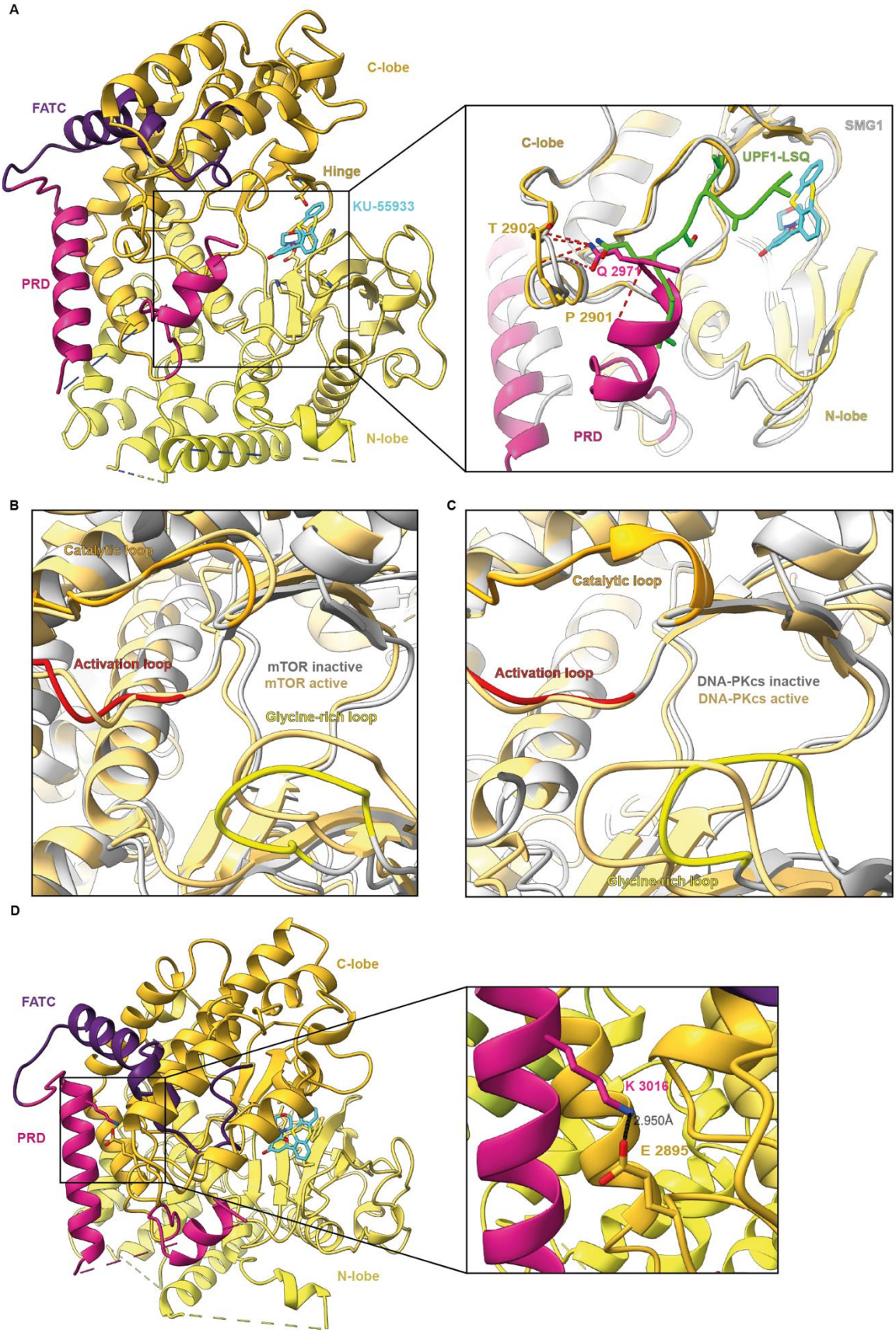
A
C-lobe
FATC
Hinge
KU-55933
PRD
N-lobe
SMG1
C-lobe
UPF1-LSQ
T 2902
Q 2971
P 2901
PRD
N-lobe
B
Catalytic loop
Activation loop
mTOR inactive
mTOR active
Glycine-rich loop
C
Catalytic loop
Activation loop
DNA-PKcs inactive
DNA-PKcs active
Glycine-rich loop
D
C-lobe
FATC
PRD
N-lobe
K 3016
2.950Å
E 2895

Figure 21. Auto-inhibition and activation mechanisms of ATM kinase. A, structure of C-terminal portion of human ATM kinase in KU-55933 (cyan) inhibitor bound state. Inset, detailed view of the superimposed substrate-bound (UPF1 substrate in green) SMG1 (PDB ID 6Z3R; gray) and KU-55933-bound ATM (color) kinase domain. Substrate-mimicking Q2971 of PRD (magenta) and its hydrogen bonds (red dotted lines) to the kinase C-lobe residues T2902 and P2901 are indicated. **B,** comparison of active (PDB: 6BCU) and inactive (PDB: 6BCX) mTOR structures with activation, catalytic and glycine-rich loops highlighted. **C,** comparison of active (PDB: 7K0Y) and inactive (PDB: 7K1N) DNA-PKcs structures with activation, catalytic and glycine-rich loops highlighted. **D,** structure of C-terminal portion of human ATM kinase in KU-55933 (cyan) inhibitor bound state. Inset, interaction between K3016, which gets acetylated during ATM activation, and E2995.

3.8 Inhibitors of ATM in cancer treatment

It has been revealed that inhibition of ATM activity increases sensitivity of different tumors to anti-cancer therapies that induce DNA double-strand breaks, for instance, radio- and chemo-therapy, and targeted therapies, like ATR and PARP inhibition[233,295–297]. Despite the targeting of ATM being a promising strategy for cancer treatment, identification of novel inhibitors was limited to library screens due to a lack of high-resolution human ATM structure. We obtained three high-resolution human ATM structures with inhibitors (KU-55933 and M4076) and ATPγS bound in the active site. These structures revealed ATP-bound state of the active site as well as binding mechanisms of two different classes of ATP-competitive small-molecule inhibitors.

M4076 is a novel, sub-nanomolar potent and selective ATM kinase inhibitor. In comparison to other ATM inhibitors that are currently in phase I clinical trials, like AZD0156 (IC_{50} = 0.58 nM) and AZD1390 (IC_{50} = 0.78 nM), M4076 shows an even higher potency with IC_{50} of 0.2 nM[241,242]. M4076 was developed in the absence of high-resolution ATM structures, but now having this information the high potency of M4076 can be explained. One of the most prominent features is an extensive π–π and amide–π stacking interactions between the M4076 and W2769 in the hinge region of ATM (Figure 22 A). This interaction is not present in the complex with a less potent KU-55933 inhibitor (Figure 22 B). In addition, binding of M4076 shifts the position of C2770, at the hinge region, towards the inhibitor. This movement of the hinge is observed in the ATPγS-bound active site, but not with KU-55933 (Figure 22 A-C). Combination of additional contacts that M4076 makes with ATM, when compared with KU-55933, explains the ~35-fold stronger enzymatic potency of M4076. Additionally, the comparison of a high-resolution structure of ATM with M4076 bound in the active site and structures of other PIKKs led to explanation of the inhibitor selectivity (Section 2.2 Figure 4 A-C)[287,289,298]. Members of PIKK family and PI3K isoforms have a highly conserved kinase domain, especially the active site[299]. However, some sequence differences are present and they

include residues, which are in direct contact with M4076 (Section 2.2 Figure 4 D). One of the most significant differences is a substitution of A2693 in ATM with much bulkier residues in ATR, DNA-PKcs, mTOR and PI3Ks, explaining the observed selectivity of M4076 towards ATM. Future structure-based drug design of specific ATM active site inhibitors can further explore these subtle differences.

An emerging alternative to ATP-mimicking kinase active site inhibitors are conformational inhibitors that specifically bind to the inactive state of the kinase and lock it[300,301]. An advantage of conformational inhibitors is that they target less conserved sites of the kinase and, therefore, can provide a high selectivity towards a specific target. In order to use this approach and design a conformational inhibitor, kinase structures in both active and inactive form are needed. Currently, high-resolution structure of active human ATM kinase is missing, but previously observed asymmetric dimer structures hint to conformational changes associated with activation[280,282]. In addition, comparing structures of other PIKKs, mTOR and DNA-PKcs, in their active and inactive forms reveal consistent structural rearrangements within kinase domain (Figure 21 B, C)[285,286]. Hence, solving the high-resolution structure of human ATM in its active conformation and identification of conformational changes involved in activation would allow structure-based design of conformational inhibitors that could provide an even better specificity and less off-target effects.

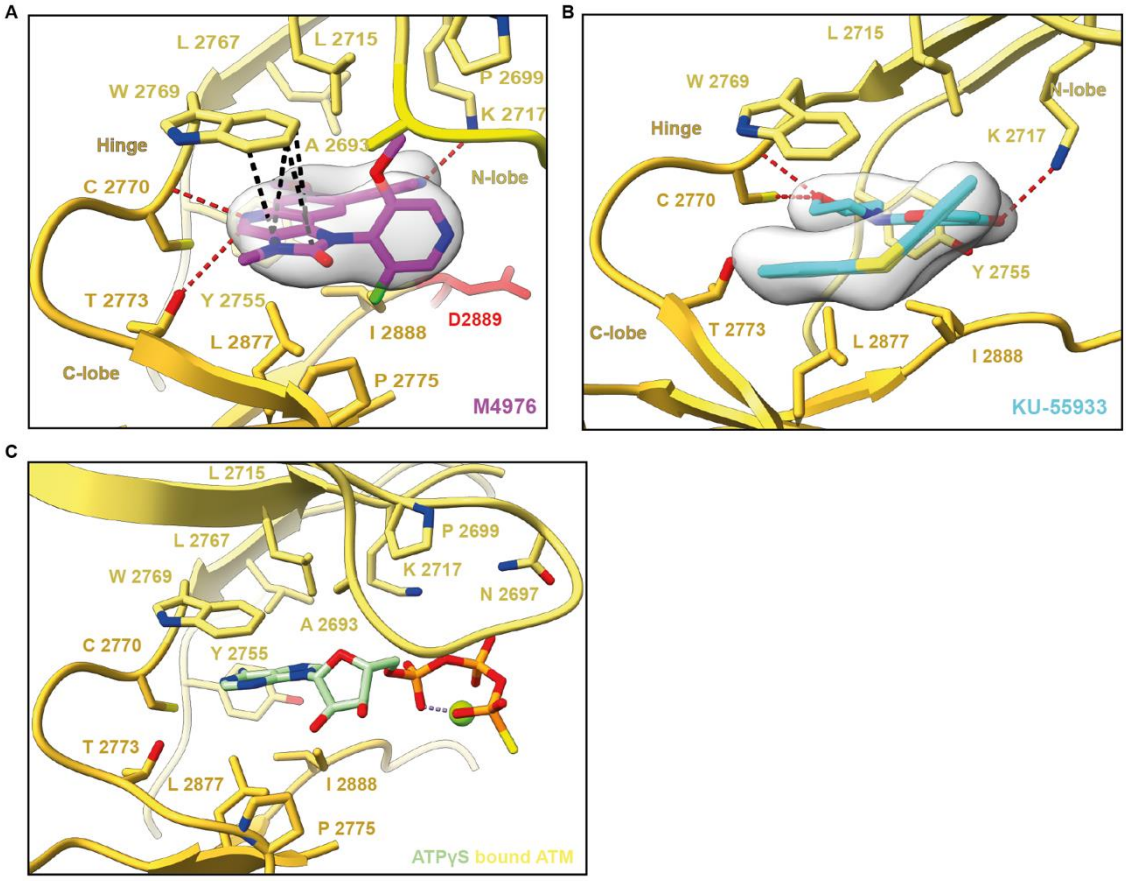

Figure 22. Structural characterization of two different classes of ATM inhibitors. A, structure of the M4076 inhibitor at the kinase active site at resolution of 3.0 Å (contoured at 0.038). Side chains of inhibitor-proximal residues and interactions are shown. Hydrogen bonds are indicated by red dotted lines and π-stacking interactions are highlighted as black dotted lines. The kinase activation loop is shown in red. **B,** structure of the KU-55933 inhibitor at the kinase active site at resolution of 2.8 Å (contoured at 0.032). Side chains of inhibitor-proximal residues and interactions are shown. Hydrogen bonds are indicated by red dotted lines. **C,** structure of ATPγS at the kinase active site at resolution of 2.8 Å. Side chains of ATPγS-proximal residues are indicated.

4. References

1. Nimrat Chatterjee and Graham C.Walker. Mechanisms of DNADamage, Repair, andMutagenesis. *Environ. Mol. Mutagen.* **405**, 391–405 (2017).

2. Huang, R. & Zhou, P. K. *DNA damage repair: historical perspectives, mechanistic pathways and clinical translation for targeted cancer therapy*. *Signal Transduction and Targeted Therapy* vol. 6 (Springer US, 2021).

3. Wallace, S. S. Base excision repair: A critical player in many games. *DNA Repair (Amst).* **19**, 14–26 (2014).

4. Petruseva, I. O., Evdokimov, A. N. & Lavrik, O. I. Molecular mechanism of global genome nucleotide excision repair. *Acta Naturae* **6**, 23–34 (2014).

5. Jiricny, J. The multifaceted mismatch-repair system. *Nat. Rev. Mol. Cell Biol.* **7**, 335–346 (2006).

6. Chang, H. H. Y., Pannunzio, N. R., Adachi, N. & Lieber, M. R. Non-homologous DNA end joining and alternative pathways to double-strand break repair. *Nat. Rev. Mol. Cell Biol.* **18**, 495–506 (2017).

7. Wright, W. D., Shah, S. S. & Heyer, W. D. Homologous recombination and the repair of DNA double-strand breaks. *J. Biol. Chem.* **293**, 10524–10535 (2018).

8. Yi, C. & He, C. DNA repair by reversal of DNA damage. *Cold Spring Harb. Perspect. Biol.* **5**, (2013).

9. Fuchs, R. P. & Fujii, S. Translesion DNA synthesis and mutagenesis in prokaryotes. *Cold Spring Harb. Perspect. Biol.* **5**, (2013).

10. Kaina, B. DNA Damage-Induced Apoptosis. in *Encyclopedia of Cancer* (ed. Schwab, M.) 1136–1139 (Springer Berlin Heidelberg, 2011). doi:10.1007/978-3-642-16483-5_1673.

11. James E Cleaver. Diagnosis of Xeroderma Pigmentosum and Related DNA Repair- Deficient Cutaneous Diseases. *Curr Med Lit Dermatol.* **23**, 1–7 (2008).

12. Coppedè, F. & Migliore, L. DNA damage in neurodegenerative diseases. *Mutat. Res. - Fundam. Mol. Mech. Mutagen.* **776**, 84–97 (2015).

13. Usborne, C. M. & Mullard, A. P. A review of systemic anticancer therapy in disease palliation. *Br. Med. Bull.* **125**, 43–53 (2018).

14. Li, L. Y., Guan, Y. Di, Chen, X. S., Yang, J. M. & Cheng, Y. DNA Repair Pathways in Cancer Therapy and Resistance. *Front. Pharmacol.* **11**, 1–13 (2021).

15. Desouky, O., Ding, N. & Zhou, G. Targeted and non-targeted effects of ionizing radiation. *J. Radiat. Res. Appl. Sci.* **8**, 247–254 (2015).

16. Vignard, J., Mirey, G. & Salles, B. Ionizing-radiation induced DNA double-strand breaks: A direct and indirect lighting up. *Radiother. Oncol.* **108**, 362–369 (2013).

17. Henner, W. D., Grunberg, S. M. & Haseltine, W. A. Sites and structure of γ radiation-induced DNA strand breaks. *J. Biol. Chem.* **257**, 11750–11754 (1982).

18. Emadi, A., Jones, R. J. & Brodsky, R. A. Cyclophosphamide and cancer: Golden anniversary. *Nat. Rev. Clin. Oncol.* **6**, 638–647 (2009).

19. Yu, H. Environmental carcinogenic polycyclic aromatic hydrocarbons: Photochemistry and phototoxicity. *J. Environ. Sci. Heal. - Part C Environ. Carcinog. Ecotoxicol. Rev.* **20**, 149–183 (2002).

20. Smela, M. E., Currier, S. S., Bailey, E. A. & Essigmann, J. M. The chemistry and biology of aflatoxin B1: From mutational spectrometry to carcinogenesis. *Carcinogenesis* **22**, 535–545 (2001).

21. Loeb, L. A. & Monnat, R. J. DNA polymerases and human disease. *Nat. Rev. Genet.* **9**, 594–604 (2008).

22. Pommier, Y. *et al.* Repair of Topoisomerase I-Mediated DNA Damage. *Prog. Nucleic Acid Res. Mol. Biol.* **81**, 179–229 (2006).

23. Bhagwat, A. S. *et al.* Strand-biased cytosine deamination at the replication fork causes cytosine to thymine mutations in Escherichia coli. *Proc. Natl. Acad. Sci. U. S. A.* **113**, 2176–2181 (2016).

24. Thompson, P. S. & Cortez, D. New insights into abasic site repair and tolerance. *DNA Repair (Amst).* **90**, 102866 (2020).

25. Konno, T., Melo, E. P., Chambers, J. E. & Avezov, E. Intracellular sources of ROS/H2O2 in health and neurodegeneration: Spotlight on endoplasmic reticulum. *Cells* **10**, 1–26 (2021).

26. Cadet, J., Douki, T. & Ravanat, J. L. Oxidatively generated base damage to cellular DNA. *Free Radic. Biol. Med.* **49**, 9–21 (2010).

27. VanderVeen, L. A. *et al.* Evaluation of the Mutagenic Potential of the Principal DNA Adduct of Acrolein. *J. Biol. Chem.* **276**, 9066–9070 (2001).

28. Hegde, M. L., Izumi, T. & Mitra, S. *Oxidized base damage and single-strand break repair in mammalian genomes: Role of disordered regions and posttranslational modifications in early enzymes*. *Progress in Molecular Biology and Translational Science* vol. 110 (Elsevier Inc., 2012).

29. Yang, S. & Lian, G. ROS and diseases: role in metabolism and energy supply. *Mol. Cell. Biochem.* **467**, (2020).

30. Warren, J. J., Forsberg, L. J. & Beese, L. S. The structural basis for the mutagenicity of O6-methyl-guanine lesions. *Proc. Natl. Acad. Sci. U. S. A.* **103**, 19701–19706 (2006).

31. Jeggo, P. A. & Löbrich, M. DNA double-strand breaks: Their cellular and clinical impact? *Oncogene* **26**, 7717–7719 (2007).

32. Mehta, A. & Haber, J. E. Sources of DNA double-strand breaks and models of recombinational DNA repair. *Cold Spring Harb. Perspect. Biol.* **6**, (2014).

33. Aida Muslimovic, Susanne Nystrom, Yue Gao, O. H. Numerical Analysis of Etoposide Induced DNA Breaks Aida. *PLoS One* **7**, 1–10 (2009).

34. Zeman, M. K. & Cimprich, K. A. Causes and consequences of replication stress. *Nat. Cell Biol.* **16**, 2–9 (2014).

35. Dudley, D. D., Chaudhuri, J., Bassing, C. H. & Alt, F. W. Mechanism and control of V(D)J recombination versus class switch recombination: Similarities and differences. *Adv. Immunol.* **86**, 43–112 (2005).

36. Malu, S., Malshetty, V., Francis, D. & Cortes, P. Role of non-homologous end joining in

V(D)J recombination. *Immunol. Res.* **54**, 233–246 (2012).

37. Xu, Z., Zan, H., Pone, E. J., Mai, T. & Casali, P. Immunoglobulin class-switch DNA recombination: Induction, targeting and beyond. *Nat. Rev. Immunol.* **12**, 517–531 (2012).

38. Soulas-Sprauel, P. *et al.* V(D)J and immunoglobulin class switch recombinations: A paradigm to study the regulation of DNA end-joining. *Oncogene* **26**, 7780–7791 (2007).

39. Ohkura, H. Meiosis: An overview of key differences from mitosis. *Cold Spring Harb. Perspect. Biol.* **7**, 1–15 (2015).

40. Lam, I. & Keeney, S. Mechanism and regulation of meiotic recombination initiation. *Cold Spring Harb. Perspect. Biol.* **7**, (2015).

41. Celerin, M., Merino, S. T., Stone, J. E., Menzie, A. M. & Zolan, M. E. Multiple roles of Spo11 in meiotic chromosome behavior. *EMBO J.* **19**, 2739–2750 (2000).

42. Chiruvella, K. K., Liang, Z. & Wilson, T. E. Repair of double-strand breaks by end joining. *Cold Spring Harb. Perspect. Biol.* **5**, 1–22 (2013).

43. Aguilera, A. & Gómez-González, B. Genome instability: A mechanistic view of its causes and consequences. *Nat. Rev. Genet.* **9**, 204–217 (2008).

44. Miné-Hattab, J. & Rothstein, R. DNA in motion during double-strand break repair. *Trends Cell Biol.* **23**, 529–536 (2013).

45. Mimori, T. & Hardin, J. A. Mechanism of interaction between Ku protein and DNA. *J. Biol. Chem.* **261**, 10375–10379 (1986).

46. Blier, P. R., Griffith, A. J., Craft, J. & Hardin, J. A. Binding of Ku protein to DNA. Measurement of affinity for ends and demonstration of binding to nicks. *J. Biol. Chem.* **268**, 7594–7601 (1993).

47. Yin, X., Liu, M., Tian, Y., Wang, J. & Xu, Y. Cryo-EM structure of human DNA-PK holoenzyme. *Cell Res.* **27**, 1341–1350 (2017).

48. Chang, H. H. Y. *et al.* Different DNA end configurations dictate which NHEJ components are most important for joining efficiency. *J. Biol. Chem.* **291**, 24377–24389 (2016).

49. Ma, Y., Pannicke, U., Schwarz, K. & Lieber, M. R. Hairpin opening and overhang processing by an Artemis/DNA-dependent protein kinase complex in nonhomologous end joining and V(D)J recombination. *Cell* **108**, 781–794 (2002).

50. Ramadan, K. *et al.* Human DNA polymerase λ possesses terminal deoxyribonucleotidyl transferase activity and can elongate RNA primers: Implications for novel functions. *J. Mol. Biol.* **328**, 63–72 (2003).

51. Ramadan, K., Shevelev, I. V., Maga, G. & Hübscher, U. De Novo DNA synthesis by human DNA polymerase λ, DNA polymerase μ and terminal deoxyribonucleotidyl transferase. *J. Mol. Biol.* **339**, 395–404 (2004).

52. Gu, J. *et al.* Erratum: XRCC4:DNA ligase IV can ligate incompatible DNA ends and can ligate across gaps (The EMBO Journal (2007) 26, (1010-1023) DOI: 10.1038/sj.emboj.7601559). *EMBO J.* **26**, 3506–3507 (2007).

53. Ahnesorg, P., Smith, P. & Jackson, S. P. XLF interacts with the XRCC4-DNA Ligase IV complex to promote DNA nonhomologous end-joining. *Cell* **124**, 301–313 (2006).

54. Xie, A., Kwok, A. & Scully, R. Role of mammalian Mre11 in classical and alternative nonhomologous end joining. *Nat. Struct. Mol. Biol.* **16**, 814–818 (2009).

55. Robert, I., Dantzer, F. & Reina-San-Martin, B. Parp1 facilitates alternative NHEJ, whereas Parp2 suppresses IgH/c-myc translocations during immunoglobulin class switch recombination. *J. Exp. Med.* **206**, 1047–1056 (2009).

56. Lee-Theilen, M., Matthews, A. J., Kelly, D., Zheng, S. & Chaudhuri, J. CtIP promotes microhomology-mediated alternative end joining during class-switch recombination. *Nat. Struct. Mol. Biol.* **18**, 75–80 (2011).

57. Ahmad, A. *et al.* ERCC1-XPF Endonuclease Facilitates DNA Double-Strand Break Repair. *Mol. Cell. Biol.* **28**, 5082–5092 (2008).

58. Wyatt, D. W. *et al.* Essential Roles for Polymerase θ-Mediated End Joining in the Repair of Chromosome Breaks. *Mol. Cell* **63**, 662–673 (2016).

59. Lu, G. *et al.* Ligase I and ligase III mediate the DNA double-strand break ligation in alternative end-joining. *Proc. Natl. Acad. Sci. U. S. A.* **113**, 1256–1260 (2016).

60. Kaniecki, K., De Tullio, L. & Greene, E. C. A change of view: Homologous recombination at single-molecule resolution. *Nat. Rev. Genet.* **19**, 191–207 (2018).

61. Stracker, T. H. & Petrini, J. H. J. The MRE11 complex: Starting from the ends. *Nat. Rev. Mol. Cell Biol.* **12**, 90–103 (2011).

62. Uziel, T. *et al.* Requirement of the MRN complex for ATM activation by DNA damage. *EMBO J.* **22**, 5612–5621 (2003).

63. Schiller, C. B., Seifert, F. U., Linke-Winnebeck, C. & Hopfner, K. P. Structural studies of DNA end detection and resection in homologous recombination. *Cold Spring Harb. Perspect. Biol.* **6**, 1–25 (2014).

64. Paull, T. T. & Gellert, M. The 3′ to 5′ exonuclease activity of Mre11 facilitates repair of DNA double-strand breaks. *Mol. Cell* **1**, 969–979 (1998).

65. Shibata, A. *et al.* DNA Double-Strand Break Repair Pathway Choice Is Directed by Distinct MRE11 Nuclease Activities. *Mol. Cell* **53**, 7–18 (2014).

66. Garcia, V., Phelps, S. E. L., Gray, S. & Neale, M. J. Bidirectional resection of DNA double-strand breaks by Mre11 and Exo1. *Nature* **479**, 241–244 (2011).

67. Cannavo, E. & Cejka, P. Sae2 promotes dsDNA endonuclease activity within Mre11-Ra1. Cannavo, E. & Cejka, P. Sae2 promotes dsDNA endonuclease activity within Mre11-Rad50-Xrs2 to resect DNA breaks. Nature 514, 122–125 (2014).d50-Xrs2 to resect DNA breaks. *Nature* **514**, 122–125 (2014).

68. Chen, L., Nievera, C. J., Lee, A. Y. L. & Wu, X. Cell cycle-dependent complex formation of BRCA1·CtIP·MRN is important for DNA double-strand break repair. *J. Biol. Chem.* **283**, 7713–7720 (2008).

69. Kowalczykowski, S. C. An overview of the molecular mechanismsof recombinational DNA repair. *Cold Spring Harb. Perspect. Biol.* **7**, 1–36 (2015).

70. Sugiyama, T. & Kowalczykowski, S. C. Rad52 protein associates with replication protein A (RPA)-single-stranded DNA to accelerate Rad51-mediated displacement of RPA and presynaptic complex formation. *J. Biol. Chem.* **277**, 31663–31672 (2002).

71. Jensen, R. B., Carreira, A. & Kowalczykowski, S. C. Purified human BRCA2 stimulates RAD51-mediated recombination. *Nature* **467**, 678–683 (2010).

72. Tavares, E. M., Wright, W. D., Heyer, W. D., Le Cam, E. & Dupaigne, P. In vitro role of Rad54 in Rad51-ssDNA filament-dependent homology search and synaptic complexes formation. *Nat. Commun.* **10**, 1–12 (2019).

73. Mcllwraith, M. J. *et al.* Human DNA polymerase η promotes DNA synthesis from strand invasion intermediates of homologous recombination. *Mol. Cell* **20**, 783–792 (2005).

74. Shah Punatar, R. & West, S. C. *Preparation and Resolution of Holliday Junction DNA Recombination Intermediates*. *Methods in Enzymology* vol. 600 (Elsevier Inc., 2018).

75. Punatar, R. S., Martin, M. J., Wyatt, H. D. M., Chan, Y. W. & West, S. C. Resolution of single and double Holliday junction recombination intermediates by GEN 1. *Proc. Natl. Acad. Sci. U. S. A.* **114**, 443–450 (2017).

76. Hustedt, N. & Durocher, D. The control of DNA repair by the cell cycle. *Nat. Cell Biol.* **19**, 1–9 (2017).

77. Bakhoum, S. F., Kabeche, L., Compton, D. A., Powell, S. N. & Bastians, H. Mitotic DNA Damage Response: At the Crossroads of Structural and Numerical Cancer Chromosome Instabilities. *Trends in Cancer* **3**, 225–234 (2017).

78. Symington, L. S. & Gautier, J. Double-strand break end resection and repair pathway choice. *Annu. Rev. Genet.* **45**, 247–271 (2011).

79. Falck, J. *et al.* CDK targeting of NBS1 promotes DNA-end resection, replication restart and homologous recombination. *EMBO Rep.* **13**, 561–568 (2012).

80. Huertas, P. & Jackason, S. P. Human CtIP mediates cell cycle control of DNA end resection and double strand break repair. *J. Biol. Chem.* **284**, 9558–9565 (2009).

81. Tomimatsu, N. *et al.* Phosphorylation of EXO1 by CDKs 1 and 2 regulates DNA end resection and repair pathway choice. *Nat. Commun.* **5**, 3561 (2014).

82. Munoz, I. M., Jowsey, P. A., Toth, R. & Rouse, J. Phospho-epitope binding by the BRCT domains of hPTIP controls multiple aspects of the cellular response to DNA damage. *Nucleic Acids Res.* **35**, 5312–5322 (2007).

83. Sharples, G. J. & Leach, D. R. F. Structural and functional similarities between the SbcCD proteins of Escherichia coli and the RAD50 and MRE11 (RAD32) recombination and repair proteins of yeast. *Mol. Microbiol.* **17**, 1215–1217 (1995).

84. Yoshida, T., Claverie, J. M. & Ogata, H. Mimivirus reveals Mre11/Rad50 fusion proteins with a sporadic distribution in eukaryotes, bacteria, viruses and plasmids. *Virol. J.* **8**, 427 (2011).

85. Paull, T. T. & Gellert, M. Nbs1 potentiates ATP-driven DNA unwinding and endonuclease cleavage by the Mre11/Rad50 complex. *Genes Dev.* **13**, 1276–1288 (1999).

86. Schiller, C. B. *et al.* Structure of Mre11-Nbs1 complex yields insights into ataxia-telangiectasia- like disease mutations and DNA damage signaling. *Nat. Struct. Mol. Biol.* **19**, 693–700 (2012).

87. Syed, A. & Tainer, J. A. The MRE11–RAD50–NBS1 Complex Conducts the Orchestration of Damage Signaling and Outcomes to Stress in DNA Replication and Repair. *Annu. Rev. Biochem.* **87**, 263–294 (2018).

88. Hopfner, K. P. *et al.* Structural biochemistry and interaction architecture of the DNA double-strand break repair Mre11 nuclease and Rad50-ATPase. *Cell* **105**, 473–485 (2001).

89. Déry, U. *et al.* A Glycine-Arginine Domain in Control of the Human MRE11 DNA Repair Protein. *Mol. Cell. Biol.* **28**, 3058–3069 (2008).

90. Williams, R. S. *et al.* Mre11 Dimers Coordinate DNA End Bridging and Nuclease Processing in Double-Strand-Break Repair. *Cell* **135**, 97–109 (2008).

91. Williams, G. J. *et al.* ABC ATPase signature helices in Rad50 link nucleotide state to Mre11 interface for DNA repair. *Nat. Struct. Mol. Biol.* **18**, 423–432 (2011).

92. Lammens, K. *et al.* The Mre11:Rad50 structure shows an ATP-dependent molecular clamp in DNA double-strand break repair. *Cell* **145**, 54–66 (2011).

93. Trujillo, K. M. & Sung, P. DNA Structure-specific Nuclease Activities in the Saccharomyces cerevisiae Rad50-Mre11 Complex. *J. Biol. Chem.* **276**, 35458–35464 (2001).

94. Trujillo, K. M., Yuan, S. S. F., Lee, E. Y. H. P. & Sung, P. Nuclease activities in a complex of human recombination and DNA repair factors Rad50, Mre11, and p95. *J. Biol. Chem.* **273**, 21447–21450 (1998).

95. Deshpande, R. A., Lee, J. H. & Paull, T. T. Rad50 ATPase activity is regulated by DNA ends and requires coordination of both active sites. *Nucleic Acids Res.* **45**, 5255–5268 (2017).

96. Deshpande, R. A., Lee, J. H., Arora, S. & Paull, T. T. Nbs1 Converts the Human Mre11/Rad50 Nuclease Complex into an Endo/Exonuclease Machine Specific for Protein-DNA Adducts. *Mol. Cell* **64**, 593–606 (2016).

97. Ogawa, H., Johzuka, K., Nakagawa, T., Leem, S.-H. & Hayashi, A. Functions of the yeast meiotic recombination genes, MREI I and MRE2. *Adv. Biophys* **31**, 67–76 (1995).

98. Hoa, N. N. *et al.* Mre11 Is Essential for the Removal of Lethal Topoisomerase 2 Covalent Cleavage Complexes. *Mol. Cell* **64**, 580–592 (2016).

99. Langerak, P., Mejia-Ramirez, E., Limbo, O. & Russell, P. Release of Ku and MRN from DNA ends by Mre11 nuclease activity and Ctp1 is required for homologous recombination repair of double-strand breaks. *PLoS Genet.* **7**, (2011).

100. Käshammer, L. *et al.* Mechanism of DNA End Sensing and Processing by the Mre11-Rad50 Complex. *Mol. Cell* 1–13 (2019) doi:10.1016/j.molcel.2019.07.035.

101. Kinoshita, E., Van Der Linden, E., Sanchez, H. & Wyman, C. RAD50, an SMC family member with multiple roles in DNA break repair: How does ATP affect function? *Chromosom. Res.* **17**, 277–288 (2009).

102. Hopfner, K.-P. *et al.* Structural Biology of Rad50 ATPase. *Cell* **101**, 789–800 (2000).

103. Hopfner, K. P. & Tainer, J. A. Rad50/SMC proteins and ABC transporters: Unifying concepts from high-resolution structures. *Curr. Opin. Struct. Biol.* **13**, 249–255 (2003).

104. Seifert, F. U., Lammens, K., Stoehr, G., Kessler, B. & Hopfner, K. Structural mechanism of ATP-dependent DNA binding and DNA end bridging by eukaryotic Rad50. *EMBO J.* **35**, 759–772 (2016).

105. Liu, Y. *et al.* ATP-dependent DNA binding, unwinding, and resection by the Mre11/Rad50 complex. *EMBO J.* **35**, 743–758 (2015).

106. Rojowska, A. *et al.* Structure of the Rad50 DNA double-strand break repair protein in complex with DNA. *EMBO J.* **33**, 2847–2859 (2014).

107. Trujillo, K. M. *et al.* Yeast xrs2 binds DNA and helps target rad50 and mre11 to DNA ends. *J. Biol. Chem.* **278**, 48957–48964 (2003).

108. Jager, M. De, Wyman, C., Gent, D. C. Van & Kanaar, R. DNA end-binding specificity of human Rad50 / Mre11. *Nucleic acids* **30**, (2002).

109. Alani, E., Padmore, R. & Kleckner, N. Analysis of wild-type and rad50 mutants of yeast suggests an intimate relationship between meiotic chromosome synapsis and recombination. *Cell* **61**, 419–436 (1990).

110. Chen, L. *et al.* Effect of amino acid substitutions in the Rad50 ATP binding domain on DNA double strand break repair in yeast. *J. Biol. Chem.* **280**, 2620–2627 (2005).

111. Moncalian, G. *et al.* The Rad50 Signature Motif: Essential to ATP Binding and Biological Function. *J. Mol. Biol.* **335**, 937–951 (2004).

112. Hohl, M. *et al.* The Rad50 coiled-coil domain is indispensable for Mre11 complex functions. *Nat. Struct. Mol. Biol.* **18**, 1124–1131 (2010).

113. Hopfner, K. P. *et al.* The Rad50 zinc-hook is a structure joining Mre11 complexes in DNA recombination and repair. *Nature* **418**, 562–566 (2002).

114. Park, Y. B. *et al.* Eukaryotic Rad50 functions as a rod-shaped dimer. *Nat. Struct. Mol. Biol.* **24**, 248–257 (2017).

115. Soh, Y., Basquin, J. & Gruber, S. A rod conformation of the Pyrococcus furiosus Rad50 coiled coil . *Proteins Struct. Funct. Bioinforma.* (2020) doi:10.1002/prot.26005.

116. Wiltzius, J. J. W., Hohl, M., Fleming, J. C. & Petrini, J. H. J. The Rad50 hook domain is a critical determinant of Mre11 complex functions. *Nat. Struct. Mol. Biol.* **12**, 403–407 (2005).

117. Zhang, Y., Zhou, J. & Lim, C. U. K. The role of NBS1 in DNA double strand break repair, telomere stability, and cell cycle checkpoint control. *Cell Res.* **16**, 45–54 (2006).

118. Becker, E., Meyer, V., Madaoui, H. & Guerois, R. Detection of a tandem BRCT in Nbs1 and Xrs2 with functional implications in the DNA damage response. *Bioinformatics* **22**, 1289–1292 (2006).

119. Durocher, D. & Jackson, S. P. The FHA domain. *FEBS Lett.* **513**, 58–66 (2002).

120. Leung, C. C. Y. & Glover, J. N. M. BRCT domains: Easy as one, two, three. *Cell Cycle* **10**, 2461–2470 (2011).

121. Williams, R. S. *et al.* Nbs1 Flexibly Tethers Ctp1 and Mre11-Rad50 to Coordinate DNA Double-Strand Break Processing and Repair. *Cell* **139**, 87–99 (2009).

122. Kobayashi, J. *et al.* NBS1 localizes to γ-H2AX foci through interaction with the FHA/BRCT domain. *Curr. Biol.* **12**, 1846–1851 (2002).

123. Tseng, S. F., Chang, C. Y., Wu, K. J. & Teng, S. C. Importin KPNA2 is required for proper nuclear localization and multiple functions of NBS1. *J. Biol. Chem.* **280**, 39594–39600 (2005).

124. Desai-Mehta, A., Cerosaletti, K. M. & Concannon, P. Distinct Functional Domains of Nibrin Mediate Mre11 Binding, Focus Formation, and Nuclear Localization. *Mol. Cell. Biol.* **21**, 2184–2191 (2001).

125. You, Z., Chahwan, C., Bailis, J., Hunter, T. & Russell, P. ATM Activation and Its Recruitment to Damaged DNA Require Binding to the C Terminus of Nbs1. *Mol. Cell. Biol.* **25**, 5363–5379 (2005).

126. Kim, J. H. *et al.* The Mre11-Nbs1 Interface Is Essential for Viability and Tumor Suppression. *Cell Rep.* **18**, 496–507 (2017).

127. Bruhn, C., Zhou, Z. W., Ai, H. & Wang, Z. Q. The essential function of the MRN complex in the resolution of endogenous replication intermediates. *Cell Rep.* **6**, 182–195 (2014).

128. Milman, N., Higuchi, E. & Smith, G. R. Meiotic DNA Double-Strand Break Repair Requires Two Nucleases, MRN and Ctp1, To Produce a Single Size Class of Rec12 (Spo11)-Oligonucleotide Complexes. *Mol. Cell. Biol.* **29**, 5998–6005 (2009).

129. Helmink, B. A. *et al.* MRN complex function in the repair of chromosomal Rag-mediated DNA double-strand breaks. *J. Exp. Med.* **206**, 669–679 (2009).

130. Blackford, A. N. & Jackson, S. P. ATM, ATR, and DNA-PK: The Trinity at the Heart of the DNA Damage Response. *Mol. Cell* **66**, 801–817 (2017).

131. Maser, R. S., Monsen, K. J., Nelms, B. E. & Petrini, J. H. hMre11 and hRad50 nuclear foci are induced during the normal cellular response to DNA double-strand breaks. *Mol. Cell. Biol.* **17**, 6087–6096 (1997).

132. Mirzoeva, O. K. & Petrini, J. H. J. DNA Damage-Dependent Nuclear Dynamics of the Mre11 Complex. *Mol. Cell. Biol.* **21**, 281–288 (2001).

133. Nelms, B. E. *et al.* In Situ Visualization of DNA Double-Strand Break Repair in Human Fibroblasts. **280**, 590–592 (1998).

134. Gottlieb, T. M. & Jackson, P. The DNA-Dependent Protein Ki for DNA Ends and AssocWbn with Ku Antigen. *Cell* **72**, 131–142 (1993).

135. Zou, L., Elledge, S. J., Zoua, L. & Elledgel, S. J. Sensing DNA Damage through ATRIP Recognition of RPA-ssDNA Complexes Published by : American Association for the Advancement of Science Stable URL : http://www.jstor.org/stable/3834467 Sensing DNA Damage Through ATRIP Recognition of RPA-ssDNA Complexes. **300**, 1542–1548 (2003).

136. Falck, J., Coates, J. & Jackson, S. P. Conserved modes of recruitment of ATM, ATR and DNA-PKcs to sites of DNA damage. *Nature* **434**, 605–611 (2005).

137. Hailemariam, S., Kumar, S. & Burgers, P. M. Activation of Tel1ATM kinase requires Rad50 ATPase and long nucleosome-free DNA but no DNA ends. *J. Biol. Chem.* **294**, 10120–10130 (2019).

138. Lee, J. H. *et al.* Ataxia Telangiectasia-Mutated (ATM) kinase activity is regulated by ATP-driven conformational changes in the Mre11/Rad50/Nbs1 (MRN) complex. *J. Biol. Chem.* **288**, 12840–12851 (2013).

139. Shiloh, Y. & Ziv, Y. The ATM protein kinase: regulating the cellular response to genotoxic stress, and more. *Nat. Rev. Mol. Cell Biol.* **14**, 197–210 (2013).

140. Duursma, A. M., Driscoll, R., Elias, J. E. & Cimprich, K. A. A Role for the MRN Complex in ATR Activation via TOPBP1 Recruitment. *Mol. Cell* **50**, 116–122 (2013).

141. Pabla, N., Huang, S., Mi, Q. S., Daniel, R. & Dong, Z. ATR-Chk2 signaling in p53 activation and DNA damage response during cisplatin-induced apoptosis. *J. Biol. Chem.* **283**, 6572–6583 (2008).

142. Lin, J. J. & Dutta, A. ATR pathway is the primary pathway for activating G2/M checkpoint induction after re-replication. *J. Biol. Chem.* **282**, 30357–30362 (2007).

143. Rass, E. *et al.* Role of Mre11 in chromosomal nonhomologous end joining in mammalian cells. *Nat. Struct. Mol. Biol.* **16**, 819–824 (2009).

144. Lamarche, B. J., Orazio, N. I. & Weitzman, M. D. The MRN complex in double-strand break repair and telomere maintenance. *FEBS Lett.* **584**, 3682–3695 (2010).

145. Zhang, X. & Paull, T. T. The Mre11/Rad50/Xrs2 complex and non-homologous end-joining of incompatible ends in S. cerevisiae. *DNA Repair (Amst).* **4**, 1281–1294 (2005).

146. Shay, J. W. & Wright, W. E. Telomeres and telomerase: three decades of progress. *Nat. Rev. Genet.* **20**, 299–309 (2019).

147. Moye, A. L. *et al.* Telomeric G-quadruplexes are a substrate and site of localization for human telomerase. *Nat. Commun.* **6**, (2015).

148. De Lange, T. Shelterin: The protein complex that shapes and safeguards human telomeres. *Genes Dev.* **19**, 2100–2110 (2005).

149. Longhese, M. P. DNA damage response at functional and dysfunctional telomeres. *Genes Dev.* **22**, 125–140 (2008).

150. Victorelli, S. & Passos, J. F. Telomeres and Cell Senescence - Size Matters Not. *EBioMedicine* **21**, 14–20 (2017).

151. Jafri, M. A., Ansari, S. A., Alqahtani, M. H. & Shay, J. W. Roles of telomeres and telomerase in cancer, and advances in telomerase-targeted therapies. *Genome Med.* **8**, (2016).

152. Mary Kironmai, K. & Muniyappa, K. Alteration of telomeric sequences and senescence caused by mutations in RAD50 of Saccharomyces cerevisiae. *Genes to Cells* **2**, 443–455 (1997).

153. Boulton, S. J. & Jackson, S. P. Components of the Ku-dependent non-homologous end-joining pathway are involved in telomeric length maintenance and telomeric silencing. *EMBO J.* **17**, 1819–1828 (1998).

154. Chamankhah, M. & Xiao, W. Formation of the yeast Mre11-Rad50-Xrs2 complex is correlated with DNA repair and telomere maintenance. *Nucleic Acids Res.* **27**, 2072–2079 (1999).

155. Takata, H., Tanaka, Y. & Matsuura, A. Late S phase-specific recruitment of Mre11 complex triggers hierarchical assembly of telomere replication proteins in Saccharomyces cerevisiae. *Mol. Cell* **17**, 573–583 (2005).

156. Lombard, D. B. & Guarente, L. Nijmegen breakage syndrome disease protein and MRE11 at PML nuclear bodies and meiotic telomeres. *Cancer Res.* **60**, 2331–2334 (2000).

157. Zhu, X., Küster, B., Mann, M., Petrini, J. H. J. & Lange, T. De. with TRF2 and human telomeres. *Nature* (2000).

158. Rai, R. *et al.* NBS1 Phosphorylation Status Dictates Repair Choice of Dysfunctional Telomeres. *Mol. Cell* **65**, 801-817.e4 (2017).

159. Ranganathan, V. *et al.* Rescue of a telomere length defect of Nijmegen breakage syndrome cells requires NBS and telomerase catalytic subunit. *Curr. Biol.* **11**, 962–966 (2001).

160. Attwooll, C. L., Akpınar, M. & Petrini, J. H. J. The Mre11 Complex and the Response to Dysfunctional Telomeres. *Mol. Cell. Biol.* **29**, 5540–5551 (2009).

161. Dimitrova, N. & de Lange, T. Cell Cycle-Dependent Role of MRN at Dysfunctional Telomeres: ATM Signaling-Dependent Induction of Nonhomologous End Joining (NHEJ) in G 1 and Resection-Mediated Inhibition of NHEJ in G 2 . *Mol. Cell. Biol.* **29**, 5552–5563 (2009).

162. Cesare, A. J. & Reddel, R. R. Alternative lengthening of telomeres: Models, mechanisms and implications. *Nat. Rev. Genet.* **11**, 319–330 (2010).

163. Rahman, S., Canny, M. D., Buschmann, T. A. & Latham, M. P. A Survey of Reported Disease-Related Mutations in the MRE11-RAD50-NBS1 Complex. *Cells* **9**, 1–25 (2020).

164. Taylor, A. M. R., Groom, A. & Byrd, P. J. Ataxia-telangiectasia-like disorder (ATLD) - Its clinical presentation and molecular basis. *DNA Repair (Amst).* **3**, 1219–1225 (2004).

165. Waltes, R. *et al.* Human RAD50 Deficiency in a Nijmegen Breakage Syndrome-like Disorder. *Am. J. Hum. Genet.* **84**, 605–616 (2009).

166. Tauchi, H., Matsuura, S., Kobayashi, J., Sakamoto, S. & Komatsu, K. Nijmegen breakage syndrome gene, NBS1, and molecular links to factors for genome stability. *Oncogene* **21**, 8967–8980 (2002).

167. Bian, L., Meng, Y., Zhang, M. & Li, D. MRE11-RAD50-NBS1 complex alterations and DNA damage response: Implications for cancer treatment. *Mol. Cancer* **18**, 1–14 (2019).

168. Wang, Y. Y., Hung, A. C., Lo, S., Hsieh, Y. C. & Yuan, S. S. F. MRE11 as a molecular signature and therapeutic target for cancer treatment with radiotherapy. *Cancer Lett.* **514**, 1–11 (2021).

169. Rothblum-Oviatt, C. *et al.* Ataxia telangiectasia: A review. *Orphanet J. Rare Dis.* **11**, 1–21 (2016).

170. Lustig, A. J. & Petes, T. D. Identification of yeast mutants with altered telomere structure. *Proc. Natl. Acad. Sci. U. S. A.* **83**, 1398–402 (1986).

171. Jansma, M. *et al.* Near-Complete Structure and Model of Tel1ATM from Chaetomium thermophilum Reveals a Robust Autoinhibited ATP State. *Structure* **28**, 83-95.e5 (2020).

172. Lee, J. H. & Paull, T. T. Cellular functions of the protein kinase ATM and their relevance to human disease. *Nat. Rev. Mol. Cell Biol.* **22**, 796–814 (2021).

173. Lee, J. H. & Paull, T. T. Direct Activation of the ATM Protein Kinase by the Mre11/Rad50/Nbs1 Complex. *Science (80-.).* **304**, 93–96 (2004).

174. Khoronenkova, S. V. & Dianov, G. L. ATM prevents DSB formation by coordinating SSB repair and cell cycle progression. *Proc. Natl. Acad. Sci.* **112**, 3997–4002 (2015).

175. Lin, C. P., Ban, Y., Lyu, Y. L. & Liu, L. F. Proteasome-dependent processing of topoisomerase I-DNA adducts into DNA double strand breaks at arrested replication forks. *J. Biol. Chem.* **284**, 28084–28092 (2009).

176. Sordet, O., Nakamura, A. J., Redon, C. E. & Pommier, Y. DNA double-strand breaks and ATM activation by transcription-blocking DNA lesions. *Cell Cycle* **9**, 274–278 (2010).

177. Xie, X. *et al.* Atm at the crossroads of reactive oxygen species and autophagy. *Int. J. Biol. Sci.* **17**, 3080–3090 (2021).

178. Jin, M. H. & Oh, D. Y. ATM in DNA repair in cancer. *Pharmacol. Ther.* **203**, 107391 (2019).

179. Zakian, V. A. ATM-related genes: What do they tell us about functions of the human gene? *Cell* **82**, 685–687 (1995).

180. Hunter, T. When is a lipid kinase not a lipid kinase? When it is a protein kinase. *Cell* **83**, 1–4 (1995).

181. Smith, G. C. M. & Jackson, S. P. *The PIKK family of protein kinases*. *Handbook of Cell Signaling, 2/e* vol. 2 (Elsevier Inc., 2010).

182. Yue, X., Bai, C., Xie, D., Ma, T. & Zhou, P. K. DNA-PKcs: A Multi-Faceted Player in DNA Damage Response. *Front. Genet.* **11**, (2020).

183. Chang, H. H. Y. & Lieber, M. R. Structure-Specific nuclease activities of Artemis and the Artemis: DNA-PKcs complex. *Nucleic Acids Res.* **44**, 4991–4997 (2016).

184. Björkman, A. *et al.* DNA-PKcs Is Involved in Ig Class Switch Recombination in Human B Cells. *J. Immunol.* **195**, 5608–5615 (2015).

185. Ashley, A. K. *et al.* DNA-PK phosphorylation of RPA32 Ser4/Ser8 regulates replication stress checkpoint activation, fork restart, homologous recombination and mitotic catastrophe. *DNA Repair (Amst).* **21**, 131–139 (2014).

186. Sui, J., Zhang, S. & Chen, B. P. C. DNA-dependent protein kinase in telomere maintenance and protection. *Cell. Mol. Biol. Lett.* **25**, 1–14 (2020).

187. Puustinen, P. *et al.* DNA-dependent protein kinase regulates lysosomal AMP-dependent protein kinase activation and autophagy. *Autophagy* **16**, 1871–1888 (2020).

188. Ferguson, B. J., Mansur, D. S., Peters, N. E., Ren, H. & Smith, G. L. DNA-PK is a DNA sensor for IRF-3-dependent innate immunity. *Elife* **2012**, 1–17 (2012).

189. Saldivar, J. C., Cortez, D. & Cimprich, K. A. The essential kinase ATR: Ensuring faithful duplication of a challenging genome. *Nat. Rev. Mol. Cell Biol.* **18**, 622–636 (2017).

190. Yazinski, S. A. & Zou, L. Functions, Regulation, and Therapeutic Implications of the ATR Checkpoint Pathway. *Annu. Rev. Genet.* **50**, 155–173 (2016).

191. Couch, F. B. *et al.* ATR phosphorylates SMARCAL1 to prevent replication fork collapse. *Genes Dev.* **27**, 1610–1623 (2013).

192. Nghiem, P., Park, P. K., Kim, Y., Vaziri, C. & Schreiber, S. L. Inhibition Selectively Ser To Cells Deficient Lethal Prem Chromatin Condensation Isitizes Ature. **98**, 9092–9097 (2014).

193. Yamashita, A., Ohnishi, T., Kashima, I., Taya, Y. & Ohno, S. Human SMG-1, a novel phosphatidylinositol 3-kinase-related protein kinase, associates with components of the mRNA surveillance complex and is involved in the regulation of nonsense-mediated mRNA decay. *Genes Dev.* **15**, 2215–2228 (2001).

194. Kurosaki, T. & Maquat, L. E. Nonsense-mediated mRNA decay in humans at a glance. *J. Cell Sci.* **129**, 461–467 (2016).

195. Saxton, R. A. & Sabatini, D. M. mTOR Signaling in Growth, Metabolism, and Disease. *Cell* **168**, 960–976 (2017).

196. Le Bacquer, O. *et al.* mTORC1 and mTORC2 regulate insulin secretion through Akt in INS-1 cells. *J. Endocrinol.* **216**, 21–29 (2013).

197. Dazert, E. & Hall, M. N. MTOR signaling in disease. *Curr. Opin. Cell Biol.* **23**, 744–755 (2011).

198. Murr, R., Vaissière, T., Sawan, C., Shukla, V. & Herceg, Z. Orchestration of chromatin-based processes: Mind the TRRAP. *Oncogene* **26**, 5358–5372 (2007).

199. Leduc, C. *et al.* Tissue-specific inactivation of HAT cofactor TRRAP reveals its essential role in B cells. *Cell Cycle* **13**, 1583–1589 (2014).

200. Li, H., Cuenin, C., Murr, R., Wang, Z. Q. & Herceg, Z. HAT cofactor Trrap regulates the mitotic checkpoint by modulation of Mad1 and Mad2 expression. *EMBO J.* **23**, 4824–4834 (2004).

201. Park, J., Kunjibettu, S., McMahon, S. B. & Cole, M. D. The ATM-related domain of TRRAP is required for histone acetyltransferase recruitment and Myc-dependent oncogenesis. *Genes Dev.* **15**, 1619–1624 (2001).

202. Sedelnikova, O. A., Pilch, D. R., Redon, C. & Bonner, W. M. Histone H2AX in DNA damage and repair. *Cancer Biol. Ther.* **2**, 233–235 (2003).

203. Wang, H. *et al.* The Interaction of CtIP and Nbs1 Connects CDK and ATM to Regulate HR-Mediated Double-Strand Break Repair. *PLoS Genet.* **9**, 25–27 (2013).

204. Bolderson, E. *et al.* Phosphorylation of Exo1 modulates homologous recombination repair of DNA double-strand breaks. *Nucleic Acids Res.* **38**, 1821–1831 (2010).

205. Ababou, M. *et al.* ATM-dependent phosphorylation and accumulation of endogenous BLM protein in response to ionizing radiation. *Oncogene* **19**, 5955–5963 (2000).

206. Ahlskog, J. K., Larsen, B. D., Achanta, K. & Sørensen, C. S. ATM / ATR -mediated phosphorylation of PALB 2 promotes RAD 51 function . *EMBO Rep.* **17**, 671–681 (2016).

207. Matsuoka, S., Huang, M. & Elledge, S. J. Linkage of ATM to Cell Cycle Regulation by the Chk2 Protein Kinase Published by : American Association for the Advancement of Science Stable URL : http://www.jstor.org/stable/2897020 Linked references are available on JSTOR for this article : Linkage of A. **282**, 1893–1897 (2016).

208. Hirao, A. *et al.* Linked references are available on JSTOR for this article : Activation of p53 by the Checkpoint Kinase Chk2 DNA DNA Damage-Induced Damage-Induced. **287**, 1824–1827 (2016).

209. Chen, B. P. C. *et al.* Ataxia telangiectasia mutated (ATM) is essential for DNA-PKcs phosphorylations at the Thr-2609 cluster upon DNA double strand break. *J. Biol. Chem.* **282**, 6582–6587 (2007).

210. Riballo, E. *et al.* A pathway of double-strand break rejoining dependent upon ATM, Artemis, and proteins locating to γ-H2AX foci. *Mol. Cell* **16**, 715–724 (2004).

211. Imamichi, S., Sharma, M. K., Kamdar, R. P., Fukuchi, M. & Matsumoto, Y. Ionizing radiation-induced XRCC4 phosphorylation is mediated through ATM in addition to DNA-PK. *Proc. Japan Acad. Ser. B Phys. Biol. Sci.* **90**, 365–372 (2014).

212. Yu, Y. *et al.* DNA-PK and ATM phosphorylation sites in XLF/Cernunnos are not required for repair of DNA double strand breaks. *DNA Repair (Amst).* **7**, 1680–1692 (2008).

213. Zhou, Y. *et al.* Regulation of the DNA Damage Response by DNA-PKcs Inhibitory Phosphorylation of ATM. *Mol. Cell* **65**, 91–104 (2017).

214. Pommier, Y., Sun, Y., Huang, S. Y. N. & Nitiss, J. L. Roles of eukaryotic topoisomerases in transcription, replication and genomic stability. *Nat. Rev. Mol. Cell Biol.* **17**, 703–721 (2016).

215. Das, B. B. *et al.* Optimal function of the DNA repair enzyme TDP1 requires its phosphorylation by ATM and/or DNA-PK. *EMBO J.* **28**, 3667–3680 (2009).

216. Álvarez-Quilón, A. *et al.* Endogenous topoisomerase II-mediated DNA breaks drive thymic cancer predisposition linked to ATM deficiency. *Nat. Commun.* **11**, 1–14 (2020).

217. Khoronenkova, S. V. & Dianov, G. L. ATM prevents DSB formation by coordinating SSB repair and cell cycle progression. *Proc. Natl. Acad. Sci. U. S. A.* **112**, 3997–4002 (2015).

218. Chou, W. C. *et al.* Chk2-dependent phosphorylation of XRCC1 in the DNA damage response promotes base excision repair. *EMBO J.* **27**, 3140–3150 (2008).

219. Rabanal-Ruiz, Y., Otten, E. G. & Korolchuk, V. I. MTORC1 as the main gateway to autophagy. *Essays Biochem.* **61**, 565–584 (2017).

220. Zhang, J. *et al.* ATM functions at the peroxisome to induce pexophagy in response to ROS. *Nat. Cell Biol.* **17**, 1259–1269 (2015).

221. Stagni, V., Cirotti, C. & Barilà, D. Ataxia-telangiectasia mutated kinase in the control of oxidative stress, mitochondria, and autophagy in cancer: A maestro with a large orchestra. *Front. Oncol.* **8**, 1–6 (2018).

222. Zhang, Y. *et al.* Mitochondrial redox sensing by the kinase ATM maintains cellular antioxidant capacity. *Sci. Signal.* **11**, (2018).

223. Lee, J. H., Ryu, S. W., Ender, N. A. & Paull, T. T. Poly-ADP-ribosylation drives loss of protein homeostasis in ATM and Mre11 deficiency. *Mol. Cell* **81**, 1515-1533.e5 (2021).

224. Choi, M., Kipps, T. & Kurzrock, R. ATM mutations in cancer: Therapeutic implications. *Mol. Cancer Ther.* **15**, 1781–1791 (2016).

225. Stakyte, K. *et al.* Molecular basis of human ATM kinase inhibition. *Nat. Struct. Mol. Biol.* **28**, 789–798 (2021).

226. Song, L. *et al.* MiR-18a impairs DNA damage response through downregulation of Ataxia telangiectasia mutated (ATM) kinase. *PLoS One* **6**, (2011).

227. Le Guezennec, X. & Bulavin, D. V. WIP1 phosphatase at the crossroads of cancer and aging. *Trends Biochem. Sci.* **35**, 109–114 (2010).

228. Begam, N., Jamil, K. & Raju, S. G. Promoter hypermethylation of the ATM gene as a novel biomarker for breast cancer. *Asian Pacific J. Cancer Prev.* **18**, 3003–3009 (2017).

229. Ripka, S. *et al.* CUX1: Target of Akt signalling and mediator of resistance to apoptosis in pancreatic cancer. *Gut* **59**, 1101–1110 (2010).

230. Vadnais, C. *et al.* CUX1 transcription factor is required for optimal ATM/ATR-mediated responses to DNA damage. *Nucleic Acids Res.* **40**, 4483–4495 (2012).

231. Cremona, C. A. & Behrens, A. ATM signalling and cancer. *Br. Dent. J.* **217**, 3351–3360 (2014).

232. Pazolli, E. *et al.* Chromatin remodeling underlies the senescence- associated secretory phenotype of tumor stromal fibroblasts that supports cancer progression. *Cancer Res.* **72**, 2251–2261 (2012).

233. Lavin, M. F. & Yeo, A. J. Clinical potential of ATM inhibitors. *Mutat. Res. - Fundam. Mol. Mech. Mutagen.* **821**, 111695 (2020).

234. Hickson, I. *et al.* Identification and characterization of a novel and specific inhibitor of the ataxia-telangiectasia mutated kinase ATM. *Cancer Res.* **64**, 9152–9159 (2004).

235. Herrero, A. B. & Gutiérrez, N. C. Targeting ongoing DNA damage in multiple myeloma: Effects of DNA damage response inhibitors on plasma cell survival. *Front. Oncol.* **7**, (2017).

236. Weber, A. M. & Ryan, A. J. ATM and ATR as therapeutic targets in cancer. *Pharmacol. Ther.* **149**, 124–138 (2015).

237. Li, K. *et al.* ATM inhibition induces synthetic lethality and enhances sensitivity of PTEN-deficient breast cancer cells to cisplatin. *Exp. Cell Res.* **366**, 24–33 (2018).

238. Batey, M. A. *et al.* Preclinical evaluation of a novel ATM inhibitor, KU59403, In Vitro and In Vivo in p53 functional and dysfunctional models of human cancer. *Mol. Cancer Ther.* **12**, 959–967 (2013).

239. Rainey, M. D., Charlton, M. E., Stanton, R. V. & Kastan, M. B. Transient inhibition of ATM kinase is sufficient to enhance cellular sensitivity to ionizing radiation. *Cancer Res.* **68**, 7466–7474 (2008).

240. Shen, M. *et al.* Inhibition of ATM reverses EMT and decreases metastatic potential of cisplatin-resistant lung cancer cells through JAK/STAT3/PD-L1 pathway. *J. Exp. Clin. Cancer Res.* **38**, 1–14 (2019).

241. Pike, K. G. *et al.* The Identification of Potent, Selective, and Orally Available Inhibitors of Ataxia Telangiectasia Mutated (ATM) Kinase: The Discovery of AZD0156 (8-{6-[3-(Dimethylamino)propoxy]pyridin-3-yl}-3-methyl-1-(tetrahydro-2 H-pyran-4-yl)-1,3-dihydro-2 H-imidazo[4. *J. Med. Chem.* **61**, 3823–3841 (2018).

242. Durant, S. T. *et al.* The brain-penetrant clinical ATM inhibitor AZD1390 radiosensitizes and improves survival of preclinical brain tumor models. *Sci. Adv.* **4**, (2018).

243. Morgado-Palacin, I. *et al.* Targeting the kinase activities of ATR and ATM exhibits antitumoral activity in mouse models of MLL-rearranged AML. *Sci. Signal.* **9**, 24–27 (2016).

244. Moreno-Herrero, F. *et al.* Mesoscale conformational changes in the DNA-repair complex Rad50/Mre11/Nbs1 upon binding DNA. *Nature* **437**, 440–443 (2005).

245. Zabolotnaya, E. *et al.* Modes of action of the archaeal Mre11/Rad50 DNA-repair complex revealed by fast-scan atomic force microscopy. *Proc. Natl. Acad. Sci.* 201915598 (2020) doi:10.1073/pnas.1915598117.

246. Canny, M. D. & Latham, M. P. LRET-derived HADDOCK structural models describe the conformational heterogeneity required for DNA cleavage by the Mre11-Rad50 DNA damage repair complex. *Elife* **11**, 1–22 (2022).

247. Saathoff, J. H., Käshammer, L., Lammens, K., Byrne, R. T. & Hopfner, K. P. The bacterial Mre11–Rad50 homolog SbcCD cleaves opposing strands of DNA by two chemically distinct nuclease reactions. *Nucleic Acids Res.* **46**, 11303–11314 (2018).

248. Furuse, M. *et al.* Distinct roles of two separable in vitro activities of yeast Mre11 in mitotic and meiotic recombination. *EMBO J.* **17**, 6412–6425 (1998).

249. Myler, L. R. *et al.* Single-Molecule Imaging Reveals How Mre11-Rad50-Nbs1 Initiates DNA Break Repair. *Mol. Cell* **67**, 891-898.e4 (2017).

250. Na, J. *et al.* SPRTN protease-cleaved MRE11 decreases DNA repair and radiosensitises cancer cells. *Cell Death Dis.* (2021) doi:10.1038/s41419-021-03437-w.

251. Forey, R. *et al.* A Role for the Mre11-Rad50-Xrs2 Complex in Gene Expression and Chromosome Organization. *Mol. Cell* **81**, 183-197.e6 (2021).

252. Salifou, K. *et al.* Chromatin-associated MRN complex protects highly transcribing genes from genomic instability. *Sci. Adv.* **7**, 1–15 (2021).

253. Lloyd, J. *et al.* A Supramodular FHA/BRCT-Repeat Architecture Mediates Nbs1 Adaptor Function in Response to DNA Damage. *Cell* **139**, 100–111 (2009).

254. Sakamoto, S. *et al.* Homologous recombination repair is regulated by domains at the N- and C-terminus of NBS1 and is dissociated with ATM functions. *Oncogene* **26**, 6002–6009 (2007).

255. Yates, L. A. *et al.* Cryo-EM Structure of Nucleotide-Bound Tel1ATM Unravels the Molecular Basis of Inhibition and Structural Rationale for Disease-Associated Mutations. *Structure* **28**, 96-104.e3 (2020).

256. Warren, C. & Pavletich, N. P. Structure of the human ATM kinase and mechanism of Nbs1 binding. *Elife* **11**, 1–23 (2022).

257. Lee, J. H. & Paull, T. T. ATM activation by DNA double-strand breaks through the Mre11-Rad50-Nbs1 complex. *Science (80-.).* **308**, 551–554 (2005).

258. Kim, J. H. *et al.* The Mre11-Nbs1 Interface Is Essential for Viability and Tumor Suppression. *Cell Rep.* **18**, 496–507 (2017).

259. Madeira, F. *et al.* Search and sequence analysis tools services from EMBL-EBI in 2022. *Nucleic Acids Res.* 1–4 (2022) doi:10.1093/nar/gkac240.

260. Drozdetskiy, A., Cole, C., Procter, J. & Barton, G. J. JPred4: A protein secondary structure prediction server. *Nucleic Acids Res.* **43**, W389–W394 (2015).

261. Hohl, M. *et al.* Interdependence of the Rad50 Hook and Globular domain functions. *Mol. Cell* **57**, 479–491 (2015).

262. De Jager, M. *et al.* Human Rad50/Mre11 is a flexible complex that can tether DNA ends. *Mol. Cell* **8**, 1129–1135 (2001).

263. Soh, Y. M., Basquin, J. & Gruber, S. A rod conformation of the Pyrococcus furiosus Rad50 coiled coil. *Proteins Struct. Funct. Bioinforma.* **89**, 251–255 (2021).

264. Gatei, M. *et al.* ATM protein-dependent phosphorylation of Rad50 protein Regulates DNA repair and cell cycle control. *J. Biol. Chem.* **286**, 31542–31556 (2011).

265. Gatei, M., Kijas, A. W., Biard, D., Dörk, T. & Lavin, M. F. RAD50 phosphorylation promotes ATR downstream signaling and DNA restart following replication stress. *Hum. Mol. Genet.* **23**, 4232–4248 (2014).

266. Tatebe, H. *et al.* Rad50 zinc hook functions as a constitutive dimerization module interchangeable with SMC hinge. *Nat. Commun.* 1–11 doi:10.1038/s41467-019-14025-0.

267. Williams, R. S. & Tainer, J. A. A nanomachine for making ends meet: MRN is a flexing scaffold for the repair of DNA double-strand breaks. *Mol. Cell* **19**, 724–726 (2005).

268. Seeber, A. *et al.* RPA Mediates Recruitment of MRX to Forks and Double-Strand Breaks to Hold Sister Chromatids Together. *Mol. Cell* **64**, 951–966 (2016).

269. Kissling, V. M. *et al.* Mre11-Rad50 oligomerization promotes DNA double-strand break repair. 1–16 (2022) doi:10.1038/s41467-022-29841-0.

270. Banani, S. F., Lee, H. O., Hyman, A. A. & Rosen, M. K. Biomolecular condensates: Organizers of cellular biochemistry. *Nat. Rev. Mol. Cell Biol.* **18**, 285–298 (2017).

271. Kilic, S. *et al.* Phase separation of 53 BP 1 determines liquid-like behavior of DNA repair compartments . *EMBO J.* **38**, 1–17 (2019).

272. Oshidari, R. *et al.* DNA repair by Rad52 liquid droplets. *Nat. Commun.* **11**, (2020).

273. Frattini, C. *et al.* TopBP1 assembles nuclear condensates to switch on ATR signaling. *Mol. Cell* **81**, 1231-1245.e8 (2021).

274. Wang, Y. *et al.* MRNIP condensates promote DNA double-strand break sensing and end resection Yun-Long. *Nat. Commun.* (2022) doi:10.1038/s41467-022-30303-w.

275. Smith, G. C. M. *et al.* Purification and DNA binding properties of the ataxia-telangiectasia gene product ATM. *Proc. Natl. Acad. Sci.* **96**, 11134–11139 (1999).

276. Dupré, A., Boyer-Chatenet, L. & Gautier, J. Two-step activation of ATM by DNA and the Mre11-Rad50-Nbs1 complex. *Nat. Struct. Mol. Biol.* **13**, 451–457 (2006).

277. Llorca, O., Rivera-Calzada, A., Grantham, J. & Willison, K. R. Electron microscopy and 3D reconstructions reveal that human ATM kinase uses an arm-like domain to clamp around double-stranded DNA. *Oncogene* **22**, 3867–3874 (2003).

278. Seidel, J. J., Anderson, C. M. & Blackburn, E. H. A Novel Tel1/ATM N-Terminal Motif, TAN, Is Essential for Telomere Length Maintenance and a DNA Damage Response. *Mol. Cell. Biol.* **28**, 5736–5746 (2008).

279. You, Z., Bailis, J. M., Johnson, S. A., Dilworth, S. M. & Hunter, T. Rapid activation of ATM on DNA flanking double-strand breaks. *Nat. Cell Biol.* **9**, 1311–1318 (2007).

280. Baretić, D. *et al.* Structures of closed and open conformations of dimeric human ATM. *Sci. Adv.* **3**, e1700933 (2017).

281. Wang, X. *et al.* Structure of the intact ATM/Tel1 kinase. *Nat. Commun.* **7**, 1–8 (2016).

282. Xiao, J. *et al.* Structural insights into the activation of ATM kinase. *Cell Res.* **0**, 1–3 (2019).

283. Langer, L. M., Gat, Y., Bonneau, F. & Conti, E. Structure of substrate-bound SMG1-8-9 kinase complex reveals molecular basis for phosphorylation specificity. *Elife* **9**, 1–14 (2020).

284. Xin, J. *et al.* Structural basis of allosteric regulation of Tel1 / ATM kinase. *Cell Res.* 1–11 (2019) doi:10.1038/s41422-019-0176-1.

285. Yang, H. *et al.* Mechanisms of mTORC1 activation by RHEB and inhibition by PRAS40. *Nature* **552**, 368–373 (2017).

286. Chen, X. *et al.* Structure of an activated DNA-PK and its implications for NHEJ. *Mol. Cell* **81**, 801-810.e3 (2021).

287. Rao, Q. *et al.* Cryo-EM structure of human ATR-ATRIP complex. *Cell Res.* **28**, 143–156 (2018).

288. Sharif, H. *et al.* Cryo-EM structure of the DNA-PK holoenzyme. *Proc. Natl. Acad. Sci.* **114**, 7367–7372 (2017).

289. Chaplin, A. K. *et al.* Dimers of DNA-PK create a stage for DNA double-strand break repair. *Nat. Struct. Mol. Biol.* (2020) doi:10.1038/s41594-020-00517-x.

290. Kozlov, S. V. *et al.* Autophosphorylation and ATM activation: Additional sites add to the complexity. *J. Biol. Chem.* **286**, 9107–9119 (2011).

291. Lee, J. H. & Paull, T. T. Activation and regulation of ATM kinase activity in response to DNA double-strand breaks. *Oncogene* **26**, 7741–7748 (2007).

292. Sun, Y., Xu, Y., Roy, K. & Price, B. D. DNA Damage-Induced Acetylation of Lysine 3016 of ATM Activates ATM Kinase Activity. *Mol. Cell. Biol.* **27**, 8502–8509 (2007).

293. Sun, Y., Jiang, X., Chen, S., Fernandes, N. & Price, B. D. A role for the Tip60 histone acetyltransferase in the acetylation and activation of ATM. *Proc. Natl. Acad. Sci. U. S. A.* **102**, 13182–13187 (2005).

294. Kastan, M. & Bakkenist, C. DNA damage activates ATM through intermolecular autophosphorylation and dimmer association. *Nature* **421**, 499–506 (2003).

295. Dohmen, A. J. C. *et al.* Identification of a novel ATM inhibitor with cancer cell specific radiosensitization activity. *Oncotarget* **8**, 73925–73937 (2017).

296. Min, A. *et al.* AZD6738, A novel oral inhibitor of ATR, induces synthetic lethality with ATM deficiency in gastric cancer cells. *Mol. Cancer Ther.* **16**, 566–577 (2017).

297. Schmitt, A. *et al.* ATM deficiency is associated with sensitivity to PARP1- and ATR inhibitors in lung adenocarcinoma. *Cancer Res.* **77**, 3040–3056 (2017).

298. Yang, H. *et al.* mTOR kinase structure, mechanism and regulation by the rapamycin-binding domain HHS Public Access. *Nature* **497**, 217–223 (2013).

299. Lempiäinen, H. & Halazonetis, T. D. Emerging common themes in regulation of PIKKs and PI3Ks. *EMBO J.* **28**, 3067–3073 (2009).

300. Liu, Y. & Gray, N. S. Rational design of inhibitors that bind to inactive kinase conformations. *Nat. Chem. Biol.* **2**, 358–364 (2006).

301. Martinez, R., Defnet, A. & Shapiro, P. Avoiding or Co-Opting ATP Inhibition: Overview of Type III, IV, V, and VI Kinase Inhibitors BT - Next Generation Kinase Inhibitors: Moving Beyond the ATP Binding/Catalytic Sites. in (ed. Shapiro, P.) 29–59 (Springer International Publishing, 2020). doi:10.1007/978-3-030-48283-1_3.

Acknowledgements

Firstly, I would like to thank my supervisor Prof. Dr. Karl-Peter Hopfner for providing me with an opportunity to do my PhD research in his laboratory and work on challenging and very exciting projects. I benefited a lot from our scientific discussions and his constant influx of new ideas. The amount of freedom and resources that I was given during my PhD allowed me to explore various biological questions, learn new skills and grow as a scientist.

I would also like to thank the members of my thesis advisory committee, Prof. Dr. Roland Beckmann and Prof. Dr. Johannes Stigler, for their interest in my work and fruitful TAC meetings.

Special thanks go to my lab partner Matthias Rotheneder, who stayed optimistic and motivated when experiments were not working and it was very hard to see the light at the end of the tunnel. I could have never had such a successful PhD without us working together.

I was lucky to work with great collogues during my time in the Hopfner lab. I am grateful to Robert Byrne and Aaron Alt for welcoming me into the lab and supervising my initial work. Huge thanks to Katja Lammens for teaching me a lot about cryo-EM and X-ray crystallography, for (literally) always being available to answer the most ridiculous questions of mine and for just keeping it cool during the stressful times. I am also very thankful to Joe Bartho for sharing his chocolate supplies with me and all his contributions to the cryo-EM side of the projects: from restarting the microscope at 3 am to invaluable advice when it came to the data processing. In addition, I want to thank Katja and Joe for all the hours spent model-building ATM and MRN. I am grateful to Erik van de Logt for willing to share his precious MRN preparations and his contribution to ATM kinase assay development. I want to acknowledge Brigitte Keßler not only for all the cloning, protein expression and purification that she did, but also for organization of the lab and making sure that we do not exceed our budget. I am also thankful to other members of DNA repair subgroup for great discussions and motivating environment: Lisa Käshammer, Fabian Gut, Hinnerk Saathoff and Yilan Fan.

I am very thankful for great scientific collaborators that I had a pleasure to work with during my PhD. Thanks to Dr. Ulrich Grädler from Merck KGaA for a very successful collaboration on ATM inhibitor story. I would like to thank Dr. Barbara Steigenberger from MPI of Biochemistry, who did numerous mass-spectrometry experiments for our MRN project. Thanks to Dr. Christophe Jung for making our anisotropy experiments with MRN complex possible and helping us understand our protein better. I am also very grateful for Dr. Wynand Roos from Institute of Toxicology at University Medicine Mainz for the DNA comet assays that he performed to analyze our Rad50 zinc-hook mutants.

Many thanks also go to Dr. Petra Runge-Wollmann and Dr. Beate Hafner for doing a great job coordinating the GRK1721 graduate school, which was such a great addition to my PhD life.

I am immensely grateful to my parents and grandparents who supported me unconditionally throughout my PhD journey. *Didžiausias ačiū mano šeimai, už beatodairišką tikėjimą manimi ir palaikymą. Myliu.* I would also like to thank my boyfriend for his patience, for always being there for me when I needed the most and, of course, for the late-night food deliveries to the lab. I am also grateful to my friends for their support and encouragements.